Okinawa Institute of Science and Technology
Graduate University

Thesis submitted for the degree

Doctor of Philosophy

Simulations of Multiphase Turbulent Flows

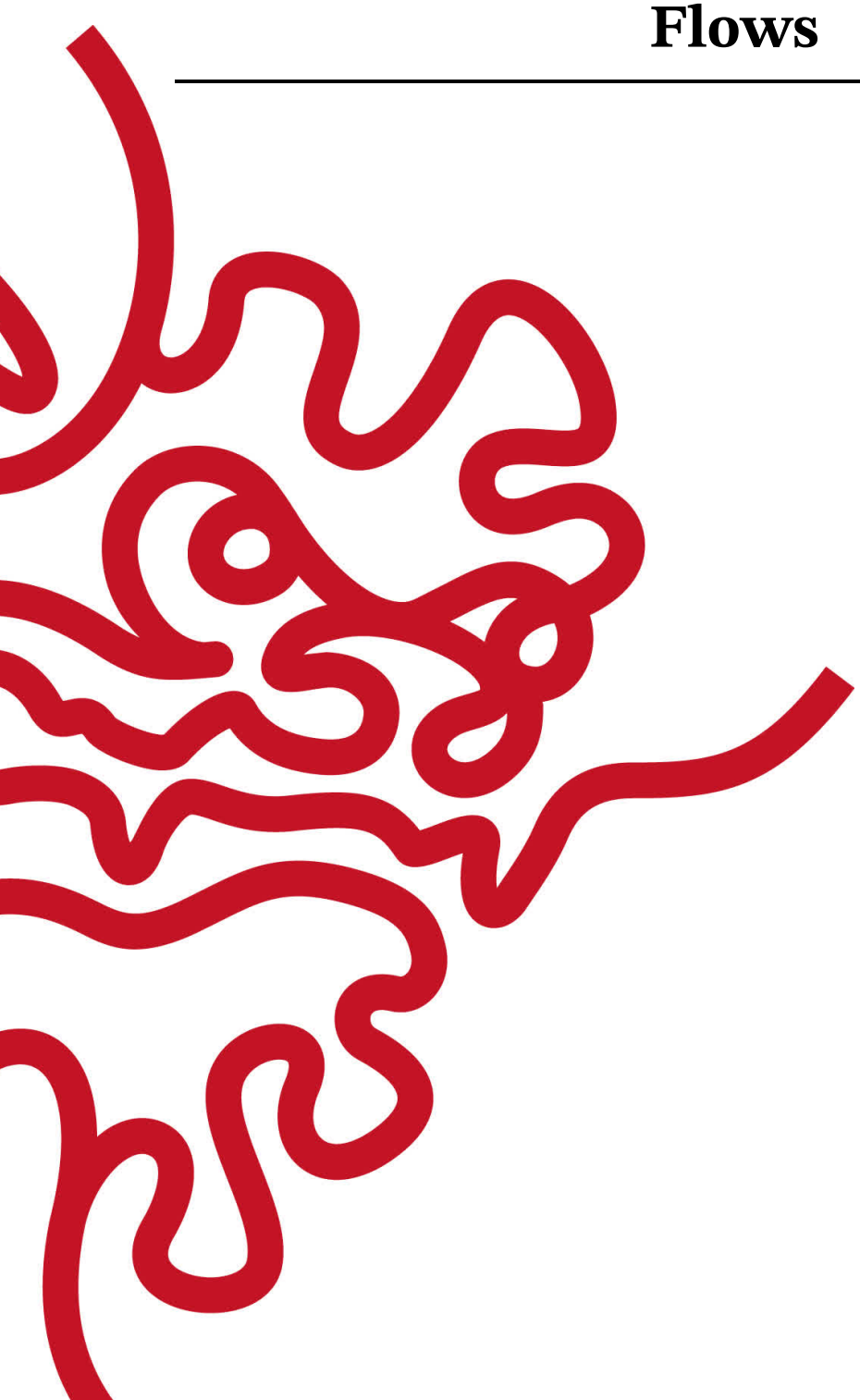

by

Ianto Cannon

Supervisor: **Marco E. Rosti**

November 2023

Declaration of Original and Sole Authorship

I, Ianto Cannon, declare that this thesis entitled *Simulations of Multiphase Turbulent Flows* and the data presented in it are original and my own work.

I confirm that:

- No part of this work has previously been submitted for a degree at this or any other university.
- References to the work of others have been clearly acknowledged. Quotations from the work of others have been clearly indicated, and attributed to them.
- In cases where others have contributed to part of this work, such contribution has been clearly acknowledged and distinguished from my own work.
- None of this work has been published elsewhere, with the exception of the following:

  Abdelgawad*, M. S., Cannon*, I., & Rosti, M. E. (2023). Scaling and intermittency in turbulent flows of elastoviscoplastic fluids. *Nature Physics*, 1–5. https://doi.org/10.1038/s41567-023-02018-2

  Cannon, I., Izbassarov, D., Tammisola, O., Brandt, L., & Rosti, M. E. (2021). The effect of droplet coalescence on drag in turbulent channel flows. *Physics of Fluids*, *33*(8), 085112. https://doi.org/10.1063/5.0058632

  Olivieri, S., Cannon, I., & Rosti, M. E. (2022). The effect of particle anisotropy on the modulation of turbulent flows. *Journal of Fluid Mechanics*, *950*, R2. https://doi.org/10.1017/jfm.2022.832

- I have permission to reprint the published manuscripts, which are licensed under the Creative Commons License (CC BY 4.0).

Date: November 2023

Signature: Ianto Cannon

*These authors contributed equally

Abstract

The flow of an incompressible fluid can be described exactly and succinctly using the Navier-Stokes equation. However, the nonlinearity of this equation leads to flow structures with detail at many length scales, known as turbulence. The only exact theory in turbulence was made in 1941 by Kolmogorov. In this thesis, we probe Kolmogorov's predictions in the case of multiphase systems by making direct numerical simulations of droplets, particles, and solid phases in turbulent flows.

Firstly, we show how the coalescence of droplets can reduce drag in a turbulent channel flow. Following on from this, in the remainder of the thesis we look more closely at the turbulent energy cascade using simulations of statistically homogeneous and isotropic flows. We show that the balance of turbulent forces and surface tension means large and small droplets form distinct shapes. Considering particles in turbulent flows, we see that isotropic and anisotropic particles couple to the cascade at different length scales, and in some cases can enhance the flow. Finally, we show that the plasticity of a fluid enhances its turbulent behaviour.

The results presented in this thesis find cases in which Kolmogorov's predictions do not hold. In each case, we aim to explain why. These results can have wide-reaching implications for health, industry and the environment, including heart disease, micro-plastic dispersal, mudslides, and cloud formation.

Acknowledgment

I want to thank my supervisor, unit members, family and friends.

Firstly, my supervisor Marco E. Rosti has been extremely generous to me, he made time to speak to me every day that I came to work. Marco was positive and enthusiastic about every project we worked on, he gave me ideas, encouragement and complete simulations. I want to thank my thesis committee member Pinaki Chakraborty, who taught a wonderful course in fluid mechanics during my first year at OIST, persuading me to switch my path from quantum mechanics to fluid mechanics. I am thankful to Daulet Izbassarov, Outi Tammisola and Luca Brandt for contributing to my first academic publication. The members of the Complex Fluids and Flows unit put a smile on my face each morning; including Stefano Olivieri who taught me how to analyse turbulent flows, Mohamed Abdelgawad for listening and caring, Alessandro Chiarini for being an unstoppable force, Rahul Kumar Singh for understanding the theory. Giovanni Soligo for spending a year writing code for the surfactant project, we did it! Aswathy M S for happy jokes. Alessandro Monti for sceptical jokes. To the new students Simone Tandurella, Christian Amor, Morie Koseki, Jean-Paul van Woensel, and Giulio Foggi Rota, you will do amazing things!

Finally, I would like to thank my family and friends. My mum, Zoë Falk for calling me every week and keeping me grounded on this island far from home. My dad, Mark Cannon for being an example; I was there when you did your PhD, and you are here for mine! My brother Marius Cannon, you make me happy. My friends in OIST will be friends forever, Barney Smith and Julian Katzke, Karol and Linda Gietka; surfing with you is the best. Lorena Andreoli, Courtney Dunphy, Will Lapsley, Josefine Reuschenbach, Sam Ross, Charlotte Denman, Yu-Pei Huang. Pour one out for the originals; Alice Taylor, Nicolas Moreno, Fosca Mirata, Claudia Cecchetto, Asa Conover, Erica Overfelt.

If you are reading this, thank you too, there is a good chance you helped me during my time at OIST.

0.1 Acknowledgements for chapter 2

All authors acknowledge the computational resources provided on the Deigo cluster by the Scientific Computing and Data Analysis section of Research Support Division at OIST, and on Oakbridge-CX provided by the Information Technology Center (The University of Tokyo) through the HPCI System Research Project (Project ID: hp220100). I.C. would like to thank Julian Katzke (OIST) for guidance with the rendering software Blender, and David O'Connell (OIST) for helpful discussion of the Euler characteristic.

0.2 Acknowledgements for chapter 4

The research was supported by the Okinawa Institute of Science and Technology Graduate University (OIST) with subsidy funding from the Cabinet Office, Government of Japan. The authors acknowledge the computer time provided by the Scientific Computing section of Research Support Division at OIST and the computational resources of the supercomputer Fugaku provided by RIKEN through the HPCI System Research Project (Project IDs: hp210229 and hp210269). SO acknowledges the support by grants FJC2021-047652-I and PID2022-142135NA-I00 by MCIN/AEI/10.13039/501100011033 and European Union NextGenerationEU/PRTR.

Abbreviations

DNS	direct numerical simulation
EVP	elastoviscoplastic
IBM	immersed boundary method
LES	large eddy simulation
MTHINC	multi-dimensional tangent of hyperbola for interface capturing
RANS	Reynolds-averaged Navier-Stokes
VOF	volume of fluid

List of Publications

Cannon, I., Izbassarov, D., Tammisola, O., Brandt, L., & Rosti, M. E. (2021). The effect of droplet coalescence on drag in turbulent channel flows. *Physics of Fluids*, *33*(8), 085112. https://doi.org/10.1063/5.0058632

IC analysed data, created plots, and wrote the initial draft of the manuscript. DI ran simulations. MER conceptualised and supervised the research and ran simulations. All authors contributed to the editing of the manuscript.

Cannon, I., Soligo, G., & Rosti, M. E. (2023). Morphology of clean and surfactant-laden droplets in homogeneous isotropic turbulence. *Under review for Journal of Fluid Mechanics*. https://doi.org/10.48550/arXiv.2307.15448

IC ran simulations, wrote code for analysing the data, analysed data, created plots, and wrote the initial draft of the manuscript. GS developed the numerical model for surfactants, analysed data, and created plots. MER conceptualised and supervised the research. All authors contributed to the editing of the manuscript.

Olivieri, S., Cannon, I., & Rosti, M. E. (2022). The effect of particle anisotropy on the modulation of turbulent flows. *Journal of Fluid Mechanics*, *950*, R2. https://doi.org/10.1017/jfm.2022.832

IC ran simulations, wrote code for analysing the data, and analysed data for sphere-laden flows. IC created the plots. SO ran simulations, wrote code for analysing the data, and analysed data for fibre-laden flows. SO wrote the initial draft of the manuscript. MER conceptualised and supervised the research. All authors contributed to the editing of the manuscript.

Cannon, I., Olivieri, S., & Rosti, M. E. (2023). Spheres and fibres in turbulent flows at various Reynolds numbers. *Under review for Physical Review Fluids*. https://doi.org/10.48550/arXiv.2310.07986

IC ran simulations, analysed data, created the plots, and wrote the initial draft of the manuscript. SO ran simulations, wrote code for analysing the data. MER conceptualised and supervised the research. All authors contributed to the editing of the manuscript.

Chiarini, A., Cannon, I., & Rosti, M. E. (2023). Anisotropic mean flow enhancement and anomalous transport of finite-size spherical particles in turbulent flows. *Under review for Physical Review Letters*. https://doi.org/10.48550/arXiv.2310.08777

IC ran simulations, wrote code for analysing the data, and provided interpretation of the results. AC ran simulations, analysed data, created plots, and wrote the initial draft of the manuscript. MER conceptualised and supervised the research. All authors contributed to the editing of the manuscript.

Abdelgawad*, M. S., Cannon*, I., & Rosti, M. E. (2023). Scaling and intermittency in turbulent flows of elastoviscoplastic fluids. *Nature Physics*, 1–5. https://doi.org/10.1038/s41567-023-02018-2

IC and MA* contributed equally. IC ran simulations, analysed spectral data, and created plots for high Bingham number cases.* MA ran simulations, analysed data and created plots for low Bingham number cases. MER conceptualised and supervised the research and ran simulations. All authors contributed to the writing and editing of the manuscript.

Contents

List of Figures

List of Tables

Introduction

Multiphase flows consist of a fluid with at least one additional phase. Examples of the additional phase include droplets, solid particles, and polymers. When flow velocities in a fluid are large, the fluid motion becomes chaotic, and kinetic energy is found at many length scales in the flow. This is known as **turbulence**. During my thesis research, I studied turbulent flows of multiphase fluids.

Multiphase turbulent flows are seen all around us. Understanding the energy transfer mechanisms in multiphase turbulent flows is essential for climate forecasting, pollen dispersal, and designing drugs to reduce the risk of heart disease (Dong et al., 2017). Figure 1 shows spray created by a breaking wave. The creation of sea spray is a complex process involving surfactants at the air-water interface. Salt in the spray can travel high into the atmosphere and act as a seed for cloud formation (de Leeuw et al., 2011). Cloud formation has the knock-on effect of increasing the scattering of sunlight back into space, and is one of the largest causes of uncertainty in climate modelling (Brooks & Thornton, 2018). Figure 2 shows two turbulent flows laden with particles. In the case of pollen, it is beneficial to the plant if the solid particles are carried large distances by the flow. In the case of sandstorms, the back-reaction of the solid phase (sand) on the fluid phase (air) influences the severity of the storm. Figure 3 shows the destruction caused by a mudslide which occurred in Okinawa at the time of writing this thesis. Mud is a complex material which behaves as a solid when shear stresses are low, but can suddenly flow like a liquid when shear stresses are high, for example, after heavy rainfall. This solid-liquid behaviour is known as plasticity.

0.3 Physics of turbulence

The flow velocity $\mathbf{u}$ of an incompressible fluid with density ρ and kinematic viscosity ν obeys the Navier-Stokes equations,

$$\partial_t u_i + \partial_j u_i u_j = \nu \partial_{jj} u_i - \partial_i p/\rho + f_i^{inj} + f_i^{mp} \tag{1}$$

$$\partial_j u_j = 0, \tag{2}$$

where indices $i, j \in \{1, 2, 3\}$ denote the Cartesian components of a vector, and repeated indices are implicitly summed over. ∂ denotes partial differentiation with respect to the subscripted index or variable. $\mathbf{f^{inj}}$ is a force which drives the flow and $\mathbf{f^{mp}}$ is a force exerted by other phases on the fluid.

Turbulence is the chaotic motion of a fluid which generally emerges at higher flow velocities. Turbulence is often referred to as "the last unsolved problem of classical physics" (Frisch, 1995), due to its chaotic and seemingly spontaneous nature, which results from the

Figure 1: Photograph of a wave breaking on the coast of Okinawa. This is an example of turbulent flow in the presence of a surfactant-laden interface. I can be seen on the right attempting to surf. Photo taken by Linda Gietka.

Figure 2: Left: Pollen dispersal from the cone of a lodgepole pine. Photo credit: Robert J. Erwin. **Right:** A sandstorm in Golmud, China. Photo credit: Barcroft media, 2010. Both of these are examples of turbulent flows laden with particles.

Figure 3: Destruction caused by a landslide in Urasoe, Okinawa, on 3rd August 2023 after heavy rains due to typhoon Khanun. Landslides are a dangerous example of a turbulent elastoviscoplastic fluid. Image from Hiroyuki Takatsuji, Ryukyu shinpo.

non-linearity of the advective term $\partial_j u_i u_j$ in equation 1. In popular culture, the chaotic property is responsible for the "the butterfly effect", whereby a butterfly flapping its wings can influence the formation of a tornado in another part of the world many days later (Lorenz, 1993). The intensity of turbulence is parametrized by the ratio of the advective and viscous ($\nu\partial_{jj}u_i$) terms in equation 1. This dimensionless parameter is known as the Reynolds number, and for a flow with characteristic velocity U and length L, we can define it as $Re = UL/\nu$.

In addition to chaos, another defining feature of turbulent flows is the propagation of kinetic energy to a range of length scales from large to small. This was first described by Richardson, 1922, who likened the process to fleas on the backs of larger fleas;

> *Big whorls have little whorls*
> *Which feed on their velocity,*
> *And little whorls have lesser whorls*
> *And so on to viscosity.*

Richardson described the turbulent flow in terms of a series of rotating structures called eddies, noting that the large eddies are unstable and break up into smaller eddies. The process continues until the eddies are small enough to feel the molecular effects of the fluid, when they are dissipated as heat. This process is known as Richardson's cascade. In 1941a, A. N. Kolmogorov made some groundbreaking predictions about Richardson's cascade. A. N. Kolmogorov assumed that, at a sufficiently high Reynolds number:

1. Turbulent motions at a length-scale $l \ll l_0$ are statistically isotropic, where l_0 is the length-scale at which energy is injected into the flow.

2. Time-averaged statistics of the small-scale motion $l \ll l_0$ are depend on only ν, ϵ and l, where ϵ is the rate of energy dissipation in the flow.

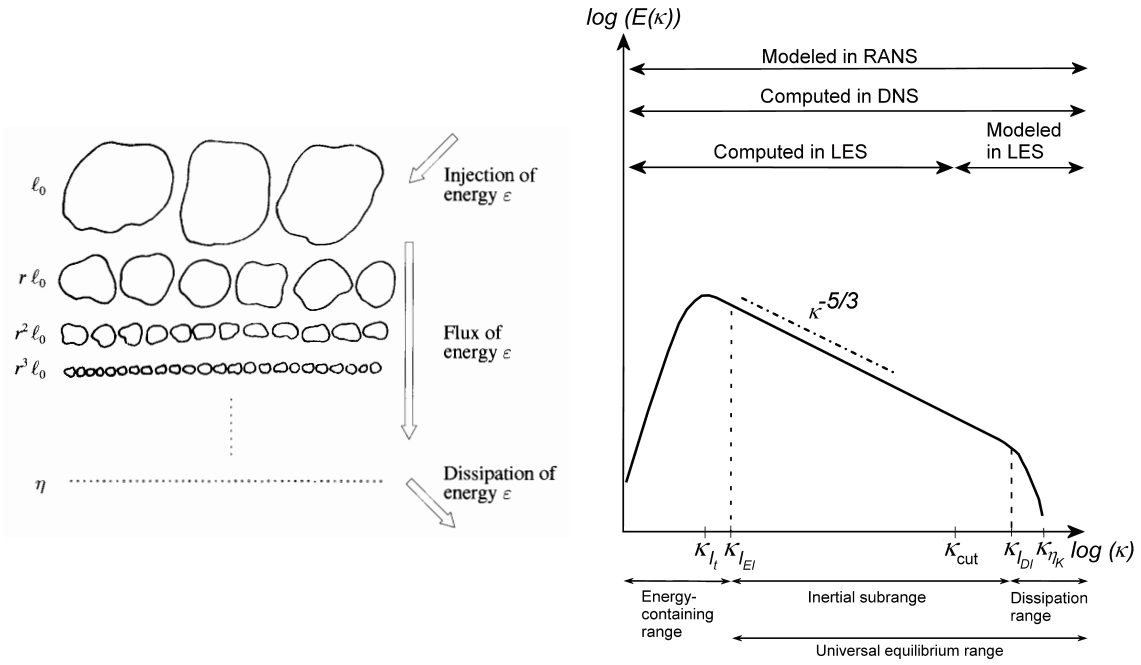

Figure 4: Left: Kolmogorov's model of the turbulent kinetic energy cascade, made up of eddies of decreasing size $r^n l_0$, where l_0 is the length scale at which energy is injected into the flow, and $0 < r < 1$. Figure from Frisch, 1995. **Right:** The energy spectrum E as a function of wavenumber κ. The energy scales as $\kappa^{-5/3}$, as predicted by A. N. Kolmogorov, 1941a. At the smallest length scales, viscous forces dominate and the energy is dissipated at a rate ϵ. The length scales considered in three common numerical methods for turbulence are labelled above, they are Reynolds-averaged Navier-Stokes (RANS), direct numerical simulation (DNS), and large-eddy simulation (LES). Figure from Tay-Wo-Chong, 2012.

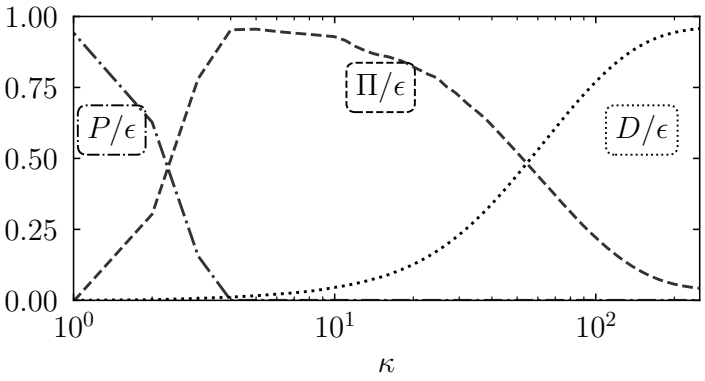

Figure 5: The balance of energy fluxes in a single-phase flow, simulated using 500^3 grid points.

3. Time-averaged statistics of the intermediate-scale motion $\eta \ll l \ll l_0$ depend only on ϵ and l, where $\eta \equiv (\nu^3/\epsilon)^{1/4}$ is now known as the Kolmogorov length.

These assumptions are motivated by symmetries in the Navier-Stokes equation (Frisch, 1995). Kolmogorov combined these assumptions with energy conservation in the flow to make what remains today the only exact theoretical result in turbulence;

$$\left\langle [u_i(\mathbf{x} + l\hat{\mathbf{e}}_i) - u_i(\mathbf{x})]^3 \right\rangle = -\frac{4}{5}\epsilon l, \tag{3}$$

where $\hat{\mathbf{e}}_\mathbf{i}$ is a unit vector, angled brackets show an ensemble average, and we sum over directions $i = 1, 2, 3$. It states that the difference in fluid velocity between two points separated by a distance l increases with the separation and the rate of energy dissipation in the fluid. Since Kolmogorov's seminal work, the same assumptions have been used to show that the pth moment $\left\langle [u_i(\mathbf{x} + l\hat{\mathbf{e}}_i) - u_i(\mathbf{x})]^p \right\rangle$ of the velocity differences over a separation l scales as $(\epsilon l)^{p/3}$. This result directly leads to the famous $-5/3$ scaling of the energy spectrum shown in figure 4. In fact, Kolmogorov's assumptions of self-similarity do not exactly hold, and discrepancies can be seen for $p \neq 3$. This has been attributed by Bec et al., 2022; Frisch, 1995 and others to irregularities in the way eddies break up in the turbulent cascade, violating assumptions 2 and 3. Evidence of these irregularities can be seen from the intermittency of the fluid dissipation ϵ in space and time.

We can measure the flux of energy through the turbulent cascade by making a Fourier transform of each term in the Navier-Stokes equation (eq. 1).

$$\partial_t \hat{u}_i(\boldsymbol{\kappa}) + \hat{G}_i(\boldsymbol{\kappa}) = -\nu\kappa_j\kappa_j\hat{u}_i(\boldsymbol{\kappa}) - \imath\kappa_i\hat{p}(\boldsymbol{\kappa})/\rho + \hat{f}_i^{inj}(\boldsymbol{\kappa}) + \hat{f}_i^{mp}(\boldsymbol{\kappa}), \tag{4}$$

where $G_i = \partial_j u_i u_j$ is the advective term, the hat $\hat{\cdot}$ denotes the Fourier coefficient for wavenumber $\boldsymbol{\kappa}$, and $\imath$ is the imaginary unit. Equation 4 can be multiplied by the complex conjugate $\hat{u}_i^*$ of the Fourier coefficient of the fluid velocity to obtain an expression for the time evolution of turbulent kinetic energy

$$\partial_t \hat{E}(\boldsymbol{\kappa}) = \hat{V}(\boldsymbol{\kappa}) + \hat{T}(\boldsymbol{\kappa}) + \hat{F}^{inj}(\boldsymbol{\kappa}) + \hat{F}^{mp}(\boldsymbol{\kappa}), \tag{5}$$

where $\hat{V} = -2\nu\kappa_j\kappa_j\hat{E}$ is due to viscous dissipation,
$\hat{T} = -\frac{1}{2}(\hat{G}_j\hat{u}_j^* + \hat{G}_j^*\hat{u}_j)$ is due to the non-linear convective term,
$\hat{F}^{inj} = \frac{1}{2}(\hat{f}_j^{inj}\hat{u}_j^* + \hat{f}_j^{inj*}\hat{u}_j)$ is due to the external forcing, and
$\hat{F}^{mp} = \frac{1}{2}(\hat{f}_j^{mp}\hat{u}_j^* + \hat{f}_j^{mp*}\hat{u}_j)$ is due to additional phases in the fluid.

Integrating over the sphere of radius κ centred on the origin in wavenumber space, we obtain the balance of energy fluxes;

$$\epsilon = D(\kappa) + \Pi(\kappa) + P(\kappa) + \mathcal{F}^{mp}(\kappa), \tag{6}$$

where $D(\kappa)$ is rate of energy removal due to viscosity up to wavenumber κ,
$\Pi(\kappa)$ is the rate of energy flux due to advection up to wavenumber κ,
$P(\kappa)$ is rate of energy injection by the forcing up to wavenumber κ, and
$\mathcal{F}^{mp}(\kappa)$ is the rate of energy flux due to additional phases at wavenumber κ.

Figure 5 shows the contribution of each term for a single phase flow. To sustain the flow we apply a force which is made up of sinusoids in space with wavenumbers $\kappa < 4$. Indeed, energy injection P only occurs at the small wavenumbers. The advective term Π enacts Richardon's cascade, taking the energy to larger wavenumbers, and the viscous term D acts at the largest wavenumbers, removing energy from the flow.

0.4 Simulations of turbulence

Accurate simulation of turbulent flow is challenging because it involves chaotic behaviour at a wide range of length and time scales. Over the years, different techniques with different levels of approximation have been developed to simulate turbulent flows. For example, Reynolds Averaged Navier-Stokes (RANS) methods solve the evolution of the time-averaged motion. Approximate methods such as this allow the simulation of turbulent flows in the complex geometries of interest in various industries, such as wind turbine design (Syawitri et al., 2021). However, such methods are poor tools for the prediction of novel turbulent phenomena as they rely on empirical models of the flow at small time and length scales (Wilcox, 2006). More recently, it has become possible to accurately simulate turbulent flows in simple geometries using a more simplistic technique known as Direct Numerical Simulation (DNS). DNSs solve the Navier-Stokes equations at all scales of motion.

DNSs were unfeasible until sufficient computing power became available. In 1982 Ghia et al. calculated the flow inside a cavity at Reynolds numbers up to 10,000. In 1985 Kim and Moin performed one of the first DNSs of a fully developed turbulent channel flow at moderate Reynolds numbers. Today, the DNS at moderate Reynolds numbers has become a valuable tool for fundamental turbulence research. DNSs are made to study geometrically simple geometries such as channel flows, pipe flows, boundary layers, and flows in ducts. The simplest DNS geometry is the triperiodic box, which has periodic boundary conditions in x, y and z, it can be used as an approximate model for any of the above-mentioned flows in a region far from solid boundaries. In addition, the triperiodic flow is well suited for spectral analysis, as the flow can be represented as a Fourier series in all three directions.

0.5 Simulations of multiphase fluids

In the case where the additional phase is droplets in the flow, the force exerted on the fluid in equation 1 is the interfacial surface tension, which can be modelled using the volumetric formulation (Popinet, 2018)

$$f_i^{mp} = \gamma \kappa n_i \, \delta_S(\boldsymbol{x}), \tag{7}$$

where γ is the surface tension coefficient, κ is the local curvature of the interface, n_i is the unit normal to the interface, and $\delta_S(\boldsymbol{x})$ is the surface delta function, which is zero everywhere except for the surface S at the interface between the droplets and the carrier phase. The interface can be computed as the locus where a volume-of-fluid (VOF) field ϕ takes the value of 0.5. The volume-of-fluid field is defined as the local concentration of the droplet phase, so it has a value of 1 inside the droplets and a value of 0 in the bulk. The volume of fluid ϕ is transported by advection

$$\partial_t \phi + \partial_i u_i H = 0, \tag{8}$$

where the MTHINC (multi-dimensional tangent of hyperbola for interface capturing) method (Ii et al., 2012) can be used to reconstruct the local volume of fluid value ϕ starting from the cell-local indicator function H. Resolving fluid motion near the interface is complex, and processes such as film drainage can affect the rate of coalescence (Chan et al., 2011). Currently the best method we have to test for sub-grid-scale effects is to re-run the simulation with a higher grid resolution.

In the case of spherical particles in the flow, the additional force in equation 1 can be modelled using an Eulerian-based immersed boundary method (IBM) (Hori et al., 2022). The velocity **U** of each particle is found using the Newton-Euler equation,

$$m\partial_t U_i = \int_S \left(\rho\nu(\partial_i u_j + \partial_j u_i) - p\delta_{ij}\right) n_j dS. \tag{9}$$

and likewise for the rotation rate,

$$I\partial_t \Omega_i = \int_S \epsilon_{ijk} \frac{c}{2} n_j \rho\nu(\partial_k u_l + \partial_l u_k) n_l dS, \tag{10}$$

where S is the surface of the sphere, and $\mathbf{n}$ is its normal. $m = \tilde{\rho}\pi c^3/6$ and $I = mc^3/20$ are the mass and moment of inertia of the sphere with diameter c and density $\tilde{\rho}$. δ_{ij} is the Kronecker delta and ϵ_{ijk} is the Levi-Civita symbol. The force $\mathbf{f^{mp}}$ on the fluid is equal and opposite to these forces, applied at the surface S.

In the case where the new phase introduces plastic effects to the flow, the additional force in equation 1 is the divergence of the non-Newtonian extra stress tensor $f_i^{mp} = \partial_k \tau_{ki}$, where the constitutive model proposed by Saramito (2007) can be used to describe its evolution in time;

$$\lambda \overset{\nabla}{\tau}_{ij} + \max\left(0, \frac{\tau_d - \tau_y}{\tau_d}\right) \tau_{ij} = \mu\left(\partial_i u_j + \partial_j u_i\right) \tag{11}$$

where λ is the relaxation time of the material, $\overset{\nabla}{\cdot}$ denotes the upper-convected time deriva-

tive, i.e.,

$$\overset{\nabla}{\tau}_{ij} = \partial_t \tau_{ij} + u_k \partial_k \tau_{ij} - \partial_k u_i \tau_{kj} - \partial_k u_j \tau_{ik}, \tag{12}$$

and μ_{n} is the non-Newtonian dynamic viscosity, τ_d is the magnitude of the deviatoric part of the stress tensor $\tau^d_{ij} \equiv \tau_{ij} - \tau_{lm}\delta_{lm}\delta_{ij}/3$, and the magnitude is, $\tau^d = \sqrt{\frac{1}{2}\tau^d_{ij}\tau^d_{ij}}$. Finally, τ^y is the yield stress, when $\tau^d \leq \tau^y$, the material behaves as a solid, and when $\tau^d > \tau^y$, the material flows like a liquid.

In each case – droplets, particles, and plastic fluids – the behaviour of the force $\mathbf{f^{mp}}$ is quite different, and via the energy flux $\mathcal{F}^{mp}$, the additional phase couples to the turbulent cascade in non-trivial ways, violating Kolmogorov's assumptions 2 and 3. In this thesis, I characterise the coupling and the effect on the cascade for all of the above-mentioned phases.

The outline of this thesis is as follows; I enclose the six articles written during my thesis research as six chapters, each with a short introductory summary. Finally, I conclude by reviewing what the results of the six chapters tell us about multiphase flows and turbulence in general and provide an outlook on questions that remain unanswered.

Chapter 1

The Effect of Droplet Coalescence on Drag in Turbulent Channel Flows

Chapter 1 focuses on the channel flow geometry. The analysis compares flows containing coalescing and non-coalescing droplets, which are ideal examples of the clean and surfactant-laden cases, respectively, as clean droplets readily coalesce, and surfactant hinders coalescence. Surprisingly, coalescing droplets have a negligible effect on drag in the channel, while non-coalescing droplets produce a substantial increase in drag which grows with their volume fraction. This difference in drag increase is attributed to the distinct behaviours of the droplets concerning their wall-normal location in the channel and the resulting interfacial shear stress. The findings presented in this chapter are relevant to a range of wall-bounded flows, such as those found in arteries, pipelines and ships.

The article is appended in section A of this thesis, it can be cited as follows:

Cannon, I., Izbassarov, D., Tammisola, O., Brandt, L., & Rosti, M. E. (2021). The effect of droplet coalescence on drag in turbulent channel flows. *Physics of Fluids*, *33*(8), 085112. https://doi.org/10.1063/5.0058632

In this chapter this chapter we show that coalescing droplets move to the channel centre where shear is lowest, whereas non-coalescing droplets experience a shear-gradient lift force which pulls them toward the channel walls. Non-coalescing droplets produce interfacial stresses this region near the walls, reducing the budget available for viscous stresses in the channel. And thereby, non-coalescing droplets produce a significant drag increase.

Chapter 2

Morphology of Clean and Surfactant-Laden Droplets in Homogeneous Isotropic Turbulence

Chapter 2 investigates the effect of surfactant in more detail. We simulate surfactant-laden droplets in homogeneous-isotropic turbulence, this time modelling the surfactant as a third phase which modifies the interfacial surface tension of the droplets. The homogeneous setup allows us to study emergent length scales of the flow. We find a pivotal length scale in the droplets' dynamics is the Kolmogorov-Hinze scale (d_H), which separates the coalescence-dominated and breakage-dominated regimes in the droplet size distribution. The study reveals distinct shapes for droplets smaller and larger than d_H, impacting their areas and providing valuable insights into their characteristics. Furthermore, the number of handles and voids on each droplet is computed, highlighting the role of surface tension in the stability of handles. This chapter shows that in turbulence without a mean flow, the effects of surfactant can simply be modelled as a reduction in surface tension.

The article can be cited as follows:

Cannon, I., Soligo, G., & Rosti, M. E. (2023). Morphology of clean and surfactant-laden droplets in homogeneous isotropic turbulence. *Under review for Journal of Fluid Mechanics*. https://doi.org/10.48550/arXiv.2307.15448

In this chapter we show that in surfactant laden flows one can define a Kolmogorov-Hinze scale d_H, based on the mean surface tension. Droplets smaller than d_H are spheroidal in shape, whereas droplets larger than d_H are filamentous in shape, with a diameter roughly equal to d_H. We find that the number of voids per unit volume is roughly constant for all droplets studied. Similarly, the number of handles per unit length of filament $\approx 0.06/d_H$ for all values of surface tension studied. Finally, we see that surfactants produce Marangoni stresses which increase the flow velocity tangential to the droplet interfaces, and produce shear flows inside the droplets.

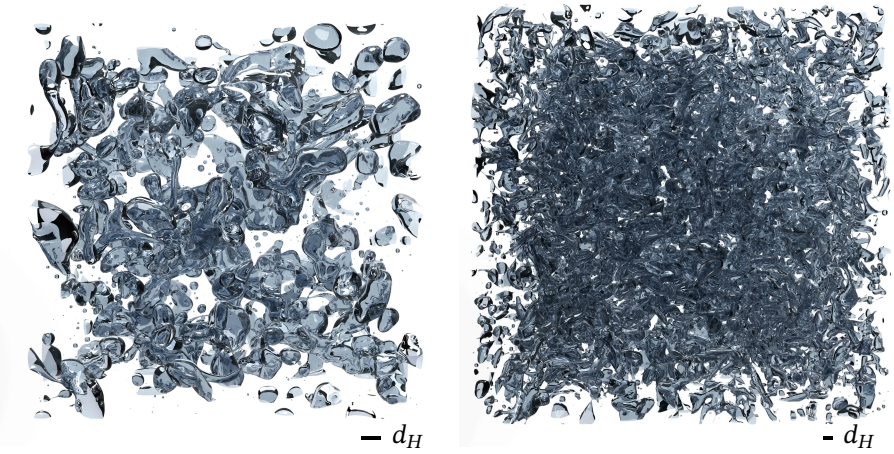

Figure 2.1: Snapshots of the simulated domain in the cases (a) S05 and (b) S20 showing the interface of the droplets; the scale bar shows the Kolmogorov-Hinze scale for each case.

2.1 Introduction

Droplet-laden turbulent flows are ubiquitous in nature and industry (Dickinson, 2010; Jähne & Haußecker, 1998; Karsa, 1999; Kralova & Sjöblom, 2009; Schramm et al., 2003). A few examples include the capture of atmospheric CO_2 at the surface of seas and oceans, which is mediated by the entrainment of air bubbles by breaking waves (Deane & Stokes, 2002; Merlivat & Memery, 1983; Pereira et al., 2018), or the dynamics of liquid jets and sprays which is of fundamental interest in combustion, cooling, irrigation and firefighting applications (Canu et al., 2018; Faeth et al., 1995; Herrmann, 2011; Kooij et al., 2018; Mugele & Evans, 1951). These flows rarely involve pure fluids: instead, they often include small amounts of impurities that may act as surface-active agents (surfactants). Surfactants are compounds that assemble at the fluid interface and modify the local surface tension. Even small amounts of surfactant can drastically change the flow behaviour, making their presence crucial in many practical scenarios (Dobbs, 1989; Koshy et al., 1988; Sjoblom, 2005; Takagi & Matsumoto, 2011).

The interface between the carrier phase and the dispersed phase, i.e. the droplets, serves as a conduit for various physical and chemical exchanges, such as heat, vapour (Onofre Ramos et al., 2022; Scapin et al., 2020), solutes, and aerosols (de Leeuw et al., 2011). The rate of these exchanges is determined by the product of the interfacial flux and the interfacial area, emphasizing the pivotal role of interfacial characteristics. There has been considerable effort to estimate these exchanges, via empirical correlations (Akita & Yoshida, 1974; Delhaye & Bricard, 1994; Kelly & Kazimi, 1982) or via population balance equations relying on the droplet size distribution and on droplet breakage and coalescence models (Andersson & Andersson, 2006a, 2006b; Babinsky & Sojka, 2002; W. H. R. Chan et al., n.d.; W. Chan et al., 2021; Gaylo et al., 2023; Luo & Svendsen, 1996; Martínez-Bazán et al., 2010). We provide an estimate for the interfacial area of each droplet and discover the presence of two universal regimes: the interfacial area of small droplets is proportional to the square of their characteristic size, whereas, for large droplets, it is proportional to the cube of their characteristic size. The information on the individual interfacial area, combined with the

droplet size distribution, provides an estimate of the total interfacial area available. The two different regimes are directly linked to the shape of the droplets: small droplets are spheroid-like or ellipsoid-like, whereas large droplets take long, filamentous shapes. We find that the length scale separating these two regimes is the Kolmogorov-Hinze scale, defined as the maximum size of a droplet that is not broken apart by turbulent fluctuations; droplet breakage becomes prevalent for droplets larger than the Kolmogorov-Hinze scale. The concept of the Kolmogorov-Hinze scale originates from the works of A. Kolmogorov (1949) and Hinze (1955), who applied A. N. Kolmogorov's (1941) assumptions to droplets in turbulence. Some recent studies, however, have disputed the theoretical framework upon which Hinze's theory is based and hence the relevance of the Kolmogorov-Hinze scale: Qi et al. (2022) showed that droplets interact with eddies of a range of length scales, rather than solely with eddies of a size similar to the droplet, and Vela-Martín and Avila (2022) showed that droplet breakup does, in fact, occur below the Kolmogorov-Hinze scale. Notwithstanding this, our numerical simulations show that the Kolmogorov-Hinze scale can still be used as a key parameter to describe the morphology of droplets in turbulence, and that the values obtained using Hinze's original formulation (Hinze, 1955) are in good agreement with a more recent formulation, which uses the work done by the interface to define a length-scale for the droplet phase (Crialesi-Esposito, Chibbaro, et al., 2023). Furthermore, we show that Hinze's theory can be extended to surfactant-laden droplets, provided that a suitable value of the surface tension is selected. In our setup, surfactant effects on the morphology of the droplets can indeed be well approximated using an averaged value of the surface tension, thereby maintaining the simplicity and efficacy of the Kolmogorov-Hinze framework.

Beyond an average reduction in surface tension, surfactants introduce more intricate dynamics into the flow: a surfactant is an additional phase that is transported by the local flow and by motion and deformation of the interface, and that reduces the value of surface tension according to its local concentration. This can lead to an inhomogeneous value of surface tension over the interface of the droplets, giving rise to Marangoni stresses, i.e. stresses that act tangentially to the interface and originate from surface tension gradients. Marangoni stresses have been shown to be crucial in hindering and preventing coalescence (Dai & Leal, 2008; Soligo et al., 2019b), reducing the rising velocity of bubbles (Elghobashi, 2019; Takagi & Matsumoto, 2011), and in the buildup of bubble layers in wall-bounded flows (Ahmed et al., 2020; Lu et al., 2017; Lu & Tryggvason, 2008; Takagi & Matsumoto, 2011; Tryggvason & Lu, 2015). An increase in the drag coefficient has been reported when adding surfactant to wall-bounded bubbly flows Takagi et al. (2009) and Takagi et al. (2008), Verschoof et al. (2016): surfactant reduces the size of the droplets, and causes a lower drag reduction compared to surfactant-free cases. Our study examines a statistically-stationary, homogeneous and isotropic multiphase flow at a moderate Reynolds number (see figure 2.1). This type of flow does not allow for the buildup of large-scale surfactant gradients commonly found in upflow and downflow setups, where the velocity difference between the carrier and the dispersed phase generates and maintains a surfactant gradient along the interface of the droplets or bubbles (Lu et al., 2017; Takagi et al., 2008). For this reason, we expect the effect of Marangoni stresses to be localized. Surfactant effects on the droplet morphology in our setup can be summarised as an average surface tension reduction, and the effect of Marangoni stresses can be appreciated by analysing the local flow dynamics at the interface.

To investigate the complex dynamics of clean and surfactant-laden droplets in turbu-

lence we use direct numerical simulations. In recent years there has been a consistent growth in the number of numerical studies on multiphase turbulence, supported as well by the increased availability and capability of high-performance computing infrastructures. Multiphase turbulence is characterized by a wide range of scales, from the smallest, molecular-size interfacial scale, to the smallest flow scales – the Kolmogorov length scale – and up to the large-scale structures of the flow. The separation of scales usually spans over about eight to ten orders of magnitude, while direct numerical simulations on leading-edge high-performance computing systems can simulate about four orders of magnitude (Soligo et al., 2021). The common choice is to simulate the larger scales of the multiphase flow, from the large-scale structures down to about the Kolmogorov length-scale, and introduce models for the smaller-scale physics (Soligo et al., 2021; Tryggvason et al., 2013; Tryggvason et al., 2010). Several authors have devoted their attention to the development of models for the unresolved scales to be used in direct numerical simulations and large eddy simulations. In their original works A. Kolmogorov (1949) and Hinze (1955) identified the maximum size of a non-breaking droplet in turbulence. Experimental measurements (Deane & Stokes, 2002; Garrett et al., 2000) later showed that the existence of two different regimes in the droplet size distribution, separated by the Kolmogorov-Hinze scale. These works laid the foundations for the understanding of the dynamics of the droplets and for the development of sub-grid-scale models for the interfacial dynamics (Evrard et al., 2019; Herrmann, 2013; Xiao et al., 2014). The power-law scaling exponents for the two regimes measured in experiments have been confirmed as well by numerical simulations: $-10/3$ for the breakage-dominated regime (Crialesi-Esposito, Chibbaro, et al., 2023; Deike et al., 2016; Mukherjee et al., 2019; Perlekar et al., 2012; Rosti, Ge, et al., 2019; Skartlien et al., 2013; Soligo et al., 2019a) and $-3/2$ for the coalescence-dominated regime (Crialesi-Esposito, Chibbaro, et al., 2023; Rivière et al., 2021). The droplet size distribution and the population balance equation for the droplets are fundamental tools in the modelling of droplets of similar size to the grid resolution and smaller. Perlekar et al. (2012) correlated the instantaneous Weber number of droplets to their deformation, showing that large Weber numbers correspond to strongly deformed droplets. They simulated emulsions at increasing volume fractions and proved the validity of the Kolmogorov-Hinze scale at low volume fractions; they reported deviations from the Kolmogov-Hinze theory for more concentrated emulsions, possibly due to the effect of coalescence, which was neglected in the original works by Kolmogorov and Hinze. Vela-Martín and Avila (2022) showed that drop-breakage is a memoryless process, i.e. the relaxation time of the droplet is much lower than its expected lifetime. In the same work, they debated the validity of the Kolmogorov-Hinze scale as an absolute threshold between breaking and non-breaking droplets, arguing that all droplets will eventually break apart, provided there is enough time for breakage. It was shown also that, in the absence of coalescence, the breakage rate depends on the Weber number alone. Gaylo et al. (2023) investigated the fragmentation of bubbles in statistically-stationary homogeneous isotropic turbulence and characterised several fundamental time scales of the bubbles: the relaxation time, the expected lifetime and the time needed for the largest bubble to break down to the Kolmogorov-Hinze scale. It is now well known that the presence of a dispersed phase strongly modifies the dynamics of the flow at all scales: the interface extracts energy at the large flow scales and re-injects it into the flow at much smaller scales, competing with the classic turbulent energy cascade (Mukherjee et al., 2019; Perlekar, 2019). This effect is reflected in a deviation from the $k^{-5/3}$ power-law scaling of the turbulent kinetic energy

spectrum. When there is a considerable slip velocity between the droplet or bubble and the carrier fluid, a completely different scaling of the energy spectrum, k^{-3}, has been reported in numerical simulations (Pandey et al., 2020; Paul et al., 2022a; Roghair et al., 2011) and experiments (Mercado et al., 2010; Prakash et al., 2016).

As part of our analysis of droplet morphology, we measure the Euler characteristic of the droplet interfaces. Similarly to the number of droplets in a flow, the Euler characteristic of an interface is an integer-valued topological invariant, and any change in its value requires a splitting or merging of interfaces. Despite its physical significance, the Euler characteristic has only recently been applied to multiphase flows: Dumouchel et al. (2022) linked the Euler characteristic to the Gaussian curvature of the droplets, and used it to parametrize the morphology of liquid droplets undergoing breakup. The Euler characteristic is commonly used in characterising the sintering of metal powders (DeHoff et al., 1972; Mendoza et al., 2006), classifying lung tissues (Boehm et al., 2008), and correcting MRI scans of the human brain (Yotter et al., 2011). In this article, we use the Euler characteristic to count the number of voids and handles on the droplets, demonstrating that the large droplets are made up of extremely interconnected filaments.

The article is structured as follows. We introduce the numerical method and the computational setup adopted for the simulations in section 2.2. Our findings are reported in section 2.3, where we first focus on the morphology of the dispersed phase, and then on the statistics of the local flow around the droplets. Finally, section 2.4 summarizes the main results presented in the present work.

2.2 Numerical model

We solve a system of equations including the momentum (2.1) and mass (2.2) conservation, the volume of fluid (2.3) and surfactant (2.4) transport equations to simulate the dynamics of an ensemble of breaking, coalescing and deforming finite-size droplets in homogenous isotropic turbulence. The two phases, the carrier fluid and the dispersed phase (i.e., the droplets) have the same density ρ and dynamic viscosity μ.

$$\rho\frac{\partial \mathbf{u}}{\partial t} + \rho\mathbf{u}\cdot\nabla\mathbf{u} = -\nabla p + \nabla\cdot\left[\mu\left(\nabla\mathbf{u} + \nabla\mathbf{u}^T\right)\right] + \nabla\cdot(\tau_c f_\sigma) + \mathbf{f_s}, \tag{2.1}$$

$$\nabla\cdot\mathbf{u} = 0, \tag{2.2}$$

$$\frac{\partial \phi}{\partial t} + \nabla\cdot(\mathbf{u}H) = 0, \tag{2.3}$$

$$\frac{\partial \psi}{\partial t} + \mathbf{u}\cdot\nabla\psi = \nabla\cdot(M_\psi\nabla\mu_\psi), \tag{2.4}$$

where $\mathbf{f_s}$ is the spectral forcing used to sustain turbulence. We use the one fluid approach, whereby the fluid velocity $\mathbf{u}$ and pressure p are defined in both phases and continuous across the interface; the volume of fluid variable ϕ is used to define the instantaneous position of the interface. The volume of fluid can be understood as a colour function characterizing the local concentration of the dispersed phase: it is equal to $\phi = 0$ in the carrier phase and to $\phi = 1$ in the droplet phase. The volume of fluid method is an interface capturing method (Prosperetti & Tryggvason, 2009) where the concentration of each phase is

transported using equation 2.3 and the interface is implicitly defined as the $\phi = 0.5$ level. The effect of the interface on the flow is accounted for in the momentum equation via the surface tension forces: the Korteweg tensor $\tau_c = \mathcal{I} - \mathbf{n} \otimes \mathbf{n}$ (Korteweg, 1901) accounts for the position and shape of the interface, and the surface tension equation of state f_σ defines the local value of surface tension. In the definition of the Korteweg tensor, $\mathcal{I}$ is the identity matrix and $\mathbf{n} = -\nabla\phi/||\nabla\phi||$ is the unit-length, outward-pointing normal to the interface. The local surfactant concentration $\psi \in [0, 1]$ is expressed as a fraction of the maximum surfactant concentration, which is usually determined by steric hindrance between surfactant molecules. Hence, ψ is dimensionless in this formulation. To account for the effect of surfactant on surface tension, we use a modified Langmuir equation of state (Muradoglu & Tryggvason, 2008, 2014; Soligo et al., 2019b) $f_\sigma = \max[\sigma_{min}, \sigma_0(1+\beta_s \log(1-\psi))]$, where σ_0 is the reference surface tension of a clean (i.e., surfactant-free interface), σ_{min} the minimum surface tension, and β_s the elasticity number. In the original formulation by Bazhlekov et al. (2006) and Pawar and Stebe (1996), the Langmuir equation of state provides a good fit at low to moderate surfactant concentration values; however, it fails to account for surfactant saturation dynamics at higher concentrations. Experimental measurements (reviewed by Chang and Franses (1995)) showed that, beyond a critical concentration of surfactant, surface tension no longer changes for increasing surfactant concentrations. Hence, to qualitatively account for surfactant saturation dynamics at the interface, we limit the surface tension to be greater than σ_{min} at all points on the interface. In equation (2.1), surface tension forces act perpendicular and tangential to the interface: a capillary component (normal to the interface) and a tangential component – Marangoni stresses – proportional to the surface tension gradient. The tangential component is characteristic of surfactant-laden flows, where surface tension changes along the interface according to the local surfactant concentration.

The volume of fluid ϕ is transported using a simple advection equation (2.3). The MTHINC (multi-dimensional tangent of hyperbola for interface capturing) method (Ii et al., 2012) is used to reconstruct the local volume of fluid value ϕ starting from the cell-local indicator function H. To compute the surfactant chemical potential landscape, we first calculate a signed-distance function s and a smoothed colour function $\hat{\phi}$. A re-distancing equation is solved to compute the signed-distance function over the pseudo-time τ

$$\frac{\partial s}{\partial \tau} = \mathrm{sgn}(s_0)(1 - ||\nabla s||), \tag{2.5}$$

where sgn is the sign function and the initial guess s_0 is found as $s_0 = (2\phi - 1)0.75\Delta$ (Albadawi et al., 2013); this choice guarantees that the zero-level of the signed-distance function always corresponds to the interface (De Vita et al., 2019; Russo & Smereka, 2000). The signed-distance function is updated at every time iteration as the volume of fluid is advected. Next, we compute the smoothed colour function as $\hat{\phi} = \tanh \frac{s}{3\Delta}$, which is bounded in $-1 \leq \hat{\phi} \leq 1$, and where the smoothing width is set to three times the grid spacing Δ.

An advection-diffusion equation (2.4), is solved to track the surfactant concentration ψ in the domain. We use a soluble surfactant: surfactant preferentially collects at the interface between the two fluids, but at the same time, it also dissolves in limited amounts in the bulk of the phases. The adsorption (accumulation of surfactant from the bulk to the interface), desorption (release of surfactant from the interface to the bulk) and diffusion dynamics

of the surfactant phase are determined by the chemical potential of the surfactant. The chemical potential is made, in order, of three contributions: a free energy of mixing term, an adsorption term and a bulk-penalty term (Engblom et al., 2013; Soligo et al., 2019b; Yun et al., 2014),

$$\mu_\psi = \alpha \ln \frac{\psi}{1-\psi} - \beta \frac{(1-\hat{\phi}^2)^2}{2} + \gamma \frac{\hat{\phi}^2}{2}. \tag{2.6}$$

The first term, the free energy of mixing term, favours a uniform surfactant distribution throughout the entire domain and plays the part of diffusion, with the coefficient α controlling the magnitude of the diffusive process. The adsorption term (second term) is a negative contribution to the free energy of the system because the accumulation of surfactant at the interface reduces the total energy of the surfactant configuration. The coefficient β controls the adsorption dynamics. The last term, the bulk-penalty term, is representative of the cost of free surfactant, i.e., of surfactant dissolved in the bulk of the phases rather than adsorbed at the interface, and the coefficient γ determines the energy cost of surfactant dissolved in the bulk phases. The adsorption term is maximum in magnitude at the interface ($\hat{\phi} = 0$), indicating a decrease in the energy of the system, while the bulk-penalty term is maximum in the bulk of the phases ($\hat{\phi} = \pm 1$) indicating an increase in the energy. The logarithmic formulation of the free energy of mixing term mandates for a non-constant mobility parameter $M_\psi = m\psi(1-\psi)$ (Engblom et al., 2013), with m being a numerical coefficient controlling the magnitude of the diffusive-like surfactant dynamics. This choice of the mobility parameter ensures the boundedness of the surfactant concentration, $\psi \in [0, 1]$.

Finally, we couple the volume of fluid method for simulating the interfacial dynamics with a phase-field-based method to track the concentration of a soluble surfactant. The volume of fluid method guarantees exact mass conservation of each phase and allows for a sharper interface compared to other diffuse-interface methods. We rely on a method to simulate surfactant dynamics that has been successfully adopted in the past to simulate flows with surfactant-laden interfaces (Engblom et al., 2013; Soligo et al., 2019a, 2019b, 2020a, 2020b; Yun et al., 2014) using a phase field method to model interfacial dynamics. In particular, we employ a volume of fluid method to simulate the dynamics of the dispersed and carrier phases, and we use a smoothed colour function, $\hat{\phi}$, to couple the interfacial dynamics (based on the volume of fluid) with the surfactant dynamics (based on a phase field method). The smoothed volume of fluid field accounts for the interfacial dynamics while at the same time providing the diffuse-interface basis onto which the surfactant model is built. We thus combine the aforementioned strengths of the volume of fluid method with the advantages of a formulation of the surfactant phase that accounts for adsorption, desorption and diffusion in a thermodynamically-consistent framework.

2.2.1 Computational method

The system of equations is discretized on a uniform Cartesian grid. The computational grid is staggered: pressure, density, viscosity, volume of fluid and surfactant concentration are defined at the cell centres, and the fluid velocities are stored at the cell faces. Spatial derivatives are approximated using a second-order finite difference scheme, and time advancement is performed via a second-order, explicit Adams-Bashforth scheme. A fractional-step method (Kim & Moin, 1985) is adopted to advance the mass and momentum conserva-

tion equations in time, with the resulting Poisson equation for the pressure solved via a fast pressure solver. The volume of fluid is transported using a directional splitting method combined with an upwind scheme (Ii et al., 2012; Rosti, De Vita, et al., 2019). The same scheme is used for the advective term in the surfactant transport equation.

The surfactant is resolved on a refined grid to capture the steep concentration gradients at the interface and to keep a sharp interfacial profile. The smoothing width of the colour function $\hat{\phi}$ should be large enough to accurately discretize the surfactant profile across the interface, and at the same time it should be small enough to keep the surfactant profile sharp. The use of a refined grid thus allows us to capture the modelled interfacial dynamics, while maintaining a thin interfacial surfactant layer. The finer computational grid used for the surfactant transport is still a staggered, uniform, Cartesian grid; linear interpolation is used to interpolate variables from/to the standard grid (for the velocity, pressure, density, viscosity and volume of fluid) to/from the fine grid (for the surfactant concentration). The surfactant transport is carried on the fine grid, with the velocity and smoothed volume of fluid fields interpolated to the fine grid. Surface tension forces are instead at first computed on the fine grid and then applied to the momentum conservation equation. Tests have been performed with different grid refinement factors: the pressure jump across the interface, the surfactant concentration value at the interface and the total surfactant concentration show minimal changes compared to the reference case (i.e., unitary refinement factor). For the sake of comparison among the different cases, the smoothing width was kept constant in all cases, while in our numerical simulations the smoothing width is adapted to the refinement factor, thus allowing for smaller values of the smoothing width and for a thinner surfactant interfacial layer.

We use the in-house code ***Fujin*** to perform all the numerical simulations presented here. The code has been used and validated in the past on a variety of different flow configurations (Abdelgawad* et al., 2023; Brizzolara et al., 2021; Cannon et al., 2021; Mazzino & Rosti, 2021; Olivieri et al., 2020; Rosti, Ge, et al., 2019; Rosti et al., 2023; Rosti & Takagi, 2021). Further validation cases are available on the group's website, https://groups.oist.jp/cffu/code. Specific validation tests for the surfactant model and its implementation are reported in appendix B.2.

2.2.2 Computational setup

We perform direct numerical simulations in a cubic box of size L with periodic boundary conditions in all spatial directions. Homogenous isotropic turbulence is sustained using the force $\mathbf{f_s}$ in equation 2.1. We use the spectral forcing scheme proposed by Eswaran and Pope (1988), whereby the flow is forced in a shell of Fourier modes $2\pi/L_a \leq |\mathbf{k}| \leq 2\pi/L_b$, and the force on each mode evolves randomly in time (Uhlenbeck & Ornstein, 1930) with variance $\rho\sigma_L^2$ and relaxation time T_L. Hence, $U_L \equiv \sigma_L^{2/3} T_L^{1/3} (L/2\pi)^{1/3}$ is the characteristic velocity scale of the forcing. We set the forcing Reynolds number $Re_L \equiv \rho U_L L/(2\pi\mu) = 41.6$ to give a turbulence intensity that is tractable on our numerical grid. We choose the dimensionless relaxation time $T_L^* \equiv 2\pi T_L U_L/L = 2.08$ to give variations at the timescale of the large eddy turnover time. To prevent droplets from spanning the entire periodic domain, we force at a length-scale smaller than L (Crialesi-Esposito, Chibbaro, et al., 2023; Mukherjee et al., 2019). Hence the minimum and maximum wavelengths of forcing are set to $L_b = L/3$ and

case		$\langle\phi\rangle$	$\langle\psi\rangle$	We	η/L	λ/L	Re_λ	$\langle\sigma\rangle_I/\sigma_0$	We_e	d_H/L	$d_{H\sigma}/L$
SP	●	0	0	-	**8.39e-04**	**0.0220**	**178**	-	-	-	-
C10	●	0.1	0	10	8.49e-04	0.0224	180	1	**9.91**	**0.0560**	**0.0565**
C20	●	0.1	0	20	8.55e-04	0.0228	184	1	20.0	0.0373	0.0392
C40	●	0.1	0	40	8.58e-04	0.0231	188	1	39.3	0.0252	0.0290
S05	◆	0.1	0.1	5	8.48e-04	0.0226	183	0.40	12.7	0.0489	0.0370
S10	◆	0.1	0.1	10	8.71e-04	0.0242	199	0.40	25.8	0.0338	0.0317
S20	◆	0.1	0.1	20	**8.85e-04**	**0.0247**	**201**	0.41	**49.5**	**0.0232**	**0.0241**

Table 2.1: List of simulations performed. Here $\langle\cdot\rangle$ denotes an average over the domain volume, and $\langle\cdot\rangle_I$ denotes an average over the interface. All simulations have been carried out at constant volume fraction $\langle\phi\rangle$; an additional reference case (single phase, $\langle\phi\rangle = 0$) is performed. We investigate four different Weber numbers (We) and two different values of the mean surfactant concentration $\langle\psi\rangle$. The measured values of the Kolmogorov length-scale η, the Taylor microscale λ, Taylor Reynolds number Re_λ, average surface tension $\langle\sigma\rangle_I$, effective Weber number We_e, and Kolmogorov-Hinze diameters d_H and $d_{H\sigma}$ are reported. The largest and smallest values of each parameter are shown in bold.

$L_a = L/2$, respectively.

The computational domain is discretized using an equispaced Cartesian grid with $N = 500$ grid points in all directions; to better resolve the sharp surfactant gradients at the interface and keep a sharper surfactant profile across the interface, the surfactant transport equation is resolved on a twice-refined grid, with $N_\psi = 1000$ grid points in all directions. A refinement factor of 2 for the surfactant concentration grid has been selected as it provides a significant improvement in the sharpness of the surfactant profile at the interface while keeping the computational cost within reasonable limits. With this refinement factor, the computational cost increases by roughly $\sim 25\%$ and the storage requirements by $\sim 115\%$.

We report in table 2.1 the chosen parameters for all cases reported in this article. We use one single-phase reference case ($\langle\phi\rangle = 0$), three cases with clean droplets ($\langle\psi\rangle = 0$), and three cases with surfactant-laden droplets ($\langle\psi\rangle = 0.1$). The droplet-laden flows were initialised using fluid velocity and pressure from the single-phase reference case once it had reached a statistically steady state. A single spherical droplet of radius $R \simeq 0.288L$ (corresponding to $\langle\phi\rangle = 0.1$) was initialized at the centre of the computational box. Due to the action of the surrounding turbulent flow, the droplet deforms and breaks apart into smaller droplets. For our surfactant-laden cases, the surfactant is initially distributed in the domain following the equilibrium profile with $\psi = 0.1$ in the bulk phase, computed by zeroing the gradient of the chemical potential. We focus on a highly-soluble surfactant and set the coefficients of the surfactant chemical potential to $\alpha = 0.0242{u'_0}^2$, $\beta = 0.0121{u'_0}^2$ and $\gamma = 0.0121{u'_0}^2$, and the the numerical coefficient of the mobility parameter to $m = 0.0307L_b/u'_0$. For the flows with droplets, we fix the reference surface tension σ_0, allowing us to define a reference Weber number $We \equiv \rho{u'_0}^2 L_b/\sigma_0$ based on the single phase root mean square

velocity u_0' and the minimum wavelength of the forcing L_b. We select a moderate-strength surfactant with elasticity number $\beta_s = 5$ and a relatively high surfactant saturation concentration, yielding a low minimum surface tension, $\sigma_{min} = 0.1\sigma_0$.

We performed an additional simulation on a more refined grid, $N_f = 1000$ grid points, with the same parameters of the surfactant-free case at $We = 10$ to verify the grid independence of the results presented in the following. A comparison of the results from the standard grid case ($N = 500$) and the fine one ($N_f = 1000$) showed negligible differences.

2.3 Results

In table 2.1, we report integral quantities from all cases studied. Length scales of the turbulent flow are the Kolmogorov scale $\eta \equiv (\mu/\rho)^{3/4}\varepsilon^{1/4}$, and the Taylor microscale $\lambda \equiv \sqrt{15\mu/(\rho\varepsilon)}u'$, where u' is the root-mean-square velocity of the flow and ε is the mean dissipation rate. The Taylor Reynolds number $Re_\lambda \equiv \rho u'\lambda/\mu$ is 178 in the single-phase case, and as was previously observed by Rosti, Ge, et al. (2019) and Crialesi-Esposito et al. (2022), Re_λ increases slightly when droplets are present. The surface tension averaged over the interface $\langle\sigma\rangle_I$, is the same as the reference surface tension σ_0 in the cases with clean droplets. However, it is reduced by more than half in the presence of surfactant. This motivates us to define an effective Weber number, $We_e \equiv \rho u'^2 L_b/\langle\sigma\rangle_I$ to better compare the differnt cases.

The Kolmogorov-Hinze diameter $d_H \equiv 0.725\langle\sigma\rangle_I^{3/5}\rho^{-3/5}\varepsilon^{-2/5}$ is an estimate of the diameter of the largest droplet which does not break up. It is made by balancing surface tension with turbulent velocity fluctuations, using an empirical constant of 0.725 (Hinze, 1955). We also use a more recent formulation of the Kolmogorov-Hinze diameter from Crialesi-Esposito, Chibbaro, et al. (2023); at large scales, droplets predominantly break up, and the interface takes energy from the flow (negative work), whereas at smaller scales, droplets predominantly coalesce and the interface returns energy to the flow (positive work). The length scale at which the work done by the interface is zero is defined as $d_{H\sigma}$. The two estimates of the Kolmogorov-Hinze diameter are in fairly good agreement in the cases with and without surfactant.

Figure 2.2a shows the kinetic energy spectra of the turbulent flows. In all cases, the most energetic modes are in the range $2 \leq kL/(2\pi) \leq 3$, where turbulent forcing is applied. The single-phase case shows the $k^{-5/3}$ scaling predicted by A. N. Kolmogorov (1941b), persisting for over a decade of wavenumbers. As has been previously reported by Perlekar (2019) and Rosti, Ge, et al. (2019) and Crialesi-Esposito et al. (2022), the cases with droplets show a slight reduction in energy at small wavenumbers, and an increase at large wavenumbers. We also see from figure 2.2 that the Kolmogorov-Hinze scale is well within the inertial range. Hence, we can assume that self-similarity applies to the turbulent velocity fluctuations which dictate droplet deformation and breakup, investigated in the following subsection. Our simulations are in a statistically steady state, and so the fluid kinetic energy contained in each wavenumber is constant in time, and the energy flux through each wavenumber k is constant and equal to the energy injection rate ϵ. This is expressed by the equation $\mathcal{F}(k) + \Pi(k) + \mathcal{D}(k) + \Sigma(k) = \epsilon$, where the terms on the left-hand side are the energy flux due to forcing, advection, viscous dissipation, and surface tension, respectively. We calculate these terms using the method given in the supplementary information of Abdelgawad* et al. (2023) (see also chapter 6 of Pope (2000)). Namely, we take a three-

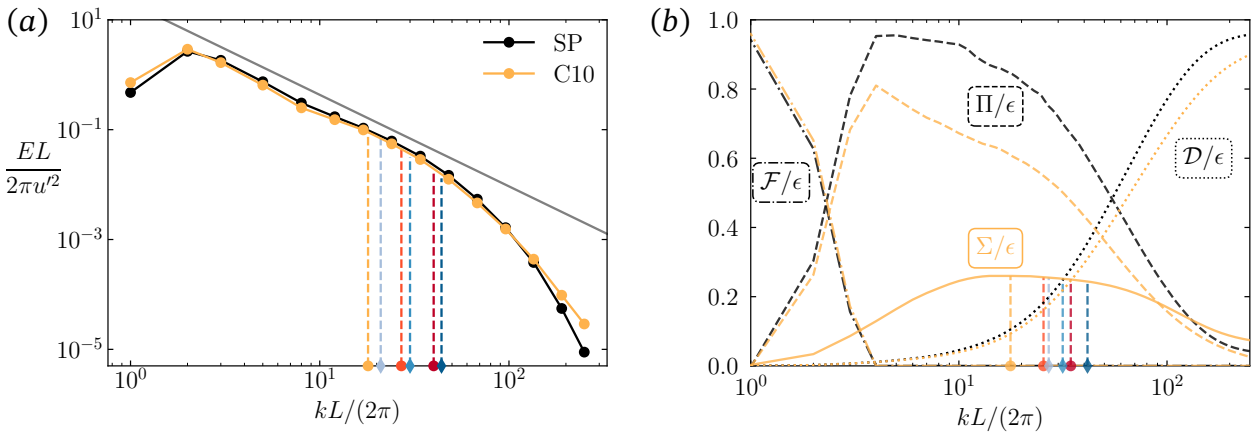

Figure 2.2: (a) Turbulent kinetic energy spectrum E for cases SP and C10, made dimensionless using the domain size L and the root mean square velocity u' of each case. Vertical dashed lines show the wavenumber of the Kolmogorov-Hinze scale $k_H \equiv 2\pi/d_H$ for all the cases with droplets. The solid grey line above reports the Kolmogorov scaling $k^{-5/3}$. (b) Scale-by-scale energy balance for cases SP and C10. Energy flux due to forcing $\mathcal{F}$, viscous dissipation $\mathcal{D}$, advection Π, and surface tension Σ are plotted using dot-dashed, dotted, dashed, and solid lines, respectively. Vertical dashed lines mark $k_{H\sigma} \equiv 2\pi/d_{H\sigma}$, the wavenumber at which Σ is maximum for every droplet case.

dimensional Fourier transform of each term in the Navier-Stokes equation (2.1), multiply by the fluid velocity, and integrate over the region bounded by a sphere of radius k in wavenumber space. For dissipation, we choose the region inside the sphere, and for the other terms, we choose the region outside the sphere. This way, as $k \to \infty$, $\mathcal{D} = \epsilon$ and $\mathcal{F} = \Pi = \Sigma = 0$. Figure 2.2b shows the energy balance for the single-phase flow and a droplet-laden flow. The single-phase case shows the canonical Richardson cascade; energy is injected by forcing at the large scales and carried to smaller scales by advection, where it is dissipated by viscosity. In the droplet-laden case, surface tension also carries energy to smaller scales.

2.3.1 Droplet statistics

The inset of figure 2.3a shows the average number of droplets $\mathcal{N}$ in our simulations. To identify and count each droplet, we use a stack-based, six-way flood-fill on the computational cells characterized by $\phi \geq 0.5$; the algorithm is a direct extension to three-dimensional space of the two-dimensional four-way flood fill algorithm (Newman & Sproull, 1979). The number of droplets has been counted over several instantaneous snapshots and averaged in time once the simulation has reached a statistically steady state, i.e. once the Taylor-Reynolds number and the number of droplets fluctuate about a constant mean value. We note that clean and surfactant-laden cases at similar values of the effective Weber number, i.e. S05 & C10, S10 & C20, S20 & C40, have approximately the same average number of droplets. This result suggests that the effect of surfactant on the dispersed phase manifests mainly as an average surface tension reduction, with negligible effects from Marangoni stresses. As

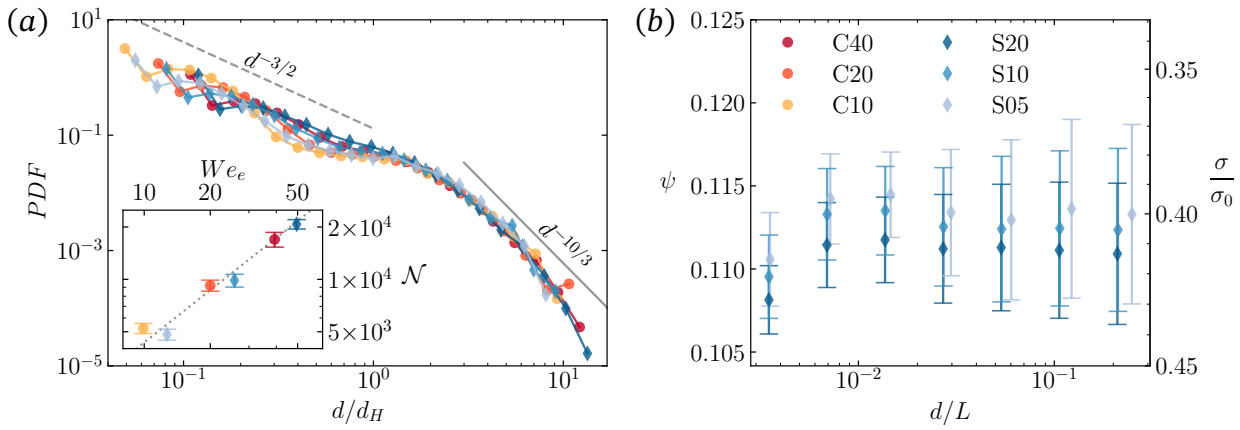

Figure 2.3: (a) PDF of the droplet diameters d, with the dashed and solid lines showing scalings previously found in the coalescence and breakup regimes (Deane & Stokes, 2002), respectively. The inset reports the total number of droplets $\mathcal{N}$ in each case, with error bars showing the root mean square variation in time. The dotted line is a fit $\mathcal{N} = 434We_e$. In (b), we calculate the mean and standard deviation of the surfactant concentration ψ on the interface of each drop; we then average these values over the ensemble of drops of the same size. The right-hand axis shows the normalized interfacial surface tension resulting from the presence of surfactant.

previously found by Rosti, Ge, et al. (2019) in shear turbulence, we see that the number of droplets is proportional to the Weber number, in our case with a factor $\mathcal{N} = 434We_e$.

The average number of droplets $\mathcal{N}$ is of the order 10^4. This large sample size allows us to make accurate statistics of the droplets, even when binned by their equivalent diameter d. We define the equivalent diameter of a droplet

$$d \equiv (6V/\pi)^{1/3}, \tag{2.7}$$

as the diameter of a sphere with volume V, where V is the volume of said droplet. The droplet size distribution for all cases is shown in figure 2.3(a). We observe a collapse of all the curves when the droplet size d is normalized by the Kolmogorov-Hinze scale in each case. Note that the Kolmogorov-Hinze scale separates two different regimes: the coalescence-dominated regime for $d/d_H < 1$ and the breakage-dominated regime for $d/d_H > 1$. The Kolmogorov-Hinze scale (Hinze, 1955) is defined as the largest droplet that resists breakage due to turbulent fluctuations. The coalescence-dominated regime characterizes droplets smaller than the Kolmogorov-Hinze scale; breakage is highly unlikely for these droplets, which instead are in a state of constant coalescence. On the other hand, droplets larger than the Kolmogorov-Hinze scale are prone to breaking apart. The droplet size distribution shows a clear power-law behaviour in the breakage- and coalescence-dominated regimes. Using dimensional arguments the exponents for the two regimes have been obtained: $-3/2$ for the coalescence-dominated regime (Deane & Stokes, 2002) and $-10/3$ for the breakage-dominated regime (Garrett et al., 2000). Deane and Stokes (2002) mea-

sured the bubble size distribution in breaking waves and found good agreement between the experimental measurements and the analytical scalings. Several previous computational works confirmed the same $-10/3$ power-law exponent in the breakage-dominated regime (Crialesi-Esposito, Chibbaro, et al., 2023; Deike et al., 2016; Mukherjee et al., 2019; Rosti, Ge, et al., 2019; Skartlien et al., 2013; Soligo et al., 2019a), while fewer works have captured the $-3/2$ power-law exponent for the coalescence-dominated regime (Crialesi-Esposito, Chibbaro, et al., 2023; Rivière et al., 2021). Our results in figure 2.3(a) show good agreement with the $-10/3$ scaling in the breakage-dominated regime. For the low We_e cases, we see some deviation from the $-3/2$ scaling just below the Kolmogorov-Hinze scale. However, further into the coalescence-dominated regime, around $d/d_H \approx 10^{-1}$, all cases follow the $-3/2$ scaling. Furthermore, we show that the macroscopic effect of surfactant on the droplet size distribution is well captured by considering a lower, average surface tension value when computing the Kolmogorov-Hinze scale. A similar result was previously obtained for surfactant-laden flows (Skartlien et al., 2013; Soligo et al., 2019a), although for the breakage-dominated regime alone. Here, we extend the result to droplets smaller than the Kolmogorov-Hinze scale.

Figure 2.3b shows the dependence of surfactant concentration ψ on the equivalent droplet diameter d. For these values and error bars, the average surfactant concentration and its standard deviation were computed at the interface of each droplet, and then averaged over all the droplets of size d. This way, the error bars capture not the variation of ψ between droplets, but the average variation on each droplet, which governs Marangoni stresses. We see that the average surfactant concentration at the interface is higher than the initial concentration in the bulk phase ($\psi = 0.1$), as from equation 2.6 it is energetically favourable for the surfactant to assemble on the interface. We observe a trend in the average surface tension value at the interface for increasing values of the Weber number: as the total amount of interfacial area increases (the total number of droplets is roughly proportional to the Weber number), the average surfactant concentration at the interface reduces. For the surfactant parameters considered in this study, there is little dependence of the mean surfactant concentration at the interface on the size of the droplets. The average surfactant concentration for all droplet sizes is about $\psi \approx 0.115$, with a slightly lower value for the smallest droplets. This results in an average reduction of the surface tension to approximately 40% of its clean value. We note that a surface tension reduction of around one-half is typical of real-world surfactant-laden interfaces, such as Tween 80 and NaCl in water (Qazi et al., 2020). Error bars show the mean standard deviation of surfactant concentration on a droplet with equivalent diameter d. The standard deviation on the droplets has instead a mild dependence on the characteristic size of the droplet, showing about a twofold increase between the smallest and the largest droplets (i.e., over a $\sim 100\times$ increase in the droplet equivalent diameter). The variation in surface tension is approximately 15% of the mean surfactant concentration at the interface, corresponding to about 8% change in surface tension on each droplet.

Next, we look at the shape of the droplets, which provides an indication of the competition between surface tension and turbulence: a droplet in a quiescent fluid takes a spherical shape and any deviation from this shape is to be attributed to the flow. We evaluate the shape of the droplets using two dimensionless parameters: the aspect ratio $\sqrt{I_1/I_3}$ and the sphericity d/d_A.

The aspect ratio is computed as the ratio between the smallest and the largest eigenvalues of the moment of inertia tensor, respectively I_1 and I_3 with $I_1 \leq I_2 \leq I_3$. The moment

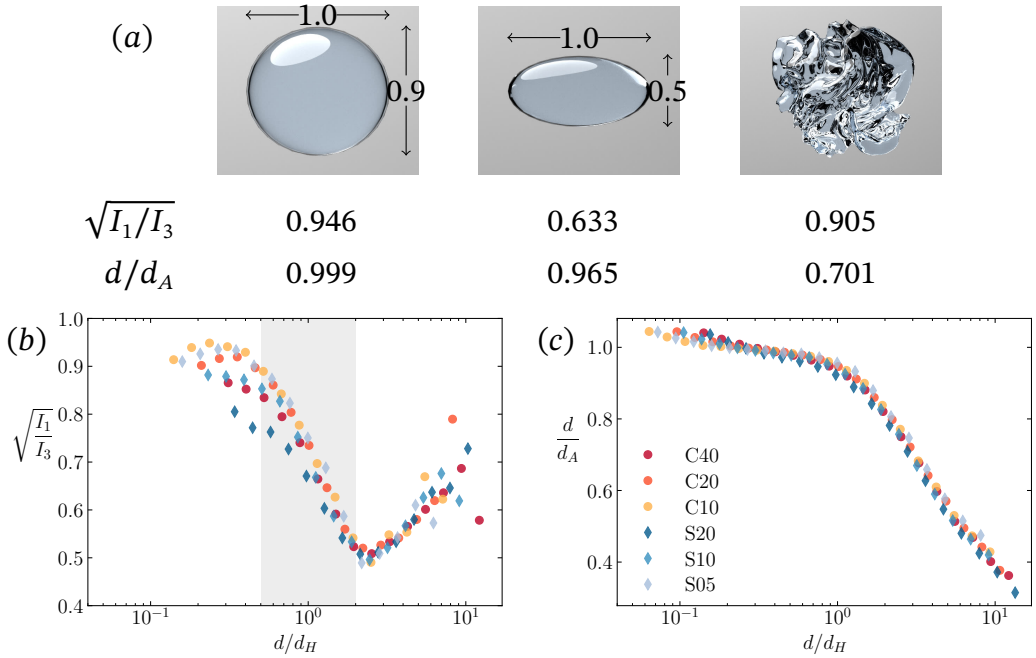

Figure 2.4: Mean droplet deformation at each equivalent diameter d normalised by the Kolmogorov-Hinze scale d_H. We plot two measures of deformation; (b) the aspect ratio of the droplets $\sqrt{I_1/I_3}$, and (c) the sphericity d/d_A. On panel (b), we shade the region $0.5 < d/d_H < 2$ where the aspect ratio is observed to decrease with equivalent diameter. Panel (a) above shows the values of deformation for (from left to right): a spheroid, an ellipsoid and a bulgy droplet.

of inertia tensor is computed as

$$\mathbf{I} \equiv \int_V \rho(||\mathbf{r}||^2 \mathcal{J} - \mathbf{r} \otimes \mathbf{r}) dV, \tag{2.8}$$

where $\mathbf{r}$ is the vector from the droplet centre of mass to a point inside the droplet, and V is the volume of the considered droplet. The aspect ratio uses a similar definition of the bubble deformation parameter defined in Bunner and Tryggvason (2003), although in their original work, the bubble deformation was defined as the square root of the largest over the smallest eigenvalue and a slightly different formulation of the moment of inertia tensor was used. Here we chose to define the aspect ratio as the inverse of the bubble deformation found in Bunner and Tryggvason (2003), such that the values of the aspect ratio are bounded between 0 (e.g., infinitely long and thin filament or sheet) and 1 (e.g., sphere or cube).

The sphericity is defined as the ratio of the volume-equivalent diameter over the surface-equivalent diameter; d/d_A. We use a different definition of sphericity from that found in the literature (Wadell, 1935), such that it is bounded between 0 and 1. The surface-equivalent diameter is defined as the diameter of a sphere having the same surface area A of the considered droplet: $d_A \equiv \sqrt{A/\pi}$. Sphericity is equal to unity for a sphere (the shape with minimal surface area for a given volume) and reduces as the droplet deforms from the spherical shape. The area A of each droplet is computed by counting the number of computational cells crossed by the interface and projecting a face of the computational cell onto the local normal $\mathbf{n}$ to the interface.

We chose these two parameters as they provide very different information, as illustrated in figure 2.4(a), where we compute the aspect ratio and sphericity for three sample droplets. The aspect ratio is very sensitive to droplet-scale deformations, for instance stretching along one of the axes, but is relatively unchanged by small-scale perturbations at the interface. Conversely, the sphericity is less sensitive to large, droplet-scale deformations, but is very effective in revealing small-scale perturbations of the interface. Qualitatively, the aspect ratio provides an estimate of the shape of a box which bounds the droplet, while the sphericity measures the total area of the droplet interface considering small-scale perturbations and droplet-scale deformations. This is reflected in figure 2.4(a): taking the spheroidal droplet as a reference ($\sqrt{I_1/I_3} \approx 1$ and $d/d_A \approx 1$), the ellipsoidal droplet shows a negligible change in the sphericity value and a $\sim$ 30% reduction in the aspect ratio. The bulgy droplet, being rather compact, has a value of the aspect ratio relatively close to that of the spheroidal droplet (about 10% difference) but a much smaller value of sphericity ($\sim$ 30% smaller).

We report the aspect ratio $\sqrt{I_1/I_3}$ in figure 2.4(b) as a function of the droplet size normalized by the Kolmogorov-Hinze scale. We observe that making the droplet size dimensionless using the Kolmogorov-Hinze scale yields a collapse of the aspect ratio for all cases onto a single curve. This suggests that even in the presence of surfactants, Hinze's (1955) assumptions hold, and droplet deformation is a universal function of d/d_H. We observe three different regimes for the aspect ratio, which can be distinguished based on the value of d/d_H. The aspect ratio of small droplets, up to approximatively $d = 0.5 d_H$, is roughly constant and close to unity, indicating that the droplets are spherical or only slightly elongated (i.e., compact shape). At this point, no information can yet be inferred on local, small-scale deformations of the interface. Droplets smaller than the Kolmogorov-Hinze scale are characterised by surface tension forces dominating over turbulent fluctuations. The sec-

ond regime, observed for $0.5d_H \lesssim d \lesssim 2d_H$, is characterised by a sharp reduction in the value of the aspect ratio (down to $\sqrt{I_1/I_3} \approx 0.5$, a similar value of an elongated ellipsoid): droplets become more elongated with an overall deformation that increases with their size. This result is coherent with the definition of the Kolmogorov-Hinze scale as the size of the largest (on average) non-breaking droplets: at about the Kolmogorov-Hinze scale, droplets start to deform significantly. Statistics on the sphericity will provide further information on the small-scale deformation within this regime and will be discussed in the following paragraph. Lastly, in larger droplets, $d > 2d_H$, there is a recovery of the droplet aspect ratio: droplets partially recover from their deformed state, with values of the aspect ratio nearing $\sqrt{I_1/I_3} \approx 0.7$. This result indicates that droplets become less deformed overall, and some rotational symmetry is restored. At first, this may be a counterintuitive result, but sphericity will help to explain this interesting behaviour.

We report the sphericity for all cases in figure 2.4(c). The droplet size is made non-dimensional using the Kolmogorov-Hinze scale for each case. We observe that data for all cases collapse on a single curve when scaled by the Kolmogorov-Hinze scale, further confirming the validity of the Kolmogorov-Hinze scale as a fundamental length scale. We observe two very distinct regimes, separated by the Kolmogorov-Hinze scale. At scales smaller than the Kolmogorov-Hinze scale, droplets have a close-to-unity and slightly decreasing sphericity, which sharply decreases above the Kolmogorov-Hinze scale. Note that, for the smallest droplets, we have values of sphericity larger than one; we would like to remark that these values are not admissible and are due to inaccuracies in the computation of interface normals and area when the droplets are only a few grid cells in volume. The sphericity for droplets smaller than the Kolmogorov-Hinze scale is close to unity and decreases for increasing droplet sizes; this information, coupled with the results from the droplet aspect ratio, indicates that droplets much smaller than Kolmogorov-Hinze scale have a spheroidal shape with limited elongation and almost no small-scale perturbations of the interface. Kolmogorov-Hinze-scale-sized droplets (but still smaller than the Kolmogorov-Hinze scale) show a substantial reduction in the aspect ratio and only a minor decrease in the sphericity: the shape of these droplets is similar to an ellipsoid, as the droplet is stretched (low aspect ratio) but the sphericity is still close to unity (indicating the absence of relevant perturbations of the interface). Conversely, droplets slightly larger than the Kolmogorov-Hinze scale show reduced aspect ratio and sphericity: these droplets are not only strongly elongated (low aspect ratio), but small-scale perturbations of the interfaces (small humps and dimples) start forming (low sphericity). The trend in sphericity is kept also for droplets much larger than the Kolmogorov-Hinze scale; these droplets show a recovery of the aspect ratio, indicating either the formation of bulgy droplets (see figure 2.4a) or of convoluted filaments. Both of these shapes are coherent with the two deformation parameters we investigated. i.e., relatively low aspect ratio and low sphericity.

To distinguish among the two possible shapes, bulgy droplets versus convoluted filaments, we compute the average radius of curvature R at the interface of each droplet, reported in figure 2.5. To compute the radius of curvature R, we first compute the mean curvature κ using the divergence of the normal n to the interface;

$$\kappa = \nabla \cdot \mathbf{n}. \tag{2.9}$$

We average the curvature κ over the droplet interface, and define the radius of curvature

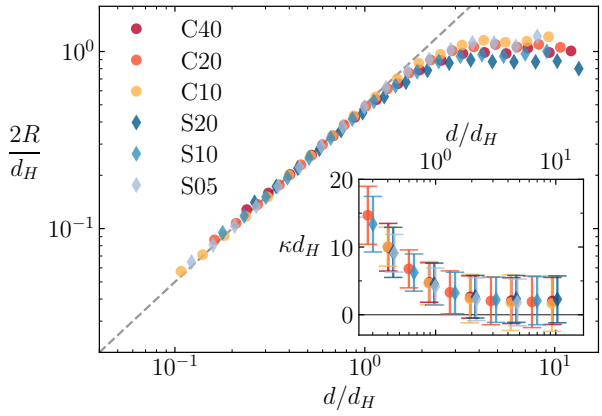

Figure 2.5: The mean radius of curvature R of the surfaces of droplets binned by their diameter d. The dashed line shows $R = d/4$, the radius of curvature of a sphere with diameter d. Inset: the same values, plotted in terms of curvature $\kappa = 1/R$. Error bars show the standard deviation of curvature on the droplets.

as the inverse of the mean curvature, $R \equiv 1/\kappa$. Note that, in equation 2.9, we do not use a minus sign in the definition of the curvature, as we have an outward-pointing normal $\mathbf{n}$ and we choose to assign positive values of curvature to convex surfaces, i.e., the curvature is positive if the surface curves away from the normal. Also, the normal is ill-defined for small droplets, so we only calculate the mean curvature of droplets with a volume greater than 10 computational cells. For a surface in three dimensions, such as our interface, the mean curvature is equal to the sum of the two principal curvatures, $\kappa = \kappa_1 + \kappa_2$. For a sphere, both principal curvatures are equal to the inverse of the sphere's radius; hence the mean curvature is twice this value and the radius of curvature is $R = d/4$. Figure 2.5 shows that droplets smaller than the Kolmogorov-Hinze scale follow this scaling (gray dashed line). This result further confirms the rather regular shape (spheroid- or ellipsoid-like) of the small droplets. Above the Kolmogorov-Hinze scale instead, we observe a departure from $d/4$: the radius of curvature becomes constant, approximately equal to half the Kolmogorov-Hinze scale, and independent of drop size.

To understand this behaviour, we consider a cylinder of radius $d_H/2$. On the curved surface of the cylinder, the two principal curvatures are $\kappa_1 = 0$ and $\kappa_2 = 2/d_H$. Neglecting the two flat ends, the mean curvature of the cylinder is thus $\kappa = 2/d_H$, i.e. the radius of curvature of the cylinder is equal to half the Kolmogorov-Hinze scale, and is independent of its length. This result, combined with the information obtained from the deformation parameters in figure 2.4, shows that, above Kolmogorov-Hinze scale droplets take the shape of filaments with a diameter equal to the Kolmogorov-Hinze scale.

The inset of figure 2.5 shows the mean curvature κ of the droplets as a function of their equivalent diameter d. Error bars indicate the standard deviation of the curvature, which was calculated at the interface of each droplet and averaged over the ensemble of droplets of similar size d. The standard deviation of the curvature of an interface is a measure of its corrugation, and can be used to quantify Plateau–Rayleigh instabilities which lead to droplet breakup (Kooij et al., 2018; Rayleigh, 1878; Villermaux & Bossa, 2009). From the

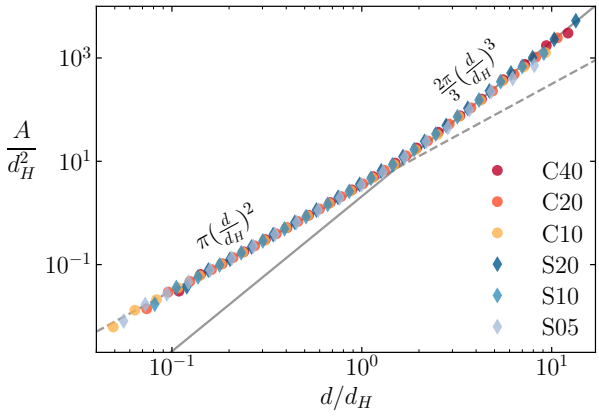

Figure 2.6: Dependence of droplets' surface area A on their equivalent diameter d. The dashed line shows the surface area of a sphere with diameter d, and the solid line shows the surface area of a filament with diameter d_H.

inset of figure 2.5, we see that droplets of all sizes show corrugation, and the standard deviation of κ is comparable to its average value. Above the Kolmogorov-Hinze scale, we report an increased probability of negative values of the mean curvature, indicative of dimples and saddle points in the surface of the droplet, which, for example, can be due to impinging jets or large Plateau-Rayleigh instabilities on the interface.

To test our hypotheses on the droplet shapes above and below the Kolmogorov-Hinze scale, we consider their surface area. Figure 2.6 shows the mean surface area of the droplets at each equivalent diameter d. As we previously noted, the droplets smaller than the Kolmogorov-Hinze scale are almost spherical in shape, and hence we see that their surface area grows quadratically with their characteristic size. Above the Kolmogorov-Hinze scale, the droplet surface areas instead grow as the cube of their sizes. As a first approximation, we can think of these droplets as long cylinders with the same diameter d_H and different lengths l. Ignoring the two end faces, the surface area of such a cylinder is $A_f = \pi d_H l$ and the volume is $V_f = \pi d_H^2 l/4$. Substituting the volume for the equivalent diameter (equation 2.7) we get an expression for the length;

$$l = \frac{2d^3}{3d_H^2}. \tag{2.10}$$

Plugging this into the formula for the cylinder surface area, we obtain $A_f = 2\pi d^3/(3d_H)$, showing that a filament with variable length l and constant diameter d_H has an interfacial surface area that grows as the cube of its volume-equivalent diameter d. The interfacial surface area of the droplets above the Kolmogorov-Hinze scale closely follows A_f, as reported in figure 2.6.

From our observations of curvature and surface area, it appears that droplets above the Kolmogorov-Hinze scale are filamentous in shape. However, their aspect ratio shows the filaments cannot be straight, since this would produce a monotonic reduction in $\sqrt{I_1/I_3}$ with d, which we do not see in figure 2.4a. Hence a natural question is: *do the filaments form loops, or are they simply connected?* Figure 2.7 shows two droplets from case S20, we see that both droplets are made up of convoluted filaments, and in many places, the filaments

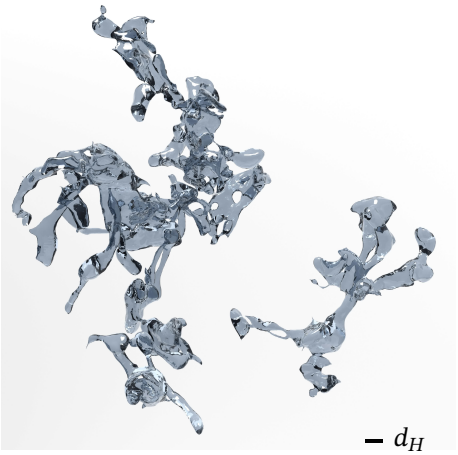

Figure 2.7: Visualisation of two droplets extracted from case S20. The left droplet has 56 handles and six voids. The right droplet has two handles and zero voids. The length of the black bar is the Kolmogorov-Hinze scale.

do in fact, form loops. To answer the question quantitatively, we measure the topology of the interface of each droplet using its Euler characteristic χ, which obeys the formula

$$1 - \chi/2 = h - v, \tag{2.11}$$

where h is the number of handles and v is the number of voids in the drop (see section B.1 in the appendix for a derivation of this equation). In the insets of figure 2.8a, we show renders of example droplets with one and two handles. Analogously to the handle on a teacup, a handle is a loop of the dispersed phase which extends through the carrier phase. The renders in the insets of figure 2.8b show example droplets with one and two voids. A void is a region of the carrier phase entirely enclosed by the dispersed phase. Note that similarly to droplet breakup and coalescence, a change in the number of handles or voids necessitates a merging or splitting of interfaces. Using a method similar to Mendoza et al.'s characterisation of dendritic metal samples, we measure the Euler characteristic using simplicial homology, that is, by dividing the interface into simple polygons and counting the number of nodes n, edges e, and faces f on the interface of each droplet. The Euler characteristic of the interface is then given by the Poincaré formula (Massey, 1997, p.26),

$$\chi = n - e + f. \tag{2.12}$$

Our volume of fluid field ϕ is defined on a cubic grid, and we can define the interface as the boundaries between cells where $\phi - 0.5$ changes sign. Hence, our interface is already divided into square faces, and χ can be calculated by counting these faces and their edges and nodes. We also count the number of voids v on each droplet. Voids are counted by rerunning the flood fill algorithm, looking for contiguous cells where $\phi < 0.5$; to do so we use a stack-based 26-way flood-fill, which is an extension to three dimensions of the two-dimensional 8-way flood fill (Newman & Sproull, 1979). Knowing χ and v for each drop, we can use equation 2.11 to obtain the number of handles h.

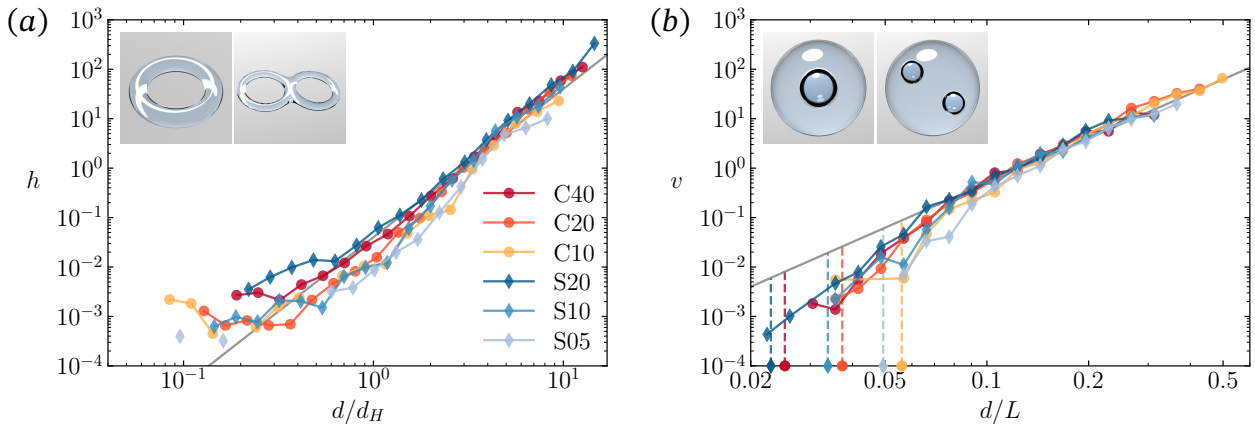

Figure 2.8: (a) Number of handles h per droplet. The grey line shows the fit $h = 0.04(d/d_H)^3$. Renders show example droplets with one and two handles ($\chi = 0$ and $\chi = -2$, respectively). (b) Number of voids v per droplet. The grey line shows the fit $v = 500(d/L)^3$. We mark the x-axis to show the Kolmogorov-Hinze scale of each case. Renders show example droplets with one and two voids ($\chi = 4$ and $\chi = 6$, respectively). The renders are obtained from droplets we artificially generated for the sole purpose of demonstrating handles and voids.

Figure 2.8a shows how the mean number of handles per droplet depends on the droplet size. We see that the largest droplets are very self-connected, having on the order of 10^2 handles. Furthermore, the number of handles in each case collapses to a single line when the equivalent diameter is normalised by the Kolmogorov-Hinze scale d_H. This universality occurs because surface tension is constantly acting to destroy the handles, so the higher the surface tension, the shorter the lifetime of the handle. The fit $h = 0.04(d/d_H)^3$ gives the number of handles as a function of the droplet volume. Using our earlier result that the large droplets are filaments with lengths given by equation 2.10, we can convert this expression into the number of handles per unit length of the filament: $h/l = 0.06/d_H$. Figure 2.8b shows us, on the other hand, that the number of voids is independent of surface tension, which is reasonable as a void inside a droplet experiences no net surface tension force. The number of voids simply scales with the volume of the droplet. Again we can obtain a fit, $v = 500(d/L)^3$; substituting the equivalent diameter for the droplet volume V (equation 2.7) we find there are roughly $v/V \approx 950/L^3$ voids per unit droplet volume in all cases. We suspect the void concentration depends on the droplet coalescence rate and turbulence intensity (Re_λ), however, we leave a proper investigation of this dependence to future works.

2.3.2 Flow statistics

We characterize the effects induced by the presence of clean and surfactant-laden interfaces on the local flow statistics using the flow topology parameter (Perry & Chong, 1987), which compares the local flow to three different base flows: purely rotational, pure shear and

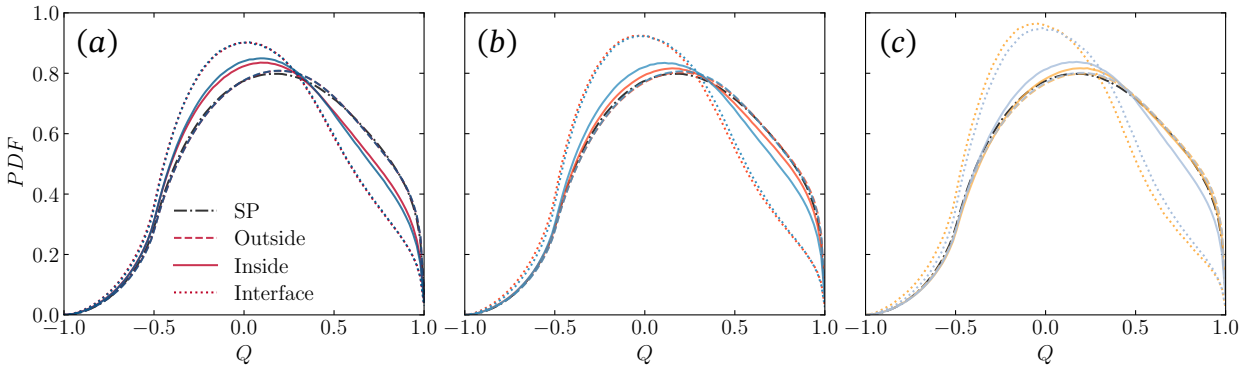

Figure 2.9: Flow topology parameter sampled in different regions of the domain: inside the droplets (solid line), in the carrier phase (dashed line) and at the interface (dotted line). The single-phase case is reported for reference (dash-dotted line). Each panel refers to an approximate value of the effective Weber: (a) $We_e \approx 10$ – panel (cases C10 and S05), (b) $We_e \approx 20$ – panel (cases C20 and S10) and (c) $We_e \approx 40$ – panel (cases C40 and S20).

purely extensional flow. The flow topology parameter Q is a combination of the rate-of-deformation tensor $D \equiv (\nabla\mathbf{u}+\nabla\mathbf{u}^T)/2$ and of the rate-of-rotation tensor $\Omega \equiv (\nabla\mathbf{u}-\nabla\mathbf{u}^T)/2$, where $\nabla\mathbf{u}$ is the velocity gradient tensor. The quantities D^2 and Ω^2 are defined as $D^2 = D : D$ and $\Omega^2 = \Omega : \Omega$, where $:$ identifies the dyadic (double-dot) product. For $D^2 = 0$ and $\Omega^2 \neq 0$ we have a purely rotational flow, whereas for $D^2 \neq 0$ and $\Omega^2 = 0$ we have a purely extensional flow; pure shear is a combination of these two cases, occurring for $D^2 = \Omega^2$.

$$Q = \frac{D^2 - \Omega^2}{D^2 + \Omega^2} = \begin{cases} -1 & \text{purely rotational,} \\ 0 & \text{pure shear,} \\ +1 & \text{purely extensional.} \end{cases} \tag{2.13}$$

We compare clean and surfactant-laden cases at similar effective Weber numbers in figure 2.9, together with the single-phase case for reference. The flow topology parameter is computed in three distinct regions: inside the droplets ($\phi > 0.5$), in the carrier phase ($\phi < 0.5$) and at the interface. This way, we can separate the contribution from the different regions of the flow (Dodd & Jofre, 2019; Rosti, De Vita, et al., 2019; Soligo et al., 2020b), and investigate the effect of Marangoni stresses at the interface for the surfactant-laden cases and of flow confinement on the flowing condition inside the droplets and at the interface.

We first consider the flow topology parameter in the carrier phase. The relatively low volume fraction of the dispersed phase reduces the overall impact of the presence of the interface on the outer flow. The flow topology parameter for all clean and surfactant-laden cases well collapses onto the single phase line, indicating indeed that the presence of a deformable interface and of Marangoni stresses does not introduce any significant modification of the outer flow at the relatively low volume fraction considered. A similar result was reported by Rosti, De Vita, et al. (2019) for clean droplets and for volume fractions of the dispersed phase up to 30%. In general, the flow topology shows a predominance of a combination of pure shear and extensional flow, with a limited rotational contribution.

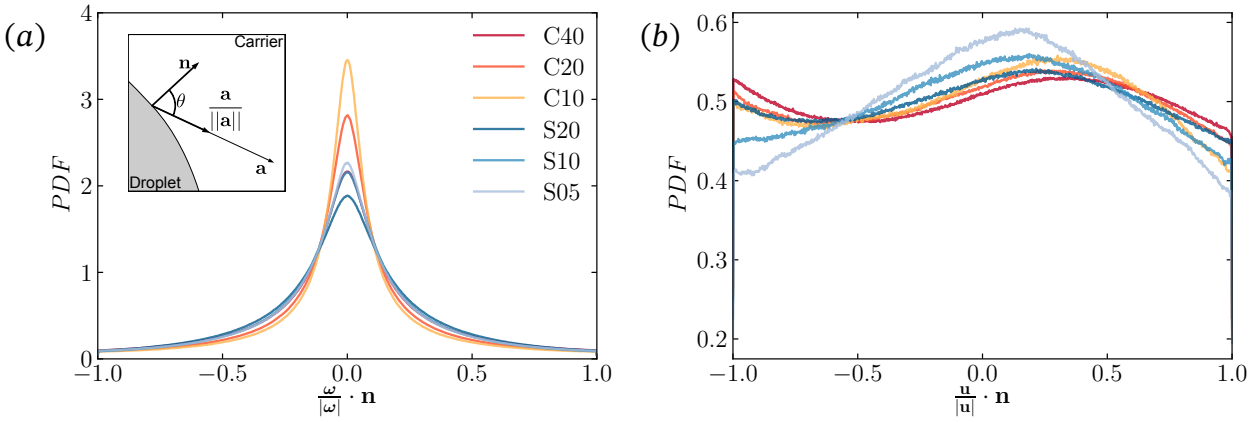

Figure 2.10: Alignment between unit-length normal to the interface $\mathbf{n}$ and: (a) vorticity at the interface, (b) velocity at the interface. The inset in panel (a) shows how the alignment has been computed: for a generic vector $\mathbf{a}$ we define the alignment as $\mathbf{n} \cdot \mathbf{a}/||\mathbf{a}||$, which is equal to the cosine of the angle θ in between the two vectors.

The flow topology computed inside the droplets highlights the effect of flow confinement. Surface tension has competing effects: while on the one hand, a large value of surface tension is more effective in decoupling internal and external flow, a low value of surface tension produces many small-size droplets that increase the flow-confinement effect. We observe a reduction in extensional flow and an increase in pure shear for increasing values of the Weber number, which has been attributed to the confinement effect of small droplets (Soligo et al., 2020b). We do not report changes in the rotational component, which can be attributed to the lack of large-scale coalescence events (Rosti, De Vita, et al., 2019). When comparing cases at similar effective Weber numbers, we observe that the addition of surfactant has a similar effect to a reduction in the surface tension value: a reduction in the extensional flow and an increase in pure shear. The difference in the flow topology between clean and surfactant-free droplets reduces as the effective Weber number increases.

It is interesting to note that, at the interface, the addition of surfactant instead has an opposite effect: the presence of surfactant, especially at low values of the effective Weber number, leads to an increase of extensional flow and a decrease in rotational flow – pure shear is unchanged. This difference results from the action of Marangoni stresses, and is indeed more apparent at low values of the effective Weber number, i.e. at high values of surface tension. We observe a shift towards extensional flow for increasing values of the effective Weber number, confirming previous findings (Soligo et al., 2020b).

We now focus on flow statistics at the interface to better understand the local surface tension effects induced by clean and surfactant-laden interfaces. We compute the alignment of vorticity at the interface of the droplets: to quantify the direction of vorticity, we use the cosine of the angle θ, see the sketch in figure 2.10a. This quantity is found by taking the scalar product between the interface normal $\mathbf{n}$ (outward-pointing, unit-length normal) and the unit-length vorticity vector, $\boldsymbol{\omega}/||\boldsymbol{\omega}||$. The probability density function of the vorticity-interface alignment is reported in figure 2.10a for all the cases we simulated. Similarly to what was found by Mukherjee et al. (2019), the vorticity is mostly orthogonal to

the interface normal. At very large values of the surface tension, i.e. $We \to 0$, the interface between the droplet and the carrier phases acts similarly to a slip wall: the high surface tension makes the interface close to undeformable but imposes no condition on the tangential component of the flow. We thus expect that at high values of surface tension the vorticity vector is tangential to the interface, i.e. $\mathbf{n} \cdot \boldsymbol{\omega}/||\boldsymbol{\omega}|| = 0$. As the interface becomes more deformable (corresponding to a higher Weber number), this condition is relaxed and the PDF widens. We observe that the PDF remains symmetric for all cases; this is an expected result as positive and negative values of the alignment correspond to flow structures at the interface rotating in the anti-clockwise and clockwise directions respectively, and the two are equally probable. The alignment of vorticity at the interface also highlights the effect of surfactant, and in particular of Marangoni stresses tangential to the interface: the cases at a similar effective Weber number (namely $We_e \approx 10$ C10 and S05; $We_e \approx 20$ C20 and S10; $We_e \approx 40$ C40 and S20) show notably different distributions, suggesting that in terms of the local fow around the droplets, the effect of surfactant cannot be approximated as only an average surface tension reduction. We indeed notice a decoupling among the various cases at approximately the same effective Weber number, with cases C40 ($We_e = 39.3$) and S10 ($We_e = 25.8$) showing the very same distribution in vorticity alignment. The presence of Marangoni stresses promotes the formation of flows tangential to the interface, whose gradients contribute to the vorticity component normal to the interface.

The alignment of the fluid velocity at the interface further corroborates the role of Marangoni stresses in modifying the local flow velocity at the interface; figure 2.10b shows the probability density function of the scalar product between the unit-length velocity vector and the normal to the interface. The surfactant-laden cases show a more peaked distribution at $\mathbf{n} \cdot \mathbf{u}/||\mathbf{u}|| \approx 0.1$, corresponding to a local fluid velocity almost tangential to the interface, with a small outward (i.e., from the droplet phase towards the carrier phase) component. This velocity alignment is clearer for the cases at low Weber number: the magnitude of Marangoni stresses directly depends on the local surface tension, hence the cases at high Weber number are characterized by weaker Marangoni stresses. Indeed, the case S20 shows similar velocity alignment to the surfactant-free cases, being the Marangoni stresses weaker compared to the other surfactant-laden cases. For the clean cases we observe two separate peaks in the distribution, one at $\mathbf{n} \cdot \mathbf{u}/||\mathbf{u}|| = -1$ and one at $\mathbf{n} \cdot \mathbf{u}/||\mathbf{u}|| \approx 0.3$. The former corresponds to an inward flow perpendicular to the interface, and the latter to a fluid velocity mainly tangential to the interface, although with a larger normal component compared to the surfactant-laden cases. We attribute this reduction in the probability of having flow tangential to the interface to the absence of Marangoni stresses for the surfactant-free cases. A similar distribution is also achieved by case S20, which is characterised by weak Marangoni stresses (due to the low reference surface tension value), further highlighting the role of Marangoni stresses.

So far we have only considered the angle between the flow velocity at the interface and the interface itself; we now proceed to analyse the magnitude of the flow velocity at the interface. The flow velocity is decomposed into two components, a normal component $u_n \equiv \mathbf{u} \cdot \mathbf{n}$ aligned with the outward-pointing normal to the interface $\mathbf{n}$, and a tangential component $u_t \equiv ||\mathbf{u} - u_n\mathbf{n}||$. The sign of the normal component is important; the interface is advected with the flow so positive u_n occurs in places where the interface moves outward in the direction of the carrier phase, and negative u_n occurs in places where the interface moves inward, in the direction of the dispersed phase. Due to volume conservation of the

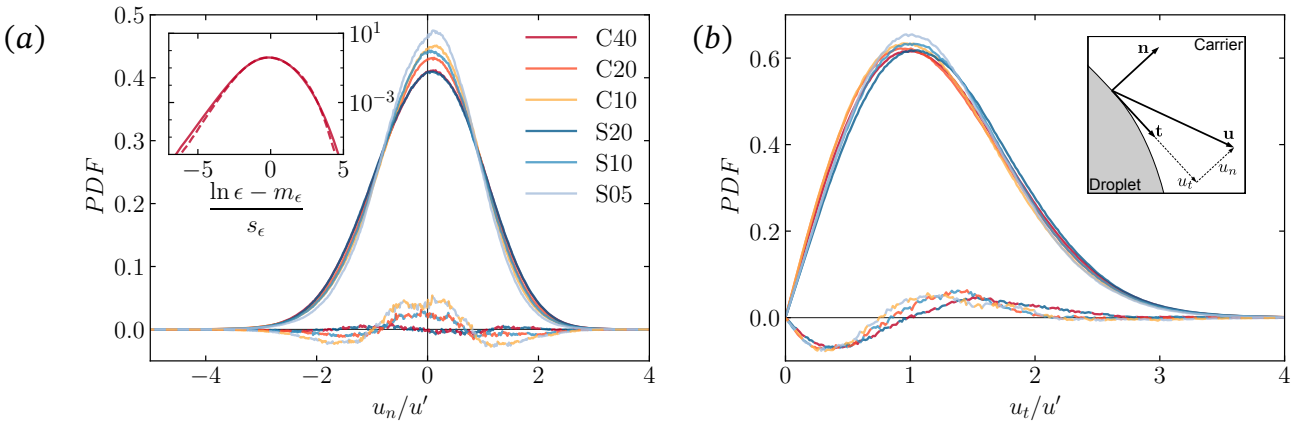

Figure 2.11: (a) Normal component of the flow velocity at the interface u_n and (b) tangential component of the flow velocity at the interface u_t. Two-colour lines show the difference between the PDF of surfactant-laden and clean pairs of cases with similar We_e (these data are magnified by a factor two for better reading). The inset in panel (a) shows histograms of the logarithm of the dissipation ϵ inside (dashed line) and outside (solid line) the droplets for case C40, where m_ϵ and s_ϵ are the mean and standard deviation of $\ln\epsilon$, respectively. The inset in panel (b) shows the decomposition of the flow velocity along a direction normal (**n**) and tangential (**t**) to the interface.

phases, u_n has zero mean. On the other hand, the choice of the tangential direction in the plane is arbitrary: it is taken as the remainder of the subtraction of the normal component from the total velocity. For this reason, we have only positive values of the tangential velocity u_t.

In figure 2.11a, the probability density functions of the normal component of the velocity u_n show peaks at relatively low positive u_n and are negatively skewed in all cases, i.e., extreme negative values (inward fluid velocity) are more probable than extreme positive values (outward fluid velocity). To elucidate the cause of the skewed distributions, we also show histograms of the logarithm of the dissipation ϵ for case C40. The tails of these histograms can be attributed to extreme events and hence to intermittency in the flow (Kaneda & Morishita, 2012). We see that the flow outside the droplets gives slightly wider tails and hence has higher intermittency than that inside the droplets (also seen by Crialesi-Esposito, Boffetta, et al. (2023) for fluid velocity differences inside and outside droplets). Therefore, we attribute the increased likelihood of extreme inward velocities at the interface to increased intermittency of the flow in the bulk phase. Returning to the main panel of figure 2.11a, we note that cases with a higher We_e show a wider distribution of u_n/u'. A higher effective Weber number implies a more deformable interface with a lesser damping effect on the normal velocity: extreme (positive and negative) events become more probable as surface tension is reduced. The difference among surfactant-laden and clean cases at similar effective Weber numbers is reported with two-colour lines (rescaled by a factor of two for improved readability). We observe that the surfactant suppresses extreme events, especially at low values of the Weber number (high surface tension), when Marangoni stresses are greatest

in magnitude. A similar turbulence suppression effect was seen by L. Shen et al. (2004) for surfactants in free shear flows, and was attributed to the elasticity of the surfactant-laden interface.

When considering the tangential component, we observe a reversal of the trend: surfactant, via Marangoni stresses, increases the probability of flow tangential to the interface. Two-colour lines show the difference between surfactant-laden and clean cases at similar We_e, with the data rescaled by a factor of two for ease of reading. It is clear that the presence of surfactant increases the probability of finding tangential velocities in the range $u' \lesssim u_t \lesssim 2u'$. All surfactant-laden cases have approximatively a similar value of the peak of the distribution, which is slightly larger than that of the surfactant-free cases, indicating that surfactant-laden cases have a higher probability of large values of the tangential velocity. Interestingly, as the Weber number increases, the peak shifts to slightly higher values, and the likelihood of large tangential velocity increases as well, as shown by the two-colour lines. This result suggests that while increasing the flow velocity tangential to the interface and suppressing large normal components, Marangoni stresses also have a modulating effect on the tangential component.

2.4 Conclusions

In this study, we perform direct numerical simulations of surfactant-laden droplets in homogeneous isotropic turbulence. The interfacial dynamics are solved using an MTHINC volume of fluid method coupled with a phase-field-based approach to simulate surfactant dynamics. By examining droplet morphology and local flow statistics, we can shed light on the interfacial characteristics and dynamics of these complex systems.

The Kolmogorov-Hinze length scale is a fundamental quantity in multiphase flows laden with clean droplets or bubbles; our numerical results show that the Kolmogorov-Hinze scale can be extended to surfactant-laden flows, provided that a lower value of surface tension, accounting for the presence of surfactant, is selected. We indeed observe a collapse of most statistics when plotted as a function of d/d_H. We compute the droplet size distribution for all clean and surfactant-laden cases and verify that: (i) the Kolmogorov-Hinze scale effectively separates the breakage- and coalescence-dominated regimes and (ii) the power-law scaling for these two regimes can be applied to surfactant-laden droplets. The combined results on the deformation of the droplets, i.e. aspect ratio and sphericity, prove that droplets smaller than the Kolmogorov-Hinze scale have a relatively compact and regular shape (spheroid- or ellipsoid-like shapes), whereas droplets larger than the Kolmogorov-Hinze scale have coiled, filamentous shape, supporting previous observations of filamentous water drops (Jackiw & Ashgriz, 2021; Villermaux & Bossa, 2009). The filamentous droplets are found to have an average diameter which is independent of the overall droplet size d and is equal to the Kolmogorov-Hinze scale, further evidencing the relevance of this length scale.

The very different shapes of large and small droplets have direct implications on the total area of the interface, which is a crucial parameter in determining the overall exchange of species, momentum and energy among the carrier and the dispersed phase. We report the existence of two regimes, separated by the Kolmogorov-Hinze scale: the area of droplets smaller than the Kolmogorov-Hinze scale is proportional to the square of the characteris-

tic size of the droplet, whereas it is proportional to the cube of the characteristic size for droplets larger than the Kolmogorov-Hinze scale. The two different scalings can be directly traced back to the shape of the droplets, spheroid-like below the Kolmogorov-Hinze scale and filamentous above the Kolmogorov-Hinze scale. The large and filamentous droplets are coiled up, as indicated by their aspect ratio. Thus we investigate their self-connectedness, using the Euler characteristic to count the number of handles and voids on each droplet. To the best of our knowledge, this is the first time the number of handles and voids on a droplet has been measured. We find that the number of handles depends directly on the size of the droplet and its surface tension, as data from all cases collapse on a single curve when normalised by the Kolmogorov-Hinze scale; we also provide a scaling for the linear density of handles, $h/l = 0.06/d_H$. Conversely, the number of voids depends on the droplet size alone. Our interpretation is that the restoring action of surface tension reduces the lifetime of a handle, whereas the dynamics of a void are unaffected by surface tension. Going further, the Poincaré-Hopf theorem relates the Euler characteristic χ of an interface to the number of topological defects in any tangent vector fields (e.g., fluid velocity, alignment of molecules, stresses) at the interface (Maroudas-Sacks et al., 2021), (a well-known example of this for $\chi = 2$ is the hairy ball theorem). A future investigation may count topological defects on the surface of droplets and relate the number to their ability to resist breakup.

Results from the morphology of the droplets highlight the validity of the Kolmogorov-Hinze scale for both clean and surfactant-laden flows: a rescaled value of the surface tension, accounting for the average surface tension reduction induced by the surfactant, can be effectively used to define the Kolmogorov-Hinze scale. This finding suggests that the effect of surfactant on droplets in homogeneous isotropic turbulence can be mainly summarised as a reduction in surface tension. The lack of a large-scale and time-persisting velocity difference among the carrier and dispersed phase, as found in upflow and downflow configurations (Lu et al., 2017; Takagi et al., 2008), prevents the formation of significant, large-scale Marangoni stresses at the interface. Hence, in our simulation setup, Marangoni stresses play a minor, local role, with negligible effects on the statistics of the droplets. Local flow statistics better show the effect of these tangential stresses: Marangoni stresses modulate the flow at the interface by reducing the velocity component normal to the interface and increasing the tangential component. When computing the flow topology parameter at the interface, we find that Marangoni stresses increase the elongational component and reduce rotational flow at the interface. This result is coherent with the action of Marangoni stresses generating an elongational type of flow with sources corresponding to low-surface-tension regions and sinks to high-surface-tension regions. Inside the droplets, Marangoni stresses reduce elongational flow and increase the pure shear contribution.

In conclusion, we find that a statistically homogeneous and isotropic flow allows for a simplified treatment of the surfactant effects. Results from Hinze's theory can thus be applied to surfactant-laden flows, by considering the average surface tension reduction operated by the surfactant. For both clean and surfactant-laden flows, the Kolmogorov-Hinze scale separates two regimes characterised by very different scaling for the surface area of the droplets: a significant increase in the surface area is observed for droplets larger than the Kolmogorov-Hinze scale. This latter result has important implications for environmental and industrial multiphase flows, where the interface serves as a conduit for all species, momentum and energy transfers among the phases.

The code used for calculating droplet morphology can be found at https://github.com/

marco-rosti/CFF-dropStats.git.

Chapter 3

The Effect of Particle Anisotropy on the Modulation of Turbulent Flows

Chapter 3 moves the focus from droplets to solid particles. Contrasting with droplets, particles have a defined size and produce a much stronger back-reaction effect on the flow. I investigate the modulation of turbulence with Taylor-Reynolds number $Re_\lambda = 435$ due to the presence of finite-size dispersed particles, comparing the effects of bluff spheres and slender fibres. Both object shapes yield similar bulk effects, characterized by large-scale energy depletion. However, a scale-by-scale analysis reveals intrinsic differences in the energy spectrum. The study highlights differences in the turbulent energy cascade between the two cases. Both particle shapes provide a "spectral shortcut" for the kinetic energy in the flow, with bluff objects shrinking the extension of the classical energy cascade but maintaining its typical features, while slender ones induce an alternative energy flux mediated by fluid-solid coupling. This chapter provides valuable insights into the influence of object shape on the modification of turbulence.

Some clarifications that arose during discussion with the thesis examiners:

- The fibres are chosen to be very slender, they have a thickness of three times the Eulerian grid spacing.
- For the interaction of fibres, we use the minimal collision model from Snook et al., 2012.
- For the interaction of spheres, we use the soft-sphere collision model from Hori et al., 2022.
- κ is the wavenumber of the flow.
- ϵ is the dissipation in the fluid.

The article is appended in section C of this thesis and can be cited as follows:

Olivieri, S., Cannon, I., & Rosti, M. E. (2022). The effect of particle anisotropy on the modulation of turbulent flows. *Journal of Fluid Mechanics*, *950*, R2. https://doi.org/10.1017/jfm.2022.832

The conclusions we draw are as follows; spheres and fibres cause a similar reduction in the Taylor-Reynolds number as their mass-fraction increases. Spheres cause a reduction in the kinetic energy of the flow at only large length scales, and return energy to the flow around the length scale of their diameter. The classical turbulent energy cascade is regained at scales smaller than the sphere diameter. Fibres cause a reduction in turbulent kinetic energy across a range of length scales. Fibres act as a conduit of kinetic energy from large to small scales, disrupting the classical turbulent energy cascade.

Chapter 4

Spheres and Fibres in Turbulent Flows at Various Reynolds Numbers

Chapter 4 extends the investigation of chapter 3 to a range of turbulence intensities $12.8 < Re_\lambda < 442$. This allows us to explore the dissipative anomaly, which is a long-studied phenomenon of single-phase turbulence. It states that the dissipation remains finite even as the fluid viscosity tends to zero. We find that sphere-laden and fibre-laden flows produce the same value of anomalous dissipation as single-phase flows for $Re_\lambda \to \infty$. Our analysis shows that the "spectral shortcut" uncovered in chapter 3 is present at all turbulence intensities investigated, even for low Re, when the particles' influence extends deep into the dissipative range. Looking at the near-particle flow, we see that spheres enhance dissipation within two-dimensional sheets, while fibres enhance dissipation in structures that exhibit dimensions between one and two. Lastly, our study uncovers the contrasting impact of spheres and fibres on vortical flow structures. Specifically, spheres impede these structures, curbing their formation, whereas fibres completely disrupt vortex stretching behaviour in their vicinity.

The article can be cited as follows:

Cannon, I., Olivieri, S., & Rosti, M. E. (2023). Spheres and fibres in turbulent flows at various Reynolds numbers. *Under review for Physical Review Fluids*. https://doi.org/10.48550/arXiv.2310.07986

In this chapter, we see that as viscosity tends to zero, the normalized dissipation tends to the same finite value for single-phase, sphere-laden, and fibre-laden flows. Spheres return energy to the flow around the length scale of their diameter, whereas fibres return energy to the flow around the length scale of their thickness. The classical turbulent energy cascade is regained at scales smaller than the sphere diameter. Spheres enhance dissipation in two-dimensional sheets. Fibres enhance dissipation in regions with dimensions greater than one and less than two. Spheres produce shearing regions in the flow and fibres disrupt the process of turbulent vortex stretching.

4.1 Introduction

Particle-laden turbulent flows abound in our environment; see, for example, volcanic ash clouds, sandstorms, and microplastics in the oceans. In these cases, the particles are seen

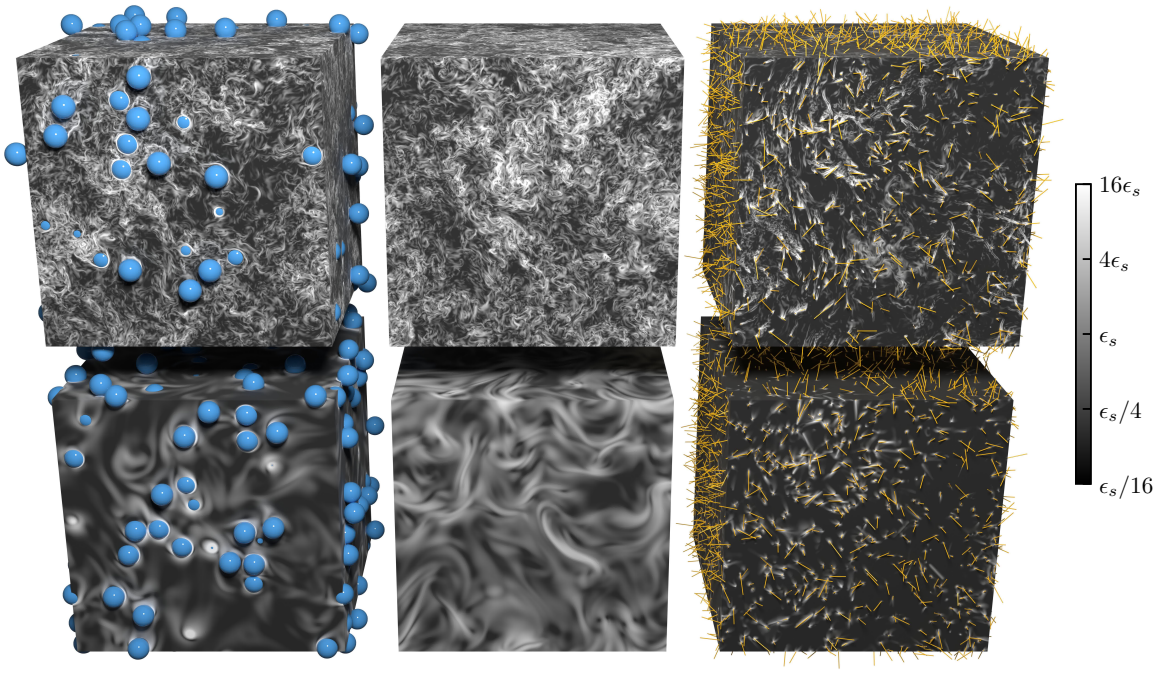

Figure 4.1: Images of the simulated domain. Left column: flows with fixed spheres. Middle column: single phase flows. Right column: flows with fixed fibres. Flows on the top row have $Re_{ABC} = 894$. Flows on the bottom row have $Re_{ABC} = 55.9$. At the boundary of each domain we show the dissipation on a logarithmic scale, where ϵ_s is the mean dissipation of the single-phase flow at $Re_{ABC} = 894$.

in a range of shapes, and the intensity of the carrier turbulent flow can significantly vary. In this context, the present study delves into the interaction between particles and turbulent flows, focusing on two distinct particle shapes, spheres and fibres, and exploring turbulent flows across a large range of Reynolds numbers.

The interaction of particles with turbulent flows has garnered significant research attention since Richardson and Proctor (1927) used balloons to track eddies in the Earth's atmosphere in 1927. Light spherical particles as tracers are now a ubiquitous experimental tool (Westerweel et al., 2013), and even fibre-shaped tracers have been employed (Brizzolara et al., 2021). For heavier particles, more complex motion is seen, such as inertial clustering (Monchaux, 2012) and preferential sampling (Goto & Vassilicos, 2008). Numerical simulations in this field have been a valuable tool, as results can be readily processed to study length-scale dependent statistics such as radial distribution functions (Ireland et al., 2016), and histograms of Voronoï area (Monchaux, 2012). Most of such particle-laden turbulent studies make the one-way coupling assumption, whereby the particles are affected by the fluid motion, but the fluid does not feel any effect of the particles. When the total mass fraction or volume fraction of particles in the system increases, the one-way coupling assumption becomes invalid, and we must model the back-reaction effect of the particles on the fluid. This opens up a zoo of new phenomena, including drag reduction (L. H. Zhao et al., 2010), cluster-induced turbulence (Capecelatro et al., 2015), and new scalings in the energy spectrum (Olivieri, Cannon, et al., 2022). A recent review by Brandt and Coletti (2022) has pointed out a gap in the current understanding of particles in turbulence, which lies between small heavy particles and large weakly buoyant particles. In addition, most real-world particle-laden flows involve particles with a high degree of anisotropy, while research in particle-laden turbulence has overwhelmingly focused on spherical particles.

This article addresses the gaps by studying a range of particle mass fractions M, ranging from single-phase ($M = 0$) to fixed particles ($M = 1$). We make simulations using a fully coupled approach to elucidate how particles modulate turbulence. Furthermore, we vary the turbulence intensity, allowing us to ask the question *at what Reynolds numbers (Re) does turbulence modulation emerge?* And *does the modulation effect persist as* $Re \to \infty$*?* Crucially, we connect our results to real-world flows by investigating isotropically-shaped particles (spheres) and anisotropically-shaped particles (fibres). The spheres have a single characteristic length, given by their diameter, whereas the fibres have two: their length and thickness. This naturally allows us to ask *how do the particle's characteristic lengths impact the scales of the turbulent flow?*

A number of works have investigated particle shape, see Voth and Soldati (2017) for a review of the behaviour of anisotropic particles in turbulence, including oblate spheroids, prolate spheroids and fibres. In 1932 Wadell (1932) defined the sphericity of a particle as its surface area divided by the area of a sphere with equivalent volume; Wadell used the sphericity to classify quartz rocks according to their shape. More recently, L. Zhao et al. (2015) made direct numerical simulations of oblate and prolate spheroids in a channel flow, and found that away from the channel walls, prolate spheroids tend to rotate about their symmetry axis (spinning), whereas oblate particles rotate about an axis perpendicular to their symmetry axis (tumbling). Ardekani et al. (2017) showed that oblate spheroids can reduce drag in a turbulent channel by aligning their major axes parallel to the wall. Yousefi et al. (2020) simulated spheres and oblate spheroids in a shear flow, and found that the rotation of the spheroids can enhance the kinetic energy of the flow. At the other shape extreme

from oblate spheroids, we have fibres, which are long and thin. In this article, we choose to study rigid fibres (also known as rods) as they are a simple example of a particle with high anisotropy. Concerning fibres, Gillissen et al. (2008) and Paschkewitz et al. (2004) and others showed that rigid fibres align with vorticity in channel flows, dissipating the vortex structures, and drag reductions up to 26% have been measured (Paschkewitz et al., 2004). In this article, we wish to investigate how the shapes and length scales of particles interact with turbulence, so we choose the triperiodic flow geometry. This geometry avoids the effects of walls and other large structures on the flow, enabling us to focus on the emergent length scales of the flow.

A few works have investigated the effect of turbulence intensity on particle-laden flows. Lucci et al. (2010) simulated spheres of various diameters c in decaying isotropic turbulence, and found that spheres reduce the fluid kinetic energy and enhance dissipation when $c > \eta$, where η is the Kolmogorov length scale. In this article, we also vary the ratio c/η, however, unlike (Lucci et al., 2010), we do it by varying the fluid viscosity, not the particle size. This enables us to keep the particle volume, particle surface area and number of particles constant across our cases. Oka and Goto (2022) studied sphere diameters in the range $7.8 < c/\eta < 64$, in turbulent flows with $Re_\lambda \approx 94$ and showed that vortex shedding and turbulence attenuation occur when $c \gtrsim \lambda\rho/\tilde{\rho}$, where λ is the Taylor length-scale, ρ and $\tilde{\rho}$ are the fluid and solid densities, respectively. J. Shen et al. (2022) investigated the effect of solid-fluid density ratio for flows with $38 < Re_\lambda < 74$, and $8.8 < c/\eta < 18$, showing that higher density spheres cause more turbulence attenuation. Peng et al. (2023) parametrized the attenuation of turbulent kinetic energy by spheres with $7.1 < c/\eta < 15$ and $41 < Re_\lambda < 63$. They found that the particle mass fraction is indeed a strong indicator of attenuation and that there is negligible dependence on the Taylor Reynolds number Re_λ for this range. Compared to the above works, we choose a wider range of turbulence intensities, such that $11.7 < c/\eta < 125$ and $12.8 < Re_\lambda < 442$, and we extend the study to include non-spherical particles.

This article is structured as follows: In the following section, we describe the numerical methods and the parameters used in our study. In section 4.3, we present and discuss the results of our simulations, and section 4.4 concludes with a summary and outlook on future research.

4.2 Methods and setup

We tackle the problem using large direct numerical simulations on an Eulerian grid of 1024^3 points with periodic boundaries in all three directions. To obtain the fluid velocity u_i and pressure p, we solve the incompressible Navier-Stokes equations for a Newtonian fluid with kinematic viscosity ν and density ρ,

$$\partial_t u_i + \partial_j(u_i u_j) = \nu\partial_{jj}u_i - \partial_i p/\rho + f_i^{ABC} + f_i^{sf}, \tag{4.1}$$

$$\partial_j u_j = 0, \tag{4.2}$$

where indices $i, j \in \{1, 2, 3\}$ denote the Cartesian components of a vector, and repeated indices are implicitly summed over. The turbulent flow is sustained by an ABC forcing (Libin & Sivashinsky, 1990; Podvigina & Pouquet, 1994a), which is made of sinusoids with

a wavelength $2\pi L$ equal to the domain size,

$$\begin{aligned} f_1^{ABC} &= F\sin(x_3/L) + F\cos(x_2/L), \\ f_2^{ABC} &= F\sin(x_1/L) + F\cos(x_3/L), \\ f_3^{ABC} &= F\sin(x_2/L) + F\cos(x_1/L). \end{aligned} \tag{4.3}$$

The amplitude F of the forcing is used to define the forcing Reynolds number $Re_{ABC} \equiv F^{1/2}L^{3/2}/\nu$. To discern the effect of increasing turbulence intensity, we conduct a number of simulations with various values of Re_{ABC}, given in table 4.1.

When the single-phase flows reach a statistically steady state, we add the solid particles at random (non-overlapping) locations in the domain. We allow the flow to reach a statistically steady state again, and measure the statistics presented in section 4.3, which were averaged in time over multiple large-eddy turnover times $\tau_f \equiv 2\pi L/u'$, where u' is the root mean square of the fluid velocity. This procedure is repeated for every solid mass fraction investigated, defined as $M \equiv m_s/(m_s + m_f)$ where m_s and m_f are the total mass of solid and fluid. The single-phase cases have $M = 0$, and the cases with fixed particles have $M = 1$. The solid phase is two-way coupled to the fluid using the immersed boundary method, and the back-reaction of the particles on the fluid is enforced by $\mathbf{f}^{\mathbf{sf}}$ in equation 4.1. As can be seen in figure 4.1, we simulate two types of particles, spheres and fibres; to isolate the effect of particle isotropy on the flow, we choose the fibres and spheres to have the same size: the spheres have diameter c, and the fibres have length c, where $c = L/2$ in all cases.

We use the in-house Fortran code *Fujin* to solve the flow numerically. Time integration is carried out using the second-order Adams-Bashforth method, and incompressibility (equation 4.2) is enforced in a pressure correction step (Kim & Moin, 1985), which uses the fast Fourier transform. Variables are defined on a staggered grid; velocities and forces are defined at the cell faces, while pressure is defined at the cell centres. Second-order finite differences are used for all spatial gradients. See https://groups.oist.jp/cffu/code for validations of the code.

4.2.1 Motion of the spheres

The sphere motion and forces are modelled using an Eulerian-based immersed boundary method developed by Hori et al. (2022). The velocity $\mathbf{U}$ and rotation rate $\mathbf{\Omega}$ of each sphere are found by integrating the Newton-Euler equations in time

$$m\partial_t U_i = \oiint_S \left(\rho\nu(\partial_i u_j + \partial_j u_i) - p\delta_{ij}\right) n_j dS - F^{col} n_i, \tag{4.4}$$

$$I\partial_t \Omega_i = \oiint_S \epsilon_{ijk}\frac{c}{2} n_j \rho\nu(\partial_k u_l + \partial_l u_k) n_l dS, \tag{4.5}$$

where δ_{ij} is the Kronecker delta and ϵ_{ijk} is the Levi-Civita symbol, S is the surface of the sphere, and $\mathbf{n}$ is its normal. $m = \tilde{\rho}\pi c^3/6$ and $I = mc^3/20$ are the mass and moment of inertia of the sphere with diameter c and density $\tilde{\rho}$. A soft-sphere collision force $F^{col}\mathbf{n}$ is applied in the radial direction when spheres overlap (Hori et al., 2022).

Table 4.2 shows our choice of parameters for the sphere-laden flows. In all cases, we use 300 spheres. The characteristic time of the spheres is $\tau_s = \tilde{\rho}c^2/(18\rho\nu)$, from which we

can define the Stokes number $St \equiv \tau_s/\tau_f$ of our flows. The particle Reynolds number of the spheres is $Re_p = c\sqrt{\langle \mathbf{\Delta u}_n \cdot \mathbf{\Delta u}_n \rangle_n}/\nu$, where $\mathbf{\Delta u}_n$ is the difference between the velocity of the nth particle and the local fluid velocity, averaged in a ball of diameter $2c$ centred on the sphere. The angled brackets $\langle\rangle_n$ denote an average over all spheres in the simulation.

4.2.2 Motion of the fibres

For the motion and coupling of the fibres, we also use an immersed boundary method, but this one is Lagrangian and solves the Euler-Bernoulli equation for the position $\mathbf{X}$ of the beam with coordinate l along its length (Alizad Banaei et al., 2020; Huang et al., 2007; Olivieri et al., 2020)

$$\frac{\pi}{4} d^2(\tilde{\rho} - \rho)\partial_t^2 X_i = \partial_l(T\partial_l X_i) + \gamma \partial_l^4 X_i - F_i^{fs} + F_i^{col}, \tag{4.6}$$

where T is the tension, enforcing the inextensibility condition;

$$\partial_t X_i \partial_t X_i = 1. \tag{4.7}$$

The volumetric density of the fibre is $\tilde{\rho}$, and its stiffness is γ. Note that, the fluid density ρ in equation 4.6 cancels the inertia of the fluid in the fictitious domain inside the fibre (Yu, 2005). To exclude deformation effects in our study, we choose a stiffness which limits the fibre deformation below 1%. The collision force $\mathbf{F^{col}}$ is the minimal collision model by Snook et al. (2012). The fluid-solid coupling force $\mathbf{F^{fs}}$ enacts the non-slip condition at the particle surface, and an equal and opposite force ($\mathbf{f^{sf}}$ in equation 4.1) acts on the fluid. The spreading kernel onto the Eulerian grid has a width of three grid spaces, giving the fibre diameter $d = 3\Delta x$ in units of the Eulerian grid spacing. Table 4.3 shows our choice of parameters for the fibre-laden flows, where we use 10^4 fibres in all cases. The characteristic time of the fibres is calculated using a formulation which takes their aspect ratio $\beta \equiv c/d$ into account (Shaik & Van Hout, 2023),

$$\tau_s = \frac{\tilde{\rho} d^2}{18\rho\nu} \frac{\beta \ln\left(\beta + \sqrt{\beta^2 - 1}\right)}{\sqrt{\beta^2 - 1}}, \tag{4.8}$$

from which we can define the Stokes number $St \equiv \tau_s/\tau_f$ of our flows. The particle Reynolds number of the fibres is $Re_p = d\sqrt{\langle \mathbf{\Delta u}_n \cdot \mathbf{\Delta u}_n \rangle_n}/\nu$, where $\mathbf{\Delta u}_n$ is the difference between the velocity of the midpoint of the nth fibre and the local fluid velocity, averaged in a ball of diameter $2c$ centred on the fibre's midpoint. The angled brackets $\langle\rangle_n$ denote an average over all fibres in the simulation.

4.3 Results and discussion

4.3.1 Bulk statistics

The Taylor Reynolds number is defined as $Re_\lambda \equiv u'\lambda/\nu$, where u' is the root-mean-square velocity averaged over space and time, $\lambda = u'\sqrt{15\nu/\epsilon}$ is the Taylor length scale, and ϵ is

marker	Re_{ABC}	M	η/L	Re_λ	$\epsilon\mathcal{L}/u'^3$
⬟	**894**	**0.0**	4.06×10^{-3}	433	0.399
■	447	**0.0**	6.31×10^{-3}	308	**0.382**
▲	224	**0.0**	1.11×10^{-2}	204	0.400
♦	112	**0.0**	1.95×10^{-2}	116	0.473
●	**55.9**	**0.0**	2.99×10^{-2}	101	0.428

Table 4.1: Single-phase flows. Re_{ABC} is the forcing Reynolds number, and M is the solid mass fraction. We measure the Kolmogorov length scale $\eta \equiv \nu^{3/4}/\epsilon^{1/4}$, the Taylor Reynolds number Re_λ, and the dissipation ϵ, which has been normalised using the integral length scale $\mathcal{L}$ and the root mean square velocity u' of the fluid. The largest and smallest values of each parameter are shown in bold.

marker	Re_{ABC}	M	$\tilde{\rho}/\rho$	η/L	Re_λ	$\epsilon\mathcal{L}/u'^3$	St	Re_p
⬟	**894**	0.1	**1.29**	4.09×10^{-3}	431	0.397	7.4	618
⬟	**894**	0.3	4.99	4.18×10^{-3}	397	0.395	26.9	857
⬟	**894**	0.6	17.4	4.09×10^{-3}	346	0.507	89.1	1.12×10^3
⬟	**894**	0.9	105	4.18×10^{-3}	280	0.625	471	1.18×10^3
⬟	**894**	**1.0**	∞	4.29×10^{-3}	247	0.708	∞	$\mathbf{1.19 \times 10^3}$
■	447	**1.0**	∞	7.31×10^{-3}	161	0.786	∞	559
▲	224	0.1	**1.29**	1.13×10^{-2}	219	0.374	1.91	142
▲	224	0.3	4.99	1.16×10^{-2}	181	0.477	6.49	198
▲	224	0.6	17.4	1.18×10^{-2}	157	0.586	20.9	243
▲	224	0.9	105	1.19×10^{-2}	123	0.751	109	266
▲	224	**1.0**	∞	1.26×10^{-2}	101	0.936	∞	260
♦	112	**1.0**	∞	2.14×10^{-2}	61.5	1.19	∞	117
●	**55.9**	**1.0**	∞	3.60×10^{-2}	34.9	1.81	∞	44.6

Table 4.2: Sphere-laden flows. We set the solid-fluid density ratio $\tilde{\rho}/\rho$ to obtain a range of solid mass fractions M. Bulk statistics for the particles are the Stokes number St and the particle Reynolds number Re_p. The largest and smallest values of each parameter are shown in bold.

marker	Re_{ABC}	M	$\tilde{\rho}/\rho$	η/L	Re_λ	$\epsilon\mathcal{L}/u'^3$	St	Re_p
⬟	**894**	0.2	47.2	4.09×10^{-3}	422	0.425	1.45	34.9
⬟	**894**	0.3	81.8	$\mathbf{4.02\times10^{-3}}$	**442**	0.432	2.6	41.2
⬟	**894**	0.6	279	4.17×10^{-3}	340	0.713	7.52	46.4
⬟	**894**	0.9	1.69×10^3	4.26×10^{-3}	223	1.15	36.1	47.2
⬟	**894**	**1.0**	∞	4.40×10^{-3}	201	1.29	∞	46.0
■	447	**1.0**	∞	7.44×10^{-3}	115	1.78	∞	20.6
▲	224	0.1	21.3	1.16×10^{-2}	192	0.434	**0.155**	8.31
▲	224	0.3	81.8	1.16×10^{-2}	196	0.465	0.605	9.9
▲	224	0.6	279	1.19×10^{-2}	167	0.63	1.85	11.2
▲	224	0.9	1.69×10^3	1.23×10^{-2}	72.5	2.25	7.16	9.11
▲	224	**1.0**	∞	1.29×10^{-2}	54.9	3.17	∞	8.22
◆	112	**1.0**	∞	2.33×10^{-2}	28.8	4.68	∞	3.32
●	**55.9**	**1.0**	∞	$\mathbf{4.27\times10^{-2}}$	**12.8**	**8.60**	∞	**1.51**

Table 4.3: Fibre-laden flows. We set the solid-fluid density ratio $\tilde{\rho}/\rho$ to obtain a range of solid mass fractions M. Bulk statistics for the particles are the Stokes number and particle Reynolds number. The largest and smallest values of each parameter are shown in bold.

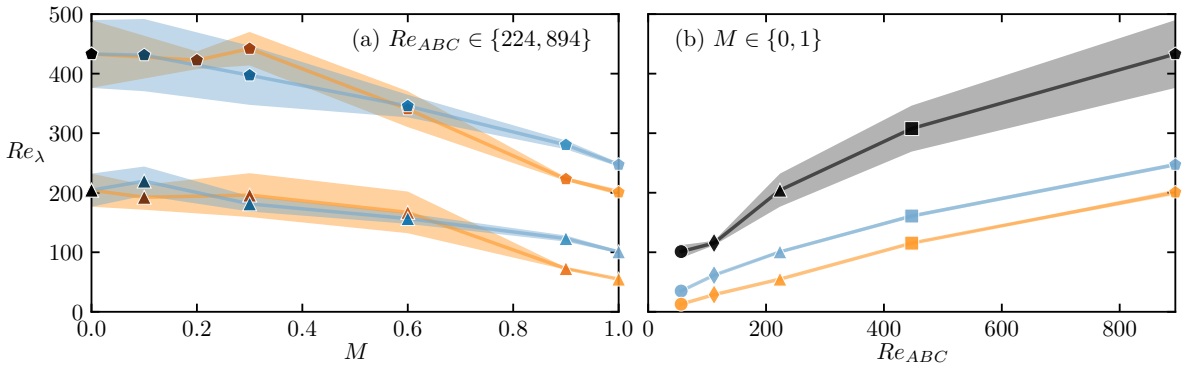

Figure 4.2: (a) Effect of the solid mass fraction M on the Taylor Reynolds number Re_λ. Flows with $Re_{ABC} = 224$ are marked using triangles, and flows with $Re_{ABC} = 894$ are marked using pentagons. (b) Effect of the forcing Reynolds number Re_{ABC} on the Taylor Reynolds number Re_λ, for the single phase and particle-laden cases with fixed particles ($M = 1$). In both plots, we show the single-phase flows in black, flows with spheres in blue, and flows with fibres in yellow; the shaded regions give the root-mean-square of Re_λ in time.

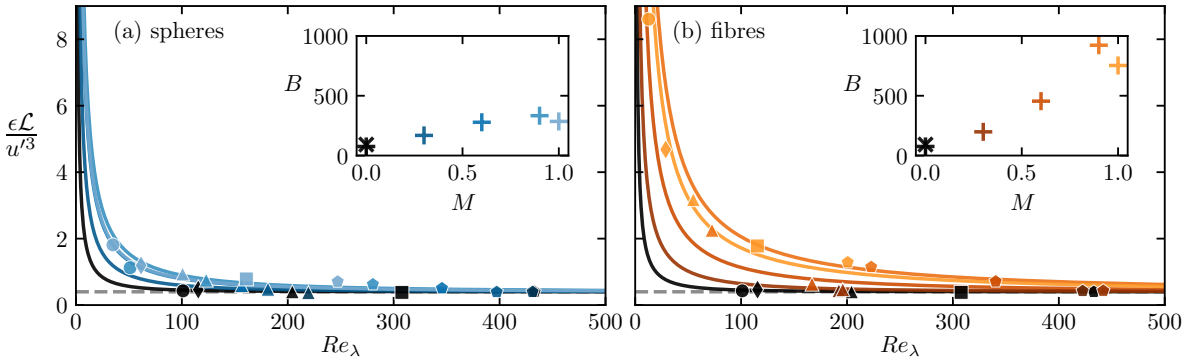

Figure 4.3: The dependence of the normalised dissipation $\epsilon\mathcal{L}/u'^3$ on the Taylor-Reynolds number Re_λ. Flows with spheres are marked blue on panel (a), flows with fibres are marked in orange on panel (b), and single-phase flows are marked in black on both panels. Dashed lines show the anomalous value of dissipation $\epsilon\mathcal{L}/u'^3 = 0.4$ measured by Donzis et al. (2005). Solid lines show fits of equation 4.10 with $A = 0.2$. The fitted values of B are given in the inset, where Donzis' result ($B = 92$) is marked with an "X".

the viscous dissipation rate averaged over space and time. The Taylor-Reynolds number is an indicator of the intensity of turbulence in the flow, and in figure 4.2, we show how Re_λ compares for all of our cases. Figure 4.2a shows that increasing the solid mass fraction M causes a reduction in Re_λ at both high and low forcing Reynolds numbers. Both spheres and fibres produce a comparable decrease in Re_λ, but the reduction effect is more substantial for very heavy fibres. Looking at the trend in Re_λ with the forcing Reynolds number Re_{ABC} in figure 4.2b, we see, as expected, a monotonic increase in all three cases, i.e., single phase, sphere-laden, and fibre-laden flows.

The dissipative anomaly is a well-studied feature in single-phase turbulent flows, first proposed by Taylor (1935). It states that, even in the limit of vanishing viscosity ($Re_\lambda \to \infty$), the normalised dissipation $\epsilon\mathcal{L}/u'^3$ remains finite. The integral length scale is given by,

$$\mathcal{L} = \frac{\pi}{2u'^2}\int_0^\infty \frac{E}{\kappa}\mathrm{d}\kappa, \tag{4.9}$$

where E is the turbulent kinetic energy spectrum and κ is the wavenumber. Donzis et al. (2005) parametrized the dissipative anomaly, based on the analysis of Doering and Foias (2002), and they fit the function

$$\frac{\epsilon\mathcal{L}}{u'^3} = A\left[1 + \sqrt{1 + (B/Re_\lambda)^2}\right] \tag{4.10}$$

to a number of single-phase flows, obtaining $A = 0.2$ and $B = 92$. Figure 4.3 shows the dependence of the normalised dissipation for our flows. We see that as $Re_\lambda \to \infty$, flows with spheres and fibres at all mass fractions appear to converge to the same anomalous value of dissipation $\epsilon\mathcal{L}/u'^3 = 0.4$. Hence, we fit equation 4.10 with $A = 0.2$ to each mass fraction of spheres and fibres, obtaining a value for B in each case, shown in the insets of

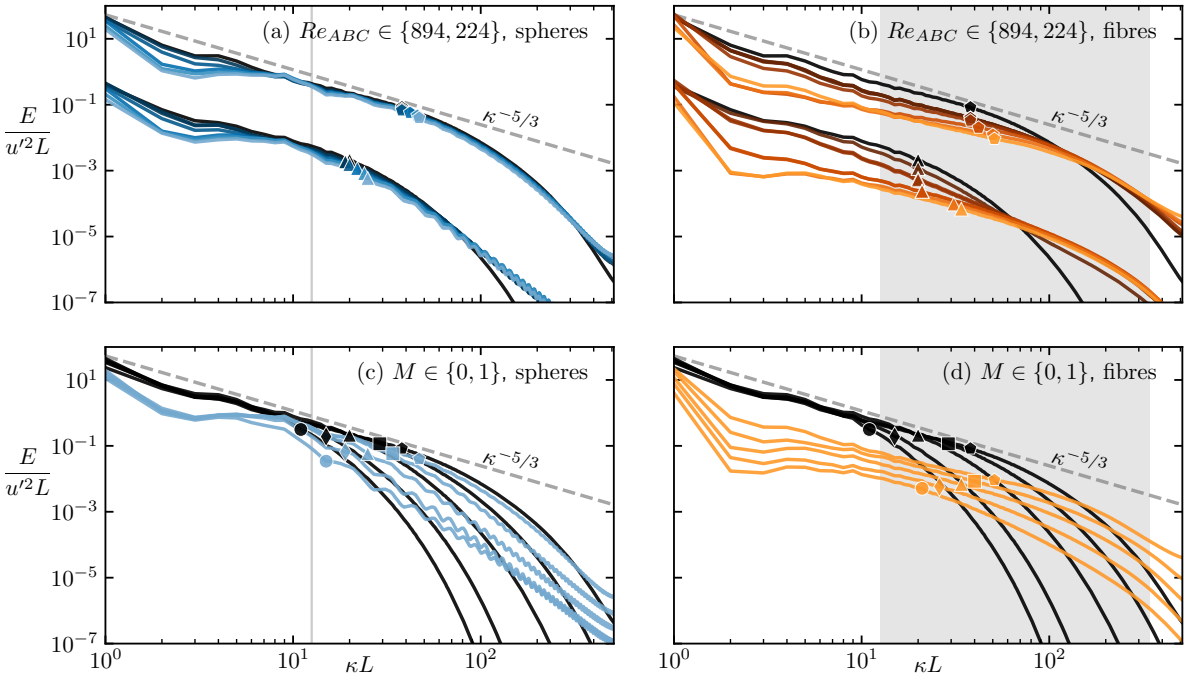

Figure 4.4: Energy spectra of all cases. On the left, we show flows with spheres, and the vertical grey lines show the wavenumber $\kappa_c = 2\pi/c$ of the sphere diameter. On the right, we show flows with fibres, and we shade the region between the wavenumber κ_c of the fibre length and the wavenumber $\kappa_d = 2\pi/d$ of the fibre diameter. (a) and (b) show $Re_{ABC} = 894$ and $Re_{ABC} = 224$, with the latter shifted downwards by a factor of 100 on the y-axis, for various mass fractions. (c) and (d) show fixed ($M = 1$) and single phase ($M = 0$) cases for various Reynolds numbers. Markers are at the wavenumber corresponding to the Taylor length scale.

figure 4.3. The fit to our single phase flows agrees closely with Donzis et al. (2005)'s result. However, both spheres and fibres cause an increase in the value of B as their mass fraction increases, with fibres producing roughly double the effect. To understand how spheres and fibres modify the dissipation in the flow, we must look at how they transport energy from large to small scales, into the dissipative range.

4.3.2 Scale-by-scale results

Figure 4.4 shows each flow's turbulent kinetic energy spectrum E. Single-phase flows exhibit the canonical Kolmogorov scaling $E \sim \kappa^{-5/3}$ for one or two decades, depending on the forcing Reynolds number. Adding spheres reduces E at wavenumbers up to the sphere diameter ($\kappa < \kappa_c$) and increases E in the dissipative range. We mention, in passing, the oscillations at the wavenumber of the sphere diameter; these are an artefact resulting from the discontinuity in the velocity gradient at the sphere boundary (Lucci et al., 2010). The addition of fibres causes a reduction in E across a broad band of wavelengths ($\kappa L \lesssim 100$)

and a pronounced increase in the dissipative range. As was previously seen by Olivieri, Cannon, et al. (2022), the energy scaling $E \sim \kappa^{-\beta}$ becomes flatter as the mass fraction M of fibres increases. Figure 4.4 also shows that both spheres and fibres cause the Taylor length scale to shift to higher wavenumbers due to the increase of the energy in the dissipative scales due to the presence of particles.

Figure 4.5 shows how each term in the Navier-Stokes equation interacts with the energy spectrum; this is expressed by the spectral energy balance

$$\mathcal{F}_{inj}(\kappa) + \Pi(\kappa) + \Pi_{sf}(\kappa) + D(\kappa) = \epsilon, \tag{4.11}$$

where $\mathcal{F}_{inj}, \Pi, \Pi_{sf}$, and D are the rate of energy transfer by the ABC forcing, advection, solid-fluid coupling, and dissipation, respectively. See the supplementary information of Ref. (Abdelgawad* et al., 2023) for a derivation of this equation. For the single-phase flows, energy is carried by the advective term Π from large to small scales, where it is dissipated by the viscous term D. When particles are added, we see that the solid-fluid coupling term Π_{sf} acts as a "spectral shortcut" (Finnigan, 2000; Olivieri, Cannon, et al., 2022); it bypasses the classical turbulent cascade, removing energy from large scales and injecting it at the length scale of the particles, through their wakes. In keeping with the spectra, the power of the solid-fluid coupling (shown by the peak value of Π_{sf}) increases with mass fraction M of both spheres and fibres. For spheres, the coupling Π_{sf} dominates only at wavenumbers less than that of the sphere diameter $\kappa < \kappa_c$ (i.e., large length scales). Around κ_c, the sphere wake returns energy to the fluid, and the classical cascade resumes for $\kappa > \kappa_c$. For fibres instead, Π_{sf} extends deep into the viscous range: in fact, markers on the Π_{sf} curves show that spheres mostly inject energy around the length scale of their diameter , and fibres mostly inject energy at a length scale between their thickness and length. This observation is supported by the images of dissipation in figure 4.1; around the spheres, we see wakes comparable in size to their diameter, while around the fibres, we see wakes comparable in size to their thickness. We presume that the fluid-sphere coupling Π_{sf} would also extend into the viscous range if the sphere diameter was in this range. Lastly, we consider the effect of Reynolds number on energy transfers in the flow, reducing Re_{ABC} limits the range of scales at which the advective flux Π occurs for single-phase flows. However, Re_{ABC} has little effect on the wavenumber range of the solid-fluid coupling term Π_{sf}, suggesting that the size of the particle wakes is governed mainly by particle geometry, with a lesser effect from fluid properties like viscosity.

Moving from wavenumber space to physical space, we show the longitudinal structure functions

$$S_p \equiv \langle [\hat{r}_i u_i(\mathbf{x}+\mathbf{r}) - \hat{r}_i u_i(\mathbf{x})]^p \rangle \tag{4.12}$$

of each flow in figure 4.6, where $\mathbf{r}$ is a separation vector between two points in the flow, it has magnitude r and direction $\hat{\mathbf{r}}$, and angled brackets show an average over space $\mathbf{x}$. For the second moment ($p = 2$), the single-phase flows closely follow Kolmogorov's scaling in the inertial range ($r \gg \eta$). However, when particles are added, S_2 decreases relative to the single-phase case. For spheres, the decrease occurs for $r \gtrsim c$, while for fibres, it occurs at even smaller separations r. Much like the $E \sim k^{-\beta}$ scalings seen in figure 4.4, the decreased regions in figure 4.6 show scalings $S_2 \sim r^{\zeta_2}$, which become flatter for larger mass fractions M. These energy spectrum and structure-function scalings are, in fact, just

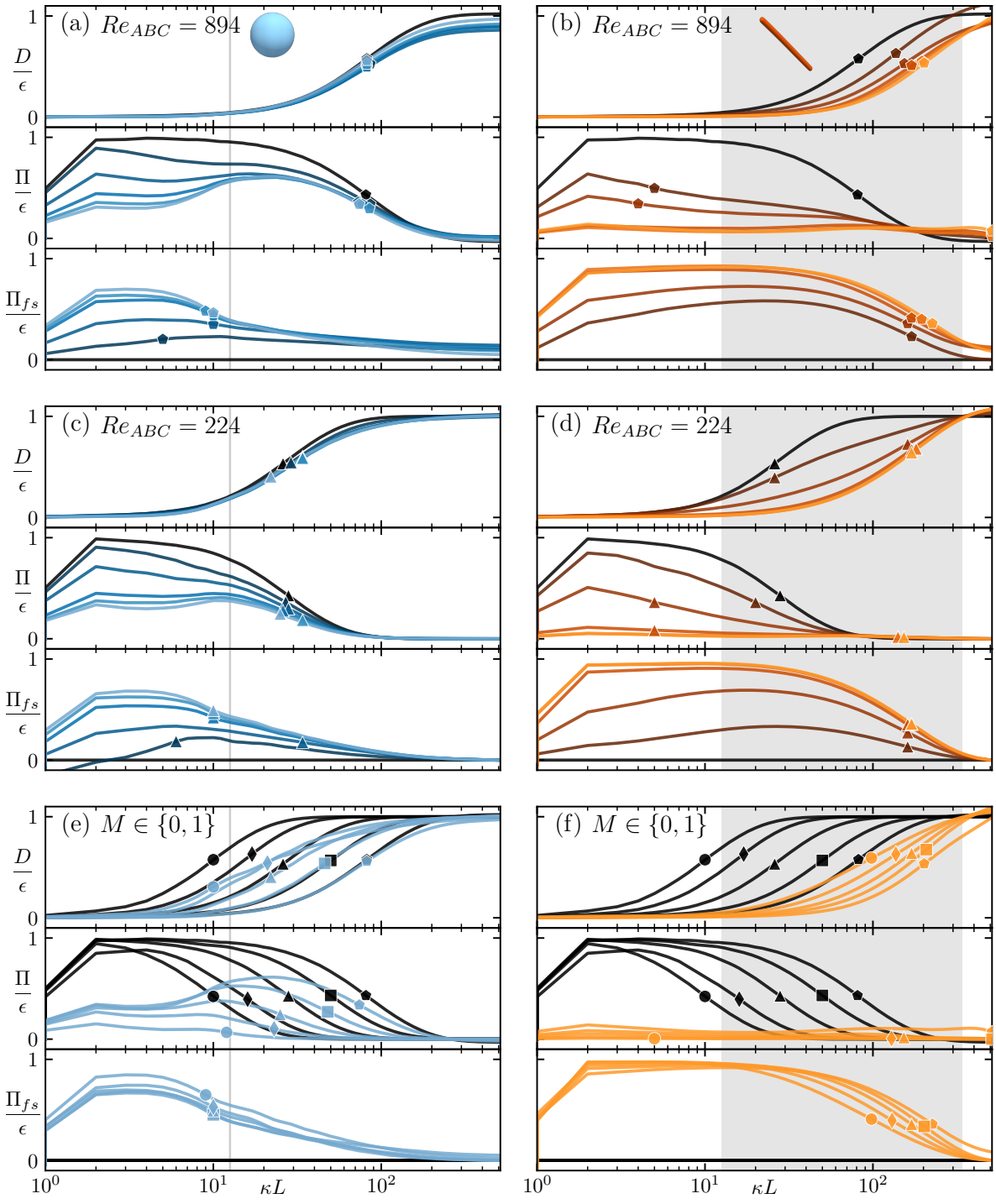

Figure 4.5: Scale-by-scale energy balance for all cases. Panels (a) and (b) show $Re_{ABC} = 894$ cases for various mass fractions. Panels (c) and (d) show $Re_{ABC} = 224$ cases for various mass fractions. Panels (e) and (f) show fixed ($M = 1$) and single-phase ($M = 0$) cases for various Reynolds numbers. On the left, we show flows with spheres, and the vertical grey lines show the wavenumber $\kappa_c = 2\pi/c$ of the sphere diameter. On the right, we show flows with fibres, and we shade the region between the wavenumber κ_c of the fibre length and the wavenumber κ_d of the fibre diameter. For each case, we plot three terms: the Dissipation D, the energy flux Π due to convection, and the energy flux Π_{sf} due to the solid-fluid coupling. Each curve is marked where the gradient is largest.

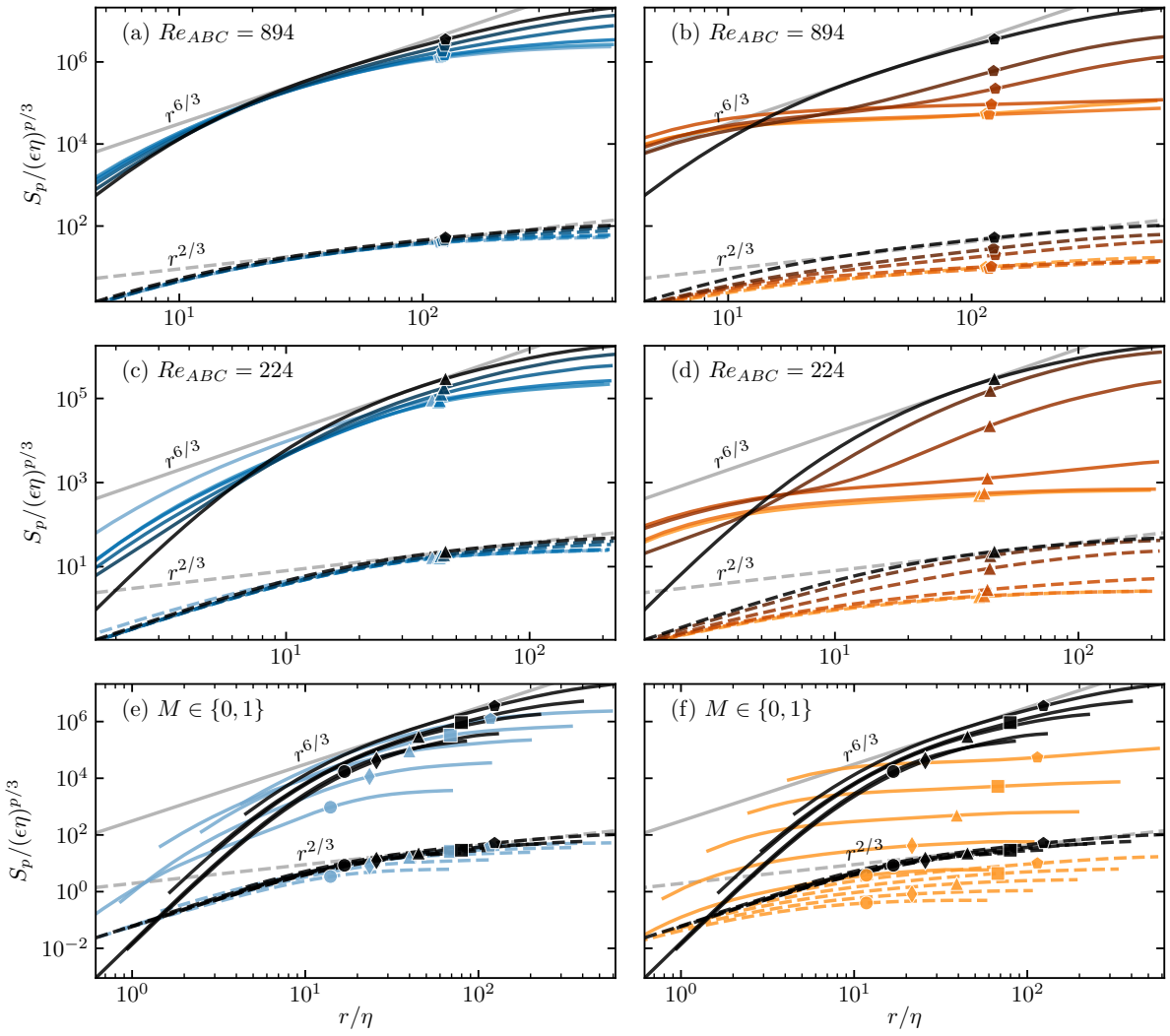

Figure 4.6: Structure functions of order $p = 2$ (dashed lines) and $p = 6$ (solid lines). Panels (a) and (b) show cases with $Re_{ABC} = 894$ for various mass fractions. Panels (c) and (d) show cases with $Re_{ABC} = 224$ for various mass fractions. Panels (e) and (f) show fixed ($M = 1$) and single-phase ($M = 0$) cases for various Reynolds numbers. Flows with spheres are on the left, and flows with fibres are on the right. Grey lines show the scalings predicted by Kolmogorov for the single-phase structure functions. We mark each line at $r = c$.

observations of the same phenomenon, as the exponents are related by $\zeta_2 = \beta - 1$ for any differentiable velocity field (Pope, 2000, p.232). In the higher moment structure function ($p = 6$), the flattening of the $S_6 \sim r^{\zeta_6}$ scaling by the particles is yet more apparent, indicating that the tails of the probability distribution of $\hat{r}_i u_i(\mathbf{x}+\mathbf{r}) - \hat{r}_i u_i(\mathbf{x})$ become wider for smaller separations r. In other words, extreme values become more common, and the velocity field becomes more intermittent in space. In the case of single-phase homogeneous-isotropic turbulence, the intermittency of the velocity field has been attributed to the non-space-filling nature of the fluid dissipation (Frisch, 1995). Next, we explore this link in the case of particle-laden turbulence by investigating the intermittency of dissipation ϵ in space.

Using the method described by Frisch (1995, p.159), we obtain the quantity ϵ_l by averaging the dissipation within a ball of radius $6\Delta x \leq l \leq 10\Delta x$ and take a moment $-6 \leq q \leq 6$ of this quantity; if the dissipation field is multifractal, the ensemble average has a scaling behaviour $\langle \epsilon_l^q \rangle \sim l^{\tau_q}$ and we can obtain the multifractal spectrum F with an inverse Legendre transformation,

$$\tau_q = \min_{\alpha}[q(\alpha - 1) + 3 - F], \tag{4.13}$$

where $\min_\alpha$ states that we take the value of α which minimizes the expression in the square brackets. Figure 4.7 shows the multifractal spectra for all cases. Similarly to Mukherjee et al. (2023), we split our analysis into separate regions: solid curves result from an ensemble average over balls not containing particles, while dashed curves result from an ensemble average over balls containing particles, where the radius l has been rescaled according to the volume V_f of fluid remaining in the ball, i.e., $l = (3V_f/4\pi)^{1/3}$. We see that the multifractal spectra of the single-phase flows and the regions not containing particles have peaks at $\alpha \approx 1, F \approx 3$, showing there is a background of space-filling dissipation in these regions (Frisch, 1995, p.163).

The multifractal spectra of the regions containing spheres (blue dashed lines in figure 4.7) have peaks which are shifted to the left. This shift can be explained by considering the high dissipation in the boundary layers around the spheres. As imaged in figure 4.1, the boundary layers are confined in space to relatively thin sheets. The volume of a thin sheet intersecting with a ball of radius l is $V \sim l^2$, hence the total dissipation in a ball intersecting with a spherical particle also scales as $\sim l^2$. When we average over the volume of the ball ($\sim l^3$) and take the qth moment, we obtain $\langle \epsilon_l^q \rangle \sim l^{2q} l^{-3q}$, and this scales as $\tau_q = -q$. By equation 4.13, this is the Legendre transformation of the point $\alpha = 0, F = 3$, which is roughly where the peaks in the multifractal spectra are located.

The multifractal spectra of the regions containing fibres (orange dashed lines in figure 4.7) have peaks which are shifted even further to the left. Again, we explain this by considering the wakes around the particles. Suppose that the dissipation around a fibre is confined to a thin tube. In this case, the volume of a tube intersecting with a ball of radius l is $V \sim l$, thus in this case $\langle \epsilon_l^q \rangle \sim l^q l^{-3q}$, so the resulting scaling is $\tau_q = -2q$, which (by equation 4.13) is the Legendre transformation of the point $\alpha = -1, F = 3$. In fact, from the bottom right panel of figure 4.7, we see that the ensemble average over balls containing $M = 1$ fibres produces peaks in the region $-0.5 < \alpha < 0$, suggesting that the wakes around the fibres are not exactly thin tubes, but more space-filling structures with a dimension greater than one. This is also supported by the images in figure 4.1, as the wakes are seen to extend behind the fibres.

The middle and upper panels of figure 4.7 show that (at $Re_{ABC} = 224$ and $Re_{ABC} = 894$)

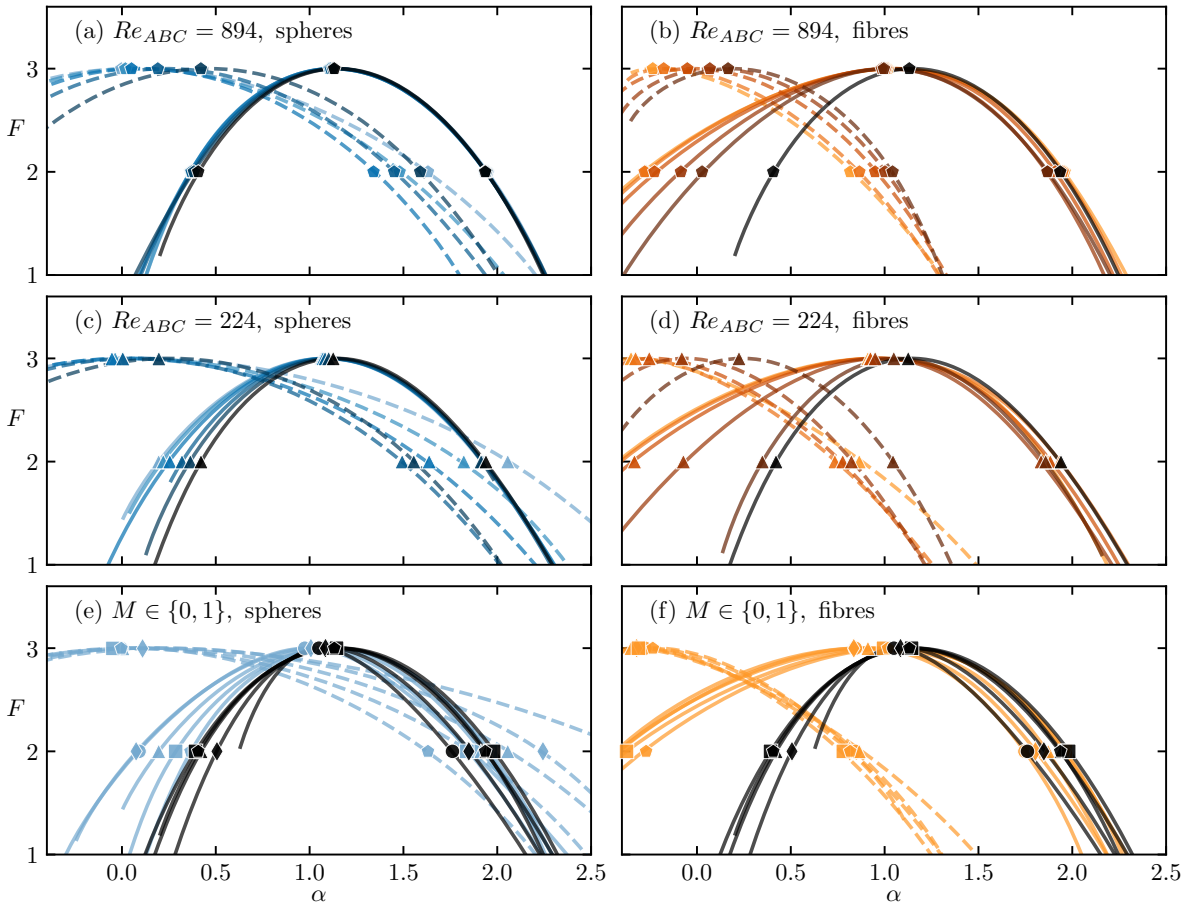

Figure 4.7: Multifractal spectra of the dissipation in regions containing particles (dashed lines) and regions not containing particles (solid lines). Panels (a) and (b) show cases with $Re_{ABC} = 894$ for various mass fractions. Panels (c) and (d) show cases with $Re_{ABC} = 224$ for various mass fractions. Panels (e) and (f) show fixed ($M = 1$) and single-phase ($M = 0$) cases for various Reynolds numbers. Flows with spheres are on the left, and flows with fibres are on the right. We mark each line where F is maximum and at $F = 2$.

the sphere- and fibre-containing multifractal spectra tend toward the single phase multifractal spectrum as M is reduced. This is expected, as the particle-fluid relative velocity is reduced and the wakes become less prominent compared to the background space-filling turbulence. On the other hand, the ensembles of balls not containing particles produce multifractal spectra with low α tails that extend beyond those of the single-phase multifractal spectra, suggesting that the wakes of spheres and fibres extend into the bulk of the fluid and that they retain their non-space-filling nature.

4.3.3 Local flow structures

To look more closely at the flow structures produced by the particles, we compute the alignment of the unit-length eigenvectors $\hat{\mathbf{a}}_\mathbf{1}, \hat{\mathbf{a}}_\mathbf{2}, \hat{\mathbf{a}}_\mathbf{3}$ of the strain-rate tensor $s_{ij} \equiv (\partial_i u_j + \partial_j u_i)/2$ with the vorticity $\boldsymbol{\omega} \equiv \epsilon_{ijk}\partial_j u_k \hat{\mathbf{e}}_i$ (Ashurst et al., 1987; Olivieri, Mazzino, et al., 2022), where $\hat{\mathbf{e}}_\mathbf{1}, \hat{\mathbf{e}}_\mathbf{2}, \hat{\mathbf{e}}_\mathbf{3}$ are the Cartesian unit vectors. We choose $\hat{\mathbf{a}}_\mathbf{1}$ to be the eigenvector corresponding to the largest eigenvalue. For an incompressible fluid, the three eigenvalues of s_{ij} sum to zero, so the largest eigenvalue is never negative. Hence, $\hat{\mathbf{a}}_\mathbf{1}$ aligns with the direction of elongation in the flow. Similarly, we choose the eigenvector $\hat{\mathbf{a}}_\mathbf{3}$ to correspond with the smallest eigenvalue, which is never positive, so $\hat{\mathbf{a}}_\mathbf{3}$ aligns with the direction of compression in the flow. Finally, due to the symmetry of the strain-rate tensor, $\hat{\mathbf{a}}_\mathbf{2}$ is orthogonal to the other two eigenvectors and, depending on the flow, there can be compression or elongation along its axis. Figure 4.8 shows probability-density functions P of the scalar product of the unit-length vorticity $\hat{\boldsymbol{\omega}}$ with $\hat{\mathbf{a}}_\mathbf{1}, \hat{\mathbf{a}}_\mathbf{2}$ and $\hat{\mathbf{a}}_\mathbf{3}$ for all of the flows studied. The quantity $\hat{\boldsymbol{\omega}} \cdot \hat{\mathbf{a}}_\mathbf{i}$ is simply the cosine of the angle between the two vectors, and we take the modulus because $\hat{\mathbf{a}}_\mathbf{i}$ and $-\hat{\mathbf{a}}_\mathbf{i}$ are degenerate eigenvectors. In the single-phase flows, P is maximum at $|\hat{\boldsymbol{\omega}} \cdot \hat{\mathbf{a}}_\mathbf{2}| = 1$, that is, we see a strong alignment of vorticity with the intermediate eigenvector $\hat{\mathbf{a}}_\mathbf{2}$. This is a well-known feature of turbulent flows that has been attributed to the axial stretching of vortices (Ashurst et al., 1987). Also in keeping with previous observations of single-phase turbulence, we see that the first eigenvector $\hat{\mathbf{a}}_\mathbf{1}$ shows very little correlation with $\hat{\boldsymbol{\omega}}$, and the last eigenvector is mostly perpendicular to the vorticity, producing a peak in P at $\hat{\boldsymbol{\omega}} \cdot \hat{\mathbf{a}}_\mathbf{3} = 0$. When spheres are added, vorticity aligns even more strongly with the intermediate eigenvector $\hat{\mathbf{a}}_\mathbf{2}$, and becomes more perpendicular to the first and last eigenvectors $\hat{\mathbf{a}}_\mathbf{1}$ and $\hat{\mathbf{a}}_\mathbf{3}$. This change is consistent with the existence of a shear layer at the surface of the spheres. To demonstrate this, we draw a laminar shearing flow and label the directions of $\hat{\mathbf{a}}_\mathbf{1}, \hat{\mathbf{a}}_\mathbf{2}, \hat{\mathbf{a}}_\mathbf{3}$ and $\hat{\boldsymbol{\omega}}$ in the inset of figure 4.8. The compression $\hat{\mathbf{a}}_\mathbf{3}$ and extension $\hat{\mathbf{a}}_\mathbf{1}$ are in the plane of the shear flow, while the vorticity $\hat{\boldsymbol{\omega}}$ and the intermediate eigenvector $\hat{\mathbf{a}}_\mathbf{3}$ are perpendicular to the shear plane; this gives rise to the $\hat{\boldsymbol{\omega}} \cdot \hat{\mathbf{a}}_\mathbf{1} = 0$, $|\hat{\boldsymbol{\omega}} \cdot \hat{\mathbf{a}}_\mathbf{2}| = 1$ and $\hat{\boldsymbol{\omega}} \cdot \hat{\mathbf{a}}_\mathbf{3} = 0$ modes in the sphere-laden flows in figure 4.8. The larger mass fraction spheres have a greater effect, as their motion relative to the fluid is larger. Also, the spheres' effect is more pronounced at lower Re_{ABC}, which can be explained by an increased thickness in the shear layer as the fluid velocity is increased. For fibre-laden flows peaks are also seen at $\hat{\boldsymbol{\omega}} \cdot \hat{\mathbf{a}}_\mathbf{1} = 0$, $|\hat{\boldsymbol{\omega}} \cdot \hat{\mathbf{a}}_\mathbf{2}| = 1$ and $\hat{\boldsymbol{\omega}} \cdot \hat{\mathbf{a}}_\mathbf{3} = 0$, but the peaks are spread over a larger range of angles, presumably due to the high curvature of the fibre surfaces, which adds variance to the local direction of vorticity and shear. At small Reynolds numbers ($Re_{ABC} = 55.9$ and 112) the peaks are widest, and $P(|\hat{\boldsymbol{\omega}} \cdot \hat{\mathbf{a}}_\mathbf{i}|)$ becomes an almost uniform distribution.

The local topology of a flow can be described entirely using the three principle invariants of the velocity gradient tensor $\partial_i u_j$ (Cheng & Cantwell, 1996). The first invariant $\partial_i u_i$ is not

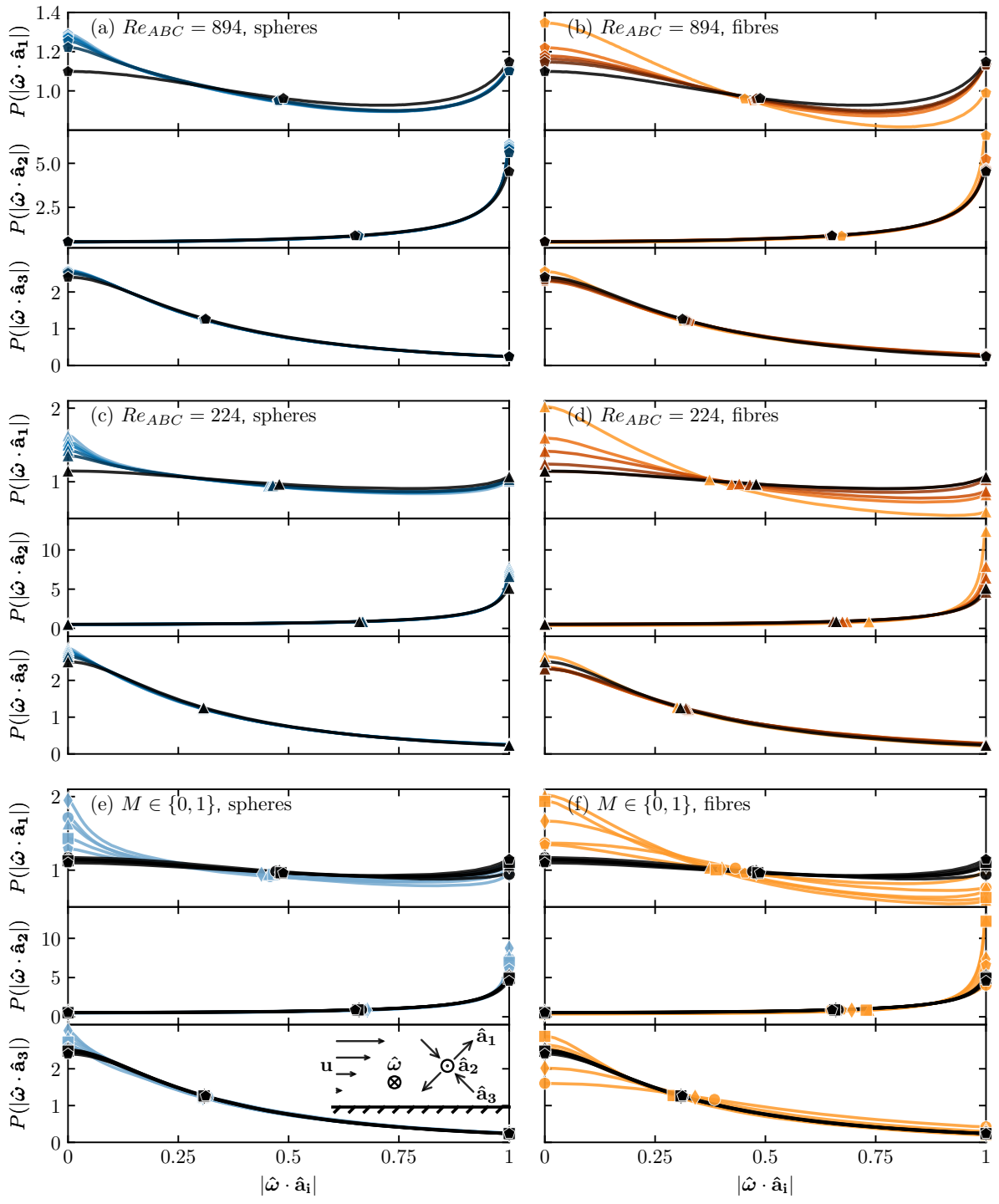

Figure 4.8: Histograms of the alignment of the vorticity unit vector $\hat{\boldsymbol{\omega}}$ with the eigenvectors $\hat{\mathbf{a}}_1, \hat{\mathbf{a}}_2, \hat{\mathbf{a}}_3$ of the strain-rate tensor. Flows with spheres are on the left, and flows with fibres are on the right. Panels (a) and (b) show cases with $Re_{ABC} = 894$ for various mass fractions. Panels (c) and (d) show cases with $Re_{ABC} = 224$ for various mass fractions. Panels (e) and (f) show fixed ($M = 1$) and single-phase ($M = 0$) cases for various Reynolds numbers. We mark each line at $|\hat{\boldsymbol{\omega}} \cdot \hat{\mathbf{a}}_i| = 0, 1$ and $\langle|\hat{\boldsymbol{\omega}} \cdot \hat{\mathbf{a}}_i|\rangle$. The inset of panel (e) shows the directions of vorticity and the eigenvectors of the strain rate in a laminar shear flow above a flat non-slip surface, where $\hat{\mathbf{a}}_1$ and $\hat{\mathbf{a}}_3$ are confined to the shear plane, while $\hat{\mathbf{a}}_2$ and $\hat{\boldsymbol{\omega}}$ are perpendicular to it.

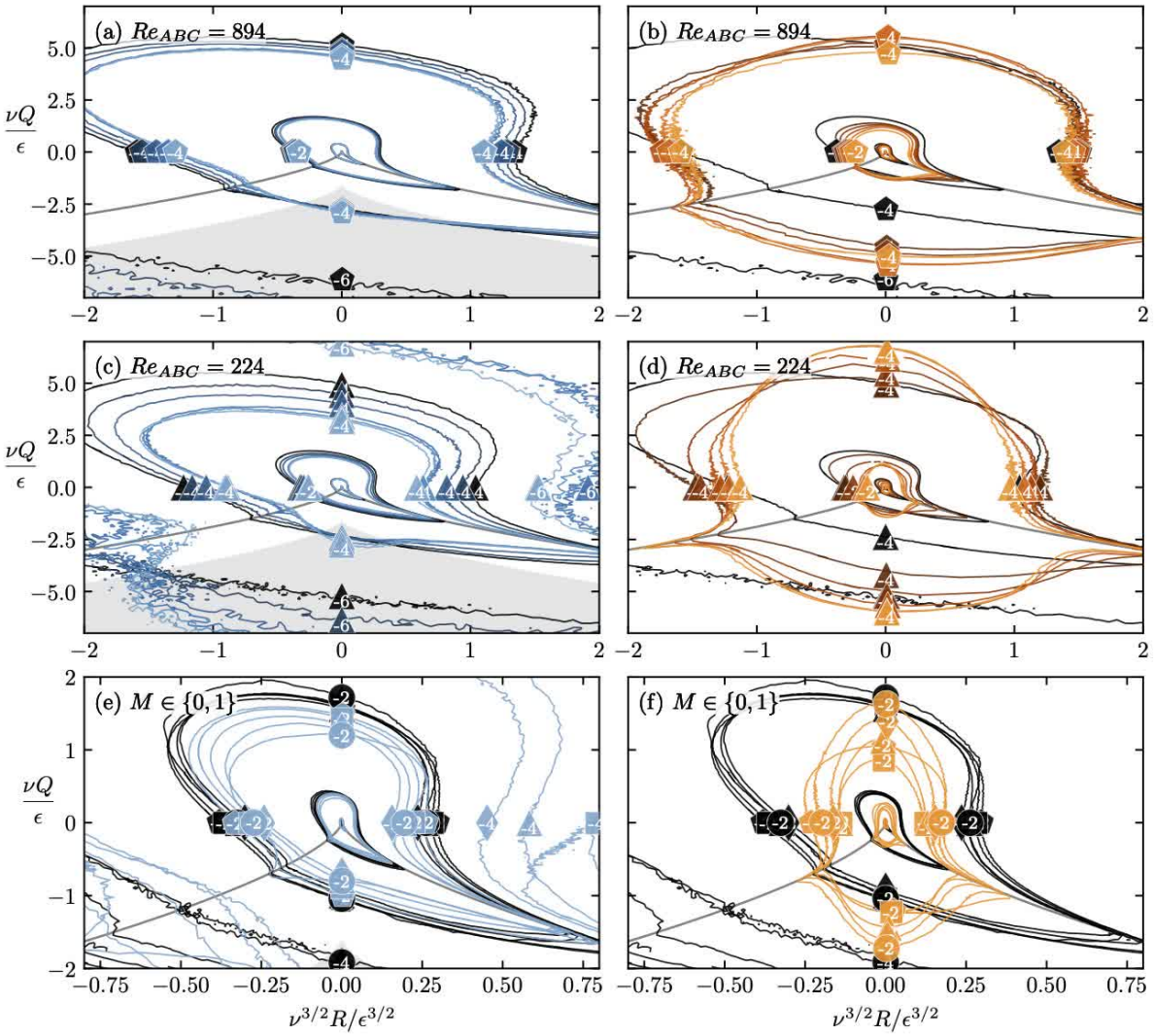

Figure 4.9: Joint histograms of the invariants Q and R of the fluid velocity gradient tensor. Panels (a) and (b) show cases with $Re_{ABC} = 894$ for various particle mass fractions. Panels (c) and (d) show cases with $Re_{ABC} = 224$ for various particle mass fractions. Panels (e) and (f) show fixed ($M = 1$) and single-phase ($M = 0$) cases for various Reynolds numbers. Numbered markers show the value of $\log p$ at each contour, where p is the joint probability density function. The grey curve show where the discriminant is zero (equation 4.16). The grey shaded regions in the left panels are the loci of equation 4.17, where we observe an increase p due to the presence of spheres.

interesting in our case because it is zero for an incompressible fluid. However, the second invariant,

$$Q = \frac{1}{4}\omega_i\omega_i - \frac{1}{2}s_{ij}s_{ij}, \tag{4.14}$$

expresses the balance of vorticity and strain, while the third invariant,

$$R = \frac{1}{4}\omega_i s_{ij}\omega_j - \frac{1}{3}s_{ij}s_{jk}s_{ki}, \tag{4.15}$$

is the balance of the production of vorticity with the production of strain (Paul et al., 2022b). The eigenvalues Λ of $\partial_i u_j$ are the roots of the polynomial equation

$$\Lambda^3 + Q\Lambda + R = 0. \tag{4.16}$$

Figure 4.9 shows the joint probability distributions $p(R, Q)$ for all of our flows. We also plot a line where the discriminant of equation 4.16 is zero: $27R^2/4 + Q^3 = 0$. Above this line $\partial_i u_j$ has one real and two complex eigenvalues and vortices dominate the flow. Below this line all three eigenvalues are real and the flow is dominated by strain. The single-phase distributions have tails in the top-left and bottom-right quadrants; these correspond to stretching vortices and regions where the flow compresses along one axis, respectively (Cheng & Cantwell, 1996). When spheres are added, both Q and R are reduced, as the non-slip boundary condition at their surfaces dampens the flow structures. Incidentally, a similar Q and R reduction has been seen with droplets (Perlekar, 2019). However, we see that the addition of spheres causes $p(R, Q)$ to increase in the lower regions of the left panels in figure 4.9. This region is well-described by

$$\frac{27R^2}{4} + Q^3 \lesssim -\frac{4\epsilon^3}{\nu^3}. \tag{4.17}$$

This region where spheres cause the probability distribution to increase corresponds to a strain-dominated flow. In fact, for pure strain, we have $Q = -s_{ij}s_{ij}/2$ and $R = 0$. Hence we can substitute for Q and R in equation 4.17 to estimate that the dissipation is $2\nu s_{ij}s_{ij} \gtrsim 4^{4/3}\epsilon \approx 6\epsilon$ in the shear layers, i.e., the dissipation in the regions around the spheres is many times greater than the mean dissipation. Fibres also create shearing regions in the flow, seen by the increased probability density functions in the lower parts ($27R^2/4 + Q^3 < 0$) of the right-hand panels in figure 4.9. As the fibre mass fraction is increased, the variance of R is reduced, showing the production of strain and vorticity is suppressed by the fibres. At high fibre mass fractions the distributions are approximately symmetrical in R, in other words, Q and R are uncorrelated (much like the decorrelation of vorticity and strain observed for fibre-laden flows in figure 4.8). This suggests that the small fibre diameter produces many small scale structures which disrupt the typical turbulent flow. For both particle types, increasing the Reynolds number Re_{ABC} reduces the effect of the particles.

4.4 Conclusion

We made simulations of finite-size isotropically- and anisotropically-shaped particles (spheres and fibres with size in the inertial range of scale) in turbulence at various Reynolds num-

bers and solid mass fractions. We used bulk flow statistics to show that particles reduce turbulence intensity relative to the single-phase case at all Reynolds numbers, with the fibres producing a more significant reduction effect than the spheres. From the trend in dissipation with Reynolds number, we see that the particle-laden flows behave like single-phase flows as $Re_\lambda \to \infty$, and the value of anomalous dissipation is $\epsilon\mathcal{L}/u'^3 \approx 0.4$ for both single-phase and particle-laden flows. However, spheres slow the convergence rate to the anomalous value, and fibres slow it further. Next, we analysed the flow at each scale of the simulation. Spheres and fibres provide a "spectral shortcut" to the flow, removing energy from the largest scales and injecting it at smaller scales. Spheres' effect is mainly limited to the large scales, and they provide a spectral shortcut down to the length scale of their diameter. Fibres' effect, on the other hand, occurs down to the length scale of the fibre thickness, even at low Reynolds numbers when it is deep in the viscous range ($d \ll \eta$). This shortcut of energy to the dissipative scales slows the dissipation's convergence to its anomalous value as $Re_\lambda \to \infty$. Our scale-by-scale analysis also showed that particles cause the velocity field to become more intermittent in space. Multifractal spectra of the near-particle dissipation show that spheres enhance dissipation in two-dimensional sheets, and fibres enhance the dissipation in structures with a dimension greater than one and less than two. These lower dimensional structures are a possible source of intermittency in the flow. Zooming in closer to the flow, we looked at the shape of flow structures using their vorticity and shear. We saw that the particles enhance local shear, spheres suppress vortical flow structures, and fibres produce intense vortical and shearing structures, which overcome the usual vortex stretching behaviour. As Reynolds number increases, the flow structures created by the particles become less significant relative to the background turbulence.

To reiterate and answer our questions from section 4.1; *at what Reynolds numbers does turbulence modulation emerge?* We see turbulence modulation at the lowest Reynolds number investigated ($Re_\lambda = 12.8$). This gives us reason to believe that particles modulate turbulence in even the most weakly turbulent flows ($Re_\lambda \to 0$). Secondly, *does the modulation effect persist as* $Re \to \infty$*?* No, all of the statistics show a tendency towards single-phase results as $Re \to \infty$. Finally, *how do the particle's characteristic lengths impact the scales of the turbulent flow?* Both spheres and particles take energy from the flow at scales larger than their size. Spheres re-inject energy around the characteristic length of their diameter, leaving the smaller scales relatively unperturbed, whereas fibres re-inject energy around the characteristic length of their thickness. The fibre thickness is at a small scale, so local flow structures are disrupted. None of the flow statistics shows any particular discerning feature at the length scale of the fibres.

These results relate to various environmental particle-laden flows, such as microplastics in the ocean, volcanic ash clouds, and sandstorms. We have explored the two extremes of isotropic and anisotropic particles, but further work is needed to investigate how intermediate aspect ratio particles such as ellipsoids interact with turbulent flows.

Chapter 5

Anisotropic Mean Flow Enhancement and Anomalous Transport of Finite-Size Spherical Particles in Turbulent Flows

Chapter 5 focuses on the influence of solid spherical particles on the largest scales of the turbulent triperiodic flow. During our exploration of the parameter space of particle mass fraction, Reynolds number, and particle size, we made dozens of large-scale simulations. At one particular particle size and mass fraction, something unexpected happened; the kinetic energy of the flow became larger than the single-phase flow. A closer investigation showed that the energy increase resulted from an enhancement of the time-averaged mean flow. This chapter shows how the particles modulate the flow toward an anisotropic, nearly two-dimensional, and more energetic state while preserving isotropy at smaller scales. The inertia of the particles plays a crucial role in this phenomenon, causing them to deviate from the cellular motion imposed by the inhomogeneous mean shear and enhancing the mean-flow velocity components aligned with their trajectories.

The article can be cited as follows:

Chiarini, A., Cannon, I., & Rosti, M. E. (2023). Anisotropic mean flow enhancement and anomalous transport of finite-size spherical particles in turbulent flows. *Under review for Physical Review Letters*. https://doi.org/10.48550/arXiv.2310.08777

In this chapter, we see that particles with intermediate Stokes number and size enhance the kinetic energy of the flow, the rotational symmetry of the mean flow is broken, and particles have ballistic motion in planes and diffusive motion perpendicular to these planes.

5.1 Introduction

Particle-laden turbulent flows have attracted the attention of many scholars over the last decades. Their significance goes beyond a fundamental interest and encompasses several applications such as blood flow in the human body, the food industry, and pyroclastic flows (Breard et al., 2016; De Lillo et al., 2014; Falkinhoff et al., 2020). Also, the modulation of

the mean flow and the enhancement/attenuation of turbulence due to particles are relevant in both environmental (Sengupta et al., 2017) and industrial flows (Ferreyra et al., 2011). However, although this is a classical problem in fluid mechanics since the seminal work by Tsuji and Morikawa (1982), the multi-scale mechanism governing the fluid-particle interaction is still an open question. In particular, the ability of suspensions of solid particles to modify and control the largest scales of a generic and complex flow is unclear.

The presence of the solid phase alters the momentum of the flow, and may result in modulation of the carrier fluid (Balachandar & Eaton, 2010; Brandt & Coletti, 2022). When the suspension is dilute enough, the fluid phase can be considered unaltered by the presence of the particles. Instead, when the suspension is non-dilute, the fluid phase undergoes macroscopic changes in a way that depends on several parameters, such as, for example, the size and density of the particles, and the volume and mass fractions of the suspension (Elgobashi, 2006; Gore & Crowe, 1989). Over the last years, the solid-fluid interaction in particle-laden turbulent flows has been the subject of several studies in various flows, ranging from homogeneous and isotropic flows (Oka & Goto, 2022) to wall-bounded flows (Costa et al., 2016). Nevertheless, the influence of the solid phase on the largest scales of a generic and complex flow has not yet been satisfactorily addressed, and the accurate characterisation of the underlying physics still requires significant effort. Here, we aim to address the following questions: *How do suspensions of solid particles modulate the largest and most energetic scales of the flow in the presence of an inhomogeneous mean shear? Is it possible to use particles to effectively modify and control the mean flow?*

In order to answer these questions, in this letter we study the modulation of the turbulent Arnold-Beltrami-Childress (ABC) flow by finite-size particles, with a focus on the largest scales. In a Cartesian reference system the laminar ABC flow is $L-$periodic in the three x, y and z directions, with a velocity field $\boldsymbol{u} = (u, v, w)$ that depends on four real parameters V_o, A, B and C, i.e.

$$\begin{cases} u/V_o &= A\sin\left(\frac{2\pi}{L}z\right) + C\cos\left(\frac{2\pi}{L}y\right), \\ v/V_o &= B\sin\left(\frac{2\pi}{L}x\right) + A\cos\left(\frac{2\pi}{L}z\right), \\ w/V_o &= C\sin\left(\frac{2\pi}{L}y\right) + B\cos\left(\frac{2\pi}{L}x\right); \end{cases} \tag{5.1}$$

A, B, and C are bounded between 0 and 1 and determine the shape of the flow, while V_o determines the magnitude. Here, we consider the turbulent ABC flow, which is obtained by forcing the incompressible Navier–Stokes equations with the ABC forcing with $A = B = C = 1$ (Podvigina & Pouquet, 1994b) (see figure 5.1). This provides an ideal instance of a complex turbulent flow with a three-dimensional (3D) mean field and an inhomogeneous mean shear, such as flow past an object or in a curved pipe. Because of the lack of solid boundaries in an ABC flow, the complex flow structures induced by the presence of a wall are avoided. Thus the particle-laden turbulent ABC flow allows us to isolate the influence of the particles on the large-scale motions, that in wall-bounded flows might be hidden by the complex near-wall phenomenology. In this idealised framework, we show that non-dilute suspensions of solid particles can substantially modify the structure of the mean flow. When tuning their size and density, indeed, particles modulate the largest scales of the flow towards an anisotropic, almost two-dimensional (2D) and more energetic state (see figure

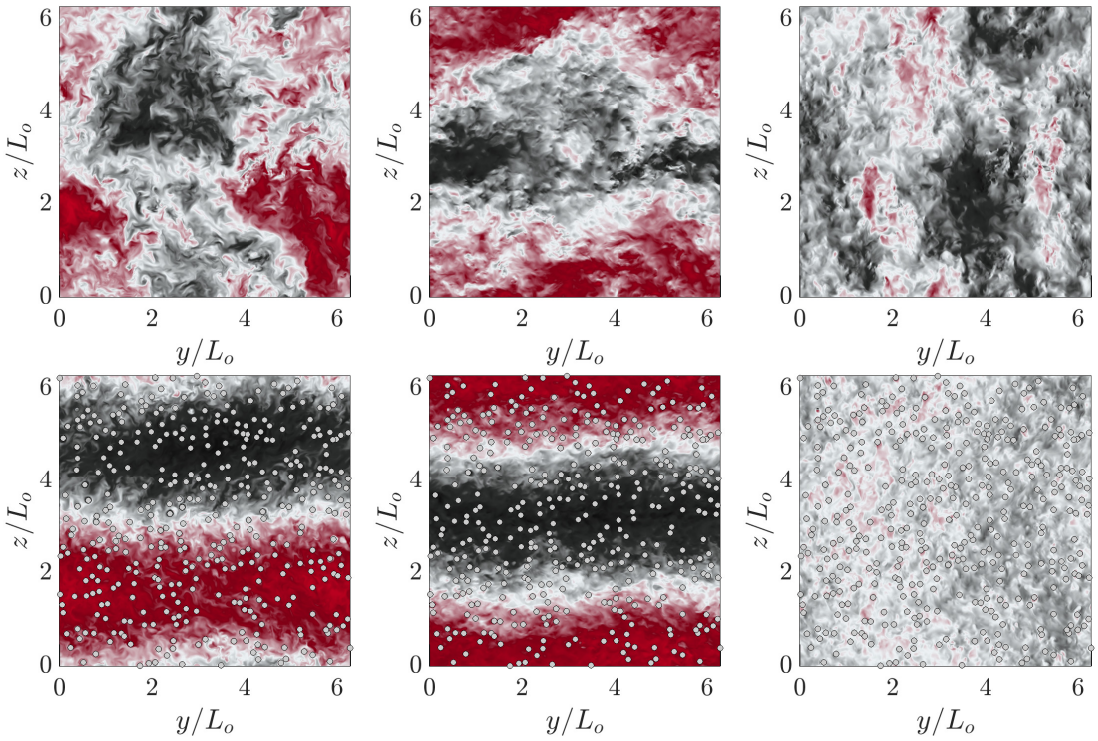

Figure 5.1: Instantaneous velocity field in the $x = L/2$ plane for the (top) single-phase case and the (bottom) particulate case with $D/L \approx 0.02$ and $M = 0.6$. Left: u; centre: v; right: w. The symmetric black-to-red colourmap goes from $-9 \leq u_i/U_o \leq 9$. We denote with z the direction orthogonal to the trajectories' plane.

5.1). Intriguingly, we show that this happens in the presence of a sustained 3D external forcing, whose effect is overcome by the presence of the solid phase. This paves the way for the use of solid particles to control complex 3D flows.

To tackle this problem, we have performed 3D direct numerical simulations of the flow within a triperiodic box of size L, with dispersed particles of various finite sizes, that lie within the inertial range of turbulence. The fluid and the solid dynamics are fully resolved, and coupled with an immersed boundary method (Hori et al., 2022). The external ABC forcing is set to achieve, in the single-phase case, a micro-scale Reynolds number of $Re_\lambda = u'\lambda/\nu \approx 435$, where u' is the root mean square of the velocity fluctuations and λ is the Taylor length scale. See the Supplemental Material for more information. The particle diameter is varied between $0.0104 \leq D/L \leq 0.0796$. For each particle size, the number of particles is set to provide a volume fraction of $\Phi_V \approx 0.08$, which is large enough for the suspension to be non-dilute and small enough for the particle-particle interactions to be sub-dominant. Finally, the ratio between the density of the particles and the fluid is varied between $1.3 \leq \rho_p/\rho_f \leq 105$, to consider both light and heavy particles, yielding a variation of the mass fraction between $0.1 \leq M \leq 0.9$.

5.2 Results

Figure 5.2 shows that the modulation of the carrier ABC flow changes with the size and density of the particles. In the top panel, we plot the total kinetic energy of the flow $\overline{\langle E(\boldsymbol{x},t)\rangle}$ for different values of D and M, where $E(\boldsymbol{x},t) = |\boldsymbol{u}(\boldsymbol{x},t)|^2/2$, while $\langle\cdot\rangle$ and $\bar{\cdot}$ indicate average along homogeneous directions and in time, respectively. Overall, the total energy decreases while reducing D and increasing M, in agreement with the findings of previous authors (Oka & Goto, 2022; Olivieri, Cannon, et al., 2022; Ten Cate et al., 2004; Uhlmann & Chouippe, 2017). However, the trend is non-monotonic, and the large increase of $\overline{\langle E\rangle}$ for $M \gtrsim 0.45$ and $D/L \lesssim 0.04$ shows that the solid phase modulates the carrier flow in a way that sharply changes with the density of the particles. Interestingly, solid suspensions of particles with $0.02 \lesssim D/L \lesssim 0.04$ and $0.45 \leq M \leq 0.6$ enhance the total energy of the carrier flow with respect to the single-phase case. In the central panels of figure 5.2, we use a temporal average to isolate the influence of the solid phase on the large and small scales of the carrier flow. We consider the $D/L \approx 0.02$ particulate cases and, after decomposing the velocity field into its temporal mean $\boldsymbol{U}(\boldsymbol{x}) = \overline{\boldsymbol{u}(\boldsymbol{x},t)}$ and fluctuations $\boldsymbol{u}'(\boldsymbol{x},t) = \boldsymbol{u}(\boldsymbol{x},t) - \boldsymbol{U}(\boldsymbol{x})$, we plot the variances of their three components. All quantities are made dimensionless with L_o and U_o, where $L_o = L/2\pi$ and $U_o = \sqrt{F_o L_o}$ with F_o denoting the intensity of the ABC forcing; see the Supplemental Material. Light particles ($M \leq 0.3$) modulate the flow without introducing a preferential direction, and attenuate the energy of the fluid phase by modifying the mean and fluctuating fields in an isotropic way. Indeed, here $\langle UU\rangle \approx \langle VV\rangle \approx \langle WW\rangle$ and $\overline{\langle u'u'\rangle} \approx \overline{\langle v'v'\rangle} \approx \overline{\langle w'w'\rangle}$. Heavier particles ($M \geq 0.45$), instead, modulate differently the mean and fluctuating fields. They continue to attenuate the energy of the fluctuations in an isotropic way, but modulate the mean field towards an anisotropic, quasi-2D and more energetic state. In this case, $\langle UU\rangle \approx \langle VV\rangle \gg \langle WW\rangle$, while $\overline{\langle u'u'\rangle} \approx \overline{\langle v'v'\rangle} \approx \overline{\langle w'w'\rangle}$. (We denote with z the direction aligned with the mean-flow component that is attenuated by the particle modulation, corresponding to the direction or-

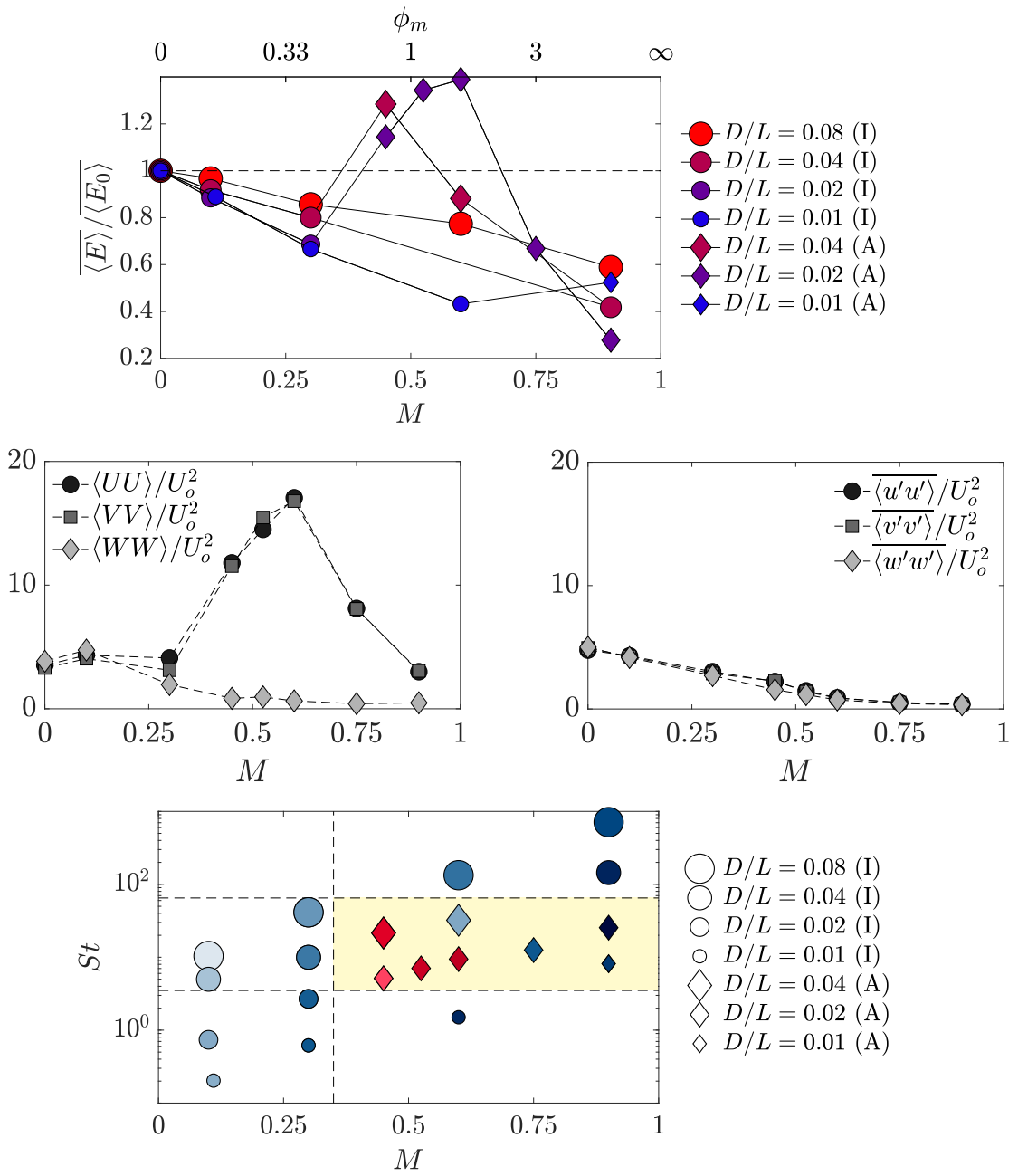

Figure 5.2: Modulation of the flow energy by finite-size solid particles. Top panel: total kinetic energy of the flow as a function of the mass fraction M and of the mass loading $\phi_m = M/(1-M)$, for different particle size. E_0 is the total kinetic energy of the single-phase flow. Circles and diamonds refer to the isotropic (I) and anisotropic (A) regimes. In the central panels the influence of the solid phase on the mean and fluctuating field is isolated for $D/L \approx 0.02$. Centre left: variance of the mean velocity components. Centre right: variance of the fluctuating velocity components. Bottom panel: modulation of the kinetic energy of the flow as a function of M and Stokes number St. Blue symbols are for $\overline{\langle E\rangle} < \overline{\langle E_0\rangle}$, red symbols for $\overline{\langle E\rangle} > \overline{\langle E_0\rangle}$. Dashed lines separate the regimes.

thogonal to the particle trajectories' plane.) The increase of the total flow energy observed for $0.45 \leq M \leq 0.6$ is thus entirely due to the mean-flow energy enhancement.

The anisotropic state is observed in a limited portion of the space of mass fraction M and Stokes number St, i.e. $5 \lesssim St \lesssim 60$ and $M \gtrsim 0.4$ (see the bottom panel of figure 5.2). Particles with $St \lesssim 5$ follow the complex fluid motion and hence do not significantly modify the flow. However, for $5 \lesssim St \lesssim 60$, inertia causes the particle trajectories to straighten, causing the fluid motion to reorganise into a quasi-2D state. When St further increases, the particles become less responsive to the fluid motion, and the 2D state does not develop. Note that the isotropic flow modulation observed for $St \gtrsim 60$ is consistent with the limit of infinite inertia: when $St \to \infty$, the particles do not move, and the quasi-2D flow does not arise. The dependence of the flow modulation on M shows that the emergence of the anisotropic state requires a strong enough backreaction of the particles to the fluid phase. Also, the ability of the particles to modulate the largest scales of the carrier flow strongly depends on the ratio D/L. In fact, the strongest flow modulation (and largest mean-flow enhancement) is observed for the intermediate $D/L \approx 0.02$, while the effect is lower for both smaller and larger particles. For $D \ll L$, indeed, particles have a small inertia and do not favour the flow two-dimensionalisation. For $D \approx L$, instead, the motion of the particles is only marginally influenced by the mean shear, as it is mainly driven by fluid velocity fluctuations with a length scale larger than their characteristic size. See the Supplemental Material for further discussions, and for the dependence of the anisotropic flow modulation on the inhomogeneous mean shear.

Next, we use Poincaré sections (Poincaré, 1892) to characterise the modulation of the mean flow $\boldsymbol{U}$. These are a 2D coding of a 3D dynamical system, in which one represents only the successive intersections of the mean-flow streamlines with one plane of the triperiodic domain. Figure 5.3 shows the $x = L/2$ Poincaré section for the mean flow of the turbulent single-phase case, and of the $D/L \approx 0.02$ particulate cases with $M = 0.3$ and $M = 0.6$. For each streamline many successive intersections with the $x = L/2$ plane are represented. At first glance, the Poincaré maps show that points associated with the same streamline are found to span a narrower range of z as the flow anisotropy increases. This confirms that in the anisotropic regime, particles attenuate the W velocity component and modulate the mean field towards a quasi 2D state (see figure 5.2). The density of the points in the Poincaré section is approximately proportional to the magnitude of the mean velocity component aligned with the direction perpendicular to the plane (Dombre et al., 1986). In the laminar case, indeed, the density of the points in the $x = L/2$ Poincaré plane falls to zero along the $U/V_o = \sin(z/L_o) + \cos(y/L_o) = 0$ line (see figure 5 of the Supplemental Material). A similar pattern is observed for the turbulent single-phase case. In fact, a remarkable property of the ABC flow is that even in the turbulent regime, the mean velocity has nearly the laminar ABC profile, as observed by others for the Kolmogorov flow (Borue & Orszag, 1996; Musacchio & Boffetta, 2014). In the particulate cases, the scenario progressively changes with M. Interestingly, the solid phase modulates the mean flow in a way that it resembles a generic ABC flow, but with different values of A, B, C and V_o. In view of this, the bottom panels of figure 5.3 report the coefficients of the generic ABC flow that best approximates the mean flow for $D/L \approx 0.02$ and $0.1 \leq M \leq 0.9$. As M (and St) increases, $A = 1$ remains constant, while $B \approx C$ decrease and reach a minimum for $M = 0.6$ ($St \approx 9.42$) where the flow anisotropy is maximum. In this case, $A \gg B \approx C$ and the streamlines of the mean flow are almost straight lines that lay in the $x - y$ planes, as $(U, V, W) \sim (\sin(z/L_o), \cos(z/L_o), 0)$.

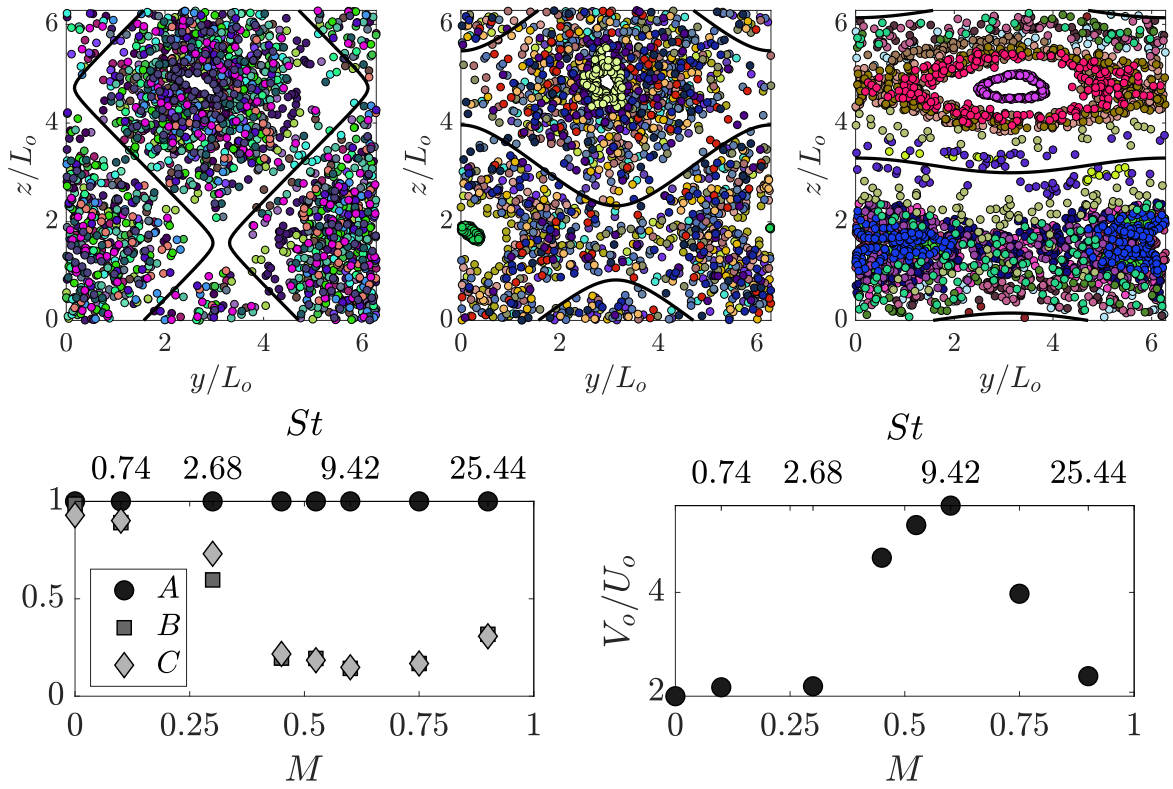

Figure 5.3: Mean flow field for $D/L \approx 0.02$. Top: Poincaré section for the mean flow of the single-phase case (right) and of the particulate cases with $M = 0.3$ (centre) and $M = 0.6$ (right). Twenty streamlines are considered, each identified by a different colour. Bottom: variation with M and St of A, B, C and V_o used in equation 5.1 to approximate the mean flow. Without losing generality we set that the maximum between A, B and C is equal to 1. The black lines in the Poincaré sections are for $U = A\sin(z) + C\cos(y) = 0$ with A and C as in the bottom left panel.

Thus, particles with $0.45 \leq M \leq 0.9$ and $5.13 \lesssim St \lesssim 25.45$ attenuate the W velocity component, and the mean flow approaches an anisotropic and 2D state, almost losing its dependence on x and y; see the black lines in figure 5.3. V_o sharply increases for $M \geq 0.45$ ($St \gtrsim 5.13$), in agreement with the enhancement of the mean-flow energy shown in figure 5.2. This anisotropic and almost 2D state resembles the bifurcated $\mathcal{A}_2$ state of the single-phase laminar ABC flow found by Podvigina and Pouquet (Podvigina & Pouquet, 1994b), spontaneously emerging at lower Reynolds numbers. Thus, it appears that the presence of the particles with $5 \lesssim St \lesssim 60$ and $M > 0.3$, and their tendency to follow straight trajectories, changes the stability of the system, enabling thus the occurrence of an anisotropic $\mathcal{A}_2$-like state also at these larger Re.

To further investigate the fluid-solid interaction, figures 5.4 and 5.5 characterise the particles' dynamics for $D/L \approx 0.02$. In the isotropic regime ($M \leq 0.3$ and $St \lesssim 2.68$), particles are able to follow the intricate ABC cellular forcing, and exhibit complex trajectories as expected by the chaotic Lagrangian structure of the ABC flow (Dombre et al., 1986). In this case, the particles do not select a preferential direction, and explore the entire computational domain. Indeed, the probability density functions (pdfs) of the three velocity components almost collapse, exhibiting a symmetric unimodal distribution. On the contrary, in the anisotropic regime ($0.45 \leq M \leq 0.9$ and $5.13 \lesssim St \lesssim 25.44$), the particles move along almost straight trajectories with $u_p \approx v_p \gg w_p$. The direction of the trajectories of the particles in the $x-y$ plane changes with z, in agreement with the fact that $A \gg B \approx C$, and $U \sim \sin(z/L_o)$ and $V \sim \cos(z/L_o)$. As a result, the in-plane components of the particle velocity exhibit a symmetric bimodal distribution, and the modes $\pm\tilde{u}_p$ and $\pm\tilde{v}_p$ change with the density of the particles (see bottom panel of figure 5.4).

Figure 5.5 shows the mean squared displacement of the particles, $R(t)^2 = \left\langle |\boldsymbol{x}_p(t) - \boldsymbol{x}_p(0)|^2 \right\rangle_p$; here, $\langle\cdot\rangle_p$ indicates average over particles. The particle motion is diffusive (ballistic) when $R^2(t) \sim t^\alpha$ with $\alpha = 1$ (2). As expected, in the isotropic regime, particles show ballistic motion for short times, while at large times, their motion becomes uncorrelated under the action of the random velocity fluctuations, and they exhibit a diffusive process; see the $M = 0.3$ case in the left panel. In the anisotropic regime, instead, particles exhibit anomalous transport with $1 < \alpha < 2$ at large times; see the $M = 0.6$ case in the right panel. The scaling of the anomalous transport slightly changes with the density of the particles in the $1.6 \lessapprox \alpha \lessapprox 1.75$ range, increasing as the particles' motion becomes more coherent and their trajectories more straight. Note that considering the z direction alone, i.e. $R_z(t)^2 = \left\langle |z_p(t) - z_p(0)|^2 \right\rangle_p$, the diffusive transport with $\alpha \approx 1$ is recovered also for heavy particles.

5.3 Conclusion

To conclude, we have shown that in the presence of a 3D and inhomogeneous mean shear, solid particles can substantially modify the structure of the largest scales of the flow. By tuning the size and the density of the particles, non-dilute suspensions can modulate the largest scales of the flow towards an anisotropic, almost 2D and more energetic state, while preserving isotropy at smaller scales. The ability of solid particles to modify the large-scale flow may pave the way for their use in flow-control purposes. For example, the cooling and cleaning

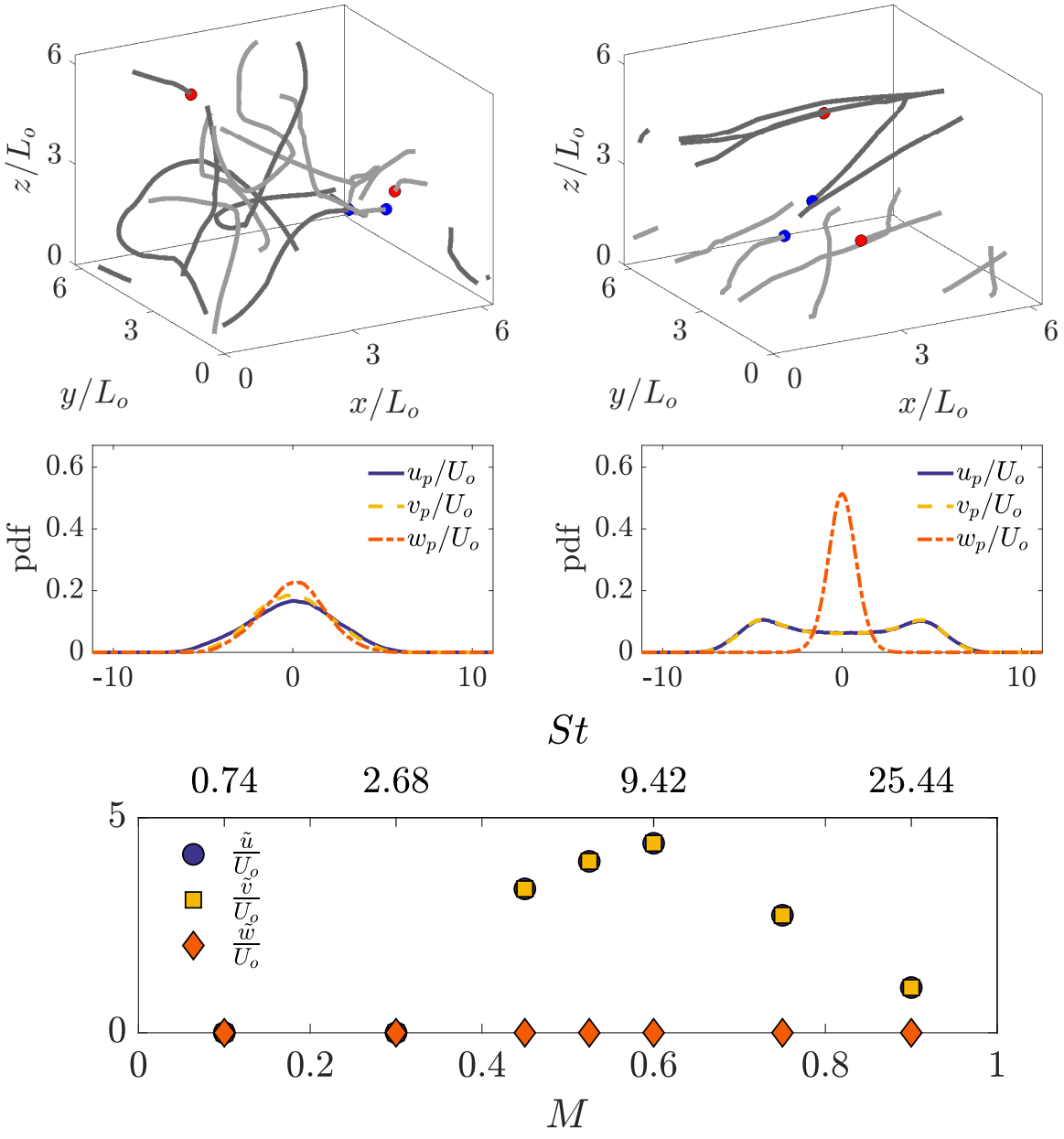

Figure 5.4: Particle dynamics for $D/L \approx 0.02$. Top panels: two representative trajectories for (left) $M = 0.3$ and (right) $M = 0.6$; the red/blue circle indicate the beginning/end of the trajectories. Central panels: probability density functions for (left) $M = 0.3$ and (right) $M = 0.6$. Bottom panel: dependence of the modes $\tilde{u}_i$ of the probability density functions on M and St.

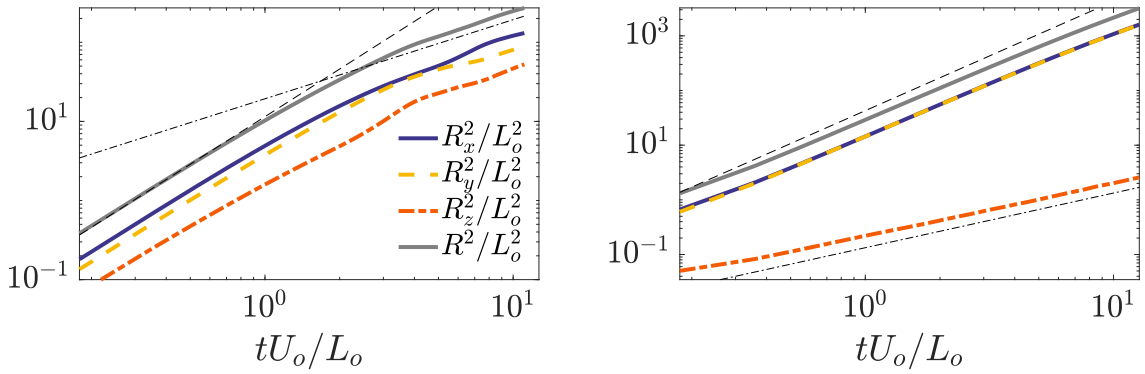

Figure 5.5: Particle mean squared displacement $R^2(t)$ for $D/L \approx 0.02$. Left: $M = 0.3$. Right: $M = 0.6$. The thin dashed line represents t^2, while the thin dash-dotted line t.

effects of oil in an engine are undermined by recirculating regions in the flow (Concli & Mastrone, 2023; Gamble et al., 2003), we showed that adding particles can potentially eliminate such recirculating regions, improving engine efficiency and lifetime. Also, our results show that there is a specific regime in which the ballistic motion of the particles is favoured over diffusive motion, with relevance for drug delivery and pollen dispersal (Hamaoui-Laguel et al., 2015; Ito et al., 2023).

Chapter 6

Scaling and intermittency in turbulent flows of elastoviscoplastic fluids

Chapter 6 combines my experience in analysing solid and liquid dispersed phases. We investigate elastoviscoplastic fluids at very high Reynolds numbers, as encountered in landslides and lava flows. The focus lies on the effect of plasticity on turbulence, revealing that increased fluid plasticity leads to a reduction in the range of active scales in the energy spectrum. A new scaling of the energy emerges between the inertial and dissipative scales when plastic effects dominate, accompanied by enhanced intermittency of the non-Newtonian dissipation in space.

The article is appended in section E of this thesis and can be cited as follows:

Abdelgawad*, M. S., Cannon*, I., & Rosti, M. E. (2023). Scaling and intermittency in turbulent flows of elastoviscoplastic fluids. *Nature Physics*, 1–5. https://doi.org/10.1038/s41567-023-02018-2

In this chapter we show that as fluid plasticity increases, the solid volume fraction and Reynolds number increase. For high plasticities, the canonical Kolmorgorov scaling is replaced by an $E \sim \kappa^{-2.3}$ wavenumber dependence of the energy spectrum. Non-Newtonian stresses dissipate energy in the fluid, and the likelihood of large non-Newtonian dissipation events increases as the fluid plasticity increases.

Conclusion

Overall, this thesis presents a comprehensive exploration of the interaction between dispersed phases and turbulent flows, elucidating the underlying mechanisms and providing valuable insights into the behaviour of turbulence itself. The findings relate to a wide range of natural and industrial processes, including blood flow, ocean waves, pollen dispersal, sandstorms and landslides.

I studied droplets, particles, and plasticity in turbulent fluids. All of the flows are described by the Navier-Stokes equation (equation 1 from the introduction) with an additional force which depends on the added phase. In all cases, a new length scale appears in the flow when the additional phase interacts with turbulence in the fluid. The existence of this new length scale violates Kolmogorov's assumptions of self-similarity in the flow. Indeed, in the case of elastoviscoplastic (EVP) fluids and dispersed fibres, Kolmogorov's result that the kinetic energy spectrum scales as $E \sim \kappa^{-5/3}$ no longer holds. We see in figure 6.1 that EVP fluids produce a steeper scaling of the energy spectrum, and dispersed fibres produce a scaling that is less steep. However, in some cases, such as with spherical particles and droplets, the $E \sim \kappa^{-5/3}$ scaling is still seen. This tells us about the strength of the interaction between the fluid and the dispersed phase.

More quantitatively, coupling of the additional phase to the turbulent cascade is described by the multi-phase energy flux $\mathcal{F}^{mp}$, and how it competes with the advective energy flux Π, defined in section 0.3. For spherical particles $\mathcal{F}^{mp}$ is present only at the large length scales in the flow, whereas for fibres, it completely replaces the advective energy flux at all scales, returning energy to the fluid only at the smallest scales. For EVP fluids, $\mathcal{F}^{mp}$ is only seen at small scales, it provides the additional roles of dissipating energy as heat, and inducing the new energy scaling $E \sim \kappa^{-2.3}$. In the case of droplets, $\mathcal{F}^{mp}$ is present at all scales, and the length scale at which $\mathcal{F}^{mp}$ is maximum can be used to define the coalescence and breakup regimes. These differences are imprinted on the energy spectra in figure 6.1.

All of the phases that we added modify the intermittency in the flow. In the case of droplets, the flow inside the dispersed phase becomes more quiescent. On addition of spheres and fibres, we see an increased intermittency, with concentrated regions of dissipation in wakes that match the particle shapes. In the case of EVP fluids, the increased intermittency of the flow is attributed to the presence of a non-Newtonian dissipation field.

A single-phase turbulent flow can be simply parametrized by a dimensionless parameter called the Reynolds number. On addition of the dispersed phases, we introduce new dimensionless parameters into the flow, such as droplet volume fraction and Weber number in the case of droplets, particle mass fraction and particle size in the case of particles, and Bingham number in the case of EVP fluids. Exploring the new parameter space leads to a rich and unpredictable range of behaviours, such as elongated droplets, turbulence reduc-

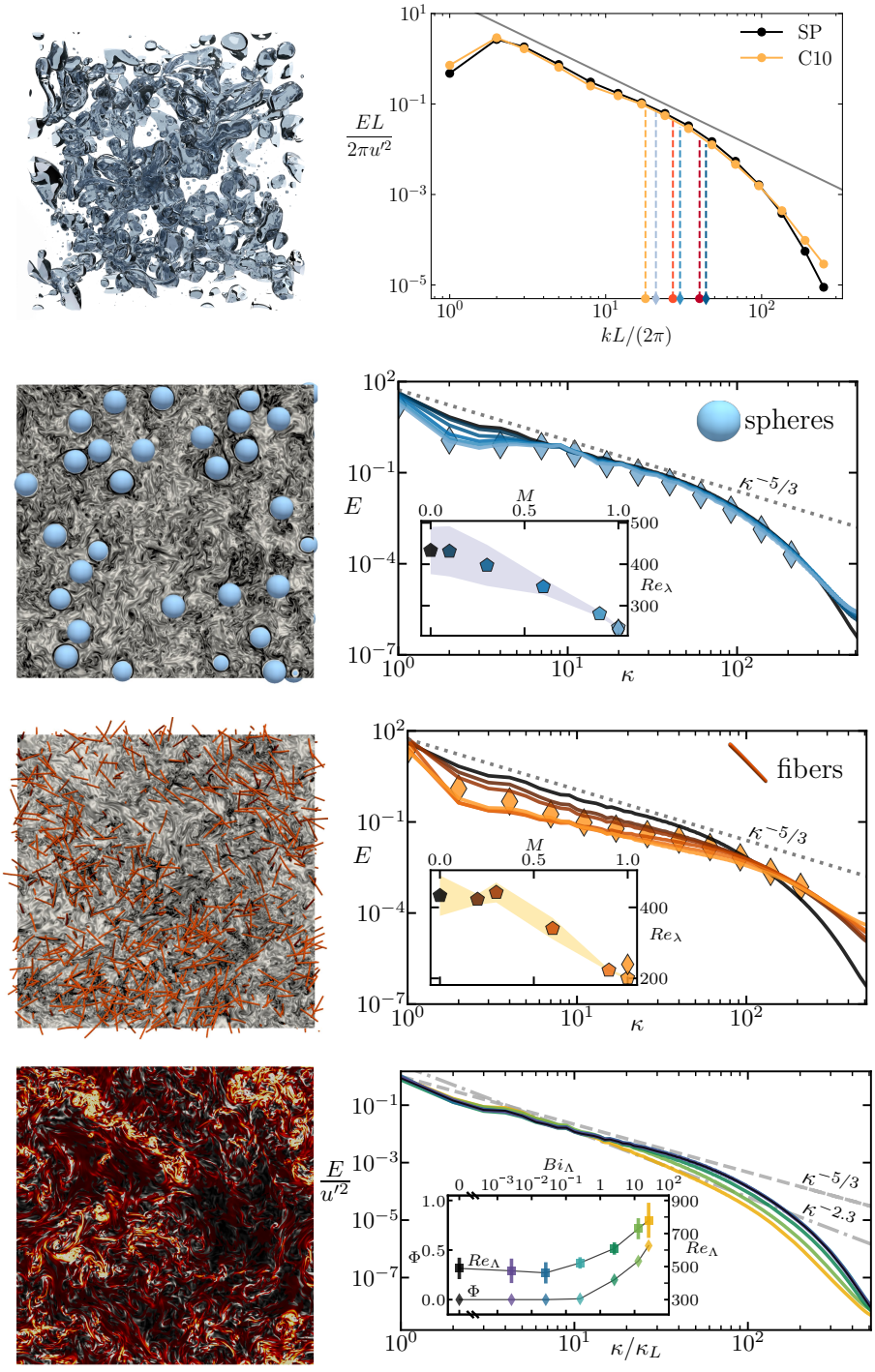

Figure 6.1: Each of the additional phases simulated during my thesis research, from bottom to top: droplets, spheres, fibres, and elastoviscoplastic fluids. The right-hand panels show the turbulent kinetic energy spectrum in each case, with a grey line depicting Kolmogorov's $E \sim \kappa^{-5/3}$ scaling. See the publications for a description of the insets and additional markings on the plots.

tion, mean-flow enhancement, anomalous particle diffusion, and increased intermittency of the flow.

For better or worse, I have more questions than when I began my thesis research. Some of my questions are as follows.

1. How do surfactants affect the rate of droplet coalescence and breakup in the presence of a mean flow, such as a channel or a Kolmogorov flow?

2. What is the size distribution of droplets in non-classical turbulence where the energy spectrum does not scale as $E \sim \kappa^{-5/3}$?

3. Can we model droplet motion in a way that inherently conserves both the droplet mass and the energy stored in the interface?

4. Does the Euler characteristic of a droplet interface correlate with the number of defects in the velocity field at the interface?

5. How do ellipsoidal particles interact with the turbulent cascade?

6. Can particles cause an inverse cascade of kinetic energy to larger scales in the flow?

7. Does dissipation in a viscoelastic fluid remain finite, even as the elastic timescale tends to zero?

A few of these questions I am already trying to answer using simulations. Some of the questions, especially number 3, I don't know how to address, and I am hoping the answer is out there somewhere. Finally, I am glad to have spent the past four years studying this beautiful subject.

Bibliography

Abdelgawad*, M. S., Cannon*, I., & Rosti, M. E. (2023). Scaling and intermittency in turbulent flows of elastoviscoplastic fluids. *Nature Physics*, 1–5. https://doi.org/10.1038/s41567-023-02018-2

Ahmed, Z., Izbassarov, D., Costa, P., Muradoglu, M., & Tammisola, O. (2020). Turbulent bubbly channel flows: Effects of soluble surfactant and viscoelasticity. *Computers & Fluids*, *212*, 104717. https://doi.org/10.1016/j.compfluid.2020.104717

Akita, K., & Yoshida, F. (1974). Bubble Size, Interfacial Area, and Liquid-Phase Mass Transfer Coefficient in Bubble Columns. *Ind. Eng. Chem. Process.*, *13*(1), 84–91. https://doi.org/10.1021/i260049a016

Albadawi, A., Donoghue, D., Robinson, A., Murray, D., & Delauré, Y. (2013). Influence of surface tension implementation in volume of fluid and coupled volume of fluid with level set methods for bubble growth and detachment. *International Journal of Multiphase Flow*, *53*, 11–28.

Alizad Banaei, A., Rosti, M. E., & Brandt, L. (2020). Numerical study of filament suspensions at finite inertia. *Journal of Fluid Mechanics*, *882*, A5. https://doi.org/10.1017/jfm.2019.794

Andersson, R., & Andersson, B. (2006a). Modeling the breakup of fluid particles in turbulent flows. *AIChE J.*, *52*(6), 2031–2038.

Andersson, R., & Andersson, B. (2006b). On the breakup of fluid particles in turbulent flows. *AIChE J.*, *52*(6), 2020–2030.

Ardekani, M. N., Costa, P., Breugem, W.-P., Picano, F., & Brandt, L. (2017). Drag reduction in turbulent channel flow laden with finite-size oblate spheroids. *Journal of Fluid Mechanics*, *816*, 43–70. https://doi.org/10.1017/jfm.2017.68

Ashurst, W. T., Kerstein, A. R., Kerr, R. M., & Gibson, C. H. (1987). Alignment of vorticity and scalar gradient with strain rate in simulated Navier–Stokes turbulence. *The Physics of Fluids*, *30*(8), 2343–2353. https://doi.org/10.1063/1.866513

Babinsky, E., & Sojka, P. (2002). Modeling drop size distributions. *Prog. Energ. Combust.*, *28*, 303–329.

Balachandar, S., & Eaton, J. K. (2010). Turbulent Dispersed Multiphase Flow. *Annu. Rev. Fluid Mech.*, *42*(1), 111–133. https://doi.org/10.1146/annurev.fluid.010908.165243

Bazhlekov, I., Anderson, P., & Meijer, H. (2006). Numerical investigation of the effect of insoluble surfactants on drop deformation and breakup in simple shear flow. *J. Colloid Interf. Sci.*, *298*(1), 369–394.

Bec, J., Krstulovic, G., Matsumoto, T., Ray, S. S., & Vincenzi, D. (2022). Editorial: Scaling the Turbulence Edifice. *Philosophical Transactions of the Royal Society A: Mathematical,*

Physical and Engineering Sciences, *380*(2218), 20210101. https://doi.org/10.1098/rsta.2021.0101

Boehm, H. F., Fink, C., Attenberger, U., Becker, C., Behr, J., & Reiser, M. (2008). Automated classification of normal and pathologic pulmonary tissue by topological texture features extracted from multi-detector CT in 3D. *European Radiology*, *18*(12), 2745–2755. https://doi.org/10.1007/s00330-008-1082-y

Borue, V., & Orszag, S. A. (1996). Numerical study of three-dimensional Kolmogorov flow at high Reynolds numbers. *J. Fluid Mech.*, *306*, 293–323.

Brandt, L., & Coletti, F. (2022). Particle-Laden Turbulence: Progress and Perspectives. *Annu. Rev. Fluid Mech.*, *54*(1), 159–189. https://doi.org/10.1146/annurev-fluid-030121-021103

Breard, E. C. P., Lube, G., Jones, J. R., Dufek, J., Cronin, S. J., Valentine, G. A., & Moebis, A. (2016). Coupling of turbulent and non-turbulent flow regimes within pyroclastic density currents. *Nat. Geosci*, *9*(10), 767–771. https://doi.org/10.1038/ngeo2794

Brizzolara, S., Rosti, M. E., Olivieri, S., Brandt, L., Holzner, M., & Mazzino, A. (2021). Fiber Tracking Velocimetry for Two-Point Statistics of Turbulence. *Physical Review X*, *11*(3), 031060. https://doi.org/10.1103/PhysRevX.11.031060

Brooks, S. D., & Thornton, D. C. (2018). Marine Aerosols and Clouds. *Annual Review of Marine Science*, *10*(1), 289–313. https://doi.org/10.1146/annurev-marine-121916-063148

Bunner, B., & Tryggvason, G. (2003). Effect of bubble deformation on the properties of bubbly flows. *J. Fluid Mech.*, *495*, 77–118.

Cannon, I., Izbassarov, D., Tammisola, O., Brandt, L., & Rosti, M. E. (2021). The effect of droplet coalescence on drag in turbulent channel flows. *Physics of Fluids*, *33*(8), 085112. https://doi.org/10.1063/5.0058632

Canu, R., Puggelli, S., Essadki, M., Duret, B., Menard, T., Massot, M., Reveillon, J., & Demoulin, F. X. (2018). Where does the droplet size distribution come from? *International Journal of Multiphase Flow*, *107*, 230–245. https://doi.org/10.1016/j.ijmultiphaseflow.2018.06.010

Capecelatro, J., Desjardins, O., & Fox, R. O. (2015). On fluid–particle dynamics in fully developed cluster-induced turbulence. *Journal of Fluid Mechanics*, *780*, 578–635. https://doi.org/10.1017/jfm.2015.459

Chan, Klaseboer, & Manica. (2011). Film drainage and coalescence between deformable drops and bubbles. *Soft Matter*, *7*(6), 2235–2264. https://doi.org/10.1039/C0SM00812E

Chan, W. H. R., Dodd, M. S., Johnson, P. L., Urzay, J., & Moin, P. (n.d.). Formation and dynamics of bubbles in breaking waves: Part II. The evolution of the bubble size distribution and breakup/coalescence statistics, 14.

Chan, W., Johnson, P., & Moin, P. (2021). The turbulent bubble break-up cascade. part 1. theoretical developments. *J. Fluid Mech.*, *912*, A42.

Chang, C., & Franses, E. (1995). Adsorption dynamics of surfactants at the air/water interface: A critical review of mathematical models, data, and mechanisms. *Colloids Surf. A*, *100*, 1–45.

Cheng, W.-P., & Cantwell, B. (1996). *Study of the velocity gradient tensor in turbulent flow* (tech. rep. JIAA TR 114).

Concli, F., & Mastrone, M. N. (2023). Advanced Lubrication Simulations of an Entire Test Rig: Optimization of the Nozzle Orientation to Maximize the Lubrication Capability. *Lubricants*, *11*(7), 300. https://doi.org/10.3390/lubricants11070300

Costa, P., Picano, F., Brandt, L., & Breugem, W.-P. (2016). Universal Scaling Laws for Dense Particle Suspensions in Turbulent Wall-Bounded Flows. *Phys. Rev. Lett.*, *117*(13), 134501. https://doi.org/10.1103/PhysRevLett.117.134501

Crialesi-Esposito, M., Chibbaro, S., & Brandt, L. (2023). The interaction of droplet dynamics and turbulence cascade. *Comm. Phys.*, *6*(11), 1–8. https://doi.org/10.1038/s42005-022-01122-8

Crialesi-Esposito, M., Boffetta, G., Brandt, L., Chibbaro, S., & Musacchio, S. (2023). Intermittency in turbulent emulsions. https://doi.org/10.48550/arXiv.2301.01537

Crialesi-Esposito, M., Rosti, M. E., Chibbaro, S., & Brandt, L. (2022). Modulation of homogeneous and isotropic turbulence in emulsions. *Journal of Fluid Mechanics*, *940*, A19. https://doi.org/10.1017/jfm.2022.179

Dai, B., & Leal, L. (2008). The mechanism of surfactant effects on drop coalescence. *Phys. Fluids*, *20*(4), 1–13.

de Leeuw, G., Andreas, E. L., Anguelova, M. D., Fairall, C. W., Lewis, E. R., O'Dowd, C., Schulz, M., & Schwartz, S. E. (2011). Production flux of sea spray aerosol. *Reviews of Geophysics*, *49*(2). https://doi.org/10.1029/2010RG000349

De Lillo, F., Cencini, M., Durham, W. M., Barry, M., Stocker, R., Climent, E., & Boffetta, G. (2014). Turbulent Fluid Acceleration Generates Clusters of Gyrotactic Microorganisms. *Phys. Rev. Lett.*, *112*(4), 044502. https://doi.org/10.1103/PhysRevLett.112.044502

De Vita, F., Rosti, M. E., Caserta, S., & Brandt, L. (2019). On the effect of coalescence on the rheology of emulsions. *Journal of Fluid Mechanics*, *880*, 969–991. https://doi.org/10.1017/jfm.2019.722

Deane, G., & Stokes, M. (2002). Scale dependence of bubble creation mechanisms in breaking waves. *Nature*, *418*(6900), 839.

DeHoff, R. T., Aigeltinger, E. H., & Craig, K. R. (1972). Experimental determination of the topological properties of three-dimensional microstructures. *Journal of Microscopy*, *95*(1), 69–91. https://doi.org/10.1111/j.1365-2818.1972.tb03712.x

Deike, L., Melville, W., & Popinet, S. (2016). Air entrainment and bubble statistics in breaking waves. *J. Fluid Mech.*, *801*, 91–129.

Delhaye, J., & Bricard, P. (1994). Interfacial area in bubbly flow: Experimental data and correlations. *Nucl. Eng. Des.*, *151*(1), 65–77.

Dickinson, E. (2010). Food emulsions and foams: Stabilization by particles. *Curr. Opin. Colloid In.*, *15*(1-2), 40–49.

Dobbs, L. (1989). Pulmonary surfactant. *Annu. Rev. Med.*, *40*(1), 431–446.

Dodd, M., & Jofre, L. (2019). Small-scale flow topologies in decaying isotropic turbulence laden with finite-size droplets. *Phys. Rev. Fluids*, *4*(6), 064303.

Doering, C. R., & Foias, C. (2002). Energy dissipation in body-forced turbulence. *Journal of Fluid Mechanics*, *467*, 289–306. https://doi.org/10.1017/S0022112002001386

Dombre, T., Frisch, U., Greene, J. M., Hénon, M., Mehr, A., & Soward, A. M. (1986). Chaotic streamlines in the ABC flows. *J. Fluid Mech.*, *167*, 353–391. https://doi.org/10.1017/S0022112086002859

Dong, J., Inthavong, K., & Tu, J. (2017). Multiphase Flows in Biomedical Applications. In *Handbook of Multiphase Flow Science and Technology* (pp. 1–24). https://doi.org/10.1007/978-981-4585-86-6_16-1

Donzis, D. A., Sreenivasan, K. R., & Yeung, P. K. (2005). Scalar dissipation rate and dissipative anomaly in isotropic turbulence. *Journal of Fluid Mechanics*, *532*, 199–216. https://doi.org/10.1017/S0022112005004039

Dumouchel, C., Thiesset, F., & Ménard, T. (2022). Morphology of contorted fluid structures. *International Journal of Multiphase Flow*, *152*, 104055. https://doi.org/10.1016/j.ijmultiphaseflow.2022.104055

Elghobashi, S. (2019). Direct numerical simulation of turbulent flows laden with droplets or bubbles. *Annu. Rev. Fluid Mech.*, *51*(1), 217–244.

Elgobashi, S. (2006). An Updated Classification Map of Particle-Laden Turbulent Flows. In S. Balachandar & A. Prosperetti (Eds.), *IUTAM Symposium on Computational Approaches to Multiphase Flow* (pp. 3–10). Springer Netherlands. https://doi.org/10.1007/1-4020-4977-3_1

Engblom, S., Do-Quang, M., Amberg, G., & Tornberg, A. (2013). On diffuse interface modeling and simulation of surfactants in two-phase fluid flow. *Commun. Comput. Phys.*, *14*(4), 879–915.

Eswaran, V., & Pope, S. B. (1988). An examination of forcing in direct numerical simulations of turbulence. *Computers & Fluids*, *16*(3), 257–278. https://doi.org/10.1016/0045-7930(88)90013-8

Evrard, F., Denner, F., & van Wachem, B. (2019). A hybrid eulerian-lagrangian approach for simulating liquid sprays. *ILASS–Europe, Paris, France*, 2–4.

Faeth, G. M., Hsiang, L. .-., & Wu, P. .-. (1995). Structure and breakup properties of sprays. *International Journal of Multiphase Flow*, *21*, 99–127. https://doi.org/10.1016/0301-9322(95)00059-7

Falkinhoff, F., Obligado, M., Bourgoin, M., & Mininni, P. D. (2020). Preferential Concentration of Free-Falling Heavy Particles in Turbulence. *Phys. Rev. Lett.*, *125*(6), 064504. https://doi.org/10.1103/PhysRevLett.125.064504

Ferreyra, S. A., Uehara, S., Ferreira, M. d. S., & Mian, O. (2011). *Engine Lubrication System for Oil Flow Reduction* (SAE Technical Paper No. 2011-36-0205). SAE International. Warrendale, PA. https://doi.org/10.4271/2011-36-0205

Finnigan, J. (2000). Turbulence in Plant Canopies. *Annual Review of Fluid Mechanics*, *32*(1), 519–571. https://doi.org/10.1146/annurev.fluid.32.1.519

Frisch, U. (1995). *Turbulence: The Legacy of A. N. Kolmogorov*. Cambridge University Press.

Gamble, R., Priest, M., & Taylor, C. (2003). Detailed analysis of oil transport in the piston assembly of a gasoline engine. *Tribology Letters*, *14*(2), 147–156. https://doi.org/10.1023/A:1021712506331

Garrett, C., Li, M., & Farmer, D. (2000). The connection between bubble size spectra and energy dissipation rates in the upper ocean. *J. Phys. Oceanogr.*, *30*(9), 2163–2171.

Gaylo, D., Hendrickson, K., & Yue, D. (2023). Fundamental time scales of bubble fragmentation in homogeneous isotropic turbulence. *J. Fluid Mech.*, *962*, A25.

Ghia, U., Ghia, K. N., & Shin, C. T. (1982). High-Re solutions for incompressible flow using the Navier-Stokes equations and a multigrid method. *Journal of Computational Physics*, *48*(3), 387–411. https://doi.org/10.1016/0021-9991(82)90058-4

Gillissen, J. J. J., Boersma, B. J., Mortensen, P. H., & Andersson, H. I. (2008). Fibre-induced drag reduction. *Journal of Fluid Mechanics*, *602*, 209–218. https://doi.org/10.1017/S0022112008000967

Gore, R. A., & Crowe, C. T. (1989). Effect of particle size on modulating turbulent intensity. *Int. J. Multiph. Flow.*, *15*(2), 279–285. https://doi.org/10.1016/0301-9322(89)90076-1

Goto, S., & Vassilicos, J. C. (2008). Sweep-Stick Mechanism of Heavy Particle Clustering in Fluid Turbulence. *Physical Review Letters*, *100*(5), 054503. https://doi.org/10.1103/PhysRevLett.100.054503

Guido, S., & Simeone, M. (1998). Binary collision of drops in simple shear flow by computer-assisted video optical microscopy. *J. Fluid Mech.*, *357*, 1–20.

Hamaoui-Laguel, L., Vautard, R., Liu, L., Solmon, F., Viovy, N., Khvorostyanov, D., Essl, F., Chuine, I., Colette, A., Semenov, M. A., Schaffhauser, A., Storkey, J., Thibaudon, M., & Epstein, M. M. (2015). Effects of climate change and seed dispersal on airborne ragweed pollen loads in Europe. *Nature Climate Change*, *5*(8), 766–771. https://doi.org/10.1038/nclimate2652

Herrmann, M. (2011). On Simulating Primary Atomization Using The Refined Level Set Grid Method. *Atomization Spray*, *21*, 283–301.

Herrmann, M. (2013). A sub-grid surface dynamics model for sub-filter surface tension induced interface dynamics. *Comp. Fluids*, *87*, 92–101.

Hinze, J. (1955). Fundamentals of the hydrodynamic mechanism of splitting in dispersion processes. *AIChE J.*, *1*(3), 289–295.

Hori, N., Rosti, M. E., & Takagi, S. (2022). An Eulerian-based immersed boundary method for particle suspensions with implicit lubrication model. *Computers & Fluids*, *236*, 105278. https://doi.org/10.1016/j.compfluid.2021.105278

Huang, W.-X., Shin, S. J., & Sung, H. J. (2007). Simulation of flexible filaments in a uniform flow by the immersed boundary method. *Journal of Computational Physics*, *226*(2), 2206–2228. https://doi.org/10.1016/j.jcp.2007.07.002

Ii, S., Sugiyama, K., Takeuchi, S., Takagi, S., Matsumoto, Y., & Xiao, F. (2012). An interface capturing method with a continuous function: The THINC method with multi-dimensional reconstruction. *Journal of Computational Physics*, *231*(5), 2328–2358. https://doi.org/10.1016/j.jcp.2011.11.038

Ireland, P. J., Bragg, A. D., & Collins, L. R. (2016). The effect of Reynolds number on inertial particle dynamics in isotropic turbulence. Part 1. Simulations without gravitational effects. *Journal of Fluid Mechanics*, *796*, 617–658. https://doi.org/10.1017/jfm.2016.238

Ito, S., Rajabi, H., & Gorb, S. N. (2023). A ballistic pollen dispersal strategy based on stylar oscillation of *Hypochaeris radicata* (Asteraceae). *Journal of Experimental Biology*, *226*(6), jeb244258. https://doi.org/10.1242/jeb.244258

Jackiw, I. M., & Ashgriz, N. (2021). On aerodynamic droplet breakup. *Journal of Fluid Mechanics*, *913*, A33. https://doi.org/10.1017/jfm.2021.7

Jähne, B., & Haußecker, H. (1998). Air-water gas exchange. *Annu. Rev. Fluid Mech.*, *30*(1), 443–468.

Kajishima, T., Takiguchi, S., Hamasaki, H., & Miyake, Y. (2001). Turbulence Structure of Particle-Laden Flow in a Vertical Plane Channel Due to Vortex Shedding. *JSME Int. J. B-Fluid T.*, *44*(4), 526–535. https://doi.org/10.1299/jsmeb.44.526

Kaneda, Y., & Morishita, K. (2012). Small-scale statistics and structure of turbulence – in the light of high resolution direct numerical simulation. In P. A. Davidson, Y. Kaneda, & K. R. Sreenivasan (Eds.), *Ten chapters in turbulence* (pp. 1–42). Cambridge University Press. https://doi.org/10.1017/CBO9781139032810.002

Karsa, D. (1999). *Industrial applications of surfactants iv*. Elsevier.

Kelly, J., & Kazimi, M. (1982). Interfacial exchange relations for two-fluid vapor-liquid flow: A simplified regime-map approach. *Nucl. Sci. Eng.*, *81*(3), 305–318.

Kim, J., & Moin, P. (1985). Application of a fractional-step method to incompressible Navier-Stokes equations. *Journal of Computational Physics*, *59*(2), 308–323. https://doi.org/10.1016/0021-9991(85)90148-2

Kolmogorov, A. (1949). On the breakage of drops in a turbulent flow. *Dokl. Akad. Navk. SSSR*, *66*, 825–828.

Kolmogorov, A. N. (1941a). Dissipation of Energy in the Locally Isotropic Turbulence. *Proceedings: Mathematical and Physical Sciences*, *434*(1890,), 15–17.

Kolmogorov, A. N. (1941b). The local structure of turbulence in incompressible viscous fluid for very large reynolds numbers. *Cr Acad. Sci. URSS*, *30*, 301–305.

Kooij, S., Sijs, R., Denn, M. M., Villermaux, E., & Bonn, D. (2018). What Determines the Drop Size in Sprays? *Physical Review X*, *8*(3), 031019. https://doi.org/10.1103/PhysRevX.8.031019

Korteweg, D. (1901). Sur la forme que prennent les equations du mouvements des fluides si l'on tient compte des forces capillaires causées par des variations de densité considérables mais continues et sur la théorie de la capillarité dans l'hypothèse d'une variation continue de la densité. *Archives Néerlandaises des Sciences Exactes et Naturelles*, *6*, 1–24.

Koshy, A., Das, T., & Kumar, R. (1988). Effect of surfactants on drop breakage in turbulent liquid dispersions. *Chem. Eng. Sci.*, *43*(3), 649–654.

Kralova, I., & Sjöblom, J. (2009). Surfactants used in food industry: A review. *J. Disper. Sci. Technol.*, *30*(9), 1363–1383.

Li, J., Renardy, Y., & Renardy, M. (2000). Numerical simulation of breakup of a viscous drop in simple shear flow through a volume-of-fluid method. *Phys. Fluids*, *12*(2), 269–282.

Libin, A., & Sivashinsky, G. (1990). Long wavelength instability of the ABC-flows. *Quarterly of Applied Mathematics*, *48*(4), 611–623. https://doi.org/10.1090/qam/1079909

Lorenz, E. N. (1993). *The essence of chaos*. UCL Press.

Lu, J., Muradoglu, M., & Tryggvason, G. (2017). Effect of insoluble surfactant on turbulent bubbly flows in vertical channels. *Int. J. Multiphas. Flow*, *95*, 135–143.

Lu, J., & Tryggvason, G. (2008). Effect of bubble deformability in turbulent bubbly upflow in a vertical channel. *Phys. Fluids*, *20*(4).

Lucci, F., Ferrante, A., & Elghobashi, S. (2010). Modulation of isotropic turbulence by particles of Taylor length-scale size. *Journal of Fluid Mechanics*, *650*, 5–55. https://doi.org/10.1017/S0022112009994022

Luo, H., & Svendsen, H. (1996). Theoretical Model for Drop and Bubble Breakup in Turbulent Dispersions. *AIChE J.*, *42*(5), 1225–1233.

Maroudas-Sacks, Y., Garion, L., Shani-Zerbib, L., Livshits, A., Braun, E., & Keren, K. (2021). Topological defects in the nematic order of actin fibres as organization centres of Hydra morphogenesis. *Nature Physics*, *17*(2), 251–259. https://doi.org/10.1038/s41567-020-01083-1

Martínez-Bazán, C., Rodríguez-Rodrìguez, J., Deane, G., Montañes, J., & Lasheras, J. (2010). Considerations on bubble fragmentation models. *J. Fluid Mech.*, *661*, 159–177.

Massey, W. S. (1997). *A basic course in algebraic topology* (Corr. 3rd print). Springer.

Mazzino, A., & Rosti, M. (2021). Unraveling the secrets of turbulence in a fluid puff. *Phys. Rev. Lett.*, *127*(9), 094501.

Mendoza, R., Thornton, K., Savin, I., & Voorhees, P. W. (2006). The evolution of interfacial topology during coarsening. *Acta Materialia*, *54*(3), 743–750. https://doi.org/10.1016/j.actamat.2005.10.010

Mercado, J., Gomez, D., Van Gils, D., Sun, C., & Lohse, D. (2010). On bubble clustering and energy spectra in pseudo-turbulence. *J. Fluid Mech.*, *650*, 287–306.

Merlivat, L., & Memery, L. (1983). Gas exchange across an air-water interface: Experimental results and modeling of bubble contribution to transfer. *J. Geophys. Res.-Oceans*, *88*(C1), 707–724.

Monchaux, R. (2012). Measuring concentration with Voronoï diagrams: The study of possible biases. *New Journal of Physics*, *14*(9), 095013. https://doi.org/10.1088/1367-2630/14/9/095013

Monti, A., Rathee, V., Shen, A. Q., & Rosti, M. E. (2021). A fast and efficient tool to study the rheology of dense suspensions. *Phys. Fluids*, *33*(10), 103314. https://doi.org/10.1063/5.0065655

Mugele, R., & Evans, H. (1951). Droplet size distribution in sprays. *Ind. Eng. Chem. Res.*, *43*(6), 1317–1324.

Mukherjee, S., Safdari, A., Shardt, O., Kenjereš, S., & Van den Akker, H. (2019). Droplet–turbulence interactions and quasi-equilibrium dynamics in turbulent emulsions. *J. Fluid Mech.*, *878*, 221–276.

Mukherjee, S., Murugan, S. D., Mukherjee, R., & Ray, S. S. (2023). Turbulent flows are not uniformly multifractal. https://doi.org/10.48550/arXiv.2307.06074

Muradoglu, M., & Tryggvason, G. (2008). A front-tracking method for computation of interfacial flows with soluble surfactants. *J. Comput. Phys.*, *227*, 2238–2262.

Muradoglu, M., & Tryggvason, G. (2014). Simulations of soluble surfactants in 3d multiphase flow. *J. Comput. Phys.*, *274*, 737–757.

Musacchio, S., & Boffetta, G. (2014). Turbulent channel without boundaries: The periodic Kolmogorov flow. *Physical Review E*, *89*(2), 023004. https://doi.org/10.1103/PhysRevE.89.023004

Newman, W., & Sproull, R. (1979). *Principles of interactive computer graphics*. McGraw-Hill, Inc.

Oka, S., & Goto, S. (2022). Attenuation of turbulence in a periodic cube by finite-size spherical solid particles. *Journal of Fluid Mechanics*, *949*, A45. https://doi.org/10.1017/jfm.2022.787

Olivieri, S., Brandt, L., Rosti, M. E., & Mazzino, A. (2020). Dispersed Fibers Change the Classical Energy Budget of Turbulence via Nonlocal Transfer. *Physical Review Letters*, *125*(11), 114501. https://doi.org/10.1103/PhysRevLett.125.114501

Olivieri, S., Cannon, I., & Rosti, M. E. (2022). The effect of particle anisotropy on the modulation of turbulent flows. *Journal of Fluid Mechanics*, *950*, R2. https://doi.org/10.1017/jfm.2022.832

Olivieri, S., Mazzino, A., & Rosti, M. E. (2022). On the fully coupled dynamics of flexible fibres dispersed in modulated turbulence. *Journal of Fluid Mechanics*, *946*, A34. https://doi.org/10.1017/jfm.2022.611

Onofre Ramos, M. M., Zhao, S., Bouali, Z., & Mura, A. (2022). DNS analysis of turbulent vaporizing two-phase flows, Part I: Topology of the velocity field. *International Journal of Multiphase Flow*, *156*, 104208. https://doi.org/10.1016/j.ijmultiphaseflow.2022.104208

Pan, D., Phan-Thien, N., & Khoo, B. C. (2014). Dissipative particle dynamics simulation of droplet suspension in shear flow at low Capillary number. *Journal of Non-Newtonian Fluid Mechanics*, *212*, 63–72. https://doi.org/10.1016/j.jnnfm.2014.08.011

Pandey, V., Ramadugu, R., & Perlekar, P. (2020). Liquid velocity fluctuations and energy spectra in three-dimensional buoyancy-driven bubbly flows. *J. Fluid Mech.*, *884*, R6.

Paschkewitz, J. S., Dubief, Y., Dimitropoulos, C. D., Shaqfeh, E. S. G., & Moin, P. (2004). Numerical simulation of turbulent drag reduction using rigid fibres. *Journal of Fluid Mechanics*, *518*, 281–317. https://doi.org/10.1017/S0022112004001144

Paul, I., Fraga, B., Dodd, M. S., & Lai, C. C. K. (2022a). The role of breakup and coalescence in fine-scale bubble-induced turbulence. I. Dynamics. *Physics of Fluids*, *34*(8), 083321. https://doi.org/10.1063/5.0094573

Paul, I., Fraga, B., Dodd, M. S., & Lai, C. C. K. (2022b). The role of breakup and coalescence in fine-scale bubble-induced turbulence. II. Kinematics. *Physics of Fluids*, *34*(8), 083322. https://doi.org/10.1063/5.0100334

Pawar, Y., & Stebe, J. (1996). Marangoni effects on drop deformation in an extensional flow: The role of surfactant physical chemistry. I. Insoluble surfactants. *Phys. Fluids*, *8*(7), 1738–1751.

Peng, C., Sun, Q., & Wang, L.-P. (2023). Parameterization of turbulence modulation by finite-size solid particles in forced homogeneous isotropic turbulence. *Journal of Fluid Mechanics*, *963*, A6. https://doi.org/10.1017/jfm.2023.317

Pereira, R., Ashton, I., Sabbaghzadeh, B., Shutler, J., & Upstill-Goddard, R. (2018). Reduced air-sea CO_2 exchange in the Atlantic Ocean due to biological surfactants. *Nat. Geosci.*, *11*, 492–496.

Perlekar, P., Biferale, L., Sbragaglia, M., Srivastava, S., & Toschi, F. (2012). Droplet size distribution in homogeneous isotropic turbulence. *Phys. Fluids*, *065101*, 1–10.

Perlekar, P. (2019). Kinetic energy spectra and flux in turbulent phase-separating symmetric binary-fluid mixtures. *Journal of Fluid Mechanics*, *873*, 459–474. https://doi.org/10.1017/jfm.2019.425

Perry, A., & Chong, M. (1987). A description of eddying motions and flow patterns using critical-point concepts. *Annu. Rev. Fluid Mech, 19*(1), 125–155.

Podvigina, O., & Pouquet, A. (1994a). On the non-linear stability of the 1:1:1 ABC flow. *Physica D: Nonlinear Phenomena*, *75*(4), 471–508. https://doi.org/10.1016/0167-2789(94)00031-X

Podvigina, O., & Pouquet, A. (1994b). On the non-linear stability of the 1:1:1 ABC flow. *Phys. D: Nonlinear Phenom.*, *75*(4), 471–508. https://doi.org/10.1016/0167-2789(94)00031-X

Poincaré, H. (1892). *Les méthodes nouvelles de la mécanique céleste.*

Pope, S. B. (2000). *Turbulent Flows*. Cambridge University Press. https://www.cambridge.org/core/product/identifier/9780511840531/type/book

Popinet, S. (2018). Numerical Models of Surface Tension. *Annual Review of Fluid Mechanics*, *50*(1), 49–75. https://doi.org/10.1146/annurev-fluid-122316-045034

Prakash, V., Mercado, J., van Wijngaarden, L., Mancilla, E., Tagawa, Y., Lohse, D., & Sun, C. (2016). Energy spectra in turbulent bubbly flows. *J. Fluid Mech.*, *791*, 174–190.

Prosperetti, A., & Tryggvason, G. (2009). *Computational methods for multiphase flow*. Cambridge Press.

Qazi, M. J., Schlegel, S. J., Backus, E. H., Bonn, M., Bonn, D., & Shahidzadeh, N. (2020). Dynamic Surface Tension of Surfactants in the Presence of High Salt Concentrations. *Langmuir*, *36*(27), 7956–7964. https://doi.org/10.1021/acs.langmuir.0c01211

Qi, Y., Tan, S., Corbitt, N., Urbanik, C., Salibindla, A. K. R., & Ni, R. (2022). Fragmentation in turbulence by small eddies. *Nature Communications*, *13*(1), 469. https://doi.org/10.1038/s41467-022-28092-3

Rallison, J. M. (1981). A numerical study of the deformation and burst of a viscous drop in general shear flows. *Journal of Fluid Mechanics*, *109*, 465–482. https://doi.org/10.1017/S002211208100116X

Rayleigh, J. W. S. B. (1878). On The Instability Of Jets. *Proceedings of the London Mathematical Society*, *s1-10*(1), 4–13. https://doi.org/10.1112/plms/s1-10.1.4

Richardson, L. F., & Proctor, D. (1927). Diffusion over distances ranging from 3 km. to 86 km. *Quarterly Journal of the Royal Meteorological Society*, *53*(222), 149–151. https://doi.org/10.1002/qj.49705322205

Richardson, L. F. (1922). *Weather Prediction by Numerical Process*. Cambridge University Press.

Rivière, A., Mostert, W., Perrard, S., Deike, L., Daniel Ruth, Princeton University, & Luc Deike, Princeton University. (2021). Sub-Hinze scale bubble production in turbulent bubble break-up. *Journal of Fluid Mechanics*, *917*. https://doi.org/10.1017/jfm.2021.243

Roghair, I., Mercado, J., Annaland, M., Kuipers, H., Sun, C., & Lohse, D. (2011). Energy spectra and bubble velocity distributions in pseudo-turbulence: Numerical simulations vs. experiments. *Int. J. Multiphas. Flow*, *37*(9), 1093–1098.

Rosti, M., De Vita, F., & Brandt, L. (2019). Numerical simulations of emulsions in shear flows. *Acta Mech.*, *230*, 667–682.

Rosti, M., Ge, Z., Jain, S., Dodd, M., & Brandt, L. (2019). Droplets in homogeneous shear turbulence. *J. Fluid Mech.*, *876*, 962–984.

Rosti, M., Perlekar, P., & Mitra, D. (2023). Large is different: Nonmonotonic behavior of elastic range scaling in polymeric turbulence at large Reynolds and Deborah numbers. *Sci. Adv.*, *9*(11), eadd3831.

Rosti, M., & Takagi, S. (2021). Shear-thinning and shear-thickening emulsions in shear flows. *Phys. Fluids*, *33*(8), 083319.

Russo, G., & Smereka, P. (2000). A remark on computing distance functions. *J. Computational Phys.*, *163*(1), 51–67.

Saramito, P. (2007). A new constitutive equation for elastoviscoplastic fluid flows. *Journal of Non-Newtonian Fluid Mechanics*, *145*(1), 1–14. https://doi.org/10.1016/j.jnnfm.2007.04.004

Scapin, N., Costa, P., & Brandt, L. (2020). A volume-of-fluid method for interface-resolved simulations of phase-changing two-fluid flows. *J. Comput. Phys.*, *407*, 109251.

Schramm, L., Stasiuk, E., & Marangoni, D. (2003). Surfactants and their applications. *Annu. Rep. Prog. Chem., Sect. C: Phys. Chem.*, *99*, 3–48.

Sengupta, A., Carrara, F., & Stocker, R. (2017). Phytoplankton can actively diversify their migration strategy in response to turbulent cues. *Nature*, *543*(7646), 555–558. https://doi.org/10.1038/nature21415

Shaik, S., & Van Hout, R. (2023). Kinematics of rigid fibers in a turbulent channel flow. *International Journal of Multiphase Flow*, *158*, 104262. https://doi.org/10.1016/j.ijmultiphaseflow.2022.104262

Shapira, M., & Haber, S. (1990). Low Reynolds number motion of a droplet in shear flow including wall effects. *Int. J. Multiphas. Flow*, *16*(2), 305–321.

Shen, J., Peng, C., Wu, J., Chong, K. L., Lu, Z., & Wang, L.-P. (2022). Turbulence modulation by finite-size particles of different diameters and particle–fluid density ratios in homogeneous isotropic turbulence. *Journal of Turbulence*, *23*(8), 433–453. https://doi.org/10.1080/14685248.2022.2096223

Shen, L., Yue, D. K. P., & Triantafyllou, G. S. (2004). Effect of surfactants on free-surface turbulent flows. *Journal of Fluid Mechanics*, *506*, 79–115. https://doi.org/10.1017/S0022112004008481

Sjoblom, J. (2005). *Emulsions and emulsion stability: Surfactant science series/61* (Vol. 132). CRC Press.

Skartlien, R., Sollum, E., & Schumann, H. (2013). Droplet size distributions in turbulent emulsions: Breakup criteria and surfactant effects from direct numerical simulations. *J. Chem. Phys.*, *139*(17).

Snook, B., Guazzelli, E., & Butler, J. E. (2012). Vorticity alignment of rigid fibers in an oscillatory shear flow: Role of confinement. *Physics of Fluids*, *24*(12), 121702. https://doi.org/10.1063/1.4770141

Soligo, G., Roccon, A., & Soldati, A. (2019a). Breakage, coalescence and size distribution of surfactant-laden droplets in turbulent flow. *J. Fluid Mech.*, *881*, 244–282.

Soligo, G., Roccon, A., & Soldati, A. (2019b). Coalescence of surfactant-laden drops by Phase Field Method. *J. Comput. Phys.*, *376*, 1292–1311.

Soligo, G., Roccon, A., & Soldati, A. (2020a). Deformation of clean and surfactant-laden droplets in shear flow. *Meccanica*, *55*, 371–386.

Soligo, G., Roccon, A., & Soldati, A. (2020b). Effect of surfactant-laden droplets on turbulent flow topology. *Phys. Rev. F.*, *5*(7), 073606.

Soligo, G., Roccon, A., & Soldati, A. (2021). Turbulent flows with drops and bubbles: What numerical simulations can tell us—Freeman Scholar Lecture. *J. Fluids Eng.*, *143*(8).

Syawitri, T. P., Yao, Y. F., Chandra, B., & Yao, J. (2021). Comparison study of URANS and hybrid RANS-LES models on predicting vertical axis wind turbine performance at low, medium and high tip speed ratio ranges. *Renewable Energy*, *168*, 247–269. https://doi.org/10.1016/j.renene.2020.12.045

Takagi, S., & Matsumoto, Y. (2011). Surfactant effects on bubble motion and bubbly flows. *Annu. Rev. Fluid Mech.*, *43*, 615–636.

Takagi, S., Ogasawara, T., Fukuta, M., & Matsumoto, Y. (2009). Surfactant effect on the bubble motions and bubbly flow structures in a vertical channel. *Fluid Dyn. Res.*, *41*(6), 065003.

Takagi, S., Ogasawara, T., & Matsumoto, Y. (2008). The effects of surfactant on the multiscale structure of bubbly flows. *Phil. Trans. R. Soc. A*, *366*(1873), 2117–2129.

Taylor, G. I. (1935). Statistical Theory of Turbulence. *Proceedings of the Royal Society of London. Series A, Mathematical and Physical Sciences*, *151*(873), 421–444. https://doi.org/10.1098/rspa.1935.0158

Taylor, G. (1934). The formation of emulsions in definable fields of flows. *Proc. Royal Soc. A*, *146*, 501–523.

Tay-Wo-Chong, L. (2012). *Numerical Simulation of the Dynamics of Turbulent Swirling Flames* (Doctoral dissertation).

Ten Cate, A., Derksen, J. J., Portela, L. M., & van Den Akker, H. E. a. (2004). Fully resolved simulations of colliding monodisperse spheres in forced isotropic turbulence. *J. Fluid Mech.*, *519*, 233–271. https://doi.org/10.1017/S0022112004001326

Tryggvason, G., Dabiri, S., Aboulhasanzadeh, B., & Lu, J. (2013). Multiscale considerations in direct numerical simulations of multiphase flows. *Phys. Fluids*, *25*(3).

Tryggvason, G., Thomas, S., Lu, J., & Aboulhasanzadeh, B. (2010). Multiscale issues in dns of multiphase flows. *Acta Math. Sci.*, *30*(2), 551–562.

Tryggvason, G., & Lu, J. (2015). Direct numerical simulations of bubbly flows. *Mechanical Engineering Reviews*, *2*(2), 15-00220-15–00220. https://doi.org/10.1299/mer.15-00220

Tsuji, Y., Kawaguchi, T., & Tanaka, T. (1993). Discrete particle simulation of two-dimensional fluidized bed. *Powder Technol.*, *77*(1), 79–87. https://doi.org/10.1016/0032-5910(93)85010-7

Tsuji, Y., & Morikawa, Y. (1982). LDV measurements of an air—solid two-phase flow in a horizontal pipe. *J. Fluid Mech.*, *120*, 385–409. https://doi.org/10.1017/S002211208200281X

Uhlenbeck, G., & Ornstein, L. S. (1930). On the theory of the brownian motion. *Phys. Rev.*, *36*(5), 823–841. https://doi.org/10.1103/PhysRev.36.823

Uhlmann, M., & Chouippe, A. (2017). Clustering and preferential concentration of finite-size particles in forced homogeneous-isotropic turbulence. *J. Fluid Mech.*, *812*, 991–1023. https://doi.org/10.1017/jfm.2016.826

Vela-Martín, A., & Avila, M. (2022). Memoryless drop breakup in turbulence. *Science Advances*, *8*(50), eabp9561. https://doi.org/10.1126/sciadv.abp9561

Verschoof, R., Van Der Veen, R., Sun, C., & Lohse, D. (2016). Bubble drag reduction requires large bubbles. *Phys. Rev. Lett*, *117*(10), 104502.

Villermaux, E., & Bossa, B. (2009). Single-drop fragmentation determines size distribution of raindrops. *Nature Physics*, *5*(9), 697–702. https://doi.org/10.1038/nphys1340

Voth, G. A., & Soldati, A. (2017). Anisotropic Particles in Turbulence. *Annual Review of Fluid Mechanics*, *49*(1), 249–276. https://doi.org/10.1146/annurev-fluid-010816-060135

Wadell, H. (1932). Volume, Shape, and Roundness of Rock Particles. *The Journal of Geology*, *40*(5), 443–451. https://doi.org/10.1086/623964

Wadell, H. (1935). Volume, Shape, and Roundness of Quartz Particles. *The Journal of Geology*, *43*(3), 250–280. https://doi.org/10.1086/624298

Westerweel, J., Elsinga, G. E., & Adrian, R. J. (2013). Particle Image Velocimetry for Complex and Turbulent Flows. *Annual Review of Fluid Mechanics*, *45*(1), 409–436. https://doi.org/10.1146/annurev-fluid-120710-101204

Wilcox, D. C. (2006). *Turbulence Modeling for CFD* (3rd edition). D C W Industries.

Xiao, F., Dianat, M., & McGuirk, J. (2014). Les of turbulent liquid jet primary breakup in turbulent coaxial air flow. *Int. J. Multiphas. Flow*, *60*, 103–118.

Yotter, R. A., Dahnke, R., Thompson, P. M., & Gaser, C. (2011). Topological correction of brain surface meshes using spherical harmonics. *Human Brain Mapping*, *32*(7), 1109–1124. https://doi.org/10.1002/hbm.21095

Yousefi, A., Ardekani, M. N., & Brandt, L. (2020). Modulation of turbulence by finite-size particles in statistically steady-state homogeneous shear turbulence. *Journal of Fluid Mechanics*, *899*, A19. https://doi.org/10.1017/jfm.2020.457

Yu, Z. (2005). A DLM/FD method for fluid/flexible-body interactions. *Journal of Computational Physics*, *207*(1), 1–27. https://doi.org/10.1016/j.jcp.2004.12.026

Yun, A., Li, Y., & Kim, J. (2014). A new phase-field model for a water-oil-surfactant system. *Appl. Math. Comput.*, *229*, 422–432.

Zhao, L. H., Andersson, H. I., & Gillissen, J. J. J. (2010). Turbulence modulation and drag reduction by spherical particles. *Physics of Fluids*, *22*(8), 081702. https://doi.org/10.1063/1.3478308

Zhao, L., Challabotla, N. R., Andersson, H. I., & Variano, E. A. (2015). Rotation of Nonspherical Particles in Turbulent Channel Flow. *Physical Review Letters*, *115*(24), 244501. https://doi.org/10.1103/PhysRevLett.115.244501

Appendix A

Chapter 1 appendix

Physics of Fluids ARTICLE scitation.org/journal/phf

The effect of droplet coalescence on drag in turbulent channel flows

Cite as: Phys. Fluids **33**, 085112 (2021); doi: 10.1063/5.0058632
Submitted: 1 June 2021 · Accepted: 17 July 2021 ·
Published Online: 4 August 2021

Ianto Cannon,[1] Daulet Izbassarov,[2] Outi Tammisola,[3] Luca Brandt,[3] and Marco E. Rosti[1,a)]

AFFILIATIONS

[1]Complex Fluids and Flows Unit, Okinawa Institute of Science and Technology Graduate University, 1919-1 Tancha, Onna-son, Okinawa 904-0495, Japan

[2]Department of Mechanical Engineering, Aalto University, FI-00076 Aalto, Finland

[3]KTH Department of Engineering Mechanics, Linné Flow Centre and SeRC (Swedish e-Science Research Centre), SE 100 44 Stockholm, Sweden

[a)]Author to whom correspondence should be addressed: marco.rosti@oist.jp

ABSTRACT

We study the effect of droplet coalescence on turbulent wall-bounded flows by means of direct numerical simulations. In particular, the volume-of-fluid and front-tracking methods are used to simulate turbulent channel flows containing coalescing and non-coalescing droplets, respectively. We find that coalescing droplets have a negligible effect on the drag, whereas the non-coalescing ones steadily increase drag as the volume fraction of the dispersed phase increases: indeed, at 10% volume fraction, the non-coalescing droplets show a 30% increase in drag, whereas the coalescing droplets show less than 4% increase. We explain this by looking at the wall-normal location of droplets in the channel and show that non-coalescing droplets enter the viscous sublayer, generating an interfacial shear stress, which reduces the budget for viscous stress in the channel. On the other hand, coalescing droplets migrate toward the bulk of the channel forming large aggregates, which hardly affect the viscous shear stress while damping the Reynolds shear stress. We prove this by relating the mean viscous shear stress integrated in the wall-normal direction to the centerline velocity.

I. INTRODUCTION

Two-fluid turbulent flows are found in many cases in industry and nature (Balachandar and Eaton, 2010), such as human arteries, industrial pipelines, and the injection of bubbles to enable drag reduction in ships (Ceccio, 2010). In all of these cases, surfactants are known to have dramatic effects on the flow, often by preventing coalescence (Takagi and Matsumoto, 2011). However, due to the multi-scale nature of the problems, the mechanisms by which coalescence affects drag are not fully known and understood yet. Thus, the objective of this work is to explain how coalescence affects drag in wall-bounded flows.

Many experimental studies of surfactants in multiphase flow have been made. Frumkin and Levich (1947) were the first to describe the mechanism by which the rising speed of bubbles in water is reduced by surfactants (see Levich, 1962 for English version). Descamps *et al.* (2008) measured the wall shear stress in pipe flows of air bubbles in water and found that larger bubbles produced less drag. Duineveld (1997) studied pairs of bubbles rising in a vertical channel; he showed that coalescence is prevented when the surfactant concentration is above a critical value. As well as preventing coalescence, surfactants produce other effects on bubbles, such as clustering (Takagi *et al.*, 2008), reduction in rising velocity (Frumkin and Levich, 1947; Levich, 1962), and reduction in shear-induced lift forces (Takagi and Matsumoto, 2011). Since all these effects can happen at the same time, the effect of different coalescence rates is difficult to highlight; on the other hand, simulations allow us to eliminate these effects and solely focus on the impact of coalescence.

The majority of numerical multiphase flow studies have been made using interface-tracking methods, such as the front-tracking (FT) method (Unverdi and Tryggvason, 1992). Front-tracking simulations of homogeneous-isotropic flows (Druzhinin and Elghobashi, 1998) are well suited for investigating the effect of droplet size on the turbulent length scales, such as bubble arrays (Esmaeeli and Tryggvason, 1998, 1999) or channel flows (Lu *et al.*, 2006; Dabiri *et al.*, 2013; Tryggvason and Lu, 2015; Tryggvason *et al.*, 2016; Lu *et al.*, 2017; Ahmed *et al.*, 2020). An advantage of shear flow and

channel-flow simulations is the ability to measure the effective viscosity and flow rate, which can then be compared with experiments. In the case of interface-tracking simulations of channel flows, Lu *et al.* (2006) simulated laminar bubbly upflows and downflows, Dabiri *et al.* (2013) showed that more deformable bubbles produced lower drag, Lu *et al.* (2017) modeled bubbles with insoluble surfactant, and Ahmed *et al.* (2020) with soluble surfactant showed their main effects. However, none of the interface-tracking studies cited here includes a model for the breakup or coalescence of droplets, with only a few recent works tackling these phenomena (Lu and Tryggvason, 2018, 2019).

Interface-capturing methods, such as the volume-of-fluid (VOF) method (Noh and Woodward, 1976), naturally allow coalescence and breakup of droplets (Elghobashi, 2019). Interface-capturing simulations of homogenous isotropic turbulence (Dodd and Ferrante, 2016; Perlekar *et al.*, 2012; Komrakova *et al.*, 2015; Bolotnov, 2013) and shear flows (De Vita *et al.*, 2019; Rosti *et al.*, 2019) have shed some light on the effect of coalescence on turbulence. Notably, Dodd and Ferrante (2016) and Maxey (2017) showed that coalescence is a source of turbulent kinetic energy, while breakup is a sink. Scarbolo *et al.* (2015) investigated the effect of Weber number on breakup and coalescence, Soligo *et al.* (2019) modeled surfactant laden drops in turbulent channel flows, while Bolotnov *et al.* (2011) used the level-set method to simulate bubbly channel flows. Roccon *et al.* (2017) investigated the coalescence and breakup of large droplets in the channel flow using the phase field method. Interface capturing methods are known to over-predict coalescence rates, because numerical coalescence occurs whenever the film thickness is less than the numerical grid spacing. In contrast, in real fluids film rupture occurs at molecular length-scales, which are in the tens of nanometers, orders of magnitude smaller than the Kolmogorov length (Tryggvason *et al.*, 2013; Soligo *et al.*, 2019). A number of methods have been used to reduce the coalescence rate of interface capturing methods, such as adaptive grid refinement (Innocenti *et al.*, 2021), film drainage models (Thomas *et al.*, 2010), coupling to molecular dynamics simulations (Chen *et al.*, 2004), and artificial forces (De Vita *et al.*, 2019).

In this paper, we use the front-tracking method to make simulations of droplets, which cannot break up or coalesce, and we use the volume-of-fluid method to make simulations of droplets that easily break up and coalesce. As we are interested in the effects of coalescence, we do not use any methods to reduce the volume-of-fluid coalescence rate. The two methods give idealized models of a mixture saturated with surfactants (FT), and completely clean mixture (VOF). Aside from coalescence and breakup, the physical properties (surface tension, viscosity, density, etc.) of the fluids in the two methods are identical. To the authors' knowledge, this is the first direct comparison of coalescing and non-coalescing droplets in a turbulent channel flow.

The manuscript is organized as follows. First, in Sec. II, we describe the mathematical model governing the problem at hand and the numerical techniques used to numerically solve them. In particular, we describe our chosen interface-tracking and interface-capturing methods in more detail. Section III reports the values of the parameters explored in our simulations. In Sec. IV, we present statistics of the flow to elucidate how coalescence is affecting drag in the channel. Finally, Sec. V gives conclusions and places them in the context of the current literature.

II. GOVERNING EQUATIONS AND FLOW GEOMETRY

We consider turbulent channel flows, such as those shown in Fig. 1. The numerical domain has size $L_x \times L_y \times L_z = 6L \times 2L \times 3L$, where L is the half-height of the channel. The flow is laden with an ensemble of N droplets, initially spherical with radius $R = L/8$ and randomly arranged. We impose periodic boundary conditions in the streamwise (x) and spanwise (z) directions, while the non-slip and non-penetration boundary conditions are enforced at the two walls $y = 0$ and $y = 2L$. An imposed pressure gradient G, uniform throughout the domain and constant in time, sustains the flow in the x direction. Balancing the forces on the fluid in the x direction, we obtain an expression for the shear stress τ at the wall, $\tau_w \equiv \langle \tau|_{y=0} \rangle_{xz} = GL$, showing that τ_w remains constant in time. Note that, here and in the rest of the manuscript, we use angled brackets to represent an average over the subscripted directions.

The Cartesian components of the fluid velocity field $(u_1, u_2, u_3) \equiv (u, v, w)$ are found by solving the incompressible multiphase Navier–Stokes equations at each location $\boldsymbol{x}$,

$$(\rho u_i)_{,t} + (\rho u_i u_j)_{,j} = (\mu u_{i,j} + \mu u_{j,i})_{,j} - p_{,i} + G\,\delta_{i1} + \gamma \kappa n_i\, \delta_S(\boldsymbol{x}), \quad (1)$$

$$u_{i,i} = 0, \quad (2)$$

where $i, j \in \{1, 2, 3\}$. Throughout this article, we use Einstein notation (Einstein, 1916) where repeated indices are summed over, and the subscript comma denotes partial differentiation, i.e., $\mathscr{F}_{,i} \equiv \frac{\partial \mathscr{F}}{\partial x_i}$. The scalar p is the pressure field used to enforce the incompressibility constraint stated in Eq. (2). The density ρ and dynamic viscosity μ are the local weighted averages among the two phases, i.e., $\rho = \phi\rho_d + (1-\phi)\rho_c$ and $\mu = \phi\mu_d + (1-\phi)\mu_c$, where subscripts $_d$ and $_c$ denote properties of the dispersed and continuum phases, respectively. In the above, ϕ represents the volume fraction of the dispersed phase in each computational cell of the domain, with $\phi = 1$ in the dispersed

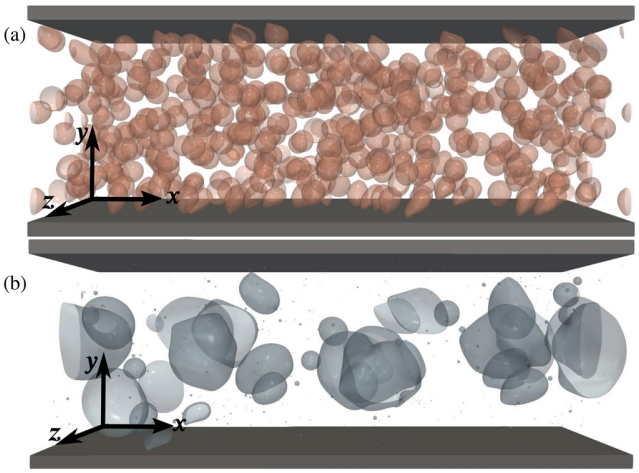

FIG. 1. A snapshot of the simulation domain for a 10% suspension of droplets simulated with (a) the front-tracking method (run FT10a in Table I), and with (b) the volume-of-fluid method (run VOF10a). The orange and blue surfaces show the interface between fluid phases. The droplets in (b) can breakup and coalesce, giving rise to a range of sizes, whereas those in (a) cannot, thus remaining monodisperse.

phase and $\phi = 0$ in the continuum phase. The Kronecker delta δ_{ij} is used to ensure that the pressure gradient is imposed in the x direction. The last term on the right hand side of Eq. (1) is the volumetric formulation of the surface tension (Popinet, 2018); it is the product of the surface tension coefficient γ, the interface local curvature κ, and the unit normal to the interface n_i. Note that we used $\delta_S(\boldsymbol{x})$ in Eq. (1) to represent the surface delta function, which is zero everywhere except for the surface S at the interface between the two phases. $\delta_S(\boldsymbol{x})$ has dimensions of inverse length.

A. Discretization of the Navier–Stokes equations

For simulations of coalescing and non-coalescing droplets, we use near-identical numerical methods to solve the momentum and continuity equations [Eqs. (1) and (2)]. This ensures that any difference in our results is due to the droplets, not the integration scheme.

Equations (1) and (2) are numerically solved using a finite difference method on a fixed Eulerian grid with a staggered arrangement, i.e., fluid velocities are located on the cell faces and all other variables (pressure, density, viscosity, volume-of-fluid, etc.) are located at the cell centers. All the spatial derivatives appearing in the equations are discretized with second-order central differences, except for the convective terms in the FT simulations where the QUICK scheme (Leonard, 1979) is used instead. In the single-phase (SP) and VOF simulations, time integration is performed with the Adams–Bashforth method. In the FT simulations, time integration is performed with a predictor–corrector method, in which the first-order solution (Euler method) serves as a predictor, which is then corrected by the trapezoidal rule (Tryggvason *et al.*, 2001; Farooqi *et al.*, 2019). Both schemes are second order in time. Finally, in regard to the pressure solver, the fractional step technique (Kim and Moin, 1985) presented by Dong and Shen (2012) and Dodd and Ferrante (2014) is adopted, allowing for the direct solution of a constant-coefficient Poisson equation using an FFT-based solver, even in the presence of density differences among the carrier and dispersed phases.

B. Volume-of-fluid method

We use the volume-of-fluid (VOF) method to simulate droplets undergoing topological changes, i.e., coalescence and breakup. This is an Eulerian–Eulerian technique in which the fluid phases are tracked using the local volume fraction scalar field ϕ. Since Noh and Woodward (1976), a number of variants of the VOF method have been developed (Youngs, 1982, 1984; Puckett *et al.*, 1997; Rider and Kothe, 1998; Xiao *et al.*, 2005; Yokoi, 2007). Here, we use the multi-dimensional tangent of hyperbola for the interface capturing (MTHINC) method, developed by Ii *et al.* (2012). In this method, we use a smooth hyperbolic tangent function to approximate the interface

$$H(X,Y,Z) = \frac{1}{2} + \frac{1}{2}\tanh(\beta(P(X,Y,Z) + d)), \tag{3}$$

where β is a parameter controlling the sharpness of the interface and d is a normalization parameter to enforce $\int\int\int H\,dX\,dY\,dZ = \phi$ in each cell. P is a three-dimensional function in the cell, with the same normal and curvature as the interface. Normals are evaluated using the Youngs approach (Youngs, 1982), while the surface tension force appearing in momentum Eq. (1) is computed using the continuum surface force (CSF) approach (Brackbill *et al.*, 1992). See Rosti *et al.* (2019) for a detailed description of the volume-of-fluid code employed in this work, and in several other works (Rosti *et al.*, 2019; De Vita *et al.*, 2019). See Ii *et al.* (2012) and De Vita *et al.* (2020) for validations against numerical benchmarks and experiments.

C. Front-tracking method

We use the front-tracking (FT) method to simulate droplets that can deform, but cannot break up or coalesce. This is an Eulerian–Lagrangian scheme in which the interface between the phases is tracked by a "front," composed of triangular elements. The method was introduced by Unverdi and Tryggvason (1992), with many refinements over the past 30 years (Tryggvason *et al.*, 2001; Tryggvason *et al.*, 2011), including techniques to correct for errors in volume conservation of the phases (Takeuchi and Tryggvason, 2020). The surface tension force acting on the Lth element is a volume integral of the surface tension force from Eq. (1),

$$\begin{aligned}\boldsymbol{F_L} &= \int\int\int_V \gamma\kappa\boldsymbol{n}\,\delta_{A_L}(\boldsymbol{x})\,dV = \int\int_{A_L} \gamma\kappa\boldsymbol{n}\,dA \\ &= \int\int_{A_L} \gamma(\boldsymbol{n}\times\nabla)\times\boldsymbol{n}\,dA = \oint_{s_L} \gamma\boldsymbol{t}\times\boldsymbol{n}\,ds,\end{aligned} \tag{4}$$

where A_L and s_L are the area and perimeter of the Lth element and $\boldsymbol{t}$ is the tangent to the perimeter. The force is then interpolated onto the Eulerian grid by means of a conservative weighting function and used to update the fluid velocity, which, in turn, is used to update the position of the interface. As the interface evolves, the unstructured grid can greatly deform, resulting in a non-uniform grid. Thus, periodical restructuring of the Lagrangian grid is performed to maintain a nearly uniform size, comparable to the Eulerian grid size. See Muradoglu and Tryggvason (2014) for a detailed description and validation of the front-tracking code employed in this work, which used in several other works (Izbassarov and Muradoglu, 2015; Lu *et al.*, 2017; Ahmed *et al.*, 2020). Extensive tests of the front tracking method are shown in Tryggvason *et al.* (2001).

III. SETUP

Due to the different nature of the numerical schemes used to describe the presence of the interface, the numerical domain is discretized on two different sets of grids, both verified to provide grid-independent results. The non-coalescing-droplet simulations use a uniform grid in the homogenous directions and a non-uniform grid in the wall-normal direction, with minimum spacing $\Delta Y_{FT} = 3L \times 10^{-3}$ at the channel wall. The minimum spacing in wall units is $\Delta Y^+_{FT} \equiv u_\tau \Delta Y_{FT}/\nu = 0.5$, where u_τ and ν are defined later in this section. Overall, the grid size for the non-coalescing droplet simulations (FT) is $N_x \times N_y \times N_z = 576 \times 240 \times 288$, which is comparable to that used in Dabiri and Tryggvason (2015), and gives around 24 Eulerian grid points per droplet diameter. Due to periodic restructuring, we also have around 24 Lagrangian grid points per droplet diameter. The single-phase and coalescing-droplet simulations (VOF) use a cubic uniform grid with spacing $\Delta Y^+_{VOF} = 0.8$, and total size $N_x \times N_y \times N_z = 1296 \times 432 \times 648$. This grid has 108 points per initial droplet diameter. We use more grid points in the VOF simulations in order to accurately resolve breakup and coalescence events throughout the domain.

TABLE I. Details of each turbulent channel flow simulation performed in the present study. The first column gives a unique name to each run for ease of reference, and the second describes the colors and markers that are used in the following figures. Input variables are shown in the subsequent columns in the middle, and output statistics are shown in the three rightmost columns.

Run	Marker	Method	Coalescence	Φ (%)	Ca_0	We_τ	N	Re_b	u^+_{cen}	We_b
SP0	—	N/A	N/A	0	N/A	N/A	0	2836	18.38	N/A
FT3a	△	FT	No	2.5	0.10	1.14	110	2813	18.24	279.0
FT3b	=	FT	No	2.5	0.05	0.57	110	2661	17.19	124.8
FT5a	◇	FT	No	5	0.10	1.14	220	2827	18.50	281.8
FT5b	—	FT	No	5	0.05	0.57	220	2602	16.93	119.4
FT10a	⬠	FT	No	10	0.10	1.14	440	2815	18.46	279.4
FT10b	—	FT	No	10	0.05	0.57	440	2524	16.54	112.3
VOF3a	▲	VOF	Yes	2.5	0.10	1.14	110	2803	18.21	277.1
VOF3b	—	VOF	Yes	2.5	0.05	0.57	110	2818	18.15	140.0
VOF5a	◆	VOF	Yes	5	0.10	1.14	220	2764	18.26	269.4
VOF5b	—	VOF	Yes	5	0.05	0.57	220	2778	18.07	136.1
VOF10a	⬟	VOF	Yes	10	0.10	1.14	440	2689	18.31	254.9
VOF10b	—	VOF	Yes	10	0.05	0.57	440	2685	17.78	127.1

The values of the non-dimensional parameters used in the simulations are shown in Table I. We consider a total volume fraction of the dispersed phase in the range $0\% \leq \Phi \leq 10\%$, with the continuum phase being denser and more viscous than the droplet phase, as the density ratio is fixed equal to $\rho_c/\rho_d = 50$ and the dynamic viscosity to $\mu_c/\mu_d = 50$ for all runs. Thus, the kinematic viscosity $\nu \equiv \mu/\rho$ has the ratio $\nu_c/\nu_d = 1$ for all runs. The problem approaches the density and viscosity ratios of air in water ($\rho_{water}/\rho_{air} \approx 830$, $\mu_{water}/\mu_{air} \approx 55$) while still being numerically tractable. The friction Reynolds number $Re_\tau \equiv u_\tau L/\nu$ is set to 180 for all runs, where $u_\tau \equiv \sqrt{\tau_w/\rho_c}$ is the friction velocity. We define the capillary number as $Ca_0 \equiv \mu_c u_0/\gamma$ (where u_0 is the bulk velocity of the single-phase channel flow) for which two values are considered, $Ca_0 = 0.05$ and 0.10. Based on these capillary numbers, the friction Weber number $We_\tau \equiv \rho_c u_\tau^2 L/\gamma$ assumes that values are smaller or larger than unity. Finally, N is the number of droplets at the start of the simulation, which are initially identical spheres in a random arrangement.

The three rightmost columns in Table I report three output statistics: the bulk Reynolds number, $Re_b \equiv u_b L/\nu$, where $u_b \equiv \langle u \rangle_{xyzt}$ is the bulk velocity; the bulk Weber number, $We_b \equiv \rho_c u_b^2 L/\gamma$; and the centerline velocity in plus units $u^+_{cen} \equiv \langle u|_{y=L} \rangle_{xzt}/u_\tau$. In Sec. IV, we present these and other statistics of the channel flows and discuss their implications.

IV. RESULTS

We consider turbulent channel flows, in which droplets can coalesce, and compare the results with a configuration where coalescence is not allowed. The flow is driven by a constant pressure drop; thus, an increase in the flow rate or bulk velocity indicates drag reduction, while its reduction is evidence for drag increase. We start by considering the profile of the streamwise velocity u^+ in the channel, reported in Fig. 2. The single-phase run SP0 shows the typical velocity profile of a turbulent channel flow, with regions of high shear at the walls and a flattened profile in the channel center. The runs with coalescing droplets (VOF) mostly collapse onto the single-phase profile, showing only a slight reduction in u^+ toward the center, whereas the runs with non-coalescing droplets (FT) show a significant reduction in u^+, which becomes more pronounced as Φ increases. Also, in the coalescing droplets runs, variation of the capillary number produces little change in u^+, while in the non-coalescing runs, the change in u^+ with Ca_0 is much more substantial.

This is quantified in the inset of Fig. 2, which shows the bulk velocity in wall units $u_b^+ \equiv \langle u \rangle_{xyzt}/u_\tau$ on the left axis, and the skin-friction coefficient $C_f \equiv 2\tau_w/\rho_c u_b^2$ on the right axis. We see that, relative to the single-phase run, the coalescing droplets produce a

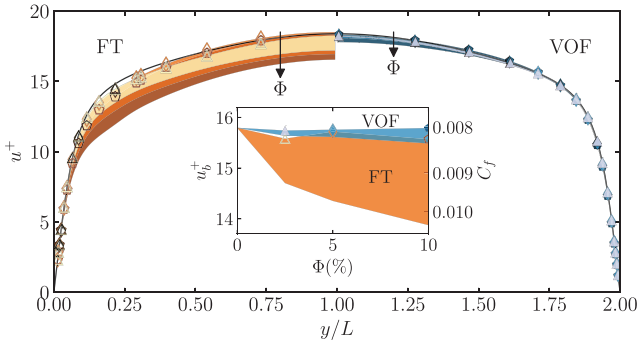

FIG. 2. Main: streamwise velocity profile in wall units u^+, against distance y from the channel wall. The single-phase run (SP0) is shown as a black line. The profiles are symmetric about the centerline ($y = L$), so we have plotted runs with non-coalescing (FT), and coalescing (VOF) droplets on the left and right, respectively. Each $Ca_0 = 0.1$ run is plotted using the marker listed in Table I, while the regions between u^+ for $Ca_0 = 0.1$ and $Ca_0 = 0.05$ are shaded in color. Inset: dependence of bulk velocity u_b^+ on the total volume fraction of droplets Φ. The skin-friction coefficient Cf is shown on the right axis. Runs with coalescing droplets (VOF) are shown in blue, while runs with non-coalescing droplets (FT) are shown in orange. Both plots show that drag increases with Φ and reduces with Ca_0 for all non-coalescing droplet runs, while very limited changes are observable for the coalescing droplet runs.

maximum increase in 4% in *Cf*, whereas the non-coalescing droplets produce a maximum increase in 30%. In the case of non-coalescing droplets, the drag is highly dependent on Ca_0. The high Ca_0 (i.e., more deformable droplets) runs show little change in *Cf*, whereas the low Ca_0 (i.e., less deformable droplets) runs show a 30% increase in *Cf*. Notably similar drag increases have been measured for rigid particles in channel flows by Picano *et al.* (2015) and Rosti and Brandt (2020). Clearly, the coalescence of droplets in the channel has a profound effect on the flow. Throughout this section, we present additional statistics of the flows in order to shed light on the mechanisms of this effect.

Figure 3 shows the velocity profile again, this time on a semi-log scale in wall units $u^+ \equiv u/u_\tau$, and $y^+ \equiv y/\delta_\nu$, where $\delta_\nu \equiv \nu/u_\tau$ is the viscous length scale (Pope, 2000). Away from the wall and the channel center $\delta_\nu \ll y \ll L$, i.e., the length scales affecting the flow are separated, and the single phase flow profile is approximately parallel to a line with constant slope (the dashed line). This is a manifestation of the log-law for turbulent channel flows (von Kármán, 1930), which can be derived by assuming that the quantity $y^+ \frac{du^+}{dy^+}$ has no dependence on y^+ or y/L (complete similarity). The flow profiles with coalescing droplets in Fig. 3 are in excellent agreement with the log-law, suggesting that coalescing droplets do not break the scale separation. However, the flow profiles with non-coalescing droplets are not in such good agreement, because these droplets have constant size R, and $y \sim R$, so scale separation is prevented; hence, $y^+ \frac{du^+}{dy^+}$ shows a dependence on y/R.

To further quantify the effect of coalescence on the flow, we fit a log-law function to each flow profile in the region $30 < y^+ < 100$. Our log law function has the form

$$u^+ = \frac{\ln y^+}{0.41} + 5.89 + \Delta u^+, \tag{5}$$

where 5.89 is the u^+ intercept for run SP0 and Δu^+ is the shift relative to SP0. The inset of Fig. 3 shows how the vertical shift Δu^+ in the log-law region of the channel is affected by the volume fraction Φ and capillary number Ca_0 for the different cases. Again, we see relatively small shifts for simulations with coalescing droplets, and large shifts for simulations with non-coalescing droplets. In particular, Δu^+ grows in magnitude with Φ, especially for the case with $Ca_0 = 0.05$. This reinforces our observations of the bulk streamwise velocity shown in the inset of Fig. 2 that the less-deformable, non-coalescing droplets produce a significant drag increase.

To understand what generates the differences observed for configurations of coalescing and non-coalescing droplets, we focus our attention on the total surface area of the droplets. The total interface area is responsible for the overall surface tension stress and impacts how droplets disperse across the channel. Figure 4 shows how the total interface area at steady state $\langle S \rangle_{xyzt}$ depends on the total volume fraction Φ of the dispersed phase. The figure shows that the non-coalescing droplets of the FT runs exhibit only 1% increase in area, due to deformation from their initial spherical shape. On the other hand, the coalescing droplets of the VOF runs show more than 80% reduction in interface area, as droplets coalesce and grow in size. In particular, when the volume fraction is large, droplets have a higher likelihood of colliding, and hence more coalescence, leading to a smaller value of $\langle S \rangle_{xyzt}/S_0$.

For the coalescing droplets, the interface area $\langle S \rangle_{xyzt}/S_0$ shows no dependence on capillary number, differently from what was observed by Lu and Tryggvason (2018) and Rosti *et al.* (2019), who found that that as Ca_0 decreases, surface tension increases, the droplets become more stable to perturbations, hence larger, thus leading to a smaller interface area $\langle S \rangle_{xyzt}/S_0$. However, in this case, $Ca_0 \ll 1$, and the coalescing droplets are limited in size by the channel height, not surface tension. Figure 1(b) supports this hypothesis, as the coalescing droplets are comparable in size to the channel height.

The inset of Fig. 4 reports the time history of the interface area: the cases with non-coalescing droplets (FT) rapidly converge to a statistically steady-state, whereas for the coalescing droplets, convergence is reached long after, at about $t^+ \approx 8000$. Interestingly, we observe

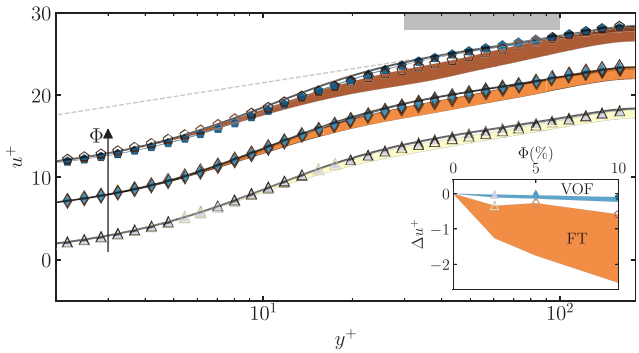

FIG. 3. Main: velocity profiles in wall units u^+ and y^+. Each run is plotted using the marker listed in Table I. For ease of comparison, we have moved the $\Phi = 5\%$ and $\Phi = 10\%$ volume fraction profiles upward by $u^+ = 5$ and $u^+ = 10$, respectively. In the region $30 < y^+ < 100$ shaded in gray, we fit a log-law equation $u^+ = \frac{\ln y^+}{0.41} + 5.89 + \Delta u^+$ (gray dashed line). Inset: the vertical shift Δu^+ for each run. Runs with coalescing droplets (VOF) are shown in blue, while runs with non-coalescing droplets (FT) are shown in orange. Runs with coalescing droplets show only small shifts, whereas the runs with non-coalescing, less deformable droplets show significant drag increase.

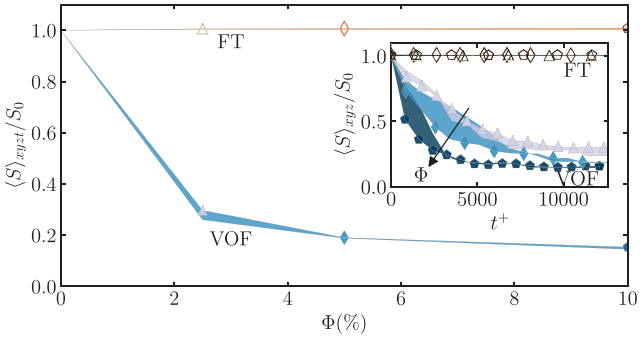

FIG. 4. Main: dependence of the total interface area of the droplets $\langle S \rangle_{xyzt}$ on the total volume fraction Φ. We have normalized each area by the total initial surface area S_0 of the droplets. The VOF runs (blue) show a major reduction in surface area due to coalescence, whereas the FT runs (orange) show a slight increase, due to droplet deformation. Inset: time history of the total interface area. Each run is plotted according to the colors and markers listed in Table I. Note how the coalescing droplets (VOF) reach statistical equilibrium after $t^+ \approx 8000$, while the non-coalescing droplets (FT) very rapidly converge because of the absence of topological changes.

that the coalescing droplet runs with larger capillary number (VOFa) converge to steady-state more rapidly than the smaller capillary number runs (VOFb), i.e., the *larger* Ca_0 runs show a higher rate of coalescence, although the steady-state areas are roughly the same. This is in contrast with simulations of droplet coalescence in simple shear flow in laminar condition by Shardt *et al.* (2013), which show droplet coalescence occurring only *below* a critical Ca_0. However, as we shall discuss in the next paragraph, the $Ca_0 = 0.1$ droplets are more tightly confined in the channel center than the $Ca_0 = 0.05$ droplets, thus leading to a higher rate of coalescence.

Figure 5 shows how the volume fraction of the dispersed phase ϕ depends on the distance y from the channel walls. The coalescing droplet profiles (VOF) clearly show a single peak at the channel center, $y = L$: this peak arises as the droplets are driven toward the region of lowest shear ($y = L$) by a "deformation-induced lift force" (Raffiee *et al.*, 2017; Hadikhani *et al.*, 2018; Alghalibi *et al.*, 2019). Confinement in the channel center leads to coalescence and the formation of large droplets, as seen in Fig. 1(b).

The FT droplets cannot coalesce, and the droplet–droplet interaction produces a volume effect, which forces them to spread across the channel: this manifests as an almost flat volume fraction in the region $0.5L < y < L$ in Fig. 5. Also, we see that the volume fraction tends to zero for $y < R = L/8$, as surface tension preserves the droplet radius R, and prevents the droplets from fully conforming with the flat channel walls. For all but one of the non-coalescing droplet runs plotted in Fig. 5, $\langle\phi\rangle_{xzt}$ has a local maximum near the wall, in the region $0.15L < y < 0.3L$. This phenomenon is due to the "shear-gradient lift force," which is known to act on particles in curved velocity profiles (Ho and Leal, 1974; Martel and Toner, 2014; Hadikhani *et al.*, 2018; Alghalibi *et al.*, 2019). Due to the curvature of the velocity profiles shown in Fig. 2, the droplets experience different flow velocities on each side, resulting in a lift force toward the wall. From Fig. 5, we also notice that the more deformable droplets (FT3a, FT5a, and FT10a) produce a maximum, which is further from the wall: this is mainly due to (i) an increase in the deformation-induced lift force, and to (ii) a greater elongation of the droplets in the shear direction, producing a wider wall layer.

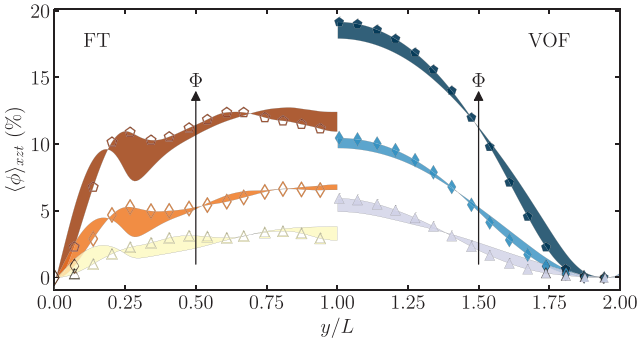

FIG. 5. Dependence of the mean volume fraction of droplets $\langle\phi\rangle_{xzt}$ on the distance y from the channel wall. Each run is plotted using the color and marker listed in Table I. The profiles are symmetric about the centerline ($y = L$), so we have plotted runs with non-coalescing (FT), and coalescing (VOF) droplets on the left and right, respectively. Note that for the runs with coalescing droplets, $\langle\phi\rangle_{xzt}$ peaks in the channel center, whereas for the non-coalescing droplet runs, $\langle\phi\rangle_{xzt}$ shows a peak near the wall.

We are now ready to investigate how droplets affect the turbulent flow, and we start by analyzing the second-order statistics of the flow, which tell us how momentum is transferred across different parts of the channel. Figure 6 shows four of the six unique components of the Reynolds stress tensor in wall units $\langle u_i' u_j' \rangle^+ \equiv \langle u_i' u_j' \rangle_{xzt} / u_\tau^2$, with the single-phase (SP0) Reynolds stresses shown in black as reference. The coalescing droplets simulations (VOF) show little change in stresses relative to single-phase flow. Going from single phase to the non-coalescing droplets, however, we see a reduction in the streamwise velocity fluctuations $\langle u'^2 \rangle^+$, and an increase in the wall-normal $\langle v'^2 \rangle^+$ and spanwise $\langle w'^2 \rangle^+$ velocity fluctuations. This shows that the isotropy of the turbulent flow has increased due to the presence of non-coalescing droplets. A similar effect has been observed for particle-laden turbulent channel flows, see, e.g., Picano *et al.* (2015), in which particles redistribute energy to a "more isotropic state," inducing an overall drag increase growing with the volume fraction of the dispersed phase. We infer that non-coalescing droplets have a back-reaction on the flow comparable to that of rigid particles, producing an increase in isotropy, which correlates with an increase in drag. On the other hand, coalescing droplets produce a weaker back reaction on the flow, which shows little change in isotropy or drag.

When compared to the other components of the Reynolds stresses, the shear stress $\langle u'v' \rangle^+$ shows only a small change due to the presence of droplets. However, as we shall see next, this shear stress opposes the pressure gradient in the channel, producing a profound impact on the drag. The full shear stress balance for the multiphase problem under investigation can be obtained as follows. We start by taking average of the streamwise ($i = 1$) component of Eq. (1),

$$\langle (\rho u_1)_{,t} + (\rho u_1 u_j)_{,j} \rangle_{xzt} = \langle (\rho \nu u_{1,j} + \rho \nu u_{j,1})_{,j} \rangle_{xzt} - \langle p_{,1} \rangle_{xzt} + \langle G \delta_{11} \rangle_{xzt} + \langle \gamma \kappa n_1 \, \delta_S(\boldsymbol{x}) \rangle_{xzt}. \quad (6)$$

In fully developed turbulent channel flows, most of these terms average to zero, and the equation simplifies to

$$\langle \rho u' v' \rangle_{xzt,y} = \nu \langle \rho u_{,y} \rangle_{xzt,y} + G + \langle \gamma \kappa n_1 \, \delta_S(\boldsymbol{x}) \rangle_{xzt}, \quad (7)$$

where we have moved from the index notation (u_1, u_2, u_3) to (u, v, w) for the sake of clarity. Hereafter, for brevity we omit the subscripts xzt

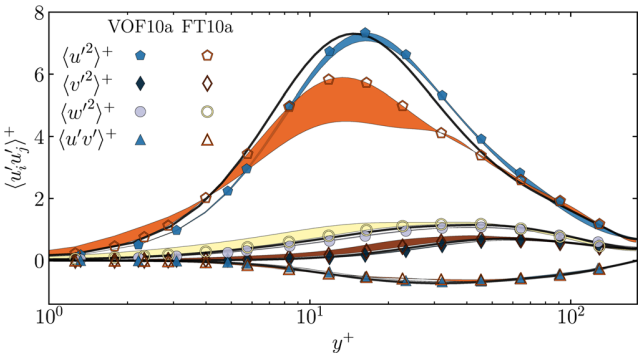

FIG. 6. Variation of Reynolds stresses with the distance y^+ from the channel walls. Stresses for run SP0 are shown by solid black lines. For runs with droplets, the difference between the $Ca_0 = 0.1$ and $Ca_0 = 0.05$ stress is shaded in color. The Reynolds stress components exhibit higher isotropy in the non-coalescing droplet runs (FT) than in the coalescing runs (VOF).

on angled brackets. Integrating from the wall $y=0$, to $y=\xi$, we obtain

$$-G\xi = \left[\langle \mu u_{,y}\rangle - \langle \rho u'v'\rangle\right]_{y=0}^{y=\xi} + \int_0^{\xi} \langle \gamma\kappa n_1\, \delta_S(\boldsymbol{x})\rangle dy. \tag{8}$$

The non-penetration boundary conditions at the walls enforce $v'=0$ and with $n_1=0$ at the wall, the lower limit of the right hand side is $\langle \mu u_{,y}\rangle|_{y=0} = \tau_w = GL$ by the definition of the wall shear stress. We relabel $y=\xi$ and obtain

$$G(L-y) = \langle \mu u_{,y}\rangle - \langle \rho u'v'\rangle + \int_0^{y} \langle \gamma\kappa n_1\, \delta_S(\boldsymbol{x})\rangle dy. \tag{9}$$

By dividing the equation by τ_w, we obtain the following dimensionless expression for the shear stress budget in the channel,

$$1 - y/L = \tau_\nu^+ + \tau_{Re}^+ + \tau_\sigma^+, \tag{10}$$

where

$$\tau_\nu^+ \equiv \langle \mu u_{,y}\rangle/\tau_w, \tag{11}$$

$$\tau_{Re}^+ \equiv -\langle \rho u'v'\rangle/\tau_w, \text{ and} \tag{12}$$

$$\tau_\sigma^+ \equiv \int_0^{y} \langle \gamma\kappa n_1 \delta_S(x)\rangle dy/\tau_w \tag{13}$$

are the viscous, Reynolds, and interfacial shear stresses, respectively. Here, we calculate the viscous stress and Reynolds stress using Eqs. (11) and (12), while the interfacial stress is calculated as the remaining part of the total budget in Eq. (10). (Assuming that the volume fraction ϕ is uncorrelated with the flow, we can separate the averages of the material properties and the flow velocity. To test our assumption, we measured the correlations $\nu\langle \rho u_{,y}\rangle - \nu\langle\rho\rangle\langle u\rangle_{,y}$ and $\langle \rho u'v'\rangle - \langle\rho\rangle\langle u'v'\rangle$ for each of the FT runs and found that the error in shear stress was always less than 3.5% of τ_w.)

Figure 7(a) shows the balance of shear stresses from the channel wall ($y=0$) to the center ($y=L$). In agreement with previous works (Pope, 2000), the single-phase run (SP0) produces a viscous stress τ_ν^+, which is the highest near the wall where the shear rate is maximum, and a Reynolds stress τ_{Re}^+ dominates for $y > 0.1L$, where turbulent fluctuations abound.

The coalescing droplet runs (VOF) in Fig. 7(a) have an interfacial stress τ_σ^+, which peaks around $y=0.5L$. This stress occurs due to the droplet interfaces, which resist the deforming effects of turbulent fluctuations, at the detriment of the Reynolds stress. Note that τ_σ^+ is larger for the smaller capillary number case (VOF10b compared to VOF10a), because the surface tension coefficient γ is larger, so surface tension forces are larger.

The non-coalescing droplet runs (FT) in Fig. 7(a), on the other hand, have very little interfacial stress τ_σ^+ above $y>0.5$: instead, the peak of τ_σ^+ occurs at roughly the same wall-normal location y as the peak in the volume fraction $\langle\phi\rangle_{xzt}$ seen in Fig. 5. In both Figs. 5 and 7, the peak moves away from the wall when capillary number increases. A similar trend is also observed for the location of the maximum turbulent kinetic energy production (not shown here). The correlation of y locations for these three statistics suggests that the "wall layering" and "shear-gradient lift forces" discussed above, which produce a peak in $\langle\phi\rangle_{xzt}$ near the channel wall, are also responsible for τ_σ^+ generation

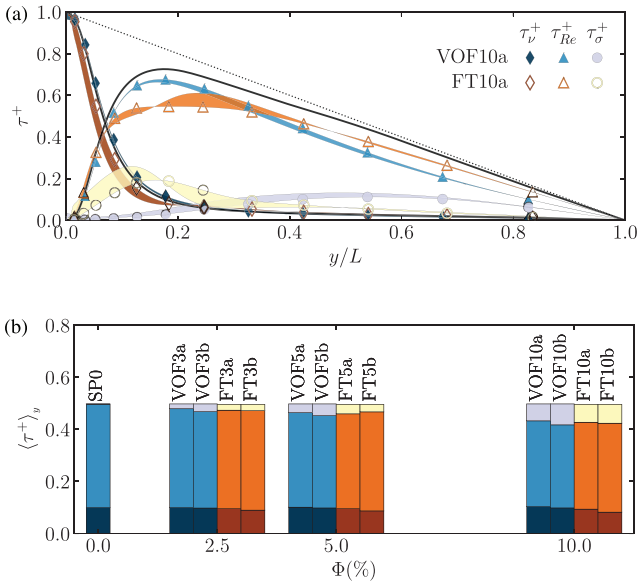

FIG. 7. (a) The balance of shear stresses as a function of the distance y from the channel wall. The dashed line is the total stress budget. Stresses for run SP0 are shown by solid black lines. The differences between VOF10a and VOF10b stresses are shown in shades of blue, whereas the differences between FT10a and FT10b stresses are shown in shades of orange. We see that τ_σ^+ peaks near the wall for the runs with non-coalescing droplets (FT), but is spread across the channel for the coalescing runs (VOF). The different stress distributions across the channel ultimately lead to different values of drag for coalescing and non-coalescing droplets. (b) Mean shear stresses for all runs. The stacked bars are $\langle\tau_\nu^+\rangle_y$, $\langle\tau_{Re}^+\rangle_y$, and $\langle\tau_\sigma^+\rangle_y$ from bottom to top.

and kinetic energy generation. The enhanced τ_σ^+ close to the wall is compensated in the budget by a reduction in τ_ν^+ for the cases of non-coalescing droplets.

The averaged stresses are shown for all runs in Fig. 7(b). The mean stresses are calculated by integrating τ_ν^+, τ_{Re}^+, and τ_σ^+ in the wall-normal direction y from 0 to L, for example,

$$\langle\tau_\nu^+\rangle_y \equiv \frac{1}{L}\int_0^L \tau_\nu^+\, dy. \tag{14}$$

The averaged form of Eq. (10) is $0.5 = \langle\tau_\nu^+\rangle_y + \langle\tau_{Re}^+\rangle_y + \langle\tau_\sigma^+\rangle_y$, showing the averaged stresses are also in balance with the wall stress budget. We observe that for coalescing droplets, the dispersed fluid produces an interfacial stress $\langle\tau_\nu^+\rangle_y$, which is entirely compensated by a reduction in Reynolds stress $\langle\tau_{Re}^+\rangle_y$, with very little change in the viscous stress $\langle\tau_\nu^+\rangle_y$. However, in the case of non-coalescing droplets the increase in interfacial stress $\langle\tau_\sigma^+\rangle_y$ is compensated by a reduction in both the Reynolds stress $\langle\tau_{Re}^+\rangle_y$, and the viscous stress $\langle\tau_\nu^+\rangle_y$.

For the single-phase case, the dynamic viscosity μ is constant throughout the channel, so the mean viscous stress is proportional to the centerline velocity,

$$\langle\tau_\nu^+\rangle_y = \frac{1}{L}\int_0^L \frac{\mu}{\tau_w}\frac{d\langle u\rangle_{xzt}}{dy}\, dy = \frac{\mu}{L\tau_w}\left[\langle u\rangle_{xzt}\right]_{y=0}^{y=L} = \frac{\mu}{L\tau_w}u_{cen}, \tag{15}$$

and hence, the variation of $\langle \tau_\nu^+ \rangle_y$ can be used to quantify drag in the channel, with a larger/smaller $\langle \tau_\nu^+ \rangle_y$ corresponding to drag reduction/increase. For the multiphase problem, dynamic viscosity is different for the carrier phase and dispersed phases, and we should integrate $d\langle \mu u \rangle_{xzt}/dy$ to the centerline, so the relationship between centerline velocity and $\langle \tau_\nu^+ \rangle_y$ is not exactly linear. However, due to the low volume fraction and low changes in viscosity, we found that considering the variation of the material properties (ρ, μ) and variation of the fluid velocity as independent produces only small changes in the averaged statistics. Hence, we can still relate the viscous stress to the centerline velocity and, thus, to the drag changes in the multiphase simulations. Indeed, the three runs with the smallest bulk velocity u_b^+ in the inset of Fig. 2 are FT10b, FT5b, and FT3b, and the three runs with the smallest mean viscous stress $\langle \tau_\nu^+ \rangle_y$ are also FT10b, FT5b, and FT3b [Fig. 7(b)]. Based on the above discussion, we can now relate the increased drag for non-coalescing droplets to the *wall normal location* of the droplets: the non-coalescing droplets in runs FT10b, FT5b, and FT3b encroach into the viscous wall region and oppose the shearing flow, reducing the viscous shear stress and thereby increasing drag.

V. CONCLUSIONS

We perform direct numerical simulations of coalescing and non-coalescing droplets in turbulent channel flows to single out the effect of coalescence. Coalescing droplets are simulated using the volume-of-fluid method, and non-coalescing droplets with the front-tracking method. We find that the droplets that are non-coalescing and less deformable produce an increase in drag, whereas the other droplets do not. We explained this by looking at the wall-normal location of droplets in the channel: the coalescing droplets experience a deformation-induced lift force, which drives them away from the shearing flow near the wall, out of the viscous sublayer; this is possible due to the coalescence, which allows droplets to accumulate at the centerline. On the other hand, the non-coalescing droplets do not; indeed, non-coalescing droplets roughly behave as particles, uniformly distributing across the channel, forming a wall layer, and increasing the isotropy of the flow. In this case, droplets remain in the viscous sublayer, generating an interfacial shear stress, which reduces the budget for viscous shear stress in the channel. From Eq. (15), we relate a reduction in the viscous shear stress to a reduction in the centerline velocity and ultimately to an increase in drag.

Our results agree well with the experiments carried out by Descamps *et al.* (2008), who found that larger bubbles produce less drag; in our study, large droplets are obtained through coalescence and, indeed, produce less drag. Our proposed mechanism for drag increase is also similar to that proposed by Dabiri *et al.* (2013), who showed that less deformable bubbles enter the viscous sublayer, leading to an increase in viscous dissipation and an increase in drag. We offer two main developments. First, we extend the study to coalescing droplets. Second, we believe that viscous shear stress is a better predictor of drag than viscous dissipation, as the proportionality between the mean viscous shear stress and centerline velocity [Eq. (15)] is exact for single-phase channel flows and only slightly affected by the change in material properties. Although we made simulations at a density ratio of $\rho_c/\rho_d = 50$, which is greater than that of oil in water ($\rho_{water}/\rho_{oil} \approx 1.5$), but less than that of air in water ($\rho_{water}/\rho_{air} \approx 830$), comparison with the experimental literature suggests that our current qualitative conclusions still hold for these flows.

Our findings can help to better understand and control multiphase flows in a variety of applications, such as arteries, pipelines, or ships. Through numerical experiments, we have been able to fully characterize the effect of coalescence alone, without the interference of other mechanisms, which often arise in experiments with surfactants. How these results are affected by surfactant concentrations will be the topic of future research.

ACKNOWLEDGMENTS

The authors acknowledge computer time provided by the Swedish National Infrastructure for Computing (SNIC) and by the Scientific Computing Section of Research Support Division at OIST. M.E.R. was supported by the JSPS KAKENHI Grant No. JP20K22402. O.T. was supported by Swedish Research Council Grant No. VR 2017–0489.

DATA AVAILABILITY

The data that support the findings of this study are openly available in OIST at https://groups.oist.jp/cffu/cannon2021pof, Cannon *et al.* (2021).

REFERENCES

Ahmed, Z., Izbassarov, D., Costa, P., Muradoglu, M., and Tammisola, O., "Turbulent bubbly channel flows: Effects of soluble surfactant and viscoelasticity," Comput. Fluids **212**, 104717 (2020).
Alghalibi, D., Rosti, M. E., and Brandt, L., "Inertial migration of a deformable particle in pipe flow," Phys. Rev. Fluids **4**, 104201 (2019).
Balachandar, S., and Eaton, J. K., "Turbulent Dispersed Multiphase Flow," Annu. Rev. Fluid Mech. **42**, 111–133 (2010).
Bolotnov, I. A., "Influence of bubbles on the turbulence anisotropy," J. Fluids Eng. **135**, 051301 (2013).
Bolotnov, I. A., Jansen, K. E., Drew, D. A., Oberai, A. A., Lahey, R. T., and Podowski, M. Z., "Detached direct numerical simulations of turbulent two-phase bubbly channel flow," Int. J. Multiphase Flow **37**, 647–659 (2011).
Brackbill, J. U., Kothe, D. B., and Zemach, C., "A continuum method for modeling surface tension," J. Comput. Phys. **100**, 335–354 (1992).
Cannon, I., Izbassarov, D., Tammisola, O., Brandt, L., and Rosti, M. E., "The effect of droplet coalescence on drag in turbulent channel flows," in *Cannon2021POF* (OIST, 2021).
Ceccio, S. L., "Friction drag reduction of external flows with bubble and gas injection," Annu. Rev. Fluid Mech. **42**, 183–203 (2010).
Chen, N., Kuhl, T., Tadmor, R., Lin, Q., and Israelachvili, J., "Large deformations during the coalescence of fluid interfaces," Phys. Rev. Lett. **92**, 024501 (2004).
Dabiri, S., Lu, J., and Tryggvason, G., "Transition between regimes of a vertical channel bubbly upflow due to bubble deformability," Phys. Fluids **25**, 102110 (2013).
Dabiri, S., and Tryggvason, G., "Heat transfer in turbulent bubbly flow in vertical channels," Chem. Eng. Sci. **122**, 106–113 (2015).
Descamps, M. N., Oliemans, R. V. A., Ooms, G., and Mudde, R. F., "Air–water flow in a vertical pipe: Experimental study of air bubbles in the vicinity of the wall," Experiments Fluids **45**, 357–370 (2008).
De Vita, F., Rosti, M. E., Caserta, S., and Brandt, L., "On the effect of coalescence on the rheology of emulsions," J. Fluid Mech. **880**, 969–991 (2019).
De Vita, F., Rosti, M. E., Caserta, S., and Brandt, L., "Numerical simulations of vorticity banding of emulsions in shear flows," Soft Matter **16**, 2854–2863 (2020).
Dodd, M., and Ferrante, A., "A fast pressure-correction method for incompressible two-fluid flows," J. Comput. Phys. **273**, 416–434 (2014).
Dodd, M. S., and Ferrante, A., "On the interaction of Taylor length scale size droplets and isotropic turbulence," J. Fluid Mech. **806**, 356–412 (2016).
Dong, S., and Shen, J., "A time-stepping scheme involving constant coefficient matrices for phase-field simulations of two-phase incompressible flows with large density ratios," J. Comput. Phys. **231**, 5788–5804 (2012).

Druzhinin, O. A., and Elghobashi, S., "Direct numerical simulations of bubble-laden turbulent flows using the two-fluid formulation," Phys. Fluids **10**, 685–697 (1998).
Duineveld, P., "Bouncing and coalescence of bubble pairs rising at high Reynolds number in pure water or aqueous surfactant solutions," Appl. Sci. Res. **58**, 409–439 (1997).
Einstein, A., "Die Grundlage der allgemeinen Relativitätstheorie," Ann. Phys. **354**, 769–822 (1916).
Elghobashi, S., "Direct numerical simulation of turbulent flows laden with droplets or bubbles," Annu. Rev. Fluid Mech. **51**, 217–244 (2019).
Esmaeeli, A., and Tryggvason, G., "Direct numerical simulations of bubbly flows. Part 1. Low Reynolds number arrays," J. Fluid Mech. **377**, 313–345 (1998).
Esmaeeli, A., and Tryggvason, G., "Direct numerical simulations of bubbly flows Part 2. Moderate Reynolds number arrays," J. Fluid Mech. **385**, 325–358 (1999).
Farooqi, M. N., Izbassarov, D., Muradoğlu, M., and Unat, D., "Communication analysis and optimization of 3D front tracking method for multiphase flow simulations," Int. J. High Perform. Comput. Appl. **33**, 67–80 (2019).
Frumkin, A., and Levich, V. G., "On surfactants and interfacial motion," Z. Fiz. Khim. **21**, 1183–1204 (1947) (in Russian), see https://ci.nii.ac.jp/naid/10028205328/.
Hadikhani, P., Hashemi, S. M. H., Balestra, G., Zhu, L., Modestino, M. A., Gallaire, F., and Psaltis, D., "Inertial manipulation of bubbles in rectangular microfluidic channels," Lab Chip **18**, 1035–1046 (2018).
Ho, B. P., and Leal, L. G., "Inertial migration of rigid spheres in two-dimensional unidirectional flows," J. Fluid Mech. **65**, 365–400 (1974).
Ii, S., Sugiyama, K., Takeuchi, S., Takagi, S., Matsumoto, Y., and Xiao, F., "An interface capturing method with a continuous function: The THINC method with multi-dimensional reconstruction," J. Comput. Phys. **231**, 2328–2358 (2012).
Innocenti, A., Jaccod, A., Popinet, S., and Chibbaro, S., "Direct numerical simulation of bubble-induced turbulence," J. Fluid Mech. **918**, A23 (2021).
Izbassarov, D., and Muradoglu, M., "A front-tracking method for computational modeling of viscoelastic two-phase flow systems," J. Non-Newtonian Fluid Mech. **223**, 122–140 (2015).
Kim, J., and Moin, P., "Application of a fractional-step method to incompressible Navier-Stokes equations," J. Comput. Phys. **59**, 308–323 (1985).
Komrakova, A. E., Eskin, D., and Derksen, J. J., "Numerical study of turbulent liquid-liquid dispersions," AIChE J. **61**, 2618–2633 (2015).
Leonard, B. P., "A stable and accurate convective modelling procedure based on quadratic upstream interpolation," Comput. Methods Appl. Mech. Eng. **19**, 59– 98 (1979).
Levich, V. G., *Physicochemical Hydrodynamics* (Prentice-Hall, Englewood Cliffs, New Jersy, 1962).
Lu, J., Biswas, S., and Tryggvason, G., "A DNS study of laminar bubbly flows in a vertical channel," Int. J. Multiphase Flow **32**, 643–660 (2006).
Lu, J., Muradoglu, M., and Tryggvason, G., "Effect of insoluble surfactant on turbulent bubbly flows in vertical channels," Int. J. Multiphase Flow **95**, 135–143 (2017).
Lu, J., and Tryggvason, G., "Direct numerical simulations of multifluid flows in a vertical channel undergoing topology changes," Phys. Rev. Fluids **3**, 084401 (2018).
Lu, J., and Tryggvason, G., "Multifluid flows in a vertical channel undergoing topology changes: Effect of void fraction," Phys. Rev. Fluids **4**, 084301 (2019).
Martel, J. M., and Toner, M., "Inertial focusing in microfluidics," Annu. Rev. Biomed. Eng. **16**, 371–396 (2014).
Maxey, M. R., "Droplets in turbulence: A new perspective," J. Fluid Mech. **816**, 1–4 (2017).
Muradoglu, M., and Tryggvason, G., "Simulations of soluble surfactants in 3D multiphase flow," J. Comput. Phys. **274**, 737–757 (2014).
Noh, W. F., and Woodward, P., "SLIC (simple line interface calculation)," in *Proceedings of the Fifth International Conference on Numerical Methods in Fluid Dynamics, Twente University, Enschede*, 28 June–2 July 1976, Lecture Notes in Physics, edited by A. I. van de Vooren and P. J. Zandbergen (Springer, Berlin, Heidelberg, 1976), pp. 330–340.
Perlekar, P., Biferale, L., Sbragaglia, M., Srivastava, S., and Toschi, F., "Droplet size distribution in homogeneous isotropic turbulence," Phys. Fluids **24**, 065101 (2012).
Picano, F., Breugem, W.-P., and Brandt, L., "Turbulent channel flow of dense suspensions of neutrally buoyant spheres," J. Fluid Mech. **764**, 463–487 (2015).
Pope, S. B., *Turbulent Flows* (Cambridge University Press, 2000).
Popinet, S., "Numerical models of surface tension," Annu. Rev. Fluid Mech. **50**, 49–75 (2018).
Puckett, E. G., Almgren, A. S., Bell, J. B., Marcus, D. L., and Rider, W. J., "A high-order projection method for tracking fluid interfaces in variable density incompressible flows," J. Comput. Phys. **130**, 269–282 (1997).
Raffiee, A. H., Dabiri, S., and Ardekani, A. M., "Elasto-inertial migration of deformable capsules in a microchannel," Biomicrofluidics **11**, 064113 (2017).
Rider, W. J., and Kothe, D. B., "Reconstructing volume tracking," J. Comput. Phys. **141**, 112–152 (1998).
Roccon, A., De Paoli, M., Zonta, F., and Soldati, A., "Viscosity-modulated breakup and coalescence of large drops in bounded turbulence," Phys. Rev. Fluids **2**, 083603 (2017).
Rosti, M. E., and Brandt, L., "Increase of turbulent drag by polymers in particle suspensions," Phys. Rev. Fluids **5**, 041301 (2020).
Rosti, M. E., De Vita, F., and Brandt, L., "Numerical simulations of emulsions in shear flows," Acta Mech. **230**, 667–682 (2019).
Rosti, M. E., Ge, Z., Jain, S. S., Dodd, M. S., and Brandt, L., "Droplets in homogeneous shear turbulence," J. Fluid Mech. **876**, 962–984 (2019).
Scarbolo, L., Bianco, F., and Soldati, A., "Coalescence and breakup of large droplets in turbulent channel flow," Phys. Fluids **27**, 073302 (2015).
Shardt, O., Derksen, J. J., and Mitra, S. K., "Simulations of droplet coalescence in simple shear flow," Langmuir **29**, 6201–6212 (2013).
Soligo, G., Roccon, A., and Soldati, A., "Breakage, coalescence and size distribution of surfactant-laden droplets in turbulent flow," J. Fluid Mech. **881**, 244–282 (2019).
Takagi, S., and Matsumoto, Y., "Surfactant effects on bubble motion and bubbly flows," Annu. Rev. Fluid Mech. **43**, 615–636 (2011).
Takagi, S., Ogasawara, T., and Matsumoto, Y., "The effects of surfactant on the multiscale structure of bubbly flows," Philos. Trans. R. Soc. A **366**, 2117–2129 (2008).
Takeuchi, S., and Tryggvason, G., "Volume conservation method for the three-dimensional front-tracking method," Mech. Eng. Lett. **6**, 20 (2020).
Thomas, S., Esmaeeli, A., and Tryggvason, G., "Multiscale computations of thin films in multiphase flows," Int. J. Multiphase Flow **36**, 71–77 (2010).
Tryggvason, G., Bunner, B., Esmaeeli, A., Juric, D., Al-Rawahi, N., Tauber, W., Han, J., Nas, S., and Jan, Y. J., "A front-tracking method for the computations of multiphase flow," J. Comput. Phys. **169**, 708–759 (2001).
Tryggvason, G., Dabiri, S., Aboulhasanzadeh, B., and Lu, J., "Multiscale considerations in direct numerical simulations of multiphase flows," Phys. Fluids **25**, 031302 (2013).
Tryggvason, G., and Lu, J., "Direct numerical simulations of bubbly flows," Mech. Eng. Rev. **2**, 15 (2015).
Tryggvason, G., Ma, M., and Lu, J., "DNS–Assisted modeling of bubbly flows in vertical channels," Nucl. Sci. Eng. **184**, 312–320 (2016).
Tryggvason, G., Scardovelli, R., and Zaleski, S., *Direct Numerical Simulations of Gas-Liquid Multiphase Flows* (Cambridge University Press, Cambridge, UK, 2011).
Unverdi, S. O., and Tryggvason, G., "A front-tracking method for viscous, incompressible, multi-fluid flows," J. Comput. Phys. **100**, 25–37 (1992).
von Kármán, T., "Mechanische Ahnlichkeit und Turbulenz," Math. Phys. Klasse **5**, 58–76 (1930).
Xiao, F., Honma, Y., and Kono, T., "A simple algebraic interface capturing scheme using hyperbolic tangent function," Int. J. Numer. Methods Fluids **48**, 1023–1040 (2005).
Yokoi, K., "Efficient implementation of THINC scheme: A simple and practical smoothed VOF algorithm," J. Comput. Phys. **226**, 1985–2002 (2007).
Youngs, D. L., "Time-dependent multi-material flow with large fluid distortion," in *Numerical Methods for Fluid Dynamics*, edited by K. W. Morton and M. J. Baines (Academic Press, New York, 1982), pp. 273–285.
Youngs, D., "An interface tracking method for a 3D Eulerian hydrodynamics code," Technical Report No. 44/92/35 (AWRE, 1984).

Appendix B

Chapter 2 appendix

B.1 Euler characteristic of a droplet interface

Here we use concepts from algebraic topology to derive equation 2.11, which relates the Euler characteristic of a droplet interface to the number of voids and handles it contains. The Euler characteristic and genus are well-defined for a single surface; however, as seen in the image in figure 2.8b, our droplets can have many distinct surfaces. For a general droplet with a number of voids v, it has an outer surface with Euler characteristic χ_0, and the voids create v distinct inner surfaces with Euler characteristics $\chi_1, \chi_2, ... \chi_v$. We define the Euler characteristic of the droplet's interface as the sum of the Euler characteristics of all the surfaces,

$$\chi = \sum_{i=0}^{v} \chi_i. \tag{B.1}$$

Both the inner and outer surfaces of the droplet can have handles. For any distinct orientable surface, the number of handles h_i is its genus, and the genus is related to the Euler characteristic by $\chi_i = 2 - 2h_i$ (Massey, 1997, p.30). Hence equation B.1 can be written and rearranged to

$$\chi = \sum_{i=0}^{v}(2 - 2h_i) = 2(1 + v) - \sum_{i=0}^{v} 2h_i \tag{B.2}$$

The number of handles on the drop is the sum of the handles on all the droplet's surfaces, i.e., $h = \sum_{i=0}^{v} h_i$, so we can write,

$$\chi = 2 + 2v - 2h. \tag{B.3}$$

This can be easily rearranged to obtain equation 2.11.

B.2 Validation of the surfactant model

We report in this appendix the validation tests of the proposed numerical method. Two benchmark tests are presented and compared against existing theories, experiments and simulations.

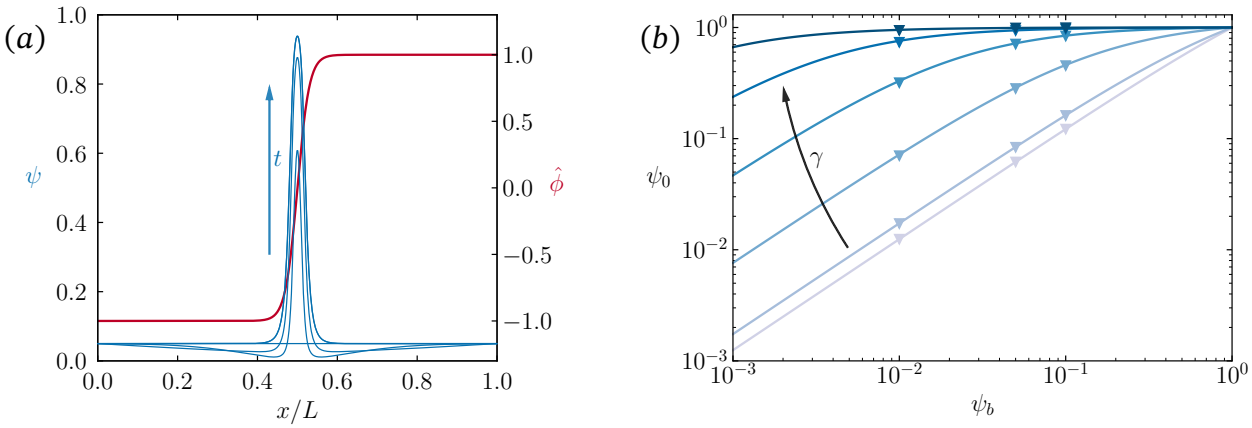

Figure B.1: (a) Adsorption of surfactant onto an interface at $x = L/2$. The right-hand axis shows the smoothed colour function $\hat{\phi}$ (in red), which has a smoothing width 3Δ. The left-hand axis shows the surfactant concentration (in blue) at four time-instants during the simulation. The bulk surfactant concentration is $\psi_b = 0.05$ and the energy cost of surfactant in the bulk is $\gamma = 11.1\alpha$. (b) The equilibrium interfacial surfactant concentration ψ_0 for a range of ψ_b and γ. Lines show Langmuir isotherms, given by equation B.4, and markers show the results of our simulations. The value of γ is represented by shading from light blue to dark blue.

We verify at first the adsorption dynamics of the surfactant at the interface: we start from a uniform surfactant concentration, equal to the surfactant concentration in the bulk ψ_b, and let the surfactant adsorb onto the interface (located at $x = L/2$, in figure B.1a). Initially, the system is out of equilibrium and surfactant diffuses towards the interface to restore the equilibrium; at equilibrium, the chemical potential is equal everywhere. We can thus equate the chemical potential in the bulk ($\hat{\phi} = \pm 1$, surfactant concentration ψ_b) and at the interface ($\hat{\phi} = 0$, surfactant concentration ψ_0) to obtain the so-called Langmuir isotherms (Engblom et al., 2013). For given values of the parameters of the chemical potential, α, β and γ, the Langmuir isotherm relates the surfactant concentration at the interface ψ_0 to that in the bulk ψ_b, in equilibrium conditions

$$\psi_0 = \frac{\psi_b}{\psi_b + (1 - \psi_b)e^{-\frac{\beta+\gamma}{2\alpha}}}. \tag{B.4}$$

Figure B.1a shows the setup we use to test our code against the Langmuir isotherm benchmark: a flat interface is located at $x = L/2$, and surfactant is initially uniformly distributed with a concentration equal to ψ_b. The flow is initially at rest and, due to the absence of any forcing, stays at rest throughout the entire simulation; similarly, the interface does not move from its initial position. At the boundaries $x = 0$ and $x = L$, we impose a far-field value of surfactant, $\psi = \psi_b$, thus allowing surfactant to enter the system. In the y and z directions, we impose periodic boundary conditions. This benchmark is, in principle, a one-dimensional test (x direction). However, we perform three-dimensional numeri-

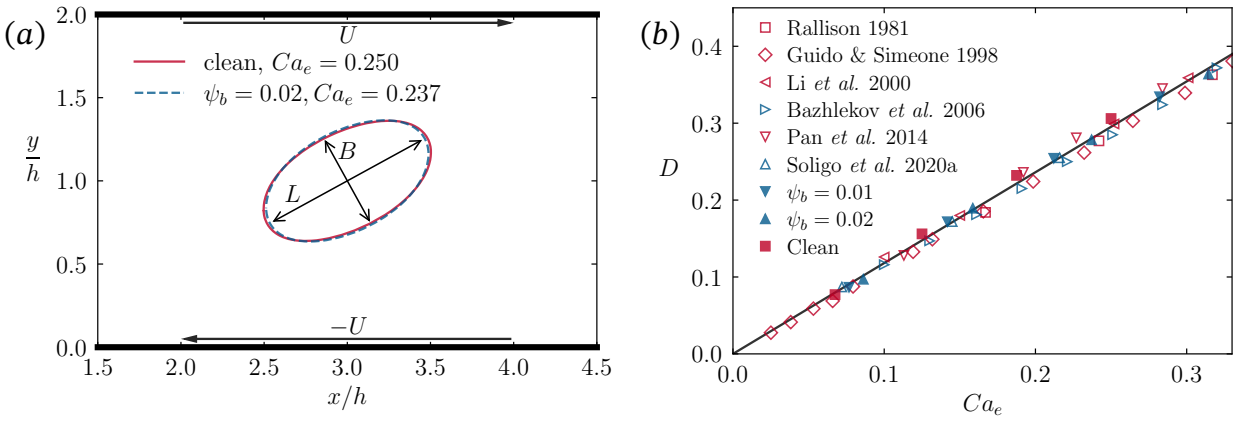

Figure B.2: Deformation of droplets in shear flows. (a) The simulated 2D domain (partially shown here) with velocity boundary conditions $u = U$ at $y = 2h$, $u = -U$ at $y = 0$, and periodic boundary conditions at $x = 0$ and $x = 6h$. We show the location of the droplet interface for a clean and surfactant-laden case. (b) Dependence of the steady-state deformation parameter D on the effective capillary number Ca_e. Our simulation results are shown with solid markers, and values from the literature are shown with empty markers. Clean droplets are marked in red, and surfactant-laden droplets are marked in blue. The solid line is the analytical relation from (Taylor, 1934) with the confinement correction proposed by Shapira and Haber (1990).

cal simulations in order to use the very same solver described in section 2.2; all variables are uniform in the y and z directions. We resolve the flow and volume of fluid equations on a $N_x \times N_y \times N_z = 100 \times 4 \times 4$ computational grid, and use a more refined grid for the surfactant transport equations, $500 \times 4 \times 4$. The smoothing width of the interface is 3Δ. We use $\beta/\alpha = 0.741$ and explore a range of values for the energy cost in the bulk $\gamma/\alpha = \{0.0741, 0.741, 3.70, 7.41, 11.1, 14.8\}$. Figure B.1*b* shows the simulated interfacial surfactant concentrations ψ_0 once they had reached equilibrium, for various values of ψ_b. The values obtained from our numerical simulations fall on top of the corresponding Langmuir isotherms, proving that the implemented numerical method is able to correctly capture the surfactant dynamics.

The second benchmark is aimed at verifying the surfactant transport on a moving interface and the computation of surface tension forces by measuring the deformation of a droplet in shear flow. Taylor (1934) quantified the deformation of a droplet in a shear flow using the deformation parameter

$$D \equiv \frac{L - B}{L + B}, \tag{B.5}$$

where L and B are the largest and smallest principal diameters of the droplet, respectively. Figure B.2a shows the simulation setup that we use to reproduce Taylor's experiment. The effective capillary number $Ca_e \equiv aU\mu/h\langle\sigma\rangle$ describes the ratio of viscous forces to surface tension forces in the system, where h is the domain half-height, $a = 0.4h$ is the initial ra-

dius of the droplet, $\pm U$ is the fluid velocity of the top and bottom walls respectively, μ is the dynamic viscosity, which is the same for the bulk and droplet phases, and $\langle\sigma\rangle$ is the (average) surface tension at the droplet interface. As was previously demonstrated by Soligo et al. (2020a), there are negligible differences between the two-dimensional (2D) and three-dimensional (3D) cases in the limit of small Reynolds and Capillary numbers, as those considered here. Hence, to reduce the computational cost of the benchmark simulations, we chose to perform two-dimensional numerical simulations. We select a computational grid with $N_x \times N_y \times N_z = 600 \times 200 \times 4$ points for the flow and volume of fluid variables, and we use a twice more refined grid to discretize the surfactant transport equation. As we use the same three-dimensional solver introduced in section 2.2, we have to use 4 grid points in the z direction; however all variables are uniform in the z direction.

We run a number of simulations with various values of Ca_e and three values of the initial surfactant concentration in the bulk phase $\psi_b \in \{0, 0.01, 0.02\}$, where $\psi_b = 0$ is the clean droplet case. In all cases, the Reynolds number of the flow $Re \equiv \rho U h/\mu$ is $Re = 0.1$. The droplets are initially circular and deform in the shearing flow. Figure B.2*b* shows our measured values of the deformation parameter D once they had reached a steady state. We compare our results (solid markers) with 2D droplets simulated using the boundary integral method (Rallison, 1981), experiments of 3D droplets (Guido & Simeone, 1998), 3D droplets simulated using the volume-of-fluid method (Li et al., 2000), 3D droplets simulated using the boundary integral method with insoluble surfactants (Bazhlekov et al., 2006), 3D droplets simulated using dissipative particle dynamics (Pan et al., 2014), and surfactant-laden droplets simulated using a phase-field method (Soligo et al., 2020a). Our results are in good agreement with all of the above and also closely follow the analytical result from Taylor (1934), with the confinement correction proposed by Shapira and Haber (1990), i.e., for droplets and carrier fluid having the same viscosity, the Taylor deformation parameter is equal to

$$D = \frac{35}{32} Ca_e \left[1 + C_{SH} \frac{3.5}{2} \left(\frac{a}{2h} \right)^3 \right], \tag{B.6}$$

where $C_{SH} = 5.6996$ is a numerical coefficient accounting for the confinement due to the top and bottom boundaries (Shapira & Haber, 1990).

In this appendix, we have shown that the proposed numerical method can accurately simulate the transport of surfactant over moving and deforming interfaces, and the action of surfactant on surface tension.

Appendix C

Chapter 3 appendix

J. Fluid Mech. (2022), *vol*. 950, R2, doi:10.1017/jfm.2022.832

The effect of particle anisotropy on the modulation of turbulent flows

Stefano Olivieri[1,2], **Ianto Cannon**[1] **and Marco E. Rosti**[1,†]

[1]Complex Fluids and Flows Unit, Okinawa Institute of Science and Technology Graduate University, 1919-1 Tancha, Onna-son, Okinawa 904-0495, Japan

[2]Department of Aerospace Engineering, Universidad Carlos III de Madrid, Avda. de la Universidad 30, 28911 Leganés, Spain

(Received 13 August 2022; revised 19 September 2022; accepted 26 September 2022)

We investigate the modulation of turbulence caused by the presence of finite-size dispersed particles. Bluff (isotropic) spheres versus slender (anisotropic) fibres are considered to understand the influence of the shape of the objects on altering the carrier flow. While at a fixed mass fraction – but different Stokes number – both objects provide a similar bulk effect characterized by a large-scale energy depletion, a scale-by-scale analysis of the energy transfer reveals that the alteration of the whole spectrum is intrinsically different. For bluff objects, the classical energy cascade shrinks in its extension but is unaltered in the energy content and its typical features, while for slender ones we find an alternative energy flux which is essentially mediated by the fluid–solid coupling.

Key words: suspensions, particle/fluid flow, turbulence simulation

1. Introduction

Particle-laden turbulent flows are multiphase systems where a carrier fluid interacts with a dispersed phase made up by a number of solid objects, e.g. spheres or fibres. Such flows concern an important class of problems with numerous applications related to both natural and industrial processes (De Lillo *et al.* 2014; Breard *et al.* 2016; Sengupta, Carrara & Stocker 2017; Falkinhoff *et al.* 2020; Rosti *et al.* 2020). In the analysis and modelling of such problems, a crucial distinction can be made regarding the mutual coupling between the carrier flow and the dispersed objects. When the suspension is dilute enough, it can be safely assumed that the fluid flow is not substantially altered by the presence of the objects (Balachandar & Eaton 2010; Maxey 2017; Brandt & Coletti 2021).

† Email address for correspondence: marco.rosti@oist.jp

However, we often deal with non-dilute conditions where the mutual coupling between the two phases is relevant and gives rise to a macroscopic alteration of the turbulent carrier flow. The resulting turbulence modulation effects have been the subject of previous studies over different classes of multiphase turbulent flows, i.e. considering isotropic (Lucci, Ferrante & Elghobashi 2010; Gualtieri *et al.* 2013; Uhlmann & Chouippe 2017; Capecelatro, Desjardins & Fox 2018; Ardekani, Rosti & Brandt 2019; Yousefi, Ardekani & Brandt 2020) or anisotropic (Andersson, Zhao & Barri 2012; Olivieri *et al.* 2020*b*,*a*; Olivieri, Mazzino & Rosti 2021, 2022; Wang *et al.* 2022) solid particles, as well as droplets or bubbles (Dodd & Ferrante 2016; Freund & Ferrante 2019; Rosti *et al.* 2019; Cannon *et al.* 2021), typically focusing on the alteration of both the bulk flow properties as well as the scale-by-scale energy distribution. In particular, Lucci *et al.* (2010) and Yousefi *et al.* (2020) showed that Taylor-length-scale-sized spheres reduce turbulent kinetic energy at the large scales and enhance its energy content at the small scales.

Nevertheless, the accurate characterization of the underlying physics in these complex systems still requires significant efforts from the theoretical, computational and experimental viewpoints, with relevant questions still not fully addressed, such as the following. (i) What are the mechanisms controlling the scale-by-scale energy distribution in the presence of immersed objects with finite size (i.e. larger than the dissipative length scale)? (ii) How do the geometrical properties of the dispersed particles (i.e. their size and isotropy) affect the back-reaction on the carrier flow and the consequent turbulence modulation?

In this work, we comprehensively investigate the multiscale nature of the turbulence modulation due to finite-size rigid particles, focusing on the role of geometrical properties and comparing, in particular, the back-reaction caused by isotropic bluff objects (i.e. spheres) versus anisotropic slender ones (i.e. fibres). Exploiting massive direct numerical simulations (DNS), it is observed, at first, that the macroscopic effect in the turbulence modulation essentially consists of a large-scale energy depletion for both configurations. However, we show that this bulk effect arises from qualitatively different mechanisms depending on the geometrical features of the dispersed objects, which becomes evident from a scale-by-scale energy-transfer balance. For isotropic objects (spheres), the back-reaction effectively acts at a well-defined length scale (i.e. the sphere diameter) and over a limited range of smaller scales, without appreciably modifying the inertial range that is obtained in the single phase (i.e. without particles) configuration. For anisotropic objects (fibres), instead, the fluid–solid coupling is responsible for a global modification of the energy distribution over all the scales of motion, which is characterized by the emergence of an alternative energy flux along with a relative enhancement of small-scale fluctuations.

The rest of the paper is structured as follows: § 2 describes the modelling and computational methodology, § 3 shows the results, and § 4 contains the conclusions.

2. Methods

To investigate the problem, we devote our attention to particles of finite size (i.e. diameter or length) that lies well within the inertial subrange of the turbulent flow. A visual example of two representative configurations is given in figure 1. Specifically, we have performed DNS where the fluid and solid dynamics are mutually coupled using the immersed boundary method (Hori, Rosti & Takagi 2022; Olivieri *et al.* 2022). An incompressible, homogeneous and isotropic turbulent (HIT) flow is generated within a tri-periodic cubic domain of size $L = 2\pi$ using Arnold–Beltrami–Childress (ABC) cellular-flow forcing

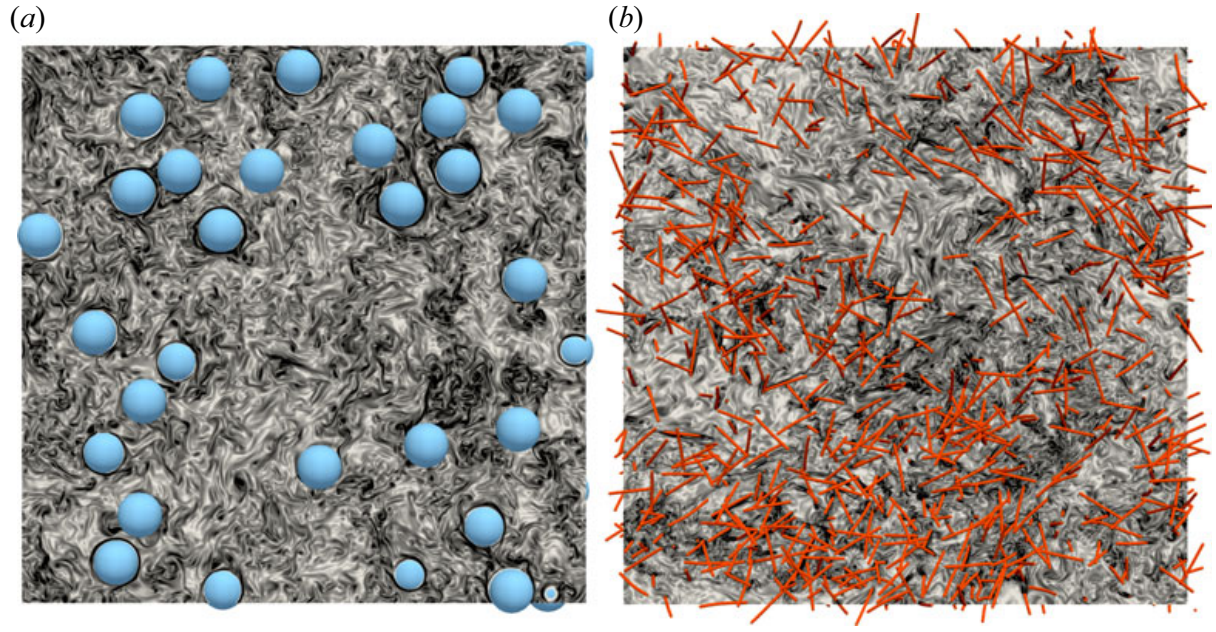

Figure 1. Two-dimensional views of the vorticity magnitude of homogeneous isotropic turbulence in the presence of dispersed, finite-size (*a*) spheres and (*b*) fibres, from two representative cases of the present DNS study.

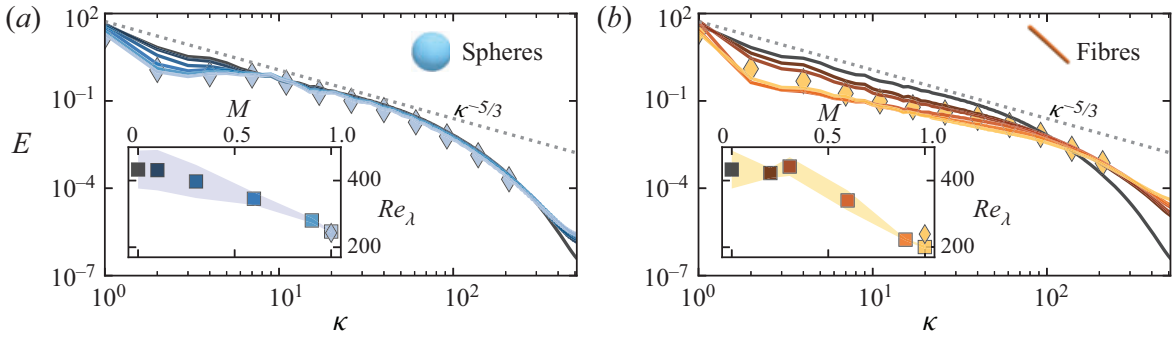

Figure 2. Energy spectra of the modulated turbulent flow for (*a*) spheres and (*b*) fibres, for different mass fractions M (increasing with the colour brightness from dark to light), along with the reference single-phase configuration (i.e. $M = 0$, black curve) and the expected Kolmogorov scaling in the inertial subrange (grey dashed line). The insets report the microscale Reynolds number Re_λ as a function of the mass fraction; error bars show the standard deviation in Re_λ from the time-averaged value. As an additional check on the accuracy of the computations, diamonds show results calculated using an Eulerian grid with halved resolution (512^3 cells), which produces little change in Re_λ and the inertial range of the spectra.

(Podvigina & Pouquet 1994), achieving in the single-phase case a microscale Reynolds number $Re_\lambda = u'\lambda/\nu \approx 435$, where u' is the root mean square of the turbulent fluctuations, λ is the Taylor microscale and ν is the kinematic viscosity. Such a high-Reynolds-number configuration is computationally explored for the first time in the framework of multiphase flows in order to achieve proper scale separation. As shown in figure 2, the energy spectrum in the single-phase configuration (black curve) shows the classical Kolmogorov scaling $\sim\kappa^{-5/3}$ (dashed line) at low-to-intermediate wavenumbers over more than one decade.

Once the single-phase case has reached the fully developed regime, N rigid spheres (characterized by diameter D and volumetric density ρ_s) or fibres (characterized by length c and linear density difference $\Delta\tilde{\rho}_s$) are added to the carrier flow at randomly initialized positions and orientations. The multiphase cases were therefore evolved until reaching a

statistically stationary state. An overview of the main configurations considered in our study is shown in table 1.

The dynamics of the bluff, spherical objects is governed by the well-known Newton–Euler equations (Hori *et al.* 2022), whereas the slender, anisotropic ones are modelled in the general framework of the Euler–Bernoulli equation for inextensible filaments, choosing a sufficiently large bending stiffness such that the deformation is always negligible (i.e. within 1 %) (Cavaiola, Olivieri & Mazzino 2020; Brizzolara *et al.* 2021). Hence, the mass fraction M of the suspension is defined as the ratio between the mass of the dispersed solid phase and the total mass (i.e. the sum of the fluid and solid masses contained in the domain). Note that for the chosen parameters and when matching M, bluff and slender particles have remarkably different Stokes numbers, here computed using expressions for small particles, i.e. of length below the dissipative scale, for the sake of a comparative estimate (Lucci, Ferrante & Elghobashi 2011; Bounoua, Bouchet & Verhille 2018). Moreover, we indicate $M = 1$ as the configurations where the dispersed objects are constrained to a fixed random position; such a setting serves as the limiting case where the dispersed phase has infinitely large inertia, as well as a representation of flows in porous media. Finally, we note that sphere and fibre cases with the same mass fractions have different volume fractions but approximately the same total wetted area.

To solve the governing equations numerically, we employ the in-house solver *Fujin* (https://groups.oist.jp/cffu/code). The code is based on the (second-order) central finite-difference method for the spatial discretization and the (second-order) Adams–Bashforth scheme for the temporal discretization. The incompressible Navier–Stokes equations are solved using the fractional step method on a staggered grid. The Poisson equation enforcing the incompressibility constraint is solved using a fast and efficient approach based on the fast Fourier transform (FFT). The solver is parallelized using the MPI protocol and the 2decomp library for domain decomposition (http://www.2decomp.org). In this work, the fluid domain is discretized onto a uniform Eulerian grid using 1024^3 cells, ensuring that, for the chosen set of domain size and fluid properties, the ratio between the Kolmogorov dissipative length scale and the grid spacing is $\eta/\Delta x = O(1)$. The carrier- and dispersed-phase dynamics are coupled by the no-slip condition $\dot{\boldsymbol{X}} = \boldsymbol{U} = \boldsymbol{u}(\boldsymbol{X}, t)$, where $\boldsymbol{X}$ is the position of a generic material point on the solid surface and $\boldsymbol{u} = \boldsymbol{u}(\boldsymbol{x}, t)$ is the fluid velocity field. In the present work, we employ two types of immersed boundary (IB) method where the mutual interaction between the two phases is achieved by means of a singular force distribution. Specifically, for bluff spherical particles we use the Eulerian IB method recently proposed by Hori *et al.* (2022), whereas for slender fibres we use the method originally proposed by Huang, Shin & Sung (2007) and recently employed for fibre-laden turbulence by Olivieri *et al.* (2020*a*,*b*, 2021, 2022). Overall, the code has been extensively validated and tested in a variety of problems; see e.g. Rosti & Brandt (2020), Rosti *et al.* (2020, 2021) and Olivieri *et al.* (2022).

3. Results

3.1. *Main features of turbulence modulation*

The presence of the dispersed phase clearly causes a complex modification of the key features of the carrier flow, as may be observed in the energy spectra for suspensions of spheres (figure 2*a*) or fibres (figure 2*b*) at different mass fractions M. At first glance, and focusing on the smallest wavenumbers (i.e. largest scales), one can note a similar phenomenology between the two kinds of particles, with an overall tendency to decrease the turbulent kinetic energy while increasing M. Indeed, for both bluff and slender

https://doi.org/10.1017/jfm.2022.832 Published online by Cambridge University Press

ρ_s/ρ_f	D/L	D/η	St	N	M	Re_λ	C_d	$\Delta\tilde{\rho}/(\rho_f L^2)$	c/L	c/η	St	N	M	Re_λ	C_d
1.3	$(4\pi)^{-1}$	123	7.4	300	0.1	431	0.11	3.0×10^{-4}	$(4\pi)^{-1}$	123	0.45	10^4	0.2	422	0.11
5.0	$(4\pi)^{-1}$	123	27	300	0.3	397	0.13	5.3×10^{-4}	$(4\pi)^{-1}$	123	0.79	10^4	0.3	442	0.11
1.7×10^1	$(4\pi)^{-1}$	123	90	300	0.6	346	0.16	1.9×10^{-3}	$(4\pi)^{-1}$	123	2.8	10^4	0.6	340	0.17
1.0×10^2	$(4\pi)^{-1}$	123	470	300	0.9	280	0.21	1.1×10^{-2}	$(4\pi)^{-1}$	123	16	10^4	0.9	223	0.29
∞	$(4\pi)^{-1}$	123	∞	300	1	247	0.23	∞	$(4\pi)^{-1}$	123	∞	10^4	1	200	0.32

Table 1. Parametric combinations investigated in our baseline study. Left: Suspensions of bluff, spherical particles (ρ_s is the volumetric density of the solid phase, and D is the sphere diameter). Right: Suspensions of anisotropic, slender particles ($\Delta\tilde{\rho}$ is the linear density difference between the solid and fluid phases, and c is the fibre length). Here, η is the Kolmogorov microscale of the single-phase case, St is the estimated Stokes number of the particle, N is the number of dispersed particles, M is the corresponding mass fraction, and Re_λ and C_d are the resulting microscale Reynolds number and drag coefficient of the modulated flow, respectively (for $M = 0$, $Re_\lambda \approx 435$ and $C_d \approx 0.12$). The cases with $\rho_s = \infty$ and $\Delta\tilde{\rho} = \infty$ correspond to the configurations where the particles are retained fixed. In addition to the cases reported in the table, we have performed another set of simulations in the fixed-particle arrangement varying N and D or c (the results of which are reported in figure 5).

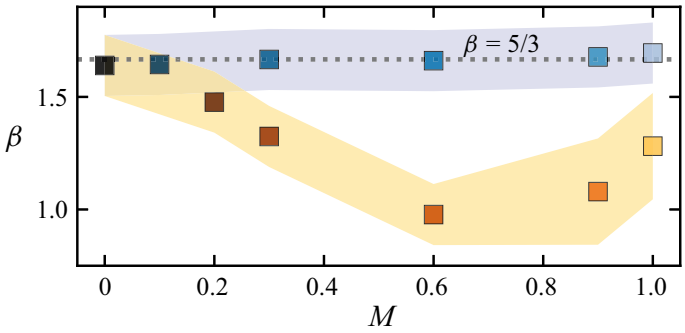

Figure 3. Dependence of the exponent β in the energy spectrum scaling $E \sim \kappa^{-\beta}$ on particle mass fraction M. Flows with spheres are marked in blue, flows with fibres in orange, and the single-phase flow in black. The blue and orange shaded regions show the approximate error in β, estimated by moving the time averaging window. The Kolmogorov scaling is marked by a grey dotted line.

particles, the energy-containing scales are depleted by the hydrodynamic drag exerted by the particles. A direct indication on how the bulk properties of the flow are altered is provided in the insets of figure 2, showing a very similar variation between spheres and fibres in terms of Re_λ with the mass fraction, notwithstanding the different Stokes numbers of the suspended objects, in agreement with previous findings (Hwang & Eaton 2006; Olivieri *et al.* 2021, 2022).

However, from figure 2 some peculiar differences between the two kinds of suspensions can also be noticed when extending the observation to the full range of active scales. For bluff particles, the alteration of the energy spectrum with M remains almost entirely limited to the low-wavenumber region (i.e. $\kappa \lesssim 5$), with only a minimal increase at the largest wavenumbers (i.e. $\kappa \gtrsim 300$) associated with the high-shear regions in the boundary layers around the spheres. Instead, for fibres, the modulation extends up to the highest wavenumber (i.e. $\kappa_{max} = 512$). At sufficiently large M, a departure from the Kolmogorov scaling indeed appears throughout the full inertial subrange. We anticipate that here the energy transfer is mainly due to the fluid–solid coupling, and not to the convective term as in the single-phase or bluff particle cases, leading to a different form of energy flux.

A quantitative evaluation of the resulting power law $E(\kappa) \sim \kappa^{-\beta}$ in the inertial subrange of both single-phase and multiphase flows is given in figure 3, showing the scaling exponent β as a function of the mass fraction for both spheres and fibres. The single-phase flow ($M = 0$) and the flows with spheres can be seen to follow the Kolmogorov scaling ($\beta = 5/3$), whereas the flows with fibres show a significant reduction in β as M increases. An heuristic explanation for the latter trend is that fibres act as a barrier to the flow between any two points with separation greater than the fibre diameter d, which influences the scaling of the second-order velocity structure function $\langle(\delta u)^2\rangle \sim r^\gamma$ for two points at a distance $r > d$, with $\gamma = \beta - 1$. In the single-phase case $\gamma = 2/3$, whereas the presence of fibres tends to decorrelate the flow, thus reducing the value of γ or, equivalently, β.

3.2. *Scale-by-scale energy transfer*

A clear distinction in the mechanism of energy distribution between the two geometrical configurations can be highlighted. To gain a more detailed insight, we look at the scale-by-scale energy transfer balance

$$\mathcal{P}(\kappa) + \Pi(\kappa) + \Pi_{fs}(\kappa) + \mathcal{D}(\kappa) = \epsilon, \tag{3.1}$$

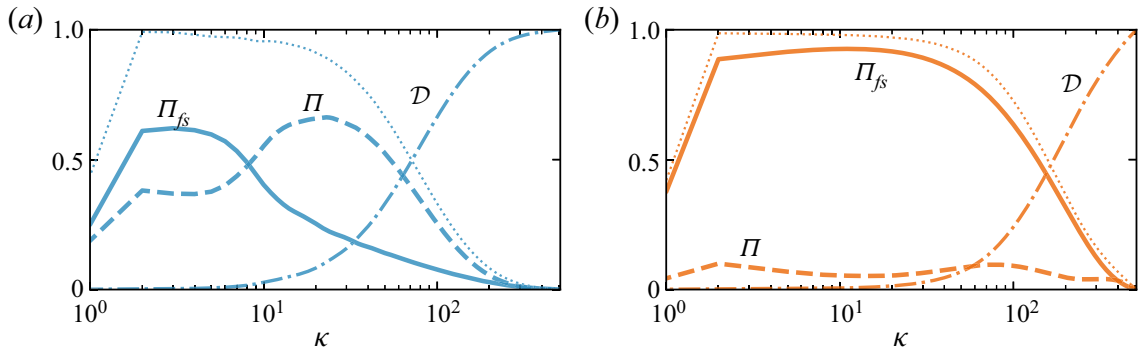

Figure 4. Scale-by-scale energy transfer balance for two representative configurations at $M = 0.9$ of (a) spheres and (b) fibres, showing the contributions of fluid–solid coupling Π_{fs} (solid line), nonlinear convection Π (dashed line) and viscous dissipation $\mathcal{D}$ (dash-dotted line), each normalized with the average dissipation rate ϵ. Furthermore, the total energy flux, $\Pi_{fs} + \Pi$, is also reported (dotted line).

where $\mathcal{P}$ is the turbulence production associated with the external forcing (acting only at the largest scale $\kappa = 1$), Π and Π_{fs} are the energy fluxes associated with the nonlinear convective term and the fluid–solid coupling term, respectively, and $\mathcal{D}$ is the viscous dissipation (Olivieri *et al.* 2021, 2022).

In figure 4, we show the energy fluxes and dissipation in two representative cases with strong back-reaction ($M = 0.9$) for (a) bluff objects and (b) slender particles. Focusing on the two different energy fluxes (i.e. Π and Π_{fs}), we note at first that the sum of these two contributions (thin dotted line) appears in both cases as a horizontal plateau for relatively low wavenumbers, as expected from (3.1) and similar to the single-phase case. However, qualitatively different scenarios can be identified for bluff versus slender objects when analysing the two distinct contributions separately. On the other hand, it can be noticed that in both cases, and similarly to the classical, single-phase case, for sufficiently large wavenumbers the energy fluxes tend to zero, and the viscous dissipation $\mathcal{D}$ recovers the totality of the balance.

For bluff objects (figure 4*a*), we first have a dominance of the fluid–solid coupling contribution Π_{fs} within a limited low-wavenumber range, and only subsequently of the convective term Π for larger κ. Indeed, two distinct plateau-like regions are found over two distinct subranges of scales, suggesting that, for increasing κ, the energy is first transferred from the largest scales (where energy is injected) to smaller ones mainly by the action of the particles, only after which the nonlinear term prevails and the balance substantially recovers the classical energy cascade predicted by Kolmogorov theory.

For slender objects (figure 4*b*), the scenario looks radically different, with Π_{fs} acting over a much wider range of scales and being responsible for transferring most of the energy across all scales, with the nonlinear term being weakened overall. It should also be noted that such alternative energy flux is overall prolonged with respect to the single-phase case, consistent with the observed alteration in the energy spectrum (figure 2*b*). Note that we refer to an energy flux also for fibre-laden turbulence, because not only is Π_{fs} constant across a wide range of scales, but also the overall drag coefficient $C_d = \epsilon/(u'^3\kappa_{in})$ here $\kappa_{in} = 1$ is the wavenumber at which the energy is injected (Alexakis & Biferale 2018), remains finite and comparable with the single-phase case (see table 1).

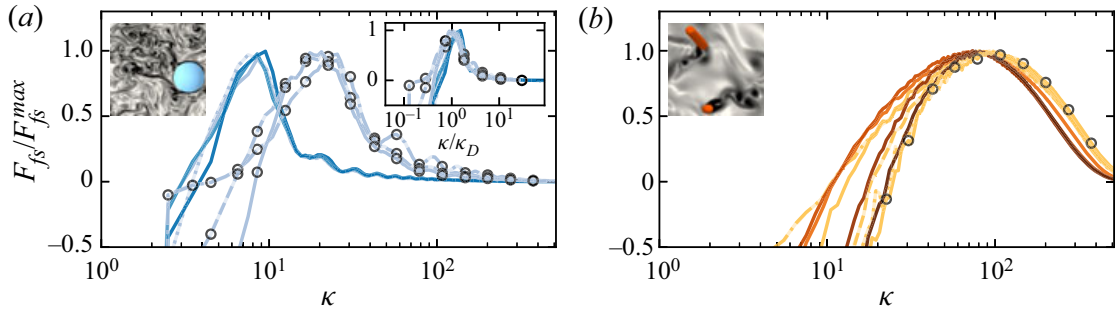

Figure 5. Fluid–solid coupling contribution to the energy-spectrum balance for (*a*) spheres and (*b*) fibres for various mass fractions M (varying with colour brightness). Circles are plotted for the cases with (*a*) smaller diameter D or (*b*) shorter length c, while different line styles are used to denote the variation of the number of objects N. For ease of comparison, the y-axis is normalized by the maximum value of the reported quantity. The inset in (*a*) shows the same data as a function of the wavenumber κ normalized with the sphere diameter D. Images show wakes that are similar in size to the (*a*) sphere diameter and (*b*) fibre diameter.

3.3. *Characteristic length scale of the fluid–solid coupling*

The reason for the observed difference between bluff and slender objects can be ascribed indeed to specific geometrical features. For bluff, isotropic particles the most representative scale is uniquely identified as the particle diameter D. For slender fibres, the back-reaction could be expected instead to act across multiple length scales, approximately ranging from the fibre length c to the cross-sectional diameter d. In fact, the latter is found to have the dominant role (as later shown in figure 5). This qualitative difference has a remarkable consequence on the properties of the modulated turbulent flow at sufficiently small scales: on the one hand, spherical particles affect the flow essentially only at a scale that is well within the inertial range, without modifying the extension and energy amplitude of the latter; on the other hand, slender fibres are directly acting on wavenumbers that are also beyond the original energy cascade.

To isolate the characteristic length scale up to which the energy is transferred by the back-reaction for the two kinds of dispersed objects, we show in figure 5 the fluid–solid coupling contribution in the energy-spectrum balance, i.e. F_{fs}, such that $\int_\kappa^\infty F_{fs} = \Pi_{fs}$. To this aim, along with the variation of the mass fraction, we also consider the influence of the sphere diameter D or fibre length c in the limiting case of fixed objects (or infinite inertia). For bluff (isotropic) objects (figure 5*a*), it can be clearly observed that the peak of F_{fs} scales with the diameter D, as also shown from the inset, where the wavenumber is normalized using such quantity. For slender (anisotropic) objects (figure 5*b*), we observe instead that the fibre length c does not appreciably change the position of the peak of F_{fs}; rather, it appears to be controlled by the fibre diameter d. Differently from spheres, here the fluid–solid contribution shows a wider distribution, therefore suggesting a quantitative role of the fibre length as well, as previously suggested. For both objects, the mass fraction appears to control not the wavenumber associated with the maximum forcing but only the strength of the back-reaction. Remarkably, the same holds also when varying the number of objects N.

3.4. *Phenomenological interpretation*

A simple and effective interpretation of our results can be proposed by considering the characteristic Reynolds number experienced by the particles, i.e. $Re_\ell = u'\ell/\nu$, in order to argue the main hydrodynamic effect caused by the solid objects and discern peculiar

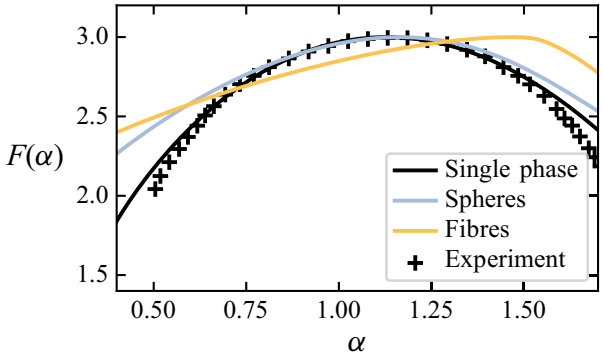

Figure 6. Multifractal distribution of the kinetic energy dissipation rate in the single-phase flow (black), flow with spheres of mass fraction $M = 1$ (blue), flow with fibres of mass fraction $M = 1$ (orange), and the single-phase experimental measure from Sreenivasan & Meneveau (1988) (black crosses).

differences between bluff and slender objects. For the sake of simplicity, we consider the root mean square of the fluid velocity fluctuations u' (accounting for its variation due to the effective back-reaction) and the sphere diameter D or the fibre diameter d as the reference length scale ℓ. For the spherical particles such a choice is natural, whilst for fibres it comes from that previously observed for the energy-transfer balance (figure 5*b*).

When computing the characteristic Reynolds number, we typically find that for spheres $Re_D \sim O(10^3)$, whereas for fibres $Re_d \sim O(10^1)$. These estimates suggest that bluff and slender objects experience qualitatively different hydrodynamic regimes, one dominated by inertial and the other by viscous forces, respectively. In particular, spheres are subject to a large-Reynolds-number flow, inducing a turbulent wake on scales comparable with and smaller than D, while fibres generate flow structures typical of laminar vortex shedding on scales comparable with d, but without any further proliferation of scales due to the dominant viscous dissipation. Note that here we refer to the range of scales smaller than the characteristic length scale associated with the individual particles. For spheres, the energy of the generated wakes is therefore converted into smaller structures by means of the well-known energy cascading process (controlled by the nonlinear term Π); for fibres, a similar phenomenology is not possible since the smaller-scale generated flow structures are essentially within the dissipative region.

3.5. *On the intermittency of the modulated turbulence*

Strong spatial and/or temporal fluctuations in the energy flux are the source of intermittency in turbulent flows. Owing to the different nature of the flux in the two configurations, it is natural to wonder how intermittency is altered. A comprehensive approach to study this is to compute the multifractal spectrum of the energy dissipation rate (Sreenivasan & Meneveau 1988), which we report in figure 6. For spheres, we find that $F(\alpha)$ is substantially similar to the single-phase case with only minor differences. On the other hand, for fibres, we have a remarkable qualitative difference in the spectrum. This further supports the idea of a standard energy cascade in particle-laden flows with finite-size spherical particles, whilst it is not the case for finite-size fibres.

4. Conclusions

By means of unprecedented high-Reynolds-number multiphase DNS, we have investigated particle-laden turbulent flows considering solid objects of finite size, i.e. well within the inertial range of scales, with the goal of understanding how the geometrical features of the

immersed objects impact on the basic mechanisms of turbulence modulation. Specifically, we have focused on two representative classes of suspensions, i.e. bluff (isotropic) spheres versus slender (anisotropic) fibres, as a benchmark for highlighting the effect of particle anisotropy.

As a common feature, we found that the presence of the dispersed phase induces a similar decrease of the turbulent kinetic energy and microscale Reynolds number for increasing mass fractions. At the same time, we unravelled the intrinsic differences in the resulting scale-by-scale energy distribution. For both kinds of dispersed objects, we have shown that the representative length scale at which the fluid–solid coupling is dominant is associated with the (sphere or fibre) diameter. For finite-size spherical objects, however, the back-reaction due to the dispersed phase is always confined to relatively large scales, with a negligible alteration of the higher-wavenumber inertial and viscous subrange. Finite-size fibres, on the other hand, transfer energy up to the smallest scales, with a consequent modification of the full energy spectrum and the emergence of a modified energy cascade. Note that, while confirming the same phenomenology, these results substantially enrich those recently reported at lower Reynolds number (Olivieri *et al.* 2022), in particular, concerning the evaluation of the scaling exponent in the modulated intermediate range of the energy spectrum. Also, the high-Reynolds-number configuration and the consequent scale separation clarified the different nature of the dominant energy flux in fibre-laden flows.

A simple phenomenological description for this complex problem is that the immersed objects subtract energy from the flow by means of hydrodynamic drag and then re-inject it by their wakes. For spheres, this happens fully within the inertial subrange and therefore results in a turbulent wake that still contributes to the classical energy cascade. For fibres, the transfer involves significantly smaller scales where viscosity eventually dominates, providing to the latter additional energy with little contribution of the nonlinear terms due to the low local Reynolds number.

In conclusion, we underline that these results are unique for finite-size objects and remarkably different from what was previously observed for small particles (i.e. those whose size is smaller than the Kolmogorov dissipative length scale). Our findings have primary relevance for advancing the fundamental understanding of particle-laden turbulence and its numerous related applications (e.g. slurry flows, combustion, papermaking and other industrial processes).

Acknowledgements. The authors acknowledge the computer time provided by the Scientific Computing section of the Research Support Division at the Okinawa Institute of Science and Technology Graduate University (OIST) and the computational resources of the supercomputer Fugaku provided by RIKEN through the HPCI System Research Project (project IDs: hp210229 and hp210269).

Funding. The research was supported by the Okinawa Institute of Science and Technology Graduate University (OIST) with subsidy funding from the Cabinet Office, Government of Japan.

Declaration of interests. The authors report no conflict of interest.

Data availability statement. The data that support the findings of this study are available from the corresponding authors upon reasonable request.

Author ORCIDs.
Stefano Olivieri https://orcid.org/0000-0002-7795-6620;
Ianto Cannon https://orcid.org/0000-0002-1676-9338;
Marco E. Rosti https://orcid.org/0000-0002-9004-2292.

References

Alexakis, A. & Biferale, L. 2018 Cascades and transitions in turbulent flows. *Phys. Rep.* **767**, 1–101.

Andersson, H.I., Zhao, L. & Barri, M. 2012 Torque-coupling and particle–turbulence interactions. *J. Fluid Mech.* **696**, 319–329.

Ardekani, M.N., Rosti, M.E. & Brandt, L. 2019 Turbulent flow of finite-size spherical particles in channels with viscous hyper-elastic walls. *J. Fluid Mech.* **873**, 410–440.

Balachandar, S. & Eaton, J.K. 2010 Turbulent dispersed multiphase flow. *Annu. Rev. Fluid Mech.* **42**, 111–133.

Bounoua, S., Bouchet, G. & Verhille, G. 2018 Tumbling of inertial fibres in turbulence. *Phys. Rev. Lett.* **121** (12), 124502.

Brandt, L. & Coletti, F. 2021 Particle-laden turbulence: progress and perspectives. *Annu. Rev. Fluid Mech.* **54**, 159–189.

Breard, E.C.P., Lube, G., Jones, J.R., Dufek, J., Cronin, S.J., Valentine, G.A. & Moebis, A. 2016 Coupling of turbulent and non-turbulent flow regimes within pyroclastic density currents. *Nat. Geosci.* **9** (10), 767–771.

Brizzolara, S., Rosti, M.E., Olivieri, S., Brandt, L., Holzner, M. & Mazzino, A. 2021 Fiber tracking velocimetry for two-point statistics of turbulence. *Phys. Rev.* X **11** (3), 031060.

Cannon, I., Izbassarov, D., Tammisola, O., Brandt, L. & Rosti, M.E. 2021 The effect of droplet coalescence on drag in turbulent channel flows. *Phys. Fluids* **33** (8), 085112.

Capecelatro, J., Desjardins, O. & Fox, R.O. 2018 On the transition between turbulence regimes in particle-laden channel flows. *J. Fluid Mech.* **845**, 499–519.

Cavaiola, M., Olivieri, S. & Mazzino, A. 2020 The assembly of freely moving rigid fibres measures the flow velocity gradient tensor. *J. Fluid Mech.* **894**, A25.

De Lillo, F., Cencini, M., Durham, W.M., Barry, M., Stocker, R., Climent, E. & Boffetta, G. 2014 Turbulent fluid acceleration generates clusters of gyrotactic microorganisms. *Phys. Rev. Lett.* **112** (4), 044502.

Dodd, M.S. & Ferrante, A. 2016 On the interaction of Taylor length scale size droplets and isotropic turbulence. *J. Fluid Mech.* **806**, 356–412.

Falkinhoff, F., Obligado, M., Bourgoin, M. & Mininni, P.D. 2020 Preferential concentration of free-falling heavy particles in turbulence. *Phys. Rev. Lett.* **125** (6), 064504.

Freund, A. & Ferrante, A. 2019 Wavelet-spectral analysis of droplet-laden isotropic turbulence. *J. Fluid Mech.* **875**, 914–928.

Gualtieri, P., Picano, F., Sardina, G. & Casciola, C.M. 2013 Clustering and turbulence modulation in particle-laden shear flows. *J. Fluid Mech.* **715**, 134–162.

Hori, N., Rosti, M.E. & Takagi, S. 2022 An Eulerian-based immersed boundary method for particle suspensions with implicit lubrication model. *Comput. Fluids* **236**, 105278.

Huang, W.-X., Shin, S.J. & Sung, H.J. 2007 Simulation of flexible filaments in a uniform flow by the immersed boundary method. *J. Comput. Phys.* **226** (2), 2206–2228.

Hwang, W. & Eaton, J.K. 2006 Homogeneous and isotropic turbulence modulation by small heavy ($St \sim 50$) particles. *J. Fluid Mech.* **564**, 361–393.

Lucci, F., Ferrante, A. & Elghobashi, S. 2010 Modulation of isotropic turbulence by particles of Taylor length-scale size. *J. Fluid Mech.* **650**, 5–55.

Lucci, F., Ferrante, A. & Elghobashi, S. 2011 Is Stokes number an appropriate indicator for turbulence modulation by particles of Taylor-length-scale size? *Phys. Fluids* **23** (2), 025101.

Maxey, M. 2017 Simulation methods for particulate flows and concentrated suspensions. *Annu. Rev. Fluid Mech.* **49**, 171–193.

Olivieri, S., Akoush, A., Brandt, L., Rosti, M.E. & Mazzino, A. 2020*a* Turbulence in a network of rigid fibers. *Phys. Rev. Fluids* **5** (7), 074502.

Olivieri, S., Brandt, L., Rosti, M.E. & Mazzino, A. 2020*b* Dispersed fibers change the classical energy budget of turbulence via nonlocal transfer. *Phys. Rev. Lett.* **125** (11), 114501.

Olivieri, S., Mazzino, A. & Rosti, M.E. 2021 Universal flapping states of elastic fibers in modulated turbulence. *Phys. Fluids* **33** (7), 071704.

Olivieri, S., Mazzino, A. & Rosti, M.E. 2022 On the fully coupled dynamics of flexible fibres dispersed in modulated turbulence. *J. Fluid Mech.* **946**, A34.

Podvigina, O. & Pouquet, A. 1994 On the non-linear stability of the 1: 1: 1 ABC flow. *Phys.* D*: Nonlinear Phenomen.* **75** (4), 471–508.

Rosti, M.E. & Brandt, L. 2020 Increase of turbulent drag by polymers in particle suspensions. *Phys. Rev. Fluids* **5** (4), 041301.

ROSTI, M.E., CAVAIOLA, M., OLIVIERI, S., SEMINARA, A. & MAZZINO, A. 2021 Turbulence role in the fate of virus-containing droplets in violent expiratory events. *Phys. Rev. Res.* **3** (1), 013091.

ROSTI, M.E., GE, Z., JAIN, S.S., DODD, M.S. & BRANDT, L. 2019 Droplets in homogeneous shear turbulence. *J. Fluid Mech.* **876**, 962–984.

ROSTI, M.E., OLIVIERI, S., CAVAIOLA, M., SEMINARA, A. & MAZZINO, A. 2020 Fluid dynamics of COVID-19 airborne infection suggests urgent data for a scientific design of social distancing. *Sci. Rep.* **10** (1), 22426.

SENGUPTA, A., CARRARA, F. & STOCKER, R. 2017 Phytoplankton can actively diversify their migration strategy in response to turbulent cues. *Nature* **543** (7646), 555–558.

SREENIVASAN, K.R. & MENEVEAU, C. 1988 Singularities of the equations of fluid motion. *Phys. Rev.* A **38** (12), 6287–6295.

UHLMANN, M. & CHOUIPPE, A. 2017 Clustering and preferential concentration of finite-size particles in forced homogeneous-isotropic turbulence. *J. Fluid Mech.* **812**, 991–1023.

WANG, C., YI, L., JIANG, L. & SUN, C. 2022 How do the finite-size particles modify the drag in Taylor–Couette turbulent flow. *J. Fluid Mech.* **937**, A15.

YOUSEFI, A., ARDEKANI, M.N. & BRANDT, L. 2020 Modulation of turbulence by finite-size particles in statistically steady-state homogeneous shear turbulence. *J. Fluid Mech.* **899**, A19.

Appendix D

Chapter 5 appendix

D.1 Governing equations

This section provides information on the physical model considered in the present study. We first introduce the governing equations for the fluid flow, and then we provide an overview of how the solid phase is modelled.

D.1.1 The carrier flow

We consider the turbulent 1:1:1 ABC flow, i.e., a Newtonian fluid that obeys the well-known incompressible Navier-Stokes equations

$$\begin{cases} \frac{\partial \boldsymbol{u}}{\partial t} + (\boldsymbol{u} \cdot \boldsymbol{\nabla})\, \boldsymbol{u} = -\frac{1}{\rho_f} \boldsymbol{\nabla} p + \nu \boldsymbol{\nabla}^2 \boldsymbol{u} + \boldsymbol{f} + \boldsymbol{f}^{\leftarrow p}, \\ \boldsymbol{\nabla} \cdot \boldsymbol{u} = 0, \end{cases} \tag{D.1}$$

where $\boldsymbol{u} = \boldsymbol{u}(\boldsymbol{x}, t)$ and $p = p(\boldsymbol{x}, t)$ are the velocity and pressure fields, ρ_f and ν are the fluid volumetric density and kinematic viscosity, and $\boldsymbol{f}^{\leftarrow p}$ is a singular force distribution used to mimic the presence of the dispersed solid objects by indirectly imposing the no-slip condition at the fluid-solid interface. The Navier–Stokes equations are forced with the ABC forcing Podvigina and Pouquet (1994b), i.e.,

$$\boldsymbol{f} = F_o \begin{pmatrix} A \sin(2\pi z/L) + C \cos(2\pi y/L) \\ B \sin(2\pi x/L) + A \cos(2\pi z/L) \\ C \sin(2\pi y/L) + B \cos(2\pi x/L) \end{pmatrix} \tag{D.2}$$

where $A = B = C = 1$, L is the forcing wavelength, and F_o is a constant that determines its intensity. The forcing is set to achieve a Reynolds number of $Re = U_o L_o/\nu \approx 894$, where L_o and U_o are the reference length and velocity scales, defined as $L_o = L/2\pi$ and $U_o = \sqrt{F_o L_o}$. In the single-phase configuration, this leads to a micro-scale Reynolds number of $Re_\lambda = u'\lambda/\nu \approx 435$, where u' is the root-mean-square of the velocity fluctuations, and λ is the Taylor length scale.

Figure D.1 depicts the resulting energy spectrum (left) and energy-transfer balance for the single-phase configuration (right). The energy-transfer balance derives after manipula-

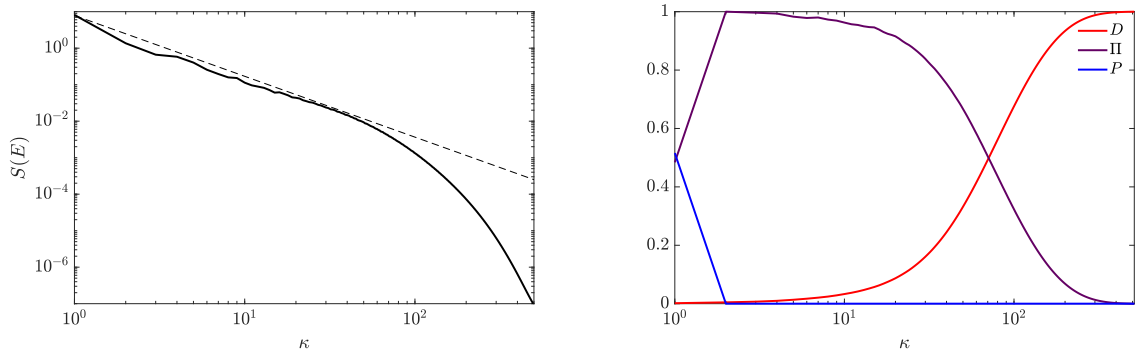

Figure D.1: Left: Energy spectrum for the single-phase configuration. The dashed line denotes the $-5/3$ power law predicted by the Kolmogorov theory. Right: energy-transfer balance for the single-phase configuration. The terms in the energy budget are normalised with the dissipation rate ϵ.

tion of the Navier–Stokes equations (Pope, 2000) and reads:

$$P(\kappa) + \Pi(\kappa) + D(\kappa) = \epsilon, \tag{D.3}$$

where

$$P(\kappa) = \int_{\kappa}^{\infty} \frac{1}{2} \left(\hat{\boldsymbol{f}} \cdot \hat{\boldsymbol{u}}^* + \hat{\boldsymbol{u}} \cdot \hat{\boldsymbol{f}}^* \right) \mathrm{d}\tilde{\kappa}, \tag{D.4a}$$

$$\Pi(\kappa) = \int_{\kappa}^{\infty} -\frac{1}{2} \left(\hat{\boldsymbol{G}} \cdot \hat{\boldsymbol{u}}^* + \hat{\boldsymbol{u}} \cdot \hat{\boldsymbol{G}}^* \right) \mathrm{d}\tilde{\kappa}, \tag{D.4b}$$

$$D(\kappa) = \int_{0}^{\kappa} \left(-2\nu\tilde{\kappa}^2 \hat{E} \right) \mathrm{d}\tilde{\kappa}. \tag{D.4c}$$

Here $\hat{\cdot}$ denotes the Fourier transform, the $*$ superscript denotes complex conjugate, $\hat{\boldsymbol{G}}$ is the Fourier transform of the non linear term $\boldsymbol{u} \cdot \boldsymbol{\nabla u}$, and ϵ is the dissipation. As clearly visible by means of the energy spectrum (left) and of the plateau of the non-linear flux Π (right), the Reynolds number considered in this work leads to a proper scale separation, with an inertial range that extends to almost two decades of wavenumbers.

D.1.2 The solid phase

We consider suspensions of solid spherical particles. The velocity at an arbitrary point $\boldsymbol{x}$ inside the particle, $\boldsymbol{u}_p(\boldsymbol{x}(t), t)$, can be described using the translational velocity, $\boldsymbol{v}_p$, and the rotational velocity, $\boldsymbol{\omega}_p$, of its centre of mass $\boldsymbol{x}_p$, as

$$\boldsymbol{u}_p = \boldsymbol{v}_p + \boldsymbol{\omega}_p \times \boldsymbol{r}, \tag{D.5}$$

where $\boldsymbol{r} = \boldsymbol{x} - \boldsymbol{x}_p$ is the vector going from $\boldsymbol{x}_p$ to $\boldsymbol{x}$. The time evolution of the spherical particles is, therefore, based on the classical Newton-Euler equations for rigid body dynamics

that read

$$\begin{cases} m_p \frac{\mathrm{d}\boldsymbol{v}_p}{\mathrm{d}t} & = \boldsymbol{f}^{\leftarrow f} + \boldsymbol{f}^{\leftrightarrow p}, \\ I_p \frac{\mathrm{d}\boldsymbol{\omega}_p}{\mathrm{d}t} & = \boldsymbol{L}_p^{\leftarrow f}, \end{cases} \tag{D.6}$$

where $m_p = \pi \rho_p D^3/6$ and $I_p = m_p D^2/10$ are the mass and inertial moment of the particle, with ρ_p being the particle density and D the particle diameter. Here $\boldsymbol{f}^{\leftrightarrow p}$ is the force due to the interaction between particles, and $\boldsymbol{f}_p^{\leftarrow f}$ and $\boldsymbol{L}_p^{\leftarrow f}$ are the force and momentum due to the fluid-solid interaction, defined as

$$\boldsymbol{f}_p^{\leftarrow f} = \oint_{\partial V_p} \boldsymbol{\sigma} \cdot \boldsymbol{n} \mathrm{d}A, \tag{D.7a}$$

$$\boldsymbol{L}_p^{\leftarrow f} = \oint_{\partial V_p} \boldsymbol{r} \times (\boldsymbol{\sigma} \cdot \boldsymbol{n}) \, \mathrm{d}A. \tag{D.7b}$$

Here, $\boldsymbol{\sigma} = -p\mathbb{I} + 2\mu\mathbb{D}$ is the Cauchy stress tensor, where $\mathbb{I}$ is the identity tensor, μ the kinematic fluid viscosity, and $\mathbb{D}$ the strain rate tensor, and $\boldsymbol{n}$ is the unit vector normal to the surface of the particle.

D.2 Numerical method

The above-discussed governing equations are numerically integrated using the in-house solver Fujin (`https://groups.oist.jp/cffu/code`), which is based on an incremental pressure-correction scheme. It considers the Navier–Stokes equations written in primitive variables in a staggered grid, and uses second-order finite differences in all the directions. The Adams-Bashforth time scheme is used for advancing the momentum equation in time. The Poisson equation for the pressure enforcing the incompressibility constraint is solved using a fast and efficient approach based on the Fast Fourier Transform. The solver is parallelised and is based on a Cartesian block decomposition of the domain in the x and y directions, and uses the Message Passing Interface (MPI) library for maximum portability. The governing equations for the particles are dealt with using the immersed boundary method introduced by Hori et al. (2022). The fluid-solid coupling is achieved in an Eulerian framework (Kajishima et al., 2001), and accounts for the inertia of the fictitious fluid inside the solid phase, to properly reproduce their behaviour in both the neutrally-buoyant case and in the presence of density difference between the fluid and solid phase. The soft sphere collision model first proposed by Tsuji et al. (1993) is used to prevent the interpenetration between particles. A fixed-radius near neighbours algorithm (see Monti et al., 2021, and references therein) is used for the particle interaction to avoid an otherwise prohibitive increase of the computational cost when the number of particles increases. The computational domain consists of a box of size L, and is discretised using $N = 1024$ equispaced points in the three directions, to ensure that for all cases, all the scales down to the smallest dissipative ones are solved, leading to $\eta/\Delta x = O(1)$, where Δx denotes the grid spacing and η is the Kolmogorov scale; see the single-phase scale-by-scale budget in the right panel of figure D.1. At the initial time, the particles are distributed randomly within the domain.

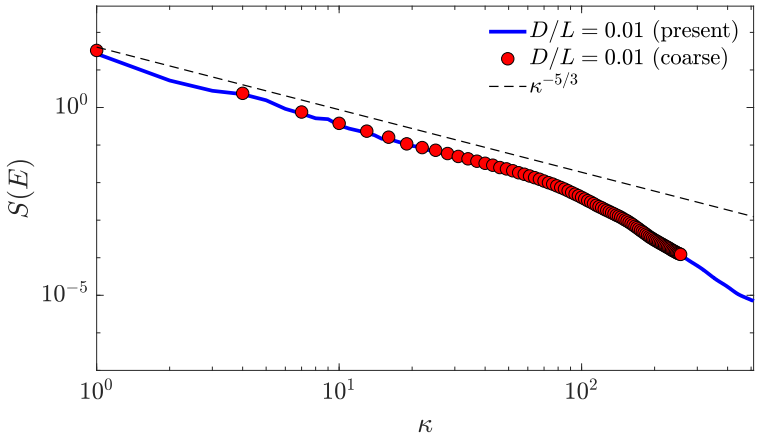

Figure D.2: Energy spectrum for $D/L = 0.0104$ ($D/\eta = 16$) and $M = 0.3$. The blue line is for the actual simulation with the $N = 1024$ grid. The red circles are for the simulation with the coarser $N = 512$ grid.

D.2.1 Grid independency

To demonstrate that the grid resolution is adequate for all particle sizes, an additional simulation has been carried out for the smallest particle size considered $D/L = 0.0104$ (or $D/\eta = 16$) and $M = 0.3$ (see table D.1). The number of grid points has been halved, leading to $N = 512$ equispaced points in the three directions. This means that the number of grid cells across each particle decreases from 16 with the standard grid, to 8 for the coarser grid. Figure D.2 shows that the energy spectra obtained with the two grids agree pretty well at all scales, confirming the adequacy of the considered grid resolution. All the presented results are obtained with the $N = 1024$ grid, to properly solve all the scales of the flow down to the Kolmogorov scale (in this case, $\eta/\delta_x = O(1)$).

D.3 List of investigated cases

Here we provide a list of the configurations that have been considered in the present work. The particle diameter is varied between $0.0207 \leq D/L \leq 0.0796$, or $16 \leq D/\eta \leq 123$ (here η refers to the single-phase Kolmogorov length-scale). The volume fraction is kept constant to a value of $\Phi_V = V_p/(V_p + V_f) = 0.0792$, where V_p is the total volume of particles, as in Olivieri, Cannon, et al. (2022), being large enough for a non-dilute suspension and small enough for the particle-particle collision to be subdominant. The number of particles N_p, thus, is increased as the particle diameter is decreased. The particle density ρ_p is varied between $1.3 \leq \rho_p/\rho_f \leq 105$ to consider both light and heavy particles, corresponding to a variation of the mass fraction $M = \rho_p V_p/(\rho_p V_p + \rho_f V_f)$ between $0.1 \leq M \leq 0.9$ and to a variation of the Stokes number St between $0.2 \lesssim St \lesssim 720$; the Stokes number is defined as $St = \tau_p/\tau_f$ where $\tau_p = (\rho_p/\rho_f)D^2/(18\nu)$ is the relaxation time of the particle velocity and $\tau_f = \mathcal{L}/\sqrt{2\overline{\langle E \rangle}/3}$ is the turnover time of the largest eddies ($\mathcal{L} = \pi/(4\overline{\langle E \rangle}/3)\int_0^\infty S(E)/\kappa \mathrm{d}\kappa$ is the fluid integral scale). Details of the numerical simulations are provided in table D.1,

together with the corresponding micro-scale Reynolds number Re_λ and the Stokes number.

All simulations have been advanced for approximately $18L_o/U_o$ time units, after reaching a statistically steady state. For $D/L = 0.0207$, or $D/\eta = 32$, the simulations have been advanced for a longer period, i.e. between $30L_o/U_o$ and $60L_o/U_o$, to ensure convergence of the large-scale statistics (e.g. the temporal mean flow) shown in the discussion.

D.4 The direction of the particles' trajectories changes with the initial condition

In this section, we show that the plane where the trajectories of the particles lay in the anisotropic state depends on the initial distribution of the particles, and that it is not dictated by the numerical code. As an example, we consider the $D/L = 0.0207$ particulate cases with $M = 0.6$ and $M = 0.75$. Here we denote with (x_s, y_s, z_s) the Cartesian reference system used in the simulation and with (x, y, z) the Cartesian reference system used for presenting the results; similarly, (U_s, V_s, W_s) and (U, V, W) are the temporal mean velocity components in the two sets of coordinates. Figure D.3 plots the three components of the mean velocity (U_s, V_s, W_s) in the $x_s = L/2$ plane for $M = 0.6$ (top) and $M = 0.75$ (bottom). For $M = 0.6$, particles are found to move along straight trajectories in the $x_s - y_s$ plane, attenuating thus the W_s component of the mean flow. In contrast, for $M = 0.75$, particles are found to move along straight trajectories in the $x_s - z_s$ plane, attenuating the V_s velocity components.

However, for the sake of clarity and uniformity of the results, when presenting the results in the main text, we adopt a Cartesian reference system (x, y, z) with the z direction being orthogonal to the particle trajectories for all cases. In the above $M = 0.75$ case, for example, $z_s \to x$, $x_s \to y$ and $y_s \to z$ ($W_s \to U$, $U_s \to V$ and $V_s \to W$).

D.5 ABC parameters that approximate the mean flow

In this section, we show how we evaluate the parameters of the generic ABC flow that approximates the mean flow, $\boldsymbol{U}$, of the turbulent single-phase and particulate configurations. The generic $2\pi L_0$-periodic ABC flow can be written as:

$$\boldsymbol{u}_{ABC} = V_o \begin{pmatrix} A\sin(z/L_o) + C\cos(y/L_o) \\ B\sin(x/L_o) + A\cos(z/L_o) \\ C\sin(y/L_o) + B\cos(x/L_o) \end{pmatrix}, \tag{D.8}$$

where A, B and C are bounded between 0 and 1 and determine the shape of the flow, and V_o is a constant that determines the flow magnitude. As discussed above, in the particulate cases, we chose the Cartesian reference system such that the z direction is aligned with the velocity component that is mostly attenuated by the particle motion (corresponding to the direction orthogonal to the particle trajectories for $D/L \leq 0.0414$ and $M \geq 0.45$). Without losing generality, thus, we set $A = 1$ for all cases and hypothesise that the solid phase modifies the values of B, C and V_o. The A, B, C and V_o parameters to use in equation D.8

Table D.1: Details of the numerical simulations carried out for the present parametric study. D is the particle diameter, η the Kolmogorov scale, N_p the number of particles, ρ_p and ρ_f the volumetric density of the fluid and the density of the particles, M the mass fraction, Re_λ is the Reynolds number based on $u' = \sqrt{2\overline{\langle E \rangle}/3}$ and on the Taylor length scale λ, St is the Stokes number (see text).

D/L	D/η	N_p	ρ_p/ρ_f	M	Re_λ	St
–	–	–	–	–	435.01	–
0.0796	123	300	1.3	0.1	434.05	10.39
0.0796	123	300	4.98	0.3	397.47	41.34
0.0796	123	300	17.44	0.6	347.48	133.43
0.0796	123	300	104.69	0.9	278.36	712.69
0.0414	64	2129	1.3	0.1	428.05	4.98
0.0414	64	2129	4.98	0.3	400.94	9.99
0.0414	64	2129	9.518	0.45	579.15	21.49
0.0414	64	2129	17.44	0.6	425.15	32.19
0.0414	64	2129	104.69	0.9	225.59	144.65
0.0207	32	17036	1.3	0.1	435.36	0.74
0.0207	32	17036	4.98	0.3	363.32	2.69
0.0207	32	17036	9.518	0.45	564.05	5.13
0.0207	32	17036	12.858	0.525	635.29	7.04
0.0207	32	17036	17.44	0.6	691.96	9.42
0.0207	32	17036	34.9	0.75	382.00	12.53
0.0207	32	17036	104.69	0.9	186.02	25.44
0.0104	16	136293	1.3	0.1	441.61	0.20
0.0104	16	136293	4.98	0.3	379.86	0.62
0.0104	16	136293	17.44	0.6	277.74	1.50
0.0104	16	136293	104.69	0.9	365.34	8.15

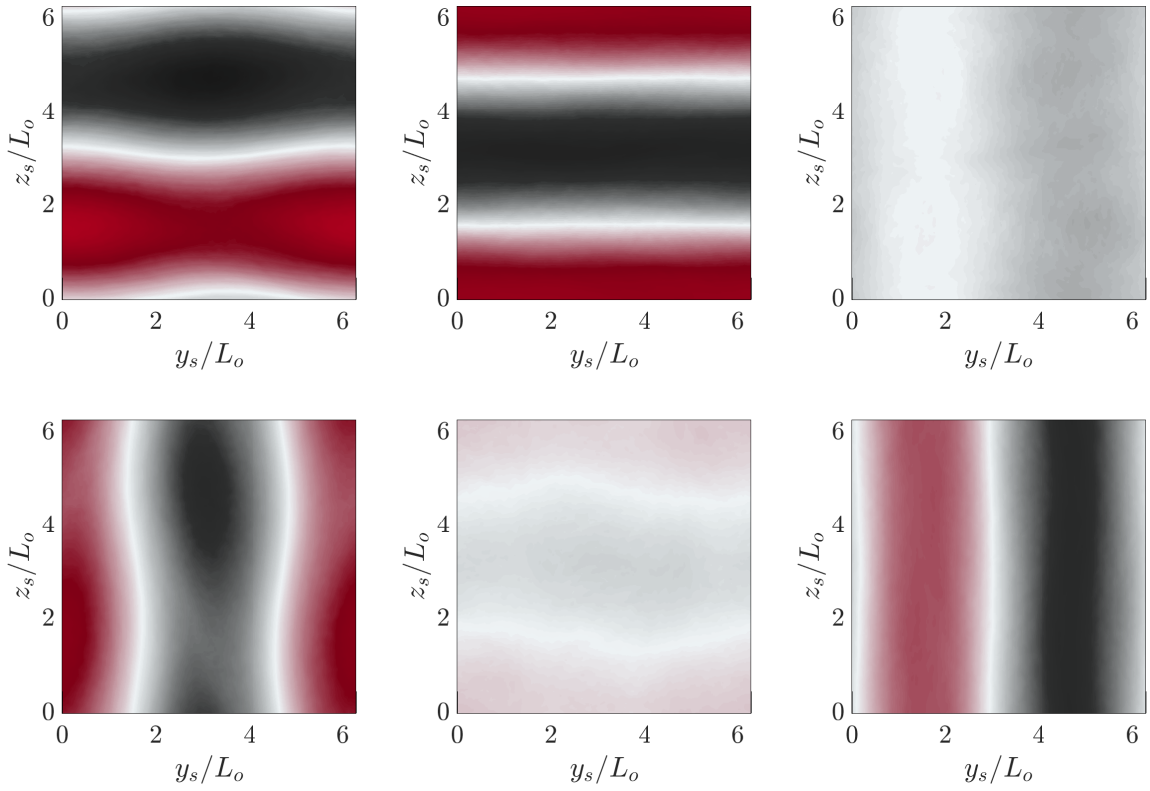

Figure D.3: Mean flow velocity components for the $D/L = 0.0207$ particulate case with $M = 0.6$ (top) and $M = 0.75$ (bottom) in the $x_s = \pi L_o$ plane, in the Cartesian reference system (x_s, y_s, z_s) of the simulation. From left to right the panels are for U_s, V_s and W_s, i.e. the components of the mean velocity aligned with three axes. The black-to-red colour map goes from $-9 \leq U_i/U_o \leq 9$.

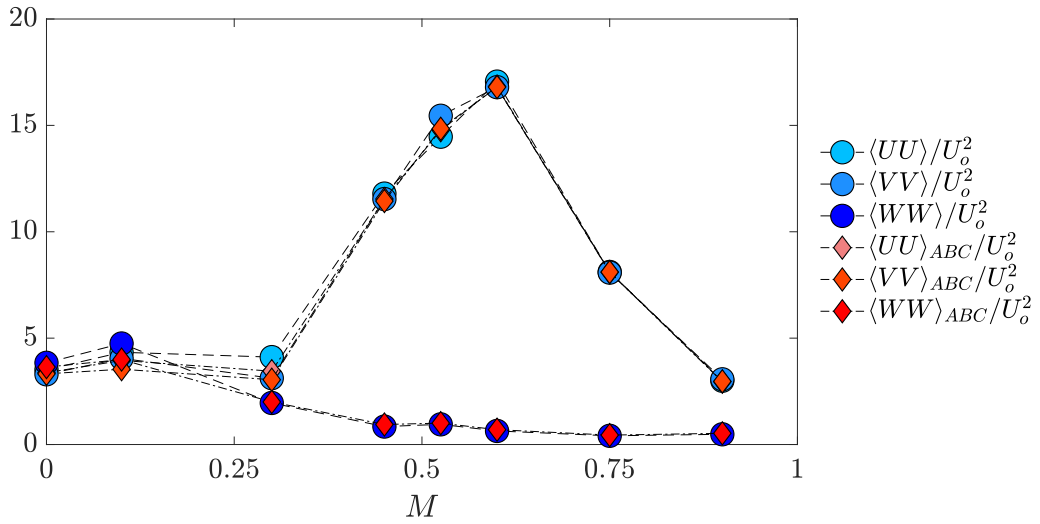

Figure D.4: Circles: variances of the mean velocity components for the single-phase case and for the $D/L = 0.0207$ particulate cases with $0.1 \leq M \leq 0.9$. Diamonds: variances of the components of the generic ABC flow that approximate the single-phase case and the $D/L = 0.0207$ particulate cases.

to approximate $\boldsymbol{U}$ are therefore obtained by solving the following system of equations:

$$\begin{cases} V_o A = \frac{1}{L^3}\int_0^L\int_0^L\int_0^L (U\sin(z/L_o) + V\cos(z/L_o))\,\mathrm{d}z\mathrm{d}y\mathrm{d}x \\ V_o B = \frac{1}{L^3}\int_0^L\int_0^L\int_0^L (V\sin(x/L_o) + W\cos(x/L_o))\,\mathrm{d}z\mathrm{d}y\mathrm{d}x \\ V_o C = \frac{1}{L^3}\int_0^L\int_0^L\int_0^L (W\sin(y/L_o) + U\cos(y/L_o))\,\mathrm{d}z\mathrm{d}y\mathrm{d}x \\ A = 1 \end{cases} . \tag{D.9}$$

Note, indeed, that when replacing (U, V, W) with the components of $\boldsymbol{u}_{ABC}$, the first three equations are identically satisfied.

As an example, figure D.4 plots the variances of the components of the temporal mean velocity $\boldsymbol{U}$ for the $D/L = 0.0207$ particulate cases with $0.1 \leq M \leq 0.9$ and shows that they are in pretty good agreement with the variances of the generic ABC flow obtained with the above-discussed procedure.

D.6 ABC laminar flow and Poincaré map

Figure D.5 shows the structure of the laminar ABC flow with $A = B = C = 1$ in the $x/L_o = \pi$ plane. The left panel is for u_{ABC}. The right panel, instead, shows the $x/L_o = \pi$ Poincaré section, which describes the Lagrangian structure of the flow. It is a two-dimensional coding of the three-dimensional ABC flow, in which we represent only successive intersections of the flow streamlines with the $x/L_o = \pi$ plane (Dombre et al., 1986; Poincaré, 1892). The density of the points in the Poincaré map is proportional to the magnitude of the velocity

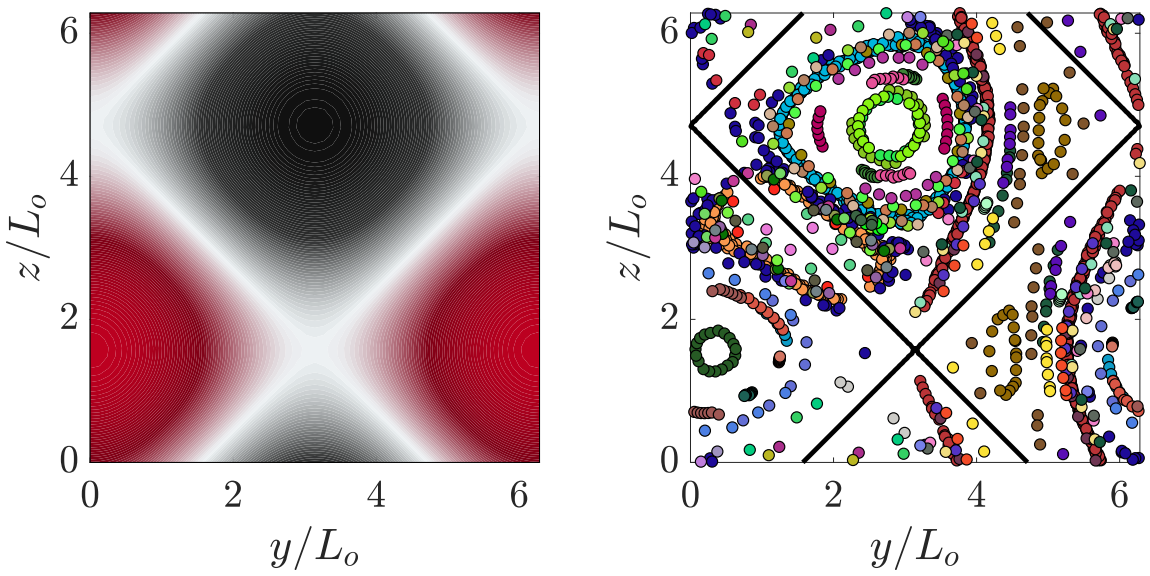

Figure D.5: Laminar ABC flow $\boldsymbol{u}_{ABC}$ with $A = B = C = 1$ in the $x/L_o = \pi$ plane. Left: u_{ABC}; the symmetric black-to-red comourmap goes from $-2 \leq u_{ABC} \leq 2$. Right: Poincaré map; each point of the same colour corresponds to a successive intersection with the $x/L_o = \pi$ plane of the same streamline. The black line is for $u_{ABC} = 0$.

component perpendicular to the plane. Here, indeed, the density of the points is null along the $\sin(z/L_o) + \cos(y/L_o) = 0$ line, where $u_{ABC} = 0$.

D.7 flow modulation as a function of m_p and ϕ_m

To provide a more exhaustive picture of the parameters at play, in this section, we show the dependence of the flow modulation on the mass loading and on the mass of the single particle.

Figure D.6 shows the flow modulation as a function of the mass loading $\phi_m = \rho_p V_p/(\rho_f V_f)$ and of the single-particle mass $m_p = \rho_p/\rho_f \pi/6\,(D/L_o)^3$. The mass loading is similar to the mass fraction, but is not bounded between 0 and 1; the two quantities are related by $\phi_m = M/(1-M)$. The dependence of $\overline{\langle E \rangle}/\overline{\langle E_o \rangle}$ on ϕ_m closely resemble the dependence on M, with the maximum energy enhancement observed for $\phi_m \approx 1.2$. Regarding m_p, instead, the right panel of figure D.6 shows that the energy enhancement and flow two-dimensionalisation occurs for a specific range of m_p, i.e. $10^{-2} \leq m_p \leq 10^{-1}$. This resembles the dependence of the results on the Stokes number St.

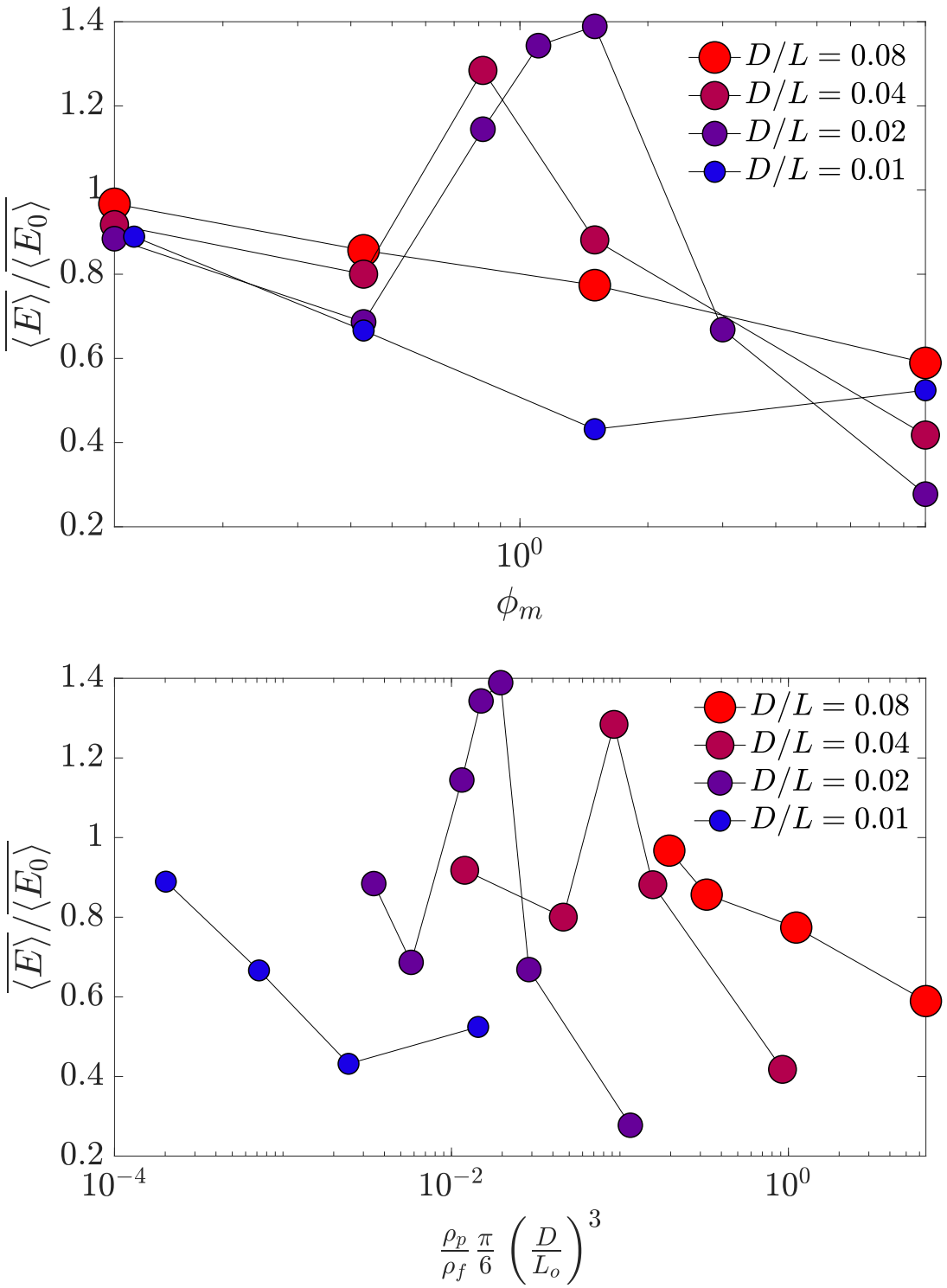

Figure D.6: Total kinetic energy of the flow as a function of the mass loading (left) and of the dimensionless particle mass $m_p = \rho_p/\rho_f \pi/6\,(D/L_o)^3$ (right).

D.8 On the physical mechanism

In this section, we shed light on the physical mechanism responsible for the flow two-dimensionalisation. Figure D.7 shows the time evolution of the anisotropy of the solid and fluid phases for $D/L = 0.02$ and $M = 0.75$. The flow approaches the isotropic regime before deviating towards the more energetic and anisotropic regime. The top panel details the instantaneous anisotropy of the fluid (symbols) and solid (lines) phases. The time signal shows that the anisotropy arises first in the fluid phase and then in the solid phase: the root mean squares of the three velocity components start differing at $t \approx 10U_o/L_o$ for the fluid phase, and at $t \approx 15U_o/L_o$ for the particles. This suggests that the transition from the isotropic state to the anisotropic one is driven by the fluid phase, and not directly by the particle motion. Based on this observation, we speculate that the flow two-dimensionalisation is the result of a bifurcation of the largest scales of the flow, triggered by the perturbations generated by the particles when they are not able to follow the cellular ABC pattern and tend to follow more straight trajectories. For small and large St, the flow remains in the isotropic regime, as the perturbation field induced by the solid phase does not have the proper spatial structure to induce this bifurcation. It is worth stressing that, when studying the sequence of bifurcations of the low-Re single-phase ABC flow, Podvigina and Pouquet (1994b) found in the chaotic regime a similar anisotropic state — referred to as $\mathcal{A}_2$ — with $B = C \approx 0.36A$, which spontaneously emerges for intermediate Re. It is thus possible that the presence of particles and their tendency to follow straight trajectories changes the stability of the system in the $5 \leq St \leq 60$ and $M > 0.3$ portion of the $M - St$ space of parameters, enabling thus the occurrence of an anisotropic $\mathcal{A}_2$-like state (which indeed favours straight streamlines) also at these larger Re.

The role of the inhomogeneous mean shear on the flow two-dimensionalisation has been investigated by considering a different volume forcing to sustain turbulence, that does not generate a coherent motion at the largest scales. In particular, we have carried out additional simulations of the flow in the 2π triperiodic box using the forcing introduced by Eswaran and Pope (1988) to sustain turbulence. For these additional simulations, the case with $D/L = 0.0207$ ($D/\eta = 32$) is considered and the Reynolds number is slightly smaller: in the single-phase reference case, it is set to $Re_\lambda \approx 330$. Figure D.8 compares the flow modulation as a function of the mass fraction for the two forcings. The blue circles refer to the results obtained with the ABC forcing, and the yellow squares refer to the random forcing. The two curves collapse pretty well for $M \leq 0.3$; here particles modulate all scales in an isotropic way in both cases. For larger M the two curves deviate: in the absence of the inhomogeneous mean shear, the flow energy monotonically decreases with M in agreement with the increase of the inertia of the system, and the energy enhancement associated with the flow two-dimensionalisation is not observed.

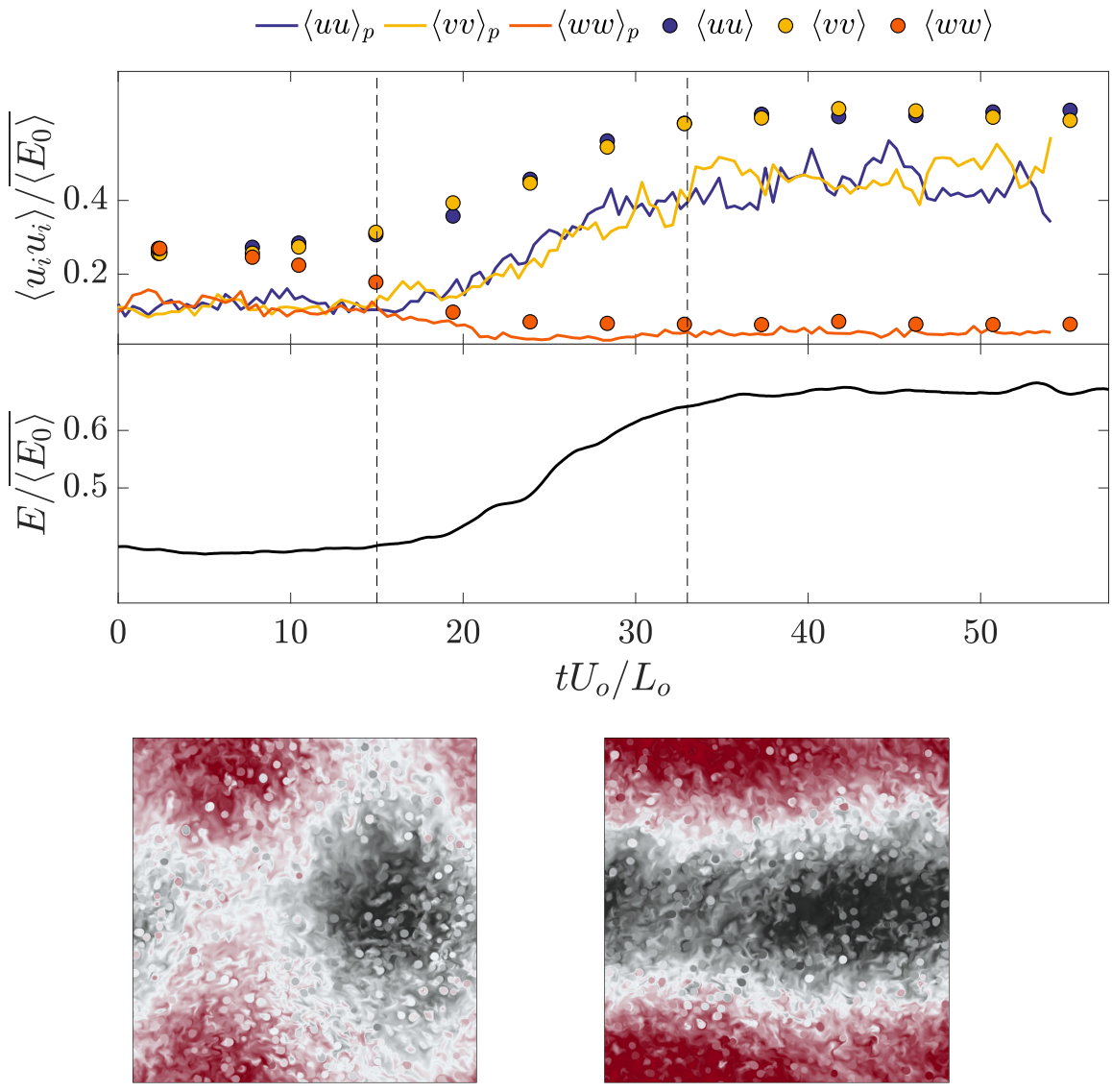

Figure D.7: Top: Evolution in time of the energy and of the particle and fluid velocity variances for $D/L = 0.02$ and $M = 0.75$. Bottom: instantaneous fluid velocity snapshots; the left panel is for the isotropic regime at $t \approx 10U_o/L_o$, while the right panel is for the anisotropic regime at $t \approx 40U_o/L_o$.

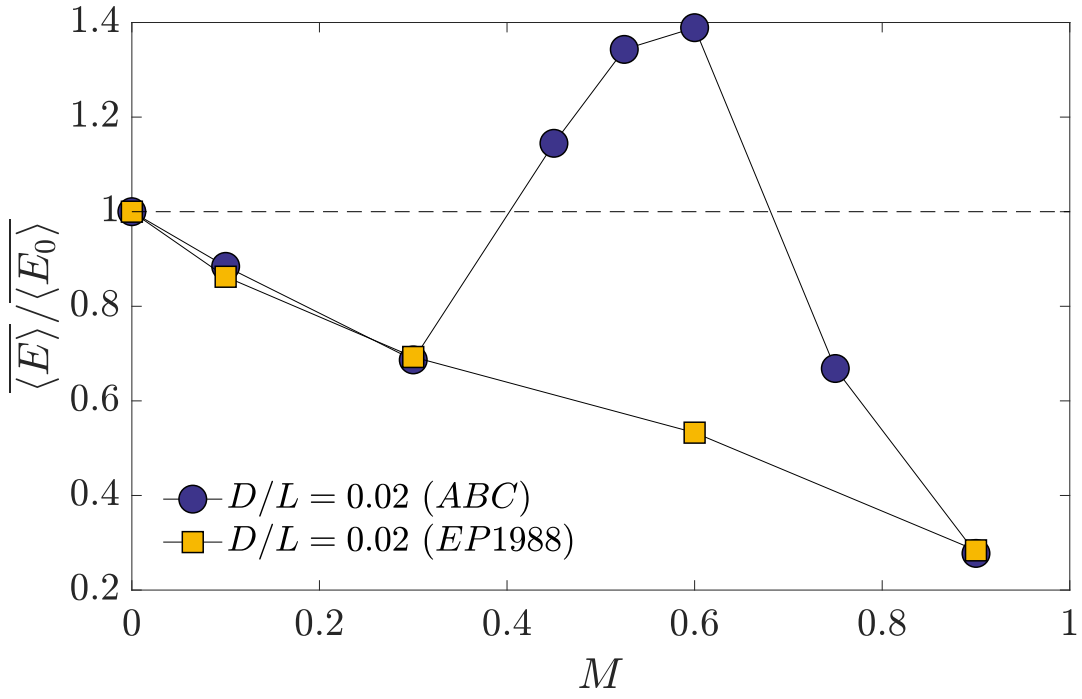

Figure D.8: Dependence of the flow modulation by particles on the external forcing. The blue circles are for the Arnold-Beltrami-Childress forcing. The yellow squares are for the Eswaran and Pope (1988)'s forcing

Appendix E

Chapter 6 appendix

nature physics

Article

https://doi.org/10.1038/s41567-023-02018-2

Scaling and intermittency in turbulent flows of elastoviscoplastic fluids

Received: 12 August 2022

Accepted: 7 March 2023

Published online: 13 April 2023

Check for updates

Mohamed S. Abdelgawad [1,2], Ianto Cannon [1,2] & Marco E. Rosti [1]

Non-Newtonian fluids have a viscosity that varies with applied stress. Elastoviscoplastic fluids, the elastic, viscous and plastic properties of which are interconnected in a non-trivial way, belong to this category. We have performed numerical simulations to investigate turbulence in elastoviscoplastic fluids at very high Reynolds-number values, as found in landslides and lava flows, focusing on the effect of plasticity. We find that the range of active scales in the energy spectrum reduces when increasing the fluid plasticity; when plastic effects dominate, a new scaling range emerges between the inertial range and the dissipative scales. An extended self-similarity analysis of the structure functions reveals that intermittency is present and grows with the fluid plasticity. The enhanced intermittency is caused by the non-Newtonian dissipation rate, which also exhibits an intermittent behaviour. These findings have relevance to catastrophic events in natural flows, such as landslides and lava flows, where the enhanced intermittency results in stronger extreme events, which are thus more destructive and difficult to predict.

Many fluids in nature and industry exhibit a nonlinear relationship between shear stress and shear rate, which is referred to as non-Newtonian behaviour. Several non-Newtonian features can exist, and they are often present simultaneously. In this Article we focus on the so-called elastoviscoplastic (EVP) fluids, which are fluids with elastic, viscous and plastic properties. EVP materials combine solid-like behaviour and fluid-like response depending on the value of the applied stress: they behave like a solid when the applied stress is below a critical value known as the 'yield stress', and flow like a liquid otherwise[1]. The elastic nature of these materials is present in their solid as well as liquid states[2]. Such fluids are common in everyday life (examples include toothpaste, jam, cosmetics and mud), and turbulent flows of EVP fluids are found in many industrial processes, including sewage treatment, crude oil transportation, concrete pumping and mud drilling[3–5], as well as in nature as landslides and lava flows[6,7].

A great deal of work has been done in the past to properly characterize the viscoelastic behaviour of a fluid in both laminar and turbulent flows[8–13], while the effect of plasticity has been studied mainly in low-Reynolds-number laminar conditions[1,14,15]. Little is known about the plastic behaviour of an EVP fluid in turbulence. Rosti et al.[16] studied a turbulent channel flow of an EVP fluid, finding that the shape of the mean velocity profile controls the regions where the fluid is unyielded, forming plugs around the channel centreline that grow in size as the yield stress increases, similar to what is observed in a laminar condition. However, the presence of the plug region has an opposite effect on drag for laminar and turbulent flow configurations, resulting in drag reduction in the turbulent case and drag increase in the laminar one; the turbulent drag behaviour is due to the tendency of the turbulent flow to relaminarize, overall leading to a strongly nonlinear relation between yield stress and drag coefficient. Simulation results were then employed by Le Clainche et al.[17], using high-order dynamic mode decomposition, to study the near-wall dynamics, comparing them to those in Newtonian and viscoelastic fluids. Their work revealed that both elasticity and plasticity have similar effects on the near-wall coherent structures, where the flow is characterized by long streaks disturbed for short periods by localized perturbations. A recent experimental study by Mitishita et al.[18] on a turbulent duct flow of Carbopol solution de facto verified the numerical results obtained by Rosti et al.[16] on the effect of plasticity on the mean flow profile and Reynolds stresses. Additionally, they observed an increase in the energy content

[1]Complex Fluids and Flows Unit, Okinawa Institute of Science and Technology Graduate University, Onna-son, Okinawa, Japan. [2]These authors contributed equally: Mohamed S. Abdelgawad, Ianto Cannon. e-mail: marco.rosti@oist.jp

https://doi.org/10.1038/s41567-023-02018-2

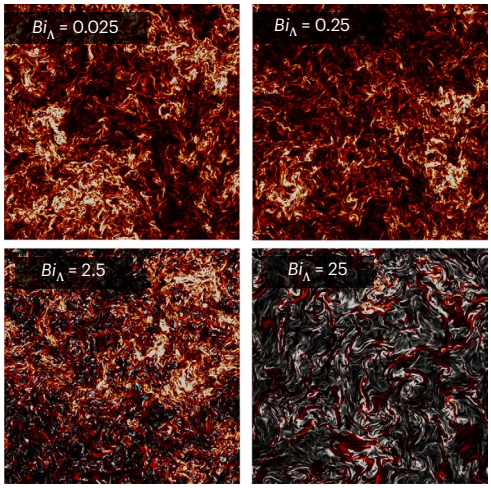

Fig. 1 | Instantaneous colourmaps of the turbulent fluid dissipation ϵ_f in homogeneous isotropic turbulence of an EVP fluid at different Bingham numbers. Yielded regions are shown with a black–red–yellow colourscale, and unyielded regions with black–grey–white.

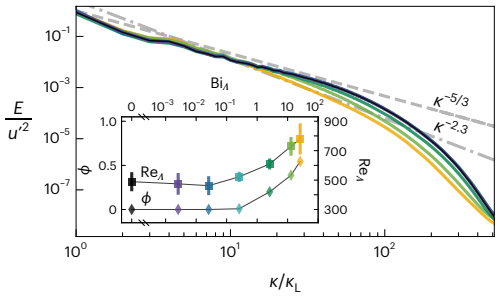

Fig. 2 | Turbulent kinetic energy spectra of EVP flows with various Bingham numbers. Different BIngham numbers are plotted in colours from dark to light; $Bi_\Lambda = 0$, 0.0025, 0.025, 0.25, 2.5, 12.5 and 25 are plotted in black, purple, dark blue, light blue, dark green, light green and orange, respectively. The expected Kolmogorov scaling for a Newtonian fluid is shown by a grey dashed line, and the grey dash-dotted line represents an apparent new non-Newtonian scaling $E \sim \kappa^{-2.3}$ that emerges at large Bi_Λ. Inset: variation of the mean values of the microscale Reynolds number Re_Λ (right axis, plotted as squares) and the volume fraction of the unyielded regions Φ (left axis, plotted as diamonds) as a function of Bi_Λ. Error bars report the s.d. of Re_Λ in time, measured using 10^3 samples. Plastic effects start to appear for $Bi_\Lambda \geq 1$, suggesting that Λ is the relevant length scale of the problem.

at large scales and a decrease at small scales, when compared with a Newtonian fluid. Mitishita et al. reported a −7/2 scaling in the energy spectra at high wavenumbers during Carbopol flows compared to −5/3 scaling in the case of water flows. The newly observed scaling was attributed either to the decrease in the inertial effect in the presence of Carbopol solutions, which shrinks the inertial range of scales because the Reynolds numbers are much lower than in water flows, or to the elastic effects that become important at large wavenumbers where the fluid experiences high frequencies. Moreover, the shear-thinning effects that Carbopol solutions exhibit affected the anisotropy and the overall flow behaviour. The elastic and shear-thinning effects are rheological features of Carbopol solutions and cannot be eliminated experimentally.

Homogeneous and isotropic turbulent flows have long been a focus of turbulence research for their simple theoretical analysis and the generality of their results. To this end, as has been extensively done in the past for viscoelastic flows, here we study tri-periodic homogeneous flow, where the celebrated K41 theory by Kolmogorov[19] can be directly applied to a classical Newtonian fluid. In this Article we study a homogeneous isotropic turbulent (HIT) flow of an EVP fluid at high Reynolds number, as shown in Fig. 1. We aim to answer the following fundamental question: how does the Kolmogorov theory change when the fluid is EVP? We will mainly focus on its plastic behaviour and investigate how the yield stress affects the multiscale energy distribution and balance, and how the turbulent energy cascade is altered by the fluid's plasticity. Our results show profound modifications of the classical picture predicted by the K41 theory for Newtonian fluids, with the emergence of a new scaling range, the dominance of the non-Newtonian flux and dissipation at small and intermediate scales, and enhanced intermittency of the flow.

Results

To investigate the problem at hand, we performed massive three-dimensional direct numerical simulations (DNS) of HIT where we solve the flow equations fully coupled with the constitutive equation of the EVP fluid, within a tri-periodic domain of size L, using 1,024 grid points per side, as described in more detail in the Methods. The flow is controlled by four main parameters: the Reynolds number Re_Λ, the Weissenberg number Wi_Λ, the viscosity ratio α and the Bingham number Bi_Λ, all based on the root-mean-square velocity fluctuations u' and Taylor's microscale Λ. We use the definitions $Re_\Lambda \equiv \rho u' \Lambda/\mu_t$, $Wi_\Lambda \equiv \lambda \mu_t/\rho \Lambda_0^2$, $\alpha = \mu_n/\mu_t$ and $Bi_\Lambda \equiv \tau_y \Lambda_0/\mu_t u'_0$, where ρ is the fluid density, $\mu_t \equiv \mu_f + \mu_n$ is the total dynamic viscosity with μ_f being the fluid viscosity and μ_n the non-Newtonian one, λ is the relaxation time, τ_y is the yield stress, and subscript 0 denotes quantities from the $Bi_\Lambda = 0$ case. The Reynolds number describes the ratio of inertial to viscous forces, and we limit our analysis to high-Reynolds-number flows, achieving a Taylor microscale Reynolds number $Re_\Lambda \approx 435$ for the Newtonian flow, at which statistics of the flow have been found to be universal and exhibiting a proper scale separation, with an extensive inertial range of scales extended to almost two decades of wavenumbers. The Reynolds number explored here is the highest in DNS of HIT of non-Newtonian fluids. The Weissenberg number describes the ratio of elastic to viscous forces, and here we limit the analysis to $Wi_\Lambda \ll 1$ (that is, $Wi_\Lambda \approx 10^{-3}$), to ensure that elastic effects are subdominant and all the observed changes are due to plasticity. We also fix a value of $\alpha = 0.1$ to represent a dilute concentration of polymers, in accordance with previous works on the subject[16,20]. Thus, the key control parameter we vary is Bi_Λ, which describes the ratio of the yield stress to the viscous stress, and thus correlates with the prevalence of unyielded regions.

Figure 2 depicts the turbulent kinetic energy spectra of the cases analysed. The $Bi_\Lambda = 0$ case is similar to the Newtonian case shown in Supplementary Fig. 1, confirming that the effect of elasticity is subdominant and can be ignored. A clear $E \sim \kappa^{-5/3}$ range is visible for more than one decade, showing that Re_Λ is high enough to achieve scale separation, with the spectra exhibiting an inertial range of scales followed by a dissipative range. As Bi_Λ increases, the inertial range is limited to the large scales (small wavenumbers κ), with the energy increasing at large scales and decreasing at small scales. A clear deviation from Kolmogorov scaling becomes noticeable for $Bi_\Lambda > 1$, resulting in the emergence of a new apparent scaling of $E \sim \kappa^{-2.3}$ that is shown more clearly by plotting compensated energy spectra (as shown in Supplementary Fig. 3). The difference in scaling between the experimental work (−7/2)[18] and the current study (−2.3) is mainly due to the higher values of Reynolds and Bingham numbers considered here. The abrupt change in the spectra with Bi_Λ is consistent with the bulk flow properties (Re_Λ and the volume fraction of the unyielded regions Φ) shown in the inset of Fig. 2: for the cases where $Bi_\Lambda < 1$, Re_Λ remains relatively unaltered, with Φ always close to zero, whereas when Bi_Λ further increases, the microscale Reynolds number Re_Λ and the volume Φ of the unyielded regions rapidly increase with a similar trend.

https://doi.org/10.1038/s41567-023-02018-2

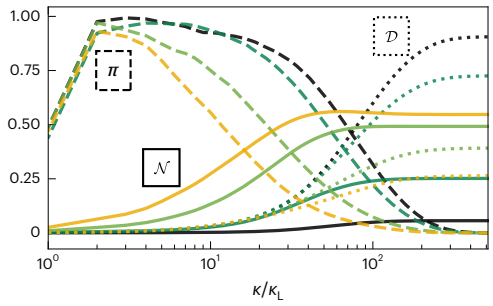

Fig. 3 | Scale-by-scale energy balance for different Bi_Λ. Plotted are the energy flux of the nonlinear convective term Π (dashed lines), solvent dissipation $\mathcal{D}$ (dotted lines) and the non-Newtonian contribution $\mathcal{N}$ (solid lines) for $Bi_\Lambda = 0$ (black), $Bi_\Lambda = 2.5$ (dark green), $Bi_\Lambda = 12.5$ (light green) and $Bi_\Lambda = 25$ (orange). Each term is normalized by the total dissipation rate $\langle\epsilon_t\rangle$. $\mathcal{N}$ grows at intermediate and small scales when Bi_Λ is increased, eventually becoming the dominant contribution.

To fully characterize the change in the energy spectra, we study the turbulent kinetic energy balance, which in wavenumber space can be expressed as

$$\mathcal{F}_{inj}(\kappa) + \Pi(\kappa) + \mathcal{D}(\kappa) + \mathcal{N}(\kappa) = \langle\epsilon_f\rangle + \langle\epsilon_n\rangle = \langle\epsilon_t\rangle, \quad (1)$$

where $\mathcal{F}_{inj}$ is the turbulence production introduced by the external forcing (injected at the largest scale, $\kappa_L \equiv 2\pi/L$), and Π, $\mathcal{D}$ and $\mathcal{N}$ are the nonlinear energy flux, the fluid dissipation and the non-Newtonian contribution, respectively. In addition to the classical bulk fluid dissipation rate ϵ_f, here we have a non-Newtonian dissipation ϵ_n, which is the rate of removal of turbulent kinetic energy from the flow due to the non-Newtonian extra stress tensor (Supplementary Sections I and II provide a derivation of this equation). Figure 3 shows the turbulent kinetic energy balance for a few representative values of Bi_Λ. When comparing with Supplementary Fig. 1b, the $Bi_\Lambda = 0$ case closely follows the classical Newtonian turbulent flow, where energy is carried by Π from the large to small scales before being dissipated by the fluid viscosity $\mathcal{D}$. The contribution of the nonlinear convective term Π, which appears as an almost horizontal plateau at relatively large scales, progressively decreases with Bi_Λ and shrinks towards larger scales, consistent with the reduction of the extension of the inertial range observed in Fig. 2. The reduced energy flux with Bi_Λ is also accompanied by a decrease of the fluid dissipation $\mathcal{D}$, which is instead compensated by the increase of non-Newtonian contribution $\mathcal{N}$. At small scales (large κ), the relative importance of the non-Newtonian contribution increases with Bi_Λ, becoming comparable to the fluid dissipation for $Bi_\Lambda \approx 2.5$ and eventually becoming the dominant term for $Bi_\Lambda \gtrsim 12.5$, corresponding to the emergence of the new scaling in the energy spectrum shown in Fig. 2; indeed, the non-Newtonian contribution can be interpreted as a combination of a pure energy flux (giving rise to the new scaling region) and a pure dissipative term, as recently suggested by Rosti and others[21]. Regarding the direction of energy flux, Supplementary Fig. 4 shows that we have a direct cascade of energy from large to small scales for all Bi_Λ (refs. 22,23).

We extend the analysis done in the spectral domain by computing the longitudinal structure functions defined as $S_p(r) = \langle(\Delta u(r))^p\rangle$, where p is the order of the structure function and $\Delta u(r) = u(x+r) - u(x)$ is the difference in the fluid velocity across a length scale r, projected in the direction of r. According to K41, $S_p(r) \sim (\langle\epsilon_t\rangle r)^{p/3}$; however, when the structure functions are displayed as a function of r, as shown in Fig. 4a, they deviate from the K41 prediction as p increases. This phenomenon is thought to be due to the intermittency of the flow, that is, extreme events that are localized in space and time, and thereby break Kolmogorov's hypothesis of self-similarity in the inertial range[24]. Intermittency results in the scaling exponent of r being a nonlinear concave function of p (instead of $p/3$)[25]. For the EVP fluid, two scaling regions appear at large Bi_Λ, with scaling consistent with those from the energy spectra, and with intermittency present in both scaling regions. The role of intermittency in the scaling exponents can be better appreciated when the structure functions are displayed in their extended self-similarity form, obtained by plotting one structure function against another[26]. In Fig. 4b, S_4 and S_6 are plotted against S_2 for all Bingham numbers considered. We note a clear power-law scaling, which deviates from Kolmogorov's prediction, even for the $Bi_\Lambda = 0$ case (shown in black). The departure from Kolmogorov's prediction progressively grows as the plasticity of the fluid increases, suggesting that the flow becomes more intermittent due to its plasticity. This becomes more obvious when we plot S_n compensated by the intermittency correction at $Bi_\Lambda = 0$ against S_2 (Supplementary Fig. 5). Also, intermittency appears to act equally in the two scaling regions present at large Bi_Λ.

Intermittency originates from the multifractal nature of the turbulent dissipation rate[24]. For Newtonian fluids, this can be quantified by the multifractal spectrum of the energy dissipation rate, ϵ_f (refs. 24,27), which we report in the inset of Fig. 4b. This graph demonstrates that $F(\alpha)$ is nearly identical for all Bi_Λ cases except for minor variations at small and large values of α. This implies that the fluid dissipation rate is not the cause of the enhanced intermittency observed in the extended self-similarity analysis.

In the present flow, the turbulent kinetic energy is dissipated by two different terms, ϵ_f and ϵ_n, as seen in Fig. 1. We thus investigate their respective behaviour by looking at their probability distribution functions (PDFs; Fig. 5). We name the non-Newtonian contribution ϵ_n a 'dissipation' because, on average, it removes energy from the flow, giving rise to the positive-skewed distributions in Fig. 5b; however, unlike the fluid dissipation, it can take positive or negative values at particular locations in space and time. Figure 5a shows that the distribution of ϵ_f narrows as Bi_Λ increases[28]; on the other hand, from Fig. 5b, we see that that the distribution of ϵ_n substantially broadens as Bi_Λ increases. Because the non-Newtonian dissipation becomes dominant for the largest Bi_Λ (as shown in Fig. 3), we can thus infer that the extreme values of ϵ_n are indeed the source of the enhanced intermittency observed from the structure function analysis in Fig. 4.

Discussion

By means of unprecedented high-Reynolds-number DNS of an EVP fluid, we have shown that plastic effects substantially alter the classical turbulence predicted by Kolmogorov theory for Newtonian fluids.

We have proved that the non-Newtonian contribution to the energy balance becomes dominant at intermediate and small scales for large Bingham numbers, inducing the emergence of a new intermediate scaling range in the energy spectra between the Kolmogorov inertial and dissipative ranges, where the energy spectrum decays with a −2.3 exponent. Interestingly, this exponent has been recently found for the turbulence of viscoelastic fluids at large Reynolds and Weissenberg numbers[21,29], suggesting a possible similarity among plastic and elastic effects on the turbulent cascade. This similarity in the scaling behaviour of the two cases could be attributed to a similar interaction mechanism in the Navier–Stokes equation between the convective and extra stress terms. It is also worth noting that in the context of viscoelastic flows at high Weissenberg number, an exponent less than or equal to −3 has been widely reported in the past[8]; however, this is only found at relatively lower Reynolds number than investigated here or explored in recent experimental and numerical work[21,29]. The present work reports the −2.3 scaling in turbulent flows of highly plastic EVP fluids, and further studies on the size and distribution of the unyielded regions could shed more light on the origin of the newly found scaling.

We have also shown that the flow in the presence of plastic effects is more intermittent than in a Newtonian fluid, due to the combination of the classical intermittency originating from the multifractal

https://doi.org/10.1038/s41567-023-02018-2

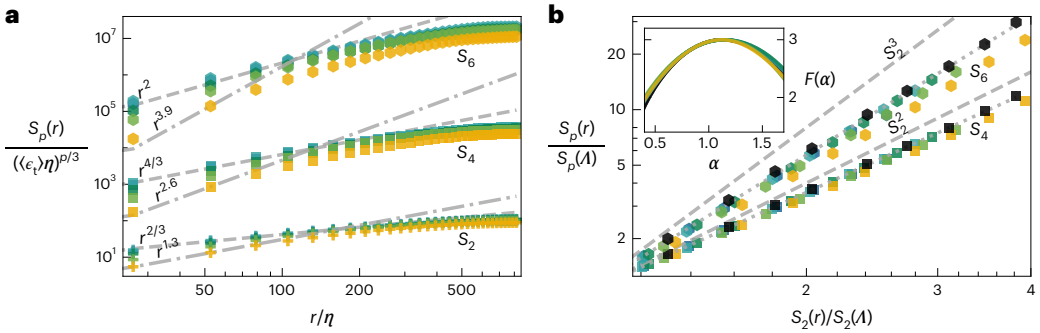

Fig. 4 | Analysis of structure functions. a, Dependence of the longitudinal velocity structure functions S_2 (pluses), S_4 (squares) and S_6 (hexagons) on separation distance r. Symbol colour denotes Bi_Λ and is the same as in Fig. 2. Dashed lines show scalings predicted by K41, and dash-dotted lines show scalings predicted using the new non-Newtonian scaling $E \sim \kappa^{-2.3}$. **b**, The two scalings collapse onto a single line when we plot the structure functions S_4 and S_6 in extended self-similarity form, that is, against S_2. To easily see changes in gradient, we have normalized the structure functions by their values at $r \approx \Lambda$. The dotted line shows a best fit through the data for $\mathrm{Bi}_\Lambda = 0$, which deviates from the K41 prediction (dashed line) due to intermittency. Increasing Bi_Λ further increases this deviation. The inset in **b** reports the multifractal spectrum of the energy dissipation rate carried out by the fluid ϵ_f.

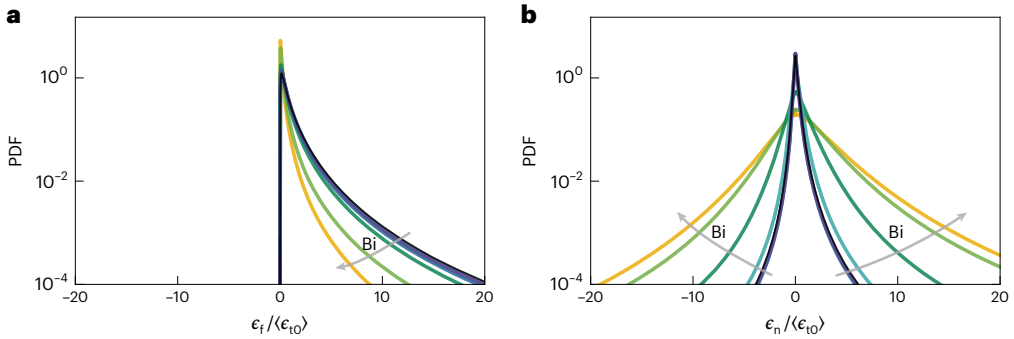

Fig. 5 | PDFs of the fluid dissipation rate ϵ_f and non-Newtonian dissipation rate ϵ_n. a,**b**, PDF of the fluid dissipation rate ϵ_f (**a**) and of the non-Newtonian dissipation rate ϵ_n (**b**) averaged over time, and normalized by $\langle\epsilon_0\rangle$, the total dissipation of the $\mathrm{Bi}_\Lambda = 0$ flow. As Bi_Λ increases, the PDF of ϵ_f narrows slightly, whereas the PDF of ϵ_n widens substantially.

nature of the turbulent dissipation rate, which remains substantially unaltered, and a new plastic contribution that instead grows with the Bingham number. A direct consequence of this result is that intermittency corrections for an EVP fluid are non-universal and dependent on the flow configuration, differently from viscoelastic flows. These results are relevant for several catastrophic natural flows with high plasticity, such as lava flows and landslides[30]. Our findings explain why such flows are usually found to be intermittent and frequently aggressive, resulting in more damage. The non-universality of the flow intermittency in EVP fluids reflects also in an increased difficulty in their modelling.

Online content

Any methods, additional references, Nature Portfolio reporting summaries, source data, extended data, supplementary information, acknowledgements, peer review information; details of author contributions and competing interests; and statements of data and code availability are available at https://doi.org/10.1038/s41567-023-02018-2.

References

1. Balmforth, N. J., Frigaard, I. A. & Ovarlez, G. Yielding to stress: recent developments in viscoplastic fluid mechanics. *Annu. Rev. Fluid Mech.* **46**, 121–146 (2014).
2. Fraggedakis, D., Dimakopoulos, Y. & Tsamopoulos, J. Yielding the yield-stress analysis: a study focused on the effects of elasticity on the settling of a single spherical particle in simple yield-stress fluids. *Soft Matter* **12**, 5378–5401 (2016).
3. Hanks, R. W. The laminar-turbulent transition for flow in pipes, concentric annuli and parallel plates. *Aiche J.* **9**, 45–48 (1963).
4. Hanks, R. W. On the flow of Bingham plastic slurries in pipes and between parallel plates. *Soc. Petrol. Eng. J.* **7**, 342–346 (1967).
5. Maleki, A. & Hormozi, S. Submerged jet shearing of visco-plastic sludge. *J. Non-Newtonian Fluid Mech.* **252**, 19–27 (2018).
6. Jerolmack, D. J. & Daniels, K. E. Viewing Earth's surface as a soft-matter landscape. *Nat. Rev. Phys.* **1**, 716–730 (2019).
7. Jones, T. J., Reynolds, C. D. & Boothroyd, S. C. Fluid dynamic induced break-up during volcanic eruptions. *Nat. Commun.* **10**, 3828 (2019).
8. Groisman, A. & Steinberg, V. Elastic turbulence in a polymer solution flow. *Nature* **405**, 53–55 (2000).
9. Poole, R. J., Alves, M. A. & Oliveira, P. J. Purely elastic flow asymmetries. *Phys. Rev. Lett.* **99**, 164503 (2007).
10. Haward, S. J., Mckinley, G. H. & Shen, A. Q. Elastic instabilities in planar elongational flow of monodisperse polymer solutions. *Sci. Rep.* **6**, 33029 (2016).
11. Steinberg, V. Elastic turbulence: an experimental view on inertialess random flow. *Annu. Rev. Fluid Mech.* **53**, 27–58 (2021).
12. Datta, S. S. et al. Perspectives on viscoelastic flow instabilities and elastic turbulence. *Phys. Rev. Fluids* **7**, 080701 (2022).
13. Abreu, H., Pinho, F. T. & da Silva, C. B. Turbulent entrainment in viscoelastic fluids. *J. Fluid Mech.* **934**, A36 (2022).

14. Pavlov, K. B., Romanov, A. S. & Simkhovich, S. L. Hydrodynamic stability of poiseuille flow of a viscoplastic non-Newtonian fluid. *Fluid Dynamics* **9**, 996–998 (1974).
15. Escudier, M. P. et al. Observations of asymmetrical flow behaviour in transitional pipe flow of yield-stress and other shear-thinning liquids. *J. Non-Newtonian Fluid Mech.* **127**, 143–155 (2005).
16. Rosti, M. E., Izbassarov, D., Tammisola, O., Hormozi, S. & Brandt, L. Turbulent channel flow of an elastoviscoplastic fluid. *J. Fluid Mech.* **853**, 488–514 (2018).
17. Le Clainche, S., Izbassarov, D., Rosti, M., Brandt, L. & Tammisola, O. Coherent structures in the turbulent channel flow of an elastoviscoplastic fluid. *J. Fluid Mech.* **888**, A5 (2020).
18. Mitishita, R. S., MacKenzie, J. A., Elfring, G. J. & Frigaard, I. A. Fully turbulent flows of viscoplastic fluids in a rectangular duct. *J. Non-Newtonian Fluid Mech.* **293**, 104570 (2021).
19. Kolmogorov, A. The local structure of turbulence in incompressible viscous fluid for very large Reynolds' numbers. *Akademiia Nauk SSSR Doklady* **30**, 301–305 (1941).
20. Perlekar, P., Mitra, D. & Pandit, R. Manifestations of drag reduction by polymer additives in decaying, homogeneous, isotropic turbulence. *Phys. Rev. Lett.* **97**, 3–6 (2006).
21. Rosti, M. E., Perlekar, P. & Mitra, D. Large is different: non-monotonic behaviour of elastic range scaling in polymeric turbulence at large Reynolds and Deborah numbers. *Sci. Adv.* **9**, eadd3831 (2023).
22. Xia, H., Byrne, D., Falkovich, G. & Shats, M. Upscale energy transfer in thick turbulent fluid layers. *Nat. Phys.* **7**, 321–324 (2011).
23. Cerbus, R. T. & Chakraborty, P. The third-order structure function in two dimensions: the Rashomon effect. *Phys. Fluids* **29**, 111110 (2017).
24. Frisch, U. *Turbulence: The Legacy of A. N. Kolmogorov* (Cambridge Univ. Press, 1995).
25. Kolmogorov, A. N. A refinement of previous hypotheses concerning the local structure of turbulence in a viscous incompressible fluid at high Reynolds number. *J. Fluid Mech.* **13**, 82–85 (1962).
26. Benzi, R. et al. Extended self-similarity in turbulent flows. *Phys. Rev. E* **48**, R29–R32 (1993).
27. Mandelbrot, B. B. Intermittent turbulence in self-similar cascades: divergence of high moments and dimension of the carrier. *J. Fluid Mech.* **62**, 331–358 (1974).
28. Donzis, D. A., Sreenivasan, K. R. & Yeung, P. K. Scalar dissipation rate and dissipative anomaly in isotropic turbulence. *J. Fluid Mech.* **532**, 199–216 (2005).
29. Zhang, Y. B., Bodenschatz, E., Xu, H. & Xi, H. D. Experimental observation of the elastic range scaling in turbulent flow with polymer additives. *Sci. Adv.* **7**, eabd3525 (2021).
30. Schaeffer, D. G. & Iverson, R. M. Steady and intermittent slipping in a model of landslide motion regulated by pore-pressure feedback. *SIAM J. Appl. Math.* **69**, 769–786 (2008).

Methods

Governing equations

The flow under investigation is governed by a system of a scalar, a vector and a tensorial equation—the incompressibility constraint, the conservation of momentum, and the constitutive equation for the non-Newtonian extra stress tensor, respectively. The incompressibility constraint and the momentum conservation equations can be written as

$$\nabla \cdot \mathbf{u} = 0, \tag{2}$$

$$\rho\left(\frac{\partial \mathbf{u}}{\partial t} + \mathbf{u} \cdot \nabla \mathbf{u}\right) = \nabla p + \mu_f \nabla^2 \mathbf{u} + \mathbf{f}_{inj} + \mathbf{f}_{evp}, \tag{3}$$

where $\mathbf{u}$ is the fluid velocity, p is the pressure, ρ is the density and μ_f is the fluid dynamic viscosity. The term $\mathbf{f}_{inj}$ represents the external force used to sustain turbulence; here we consider the Arnold–Beltrami–Childress (ABC) flow with forcing

$$\begin{aligned}\mathbf{f}_{inj} = {} & \mathbf{i}\mu_f(A \sin z/L + C \cos y/L) + \mathbf{j}\mu_f(B \sin y/L + A \cos z/L) \\ & + \mathbf{k}\mu_f(C \sin y/L + B \cos x/L),\end{aligned} \tag{4}$$

where $\mathbf{i}$, $\mathbf{j}$ and $\mathbf{k}$ are the Cartesian unit vectors, A, B and C are real parameters, and the flow has periodicity L in x, y and z. In our simulations, we choose $A = B = C$ and use an appropriate value of μ_f to give a microscale Reynolds number $\mathrm{Re}_\lambda \approx 435$ for the Newtonian flow. The last term in equation (3) is defined as $\mathbf{f}_{evp} \equiv \nabla \cdot \boldsymbol{\tau}$, where $\boldsymbol{\tau}$ is the non-Newtonian extra stress tensor of the EVP fluid. We adopt the constitutive model proposed by Saramito[31] to express the evolution of the extra stress tensor, which can be written as

$$\lambda \overset{\nabla}{\boldsymbol{\tau}} + \max\left(0, \frac{\tau_d - \tau_y}{\tau_d}\right)\boldsymbol{\tau} = \mu_n\left(\nabla \mathbf{u} + (\nabla \mathbf{u})^T\right) \tag{5}$$

where $(\overset{\nabla}{})$ denotes the upper convected derivative, that is, $\overset{\nabla}{\boldsymbol{\tau}} = \frac{\partial \boldsymbol{\tau}}{\partial t} + \mathbf{u} \cdot \nabla \boldsymbol{\tau} - \boldsymbol{\tau} \cdot \nabla \mathbf{u} - (\nabla \mathbf{u})^T \cdot \boldsymbol{\tau}$. μ_n is the non-Newtonian dynamic viscosity, τ_d is the magnitude of the deviatoric part of the stress tensor $\boldsymbol{\tau}_d \equiv \boldsymbol{\tau} - \mathrm{tr}(\boldsymbol{\tau})\mathbf{I}/3$, and $\mathbf{I}$ is the identity tensor, that is, $\tau_d = \sqrt{\frac{1}{2}(\boldsymbol{\tau}_d : \boldsymbol{\tau}_d)}$. Before yielding, that is, $\tau_d \le \tau_y$, the model predicts only recoverable Kelvin–Voigt viscoelastic deformation; after yielding, that is, $\tau_d > \tau_y$, it predicts Oldroyd-B viscoelastic behaviour. This transition occurs in a continuous manner. There are other EVP models that take into account shear-thinning[32] or thixotropic behaviour[33]; however, we chose the one described above for its simplicity and the least number of involved parameters. Also, this model proved able to capture the main flow characteristics in a turbulent channel flow[16,18].

Numerical method

We use the in-house flow solver Fujin (https://groups.oist.jp/cffu/code) to solve the governing equations numerically on a staggered uniform Cartesian grid. Velocities are located on the cell faces, and pressure, stresses and the other material properties are located at the cell centres. The second-order central finite-difference scheme is used for spatial discretization except for the advection term that comes from the upper convective derivative in equation (5), where the fifth-order WENO (weighted essentially non-oscillatory) scheme is adopted[34]. The second-order Adams–Bashforth scheme coupled with a fractional step method[35] is used for the time advancement of all terms except for the non-Newtonian extra stress tensor, which is advanced with the Crank–Nicolson scheme. To enforce a divergence-free velocity field, a fast Poisson solver based on the fast Fourier transform is used for the pressure. The domain decomposition library 2decomp (http://www.2decomp.org) and the MPI protocol are used to parallelize the solver. The evolution equation of the extra EVP stress is formulated and solved using the log-conformation method[36] to ensure the positive-definiteness of the conformation tensor. The fluid domain is a periodic cubic box of length L discretized using 1,024 grid points per side, resulting in a large grid resolution sufficient to represent the fluid properties at all the scales of interest with $\eta/\Delta x = \mathcal{O}(1)$, where η is the Kolmogorov length-scale, and Δx is the grid spacing.

Data availability

All data needed to evaluate the conclusions are presented in the paper and/or the Supplementary Information. Data that support the findings of this study are openly available in OIST at https://groups.oist.jp/cffu/abdelgawad2023natphys.

Code availability

The code used for the present research is a standard direct numerical simulation solver for the Navier–Stokes equations. Full details of the code used for the numerical simulations are provided in the Methods and references therein.

References

31. Saramito, P. A new constitutive equation for elastoviscoplastic fluid flows. *J. Non-Newtonian Fluid Mech.* **145**, 1–14 (2007).
32. Saramito, P. A new elastoviscoplastic model based on the Herschel-Bulkley viscoplastic model. *J. Non-Newtonian Fluid Mech.* **158**, 154–161 (2009).
33. Dimitriou, C. J. & McKinley, G. H. A canonical framework for modeling elasto-viscoplasticity in complex fluids. *J. Non-Newtonian Fluid Mech.* **265**, 116–132 (2019).
34. Shu, C. W. High order weighted essentially nonoscillatory schemes for convection dominated problems. *SIAM Rev.* **51**, 82–126 (2009).
35. Kim, J. & Moin, P. Application of a fractional-step method to incompressible Navier-Stokes equations. *J. Comput. Phys.* **59**, 308–323 (1985).
36. Izbassarov, D. et al. Computational modeling of multiphase viscoelastic and elastoviscoplastic flows. *Int. J. Numer. Methods Fluids* **88**, 521–543 (2018).

Acknowledgements

The research was supported by the Okinawa Institute of Science and Technology Graduate University (OIST) with subsidy funding from the Cabinet Office, Government of Japan. We acknowledge the computer time provided by the Scientific Computing section of the Research Support Division at OIST and the computational resources of the supercomputer Fugaku provided by RIKEN through the HPCI System Research Project (project IDs, hp210229 and hp210269).

Author contributions

M.E.R. conceived the original idea, planned the research and developed the code. All authors performed the numerical simulations, analysed data, outlined the manuscript content and wrote the manuscript.

Competing interests

The authors declare no competing interests.

Additional information

Supplementary information The online version contains supplementary material available at https://doi.org/10.1038/s41567-023-02018-2.

Correspondence and requests for materials should be addressed to Marco E. Rosti.

Peer review information *Nature Physics* thanks Cherif Nouar and the other, anonymous, reviewer(s) for their contribution to the peer review of this work.

nature physics

Article

https://doi.org/10.1038/s41567-023-02018-2

Scaling and intermittency in turbulent flows of elastoviscoplastic fluids

In the format provided by the authors and unedited

SUPPLEMENTARY INFORMATION

Scaling and intermittency in turbulent flows of elastoviscoplastic fluids

Mohamed S. Abdelgawad, Ianto Cannon, and Marco E. Rosti

I. SCALE-BY-SCALE ENERGY BALANCE

This section gives a derivation of equation (1) from the main article. Firstly, we perform the Fourier transform of the Navier-Stokes equations to obtain an expression for the turbulent kinetic energy spectrum $\hat{E}(\boldsymbol{\kappa},t) \equiv \frac{1}{2}\rho\langle\hat{\boldsymbol{u}}^* \cdot \hat{\boldsymbol{u}}\rangle$, where $\hat{(.)}$ denotes the Fourier transform into the spectral space, $\boldsymbol{\kappa}$ denotes the wave vector with a magnitude κ, and the superscript $*$ denotes the complex conjugate;

$$\boldsymbol{\kappa} \cdot \hat{\boldsymbol{u}} = 0, \tag{S1}$$

$$\rho\frac{\mathrm{d}\hat{\boldsymbol{u}}}{\mathrm{d}t} + \hat{\boldsymbol{G}} = -\iota\boldsymbol{\kappa}\hat{p} - \mu_\mathrm{f}\kappa^2\hat{\boldsymbol{u}} + \hat{\boldsymbol{f}}_\mathrm{inj} + \hat{\boldsymbol{f}}_\mathrm{evp}, \tag{S2}$$

where $\hat{G}$ is the Fourier coefficient of the non-linear convective term appearing in Eq. (3) of the main article, and ι is the imaginary unit. Similar equations can be obtained for the complex conjugate $\hat{\boldsymbol{u}}^*$. When Eq. (S2) is multiplied by $\hat{\boldsymbol{u}}^*$, the pressure term $-\iota\boldsymbol{\kappa}\cdot\hat{\boldsymbol{u}}^*\hat{p}$ vanishes due to the incompressibility constraint (Eq. (S1)), and the viscous term $-\mu_\mathrm{f}\kappa^2\hat{\boldsymbol{u}}\cdot\hat{\boldsymbol{u}}^*$ can be expressed in terms of the kinetic energy; $-2\mu_\mathrm{f}\kappa^2\hat{E}$. The same holds when multiplying the momentum equation of $\hat{\boldsymbol{u}}^*$ by $\hat{\boldsymbol{u}}$. By summing the two equations for $\hat{\boldsymbol{u}}$ and $\hat{\boldsymbol{u}}^*$ and dividing by 2, we have an expression for the time evolution of turbulent kinetic energy $\hat{E}(\boldsymbol{\kappa},t)$

$$\frac{\mathrm{d}\hat{E}(\boldsymbol{\kappa})}{\mathrm{d}t} = \hat{T}(\boldsymbol{\kappa}) + \hat{V}(\boldsymbol{\kappa}) + \hat{F}_\mathrm{inj}(\boldsymbol{\kappa}) + \hat{F}_\mathrm{evp}(\boldsymbol{\kappa}), \tag{S3}$$

where the terms on the right-hand side represent the following contributions: $\hat{T} = -\frac{1}{2}(\hat{\boldsymbol{G}}\cdot\hat{\boldsymbol{u}}^* + \hat{\boldsymbol{G}}^*\cdot\hat{\boldsymbol{u}})$ is due to the non-linear convective term, $\hat{V} = -2\mu_\mathrm{f}\kappa^2\hat{E}$ is due to the fluid dissipation term, $\hat{F}_\mathrm{inj} = \frac{1}{2}(\hat{\boldsymbol{f}}_\mathrm{inj}\cdot\hat{\boldsymbol{u}}^* + \hat{\boldsymbol{f}}^*_\mathrm{inj}\cdot\hat{\boldsymbol{u}})$ is due to the external forcing, and $\hat{F}_\mathrm{evp} = \frac{1}{2}(\hat{\boldsymbol{f}}_\mathrm{evp}\cdot\hat{\boldsymbol{u}}^* + \hat{\boldsymbol{f}}^*_\mathrm{evp}\cdot\hat{\boldsymbol{u}})$ is due to the non-Newtonian stress. The one-dimensional energy spectrum $E(\kappa,t)$ can be obtained by isotropically averaging Eq. (S3) over the sphere of radius κ (i.e., $E(\kappa,t) = \iint_{S(\kappa)}\hat{E}(\boldsymbol{\kappa},t)\mathrm{d}S(\kappa)$, where $S(\kappa)$ is the sphere defined by $\boldsymbol{\kappa}\cdot\boldsymbol{\kappa} = \kappa^2$),

$$\frac{\mathrm{d}E(\kappa)}{\mathrm{d}t} = T(\kappa) + V(\kappa) + F_\mathrm{inj}(\kappa) + F_\mathrm{evp}(\kappa). \tag{S4}$$

where $\frac{\mathrm{d}E}{\mathrm{d}t}$ becomes zero for a statistically stationary flow. Integrating Eq. (S4) from κ to infinity, we obtain the energy-transfer balance

$$0 = \Pi + \mathcal{D}' + \mathcal{F}_\mathrm{inj} + \mathcal{N}', \tag{S5}$$

where $\Pi(\kappa) \equiv \int_\kappa^\infty T(\kappa)\,\mathrm{d}\kappa$, $\mathcal{D}'(\kappa) \equiv \int_\kappa^\infty V(\kappa)\,\mathrm{d}\kappa$, $\mathcal{F}_\mathrm{inj}(\kappa) \equiv \int_\kappa^\infty F_\mathrm{inj}(\kappa)\,\mathrm{d}\kappa$, and $\mathcal{N}'(\kappa) \equiv \int_\kappa^\infty F_\mathrm{evp}(\kappa)\,\mathrm{d}\kappa$ represent the contributions to the spectral power balance from the non-linear convective, fluid dissipation, turbulence forcing, and non-Newtonian terms, respectively. The fluid dissipation term can be expressed as $\mathcal{D}(\kappa) = -\int_0^\kappa V(\kappa)\,\mathrm{d}\kappa = \mathcal{D}'(\kappa) + \langle\epsilon_\mathrm{f}\rangle$, where $\langle\epsilon_\mathrm{f}\rangle = -\int_0^\infty V(\kappa)\,\mathrm{d}\kappa$ is the rate of energy dissipated by the fluid viscosity. Similarly, the non-Newtonian contribution can be written as $\mathcal{N}(\kappa) = -\int_0^\kappa F_\mathrm{evp}(\kappa)\,\mathrm{d}\kappa = \mathcal{N}'(\kappa) + \langle\epsilon_\mathrm{n}\rangle$, where $\langle\epsilon_\mathrm{n}\rangle = -\int_0^\infty F_\mathrm{evp}(\kappa)\,\mathrm{d}\kappa$ is the non-Newtonian dissipation. Substituting these in Eq. (S5), we obtain the energy balance equation (Eq. (1)) used in the main article.

II. FLUID DISSIPATION AND NON-NEWTONIAN DISSIPATION

The rate of turbulent kinetic energy dissipated by the fluid viscosity is $\epsilon_\mathrm{f} \equiv 2\mu_\mathrm{f} s_{ij} s_{ij}$, where i and j are indices for the Cartesian components of a tensor, repeated indices are summed over, and $s_{ij} \equiv (\partial u_i/\partial x_j + \partial u_j/\partial x_i)/2$ is the strain rate. Analogously, we can define the rate of turbulent kinetic energy dissipated by the non-Newtonian extra stresses $\epsilon_\mathrm{n} \equiv -\boldsymbol{u} \cdot (\nabla \cdot \boldsymbol{\tau})$. When averaged throughout a triperiodic volume in statistically steady state, this can be expressed as $\langle \epsilon_\mathrm{n} \rangle = \left\langle \frac{\mathrm{tr}(\boldsymbol{\tau})}{2\lambda} \max(0, \frac{\tau_d - \tau_y}{\tau_d}) \right\rangle$.

III. SUPPLEMENTARY RESULTS

In this section, we provide additional results that support our findings explained in the main article. Fig. S1 shows the good agreement between $Bi_\Lambda = 0$ case and the Newtonian case in the energy spectrum (Fig. S1a) and energy-transfer balance (Fig. S1b) despite the small contribution of the non-Newtonian stress appearing in the energy balance of the $Bi_\Lambda = 0$ case, which is due to the tiny amount of elasticity given to the flow ($Wi_\Lambda = 10^{-3}$). To further verify that the elastic effect is negligible in our results, we run simulations at two different Weissenberg numbers $Wi_\Lambda = 10^{-3}$ and $Wi_\Lambda = 10^{-4}$ for the highest Bingham number considered, i.e., $Bi_\Lambda = 25$. Fig. S5 shows the two cases give the same intermittency correction, and Fig. S2 shows the probability distribution functions of the fluid dissipation ϵ_f and the non-Newtonian dissipation ϵ_n remain unaltered for both cases.

The emergence of the new scaling $E \sim \kappa^{-2.3}$ observed in between the small and intermediate scales in the energy cascade for high Bi_Λ can be seen more clearly when the spectrum is pre-multiplied by the scaling, as shown in Fig. S3. For the two highest Bingham numbers, approximately constant regions emerge where the scaling holds. We can use this new scaling and the fact that the energy spectrum and structure functions form a Fourier transform pair [2] to predict how the structure functions depend on separation r: $S_2 \sim r^{1.3}$, $S_3 \sim r^{1.95}$, $S_4 \sim r^{2.6}$, and $S_6 \sim r^{3.9}$.

The third order structure function is shown in Fig. S4. At low Bingham numbers S_3 follows the K41 exact result $S_3 = -\frac{4}{5}\langle \epsilon_\mathrm{f} \rangle r$[3]. Whereas the $Bi_\Lambda > 10$ structure functions support the new scaling $S_3 \sim r^{1.95}$ at small scales ($20\eta < r < 80\eta$). The third order structure function also gives a measure of the direction of turbulent kinetic energy cascade in the flow, S_3 negative indicates a direct cascade of energy from large to small scales, whereas S_3 positive indicates an inverse cascade [4, 5].

Finally, in Fig. S5, we demonstrate further the increased intermittency of the EVP flow due to the fluid plasticity. We do this by showing in the extended self-similarity form the structure functions S_4 (Fig. S5a) and S_6 (Fig. S5b), compensated by the intermittency correction of $Bi_\Lambda = 0$, and plotted against S_2. We can see clearly how intermittency grows as the fluid becomes more plastic.

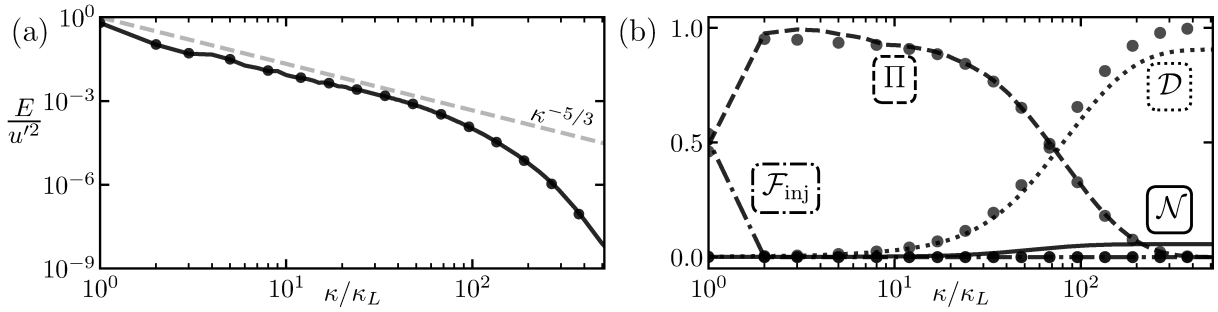

FIG. S1. (a) Turbulent kinetic energy spectrum and (b) energy-transfer balance for the Newtonian flow (circles) and $Bi_\Lambda = 0$ (lines).

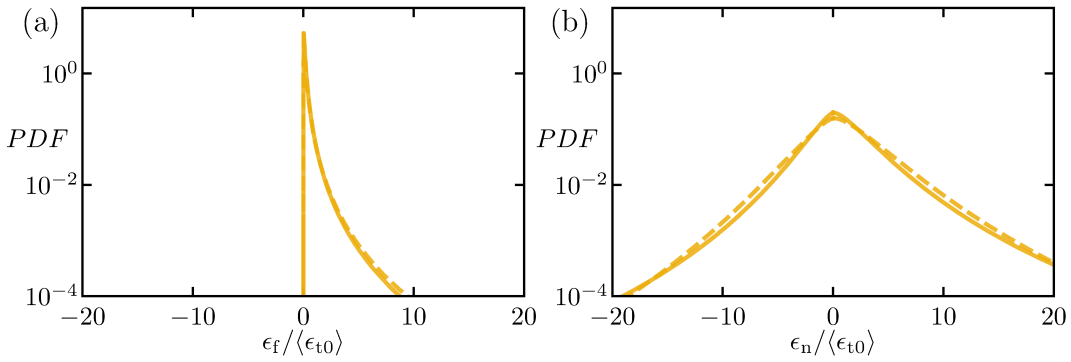

FIG. S2. Probability distribution function (PDF) of (a) the fluid dissipation rate ϵ_f and of (b) the non-Newtonian dissipation rate ϵ_n averaged over time for $Bi_\Lambda = 25$ at $Wi_\Lambda = 10^{-3}$ (solid line) and $Wi_\Lambda = 10^{-4}$ (dashed line). Here, the finite value of ϵ_n in the limit of $Wi_\Lambda \to 0$ is reminiscent of the dissipative anomaly in Newtonian flows [1]

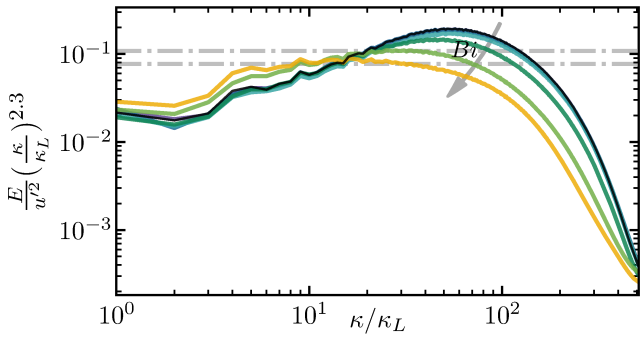

FIG. S3. Compensated turbulent kinetic energy spectra ($E\,\kappa^{2.3}$) of EVP flows with various Bingham numbers, plotted using the same representative colors used in Fig. 2 in the main article. The dash-dotted lines represent an apparent -2.3 scaling which emerges at high Bi_Λ.

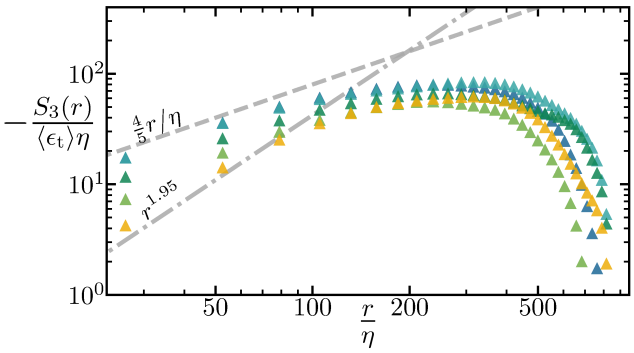

FIG. S4. The third order structure functions. The dashed line shows the K41 exact result, while the dash-dotted line represents the expected scaling of S_3 using the apparent new non-Newtonian scaling $E \sim \kappa^{-2.3}$.

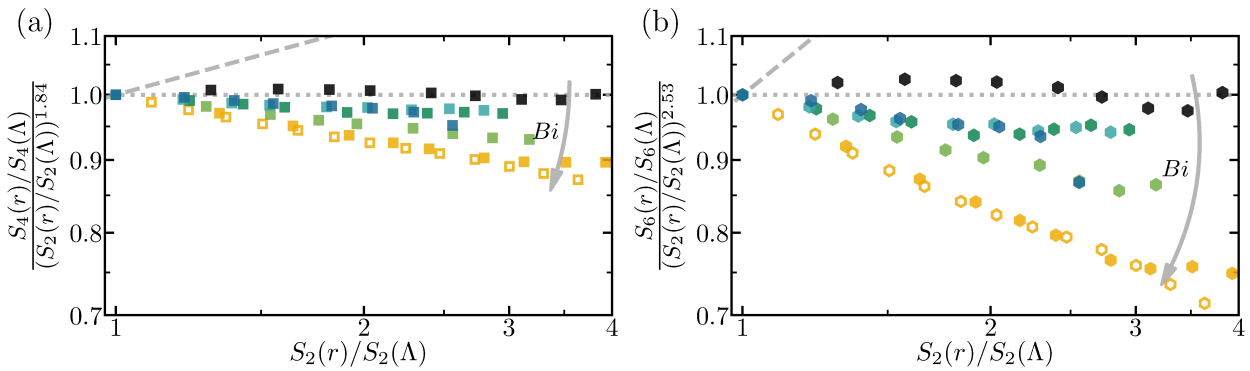

FIG. S5. The extended self-similarity form of the structure functions (a) S_4 and (b) S_6, compensated by the intermittency correction at $Bi_\Lambda = 0$. Filled markers show flows with $Wi_\Lambda = 10^{-3}$ and empty markers show the lower elasticity case $Wi_\Lambda = 10^{-4}$. The dotted line shows the best fit through the $Bi_\Lambda = 0$ data, while the dashed line represents the K41 prediction without intermittency.

REFERENCES

[1] D. A. Donzis, K. R. Sreenivasan, and P. K. Yeung, Journal of Fluid Mechanics **532**, 199 (2005), ISSN 0022-1120, 1469-7645.
[2] P. Davidson, *Turbulence: An Introduction for Scientists and Engineers* (Oxford University Press, 2015), ISBN 978-0-19-872259-5.
[3] A. Kolmogorov, Akademiia Nauk SSSR Doklady **30**, 301 (1941).
[4] H. Xia, D. Byrne, G. Falkovich, and M. Shats, Nature Physics **7**, 321 (2011), ISSN 1745-2473, 1745-2481.
[5] R. T. Cerbus and P. Chakraborty, Physics of Fluids **29**, 111110 (2017), ISSN 1070-6631.

Figure E.1: On final page: render of droplets in a turbulent flow. See chapter 2 for details of the setup.